UC Santa Cruz

UC Santa Cruz Electronic Theses and Dissertations

Title

No Galaxy Left Behind: Measuring the Transfer Function of the Dark Energy Survey with Balrog

Permalink

https://escholarship.org/uc/item/20j538t5

Author

Everett, Spencer Weston

Publication Date

2021

Copyright Information

This work is made available under the terms of a Creative Commons Attribution License, availalbe at https://creativecommons.org/licenses/by/4.0/

Peer reviewed|Thesis/dissertation

eScholarship.org Powered by the California Digital Library
University of California

UNIVERSITY OF CALIFORNIA
SANTA CRUZ

NO GALAXY LEFT BEHIND: MEASURING THE TRANSFER FUNCTION OF THE DARK ENERGY SURVEY WITH BALROG

A dissertation submitted in partial satisfaction of the
requirements for the degree of

DOCTOR OF PHILOSOPHY

in

PHYSICS

by

Spencer Everett

June 2021

The Dissertation of Spencer Everett
is approved:

Professor Tesla Jeltema, Chair

Professor Steve Ritz

Professor Alexie Leauthaud

Dean Quentin Williams
Interim Vice Provost and Dean of Graduate Studies

Copyright © by

Spencer Everett

2021

Table of Contents

List of Figures

List of Tables

Abstract

No Galaxy Left Behind: Measuring the Transfer Function of the Dark Energy Survey with Balrog

by

Spencer Everett

In this dissertation, we describe a calibration and diagnostic framework called `Balrog` which was used to directly sample the selection and photometric biases of the Dark Energy Survey (DES) Year 3 (Y3) dataset. We systematically inject onto the single-epoch images of a random 20% subset of the DES footprint an ensemble of nearly 30 million realistic galaxy models derived from DES Deep Field observations. These augmented images are analyzed in parallel with the original data to automatically inherit measurement systematics that are often too difficult to capture with traditional generative models. The resulting object catalog is a Monte Carlo sampling of the DES transfer function and is used as a powerful diagnostic and calibration tool for a variety of DES Y3 science, particularly for the calibration of the photometric redshifts of distant "source" galaxies and magnification biases of nearer "lens" galaxies. The recovered `Balrog` injections are shown to closely match the photometric property distributions of the fiducial Y3 GOLD catalog, particularly in color, and capture the number density fluctuations from observing conditions of the real data within 1% for a typical galaxy sample. We find that Y3 colors are extremely well calibrated, typically within $\sim$1-8 millimagnitudes, but for a small subset of objects we detect significant magnitude biases correlated with large overestimates of the injected object size due to proximity effects and blending. Finally, we discuss approaches to extend the current methodology to capture more aspects of the transfer function for future analyses.

Acknowledgments

I would like to begin by expressing my extreme gratitude for the endless support of my advisor Tesla Jeltema. You not only guided my transition from student to scientist, but always ensured that I kept perspective on what actually mattered - especially when I was struggling to find a path forward. You truly are a role model for everyone in the group, and I hope to carry your passion and empathy for your students with me as I begin to mentor students of my own. I owe you so much, but I know you will want me to pay it forward.

Much of the presented work in this dissertation would not exist without many great conversations with Eric Huff who in many ways acted as a second advisor to me. Your enthusiasm for finding creative solutions (and paper titles) is infectious, and watching how you approach problems has changed the way I think for the better. I am excited to learn more from you as we work together going forward.

My favorite work memories during my PhD came from the many collaboration meetings, workshops, and even lighthouse hostel stays as part of the Dark Energy Survey where we drank more coffee and espresso than I thought possible. Besides the amazing opportunities to travel widely and observe over 20 nights in Chile, DES introduced me to an incredible community of scientists from whom I've learned nearly everything I know about astronomy and cosmology. A huge thank you to Brian Yanny, Gary Bernstein, and Daniel Gruen for being fantastic mentors as I learned how to navigate both the science and the collaboration, and to Justin Myles, Alex Amon, Devon Hollowood, Alyssa Garcia, Ian Harrison, and especially Sunayana Bhargava for making the experience so much fun. It takes a village, and I am very lucky that DES was mine.

I am forever grateful to Phil Marshall who took a chance on me when I needed it most, and to Risa Wechsler for inviting me to her group meetings where I learned

an enormous amount about cosmology. My brief time at SLAC and Stanford was crucial in setting up my success in grad school and for confirming that this was the right path for me.

I would never have made it this far without the years of guidance and support from my undergraduate advisor Jesús Pando. You not only introduced me to cosmology, but far more importantly taught me so much about the scientist I wanted to become. You've greatly influenced how I interact with academia, and I'm much better off for it.

I'd also like to thank my committee members Steve Ritz and Alexie Leauthaud for their valuable comments and questions about this work both during my qualifying exam and defense, which not only improved the work presented here but made me grapple with bigger questions about the future of the field.

UC Santa Cruz has been an amazing place to be a PhD student and I will greatly miss the many friends I have made here, especially my housemates Maverick, Patrick, Arturo, Johnny, Carey, Ryan, and Jack. I will always remember the surf sessions, redwood hikes, and bouldering outings with you as some of the best moments in my time here.

Finally, I would like to thank my family for their endless love and support. This journey started with countless trips to the library as a child and your constant encouragement to stay curious. Most of all, thank you for always believing in me.

"Though here at journey's end I lie
in darkness buried deep,
beyond all towers strong and high,
beyond all mountains steep,
above all shadows rides the Sun
and Stars forever dwell:
I will not say the Day is done,
nor bid the Stars farewell."

– J.R.R. Tolkien, *The Return of the King*

Part I

Cosmology from Galaxy Surveys

Chapter 1

Introduction

Our understanding of the universe has evolved dramatically over the past century. Once thought to be static and unchanging, we now have overwhelming evidence that the universe had a definite beginning with all known cosmic structure evolving from slight deviations in the initial spatial distribution of matter and energy. Using ever larger telescopes to peer further back in time, astronomers have made numerous surprising discoveries that have culminated in a modern theory of the universe based upon structure formation primarily driven by a "dark" component of the matter distribution and an accelerating expansion of space due to the even more mysterious dark energy. Far from being small, necessary corrections to explain astronomical observations, these dark components dominate over "normal" baryonic matter in the total energetic content of the universe; the relative energy densities of each component are shown in Figure 1.1.

Measuring the properties of these dark phenomena have been a central goal in physics and cosmology ever since their respective discoveries – in part because they offer some of the most convincing evidence that our theories of particle physics and gravity may be incorrect, or at least incomplete. While experiments that hope to directly detect dark matter have been ongoing for decades (see [2] for a

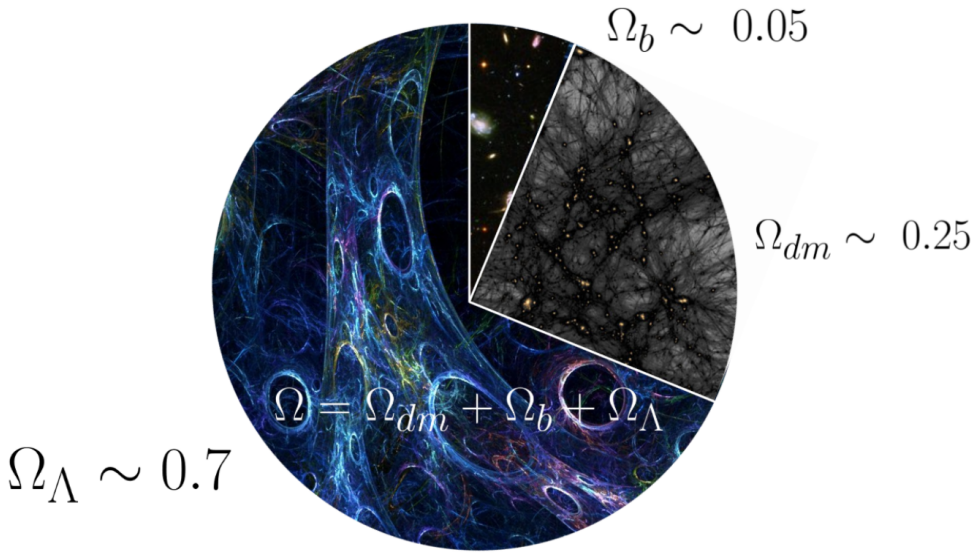

Figure 1.1: The approximate relative energy densities of "normal" baryonic matter Ω_b, dark matter Ω_m, and dark energy Ω_Λ, inferred from measurements of the cosmic microwave background in the early universe. These numbers come from [1] and carry certain assumptions – we discuss this further in Section 2.1.2.

review), no convincing detection has yet been made. In contrast, prospects for the direct detection of dark energy are currently remote. Even worse, there is yet to be a compelling theoretical explanation for its existence or magnitude; the discrepancy between the measured density of dark energy and predictions for the zero-point energy in quantum field theory is often estimated to be 60-120 orders of magnitude [3, 4]. With such a limited theoretical foundation and sparse direct evidence other than their implied existence and aggregate energy contribution, even the most basic constraints on the properties of these important phenomena can have a significant impact on our ability to understand their underlying nature. Just how much dark matter is there? Is it self-interacting? Is dark energy uniform across space, and does it evolve over time?

Recently, some of the most competitive cosmological constraints have come from large galaxy surveys. These systematic scans of the sky, in contrast to tar-

geted studies, aim to capture all sources in a region of the sky down to some limiting flux value, or *depth*, determined by the instrument, aggregate exposure time, and various observational properties such as the sky brightness. The resulting mosaic of the sky is in essence a partial census of the universe across both space and time due to the finite speed of light. These immense catalogs of galaxies – hundreds of millions for the largest current surveys and up to a billion for upcoming Stage IV[1] experiments – allow for statistical measurements of cosmic signals dispersed across the luminous matter distribution, even for quite weak signals.

Dark matter and dark energy affect the geometry, expansion history, and growth of cosmic structures in distinct ways that are captured in the measured properties of sources we observe on the sky. While the net signal is a complex interplay between many competing effects, such as dark energy suppressing the growth of structure that dark matter accelerates, individual *cosmic probes* such as the spatial clustering of galaxies or the distortions in their shapes from gravitational lensing are sensitive to different aspects of the underlying cosmology. The large number of measured sources by galaxy surveys allow us to detect these subtle signals by decreasing the statistical uncertainty of noisy measurements to make increasingly precise estimates of cosmological parameters. A diagram of how a set of common cosmological probes are sensitive to the expansion history and growth of structure is shown in Figure 1.2, as well as whether they probe the state of the universe at early or late times. This distinction is critical as we can compare constraints derived from different epochs to distinguish between models of dark energy that are static from those that evolve over time. In addition, measuring the growth of structure at different epochs can determine whether the expansion

[1]The name commonly given to the next generation of large-scale dark energy experiments, first introduced by the Dark Energy Task Force in [5].

is more likely described by existing cosmological models with dark energy or by modified theories of gravity [6].

The emergence of galaxy surveys has catalyzed a radical transformation of cosmology in the past two decades, evolving it from a data-starved field to one that is now a driver of data science research to fulfill the measurement demands of the ever-growing surveys. Yet this massive influx of data has not resolved the disagreements in the content and evolution of our universe; it has often fueled them! The modern tension in the measured value of the Hubble constant [7] is reminiscent of a similar divergence in experimental conclusions famously debated by astronomers Allan Sandage and Gérard de Vaucouleurs half a century ago [8] despite the accumulation of many orders of magnitude more data than our predecessors. More recent tensions such as the the surprisingly low weak gravitational lensing signal measured around massive galaxies in the Baryon Oscillation Spectroscopic Survey (BOSS; [9]) at small scales ("lensing is low"; [10]) and low-mass galaxy clusters in the first year of data from The Dark Energy Survey[2] (DES; [11]) [12] further emphasize our current predicament: We may live in the era of precision cosmology, but not yet one of *accurate* cosmology.

The largest modern surveys such as DES collect such large data volumes that their analyses are often limited not by noise but by systematics. This will increasingly be the case for Stage IV experiments such as Euclid[3] [13], the Nancy Grace Roman Space Telescope[4] (Roman; [14]), and the The Vera Rubin Observatory's Legacy Survey of Space and Time[5] (LSST; [15]). However, this problem is not solely limited to large surveys. Insufficient (or improper) modeling of systematics can bias measurements and lead to reported uncertainties being significantly

[2] https://www.darkenergysurvey.org/
[3] https://www.euclid-ec.org/
[4] https://roman.gsfc.nasa.gov/
[5] https://www.lsst.org/

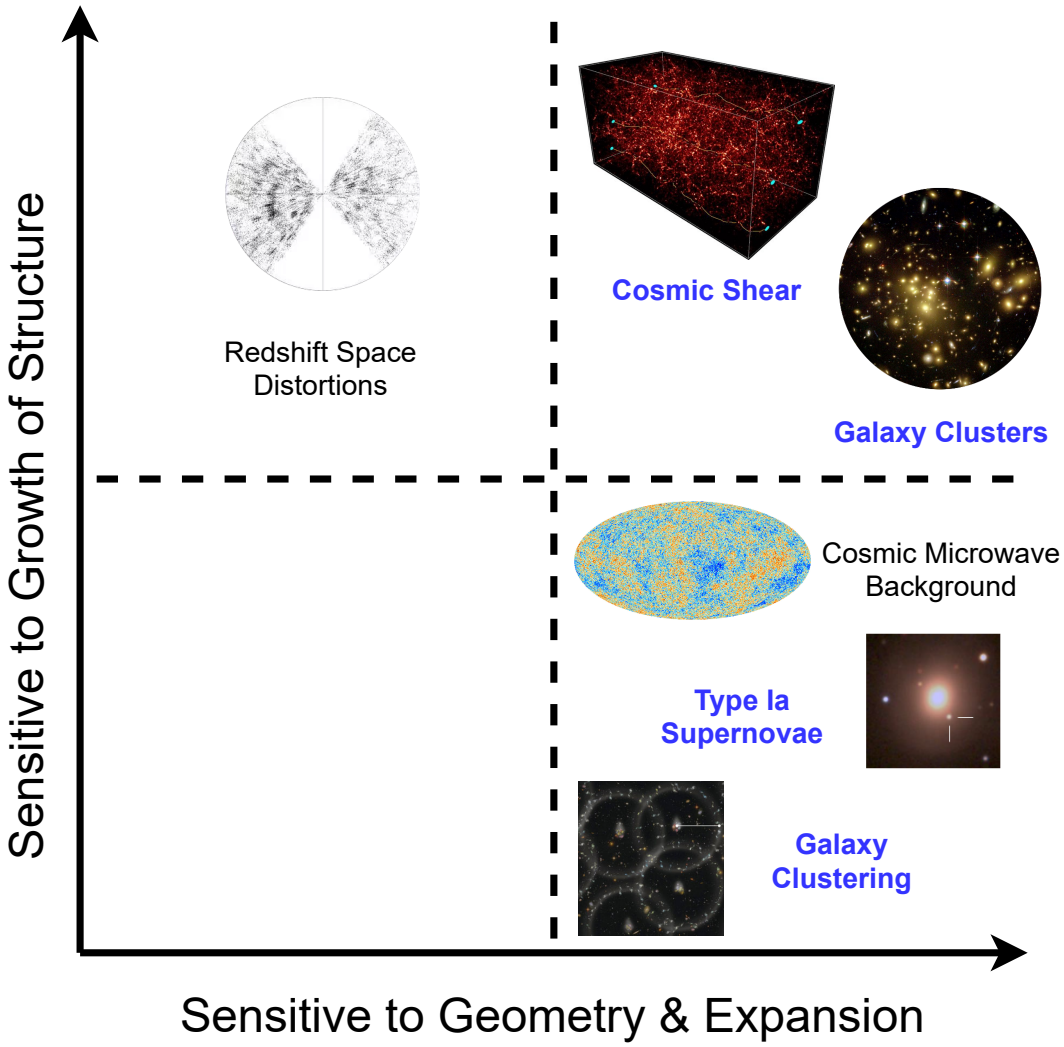

Figure 1.2: An approximate representation of various cosmological probes in relation to whether they are sensitive to the geometry and expansion of space and/or the growth of matter structures. Probes that are directly measured by the Dark Energy Survey, whose photometric calibration and cosmological measurements are the main topic of this dissertation, are designated in blue. Graphic inspired by a talk given by D. Gruen at UC Santa Cruz in January of 2019.

underestimated; this is of critical importance as it determines whether tensions in cosmological parameters are the result of errors in methodology or an indication of new physics beyond the standard model of cosmology. Despite heroic efforts, survey collaborations universally throw out significant fractions of their data in cosmological analyses to keep samples as statistically complete and pure as possible in an effort to combat unknown systematics from contaminating their measurements. Such methods are unnecessarily wasteful and do not fully leverage the available information from our hard-earned (and expensive) photons.

Many of these undesired effects are captured by a survey's *transfer function*, which maps how the properties of the real set of objects in the universe are modulated when measured by a detector with defects and noise, mis-estimated by the complex measurement pipelines of modern surveys, and undergo often arbitrary sample selection cuts on noisy quantities. To make unbiased measurements of cosmic signals, surveys must have a robust estimate of the probability of measuring their sample of sources along with their high-dimensional distribution of photometric properties given an unknowable true distribution. A high-level representation of this crucial process is shown in Figure 1.3. While the transfer function can in principle be forward modeled and validated with simulations, the innumerable set of subtle effects that must be identified and modeled is both impractical and likely futile for the desired measurement precision of current and upcoming surveys. In addition, any such probabilistic models will inevitably be imperfect which introduces model-misspecification biases. This can result in underestimating the true uncertainties of the transfer function by sampling from inaccurate realizations of the data or from universes other than our own.

In this dissertation, we present a way to directly sample the DES transfer function by injecting an ensemble of realistic sources from the DES Deep Fields

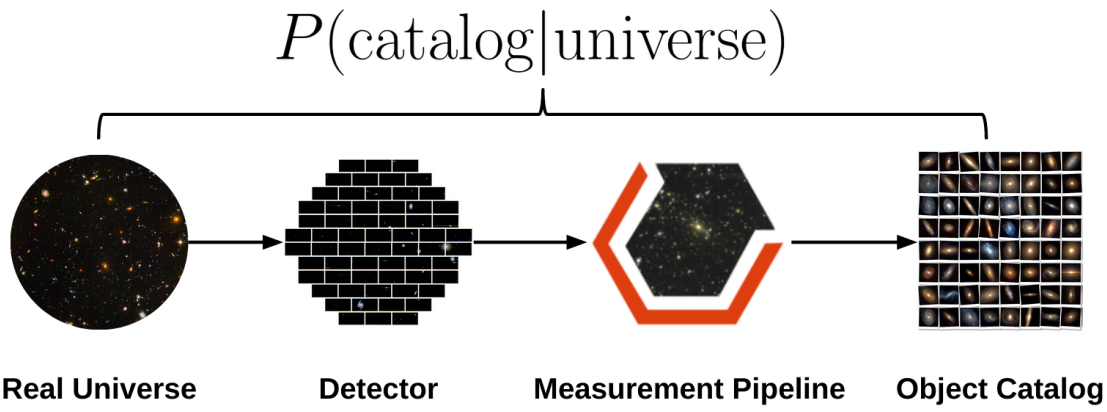

Figure 1.3: A simplified representation of the DES transfer function. In essence, it captures how the true property distribution of objects in the universe are distorted by the detector, the measurement pipeline (including source detection), and sample selection. The detailed characterization of this function is described in Chapters 4 and 5.

(DF) across the real survey images with the `Balrog`[6] framework to automatically inherit the multitude of systematic effects that are often too difficult to model or even identify. This approach by the same name was introduced in [17] but with significant limitations in the realism of its emulation of the survey measurement pipeline and of the properties of its injected sources. While [17] demonstrated an incredibly promising proof of concept to revolutionize precision measurements from galaxy surveys and potentially allow for some of the most ambitious measurements currently proposed by the community, these methodological inaccuracies at such a high computational cost prevented the technique from being used more widely as a general diagnostics tool or for the direct calibration of cosmological measurements in the analysis of the first year of DES data. Taking inspiration from this powerful methodology but creating a completely new framework to incorporate far more aspects of the real DES transfer function, we present here the implementation and application of this new `Balrog` to characterize the transfer

[6] `Balrog` is *not* an acronym. The software was born out of the original authors delving "too greedily and too deep" [16] into their data, hence the name.

function of the Year 3 (Y3) DES data set – comprised of the first three years of observations. In addition, we summarize a few novel uses of an injection pipeline for a variety cosmological measurements and calibrations that facilitate key DES science goals.

1.1 Outline of Dissertation

The structure of this dissertation is as follows: In Chapter 2 we review the relevant cosmological background that forms the basis of modern cosmological models as well as two of the primary cosmic signals measured by galaxy surveys: galaxy clustering and weak gravitational lensing. In Chapter 3 we describe the survey strategy, measurement pipeline, and early cosmological results of DES, and in particular how the various cosmological probes are combined in a joint analysis for stronger constraints. We then introduce the new `Balrog` framework in Chapter 4 which emulates significantly more of the DES measurement pipeline, including single-epoch processing, for the characterization of the survey transfer function using realistic injections derived from the DES DF. The photometric results for `Balrog` stars and galaxies applied to DES Y3 images are presented in Chapter 5 including a detailed examination of the consistency of the resulting `Balrog` catalog with the Y3 data. Many subtle features of the transfer function are highlighted such as a small chromatic bias in the recovery of galaxy magnitudes and a class of catastrophic photometry failures correlated with object size and proximity to other sources.

This is followed in Chapter 6 by a summary of three important applications of `Balrog` to the Y3 cosmological analysis: the calibration of photometric redshifts for the weak lensing "source" galaxies, the impact of magnification bias on constraints from the "lens" galaxy samples, and the discovery of a significant con-

tribution to the noise of Y3 images by undetected sources, which led to incorrect estimates of the sky background. Finally, we close in Chapter 7 with concluding remarks on the current methodological limitations of using injection pipelines at scale for the most ambitious measurements in modern galaxy surveys as well as possible remedies and improvements to `Balrog` for future measurements in DES and upcoming surveys.

Chapter 2

Cosmological Background

Here we overview the necessary cosmological background that informs the design choices and measurements made by galaxy surveys such as DES in order to discover the underlying nature and evolution of our universe. The goal of this chapter is to provide context over completeness; each of the following topics are discussed in much greater detail in either any standard textbook on physical cosmology such as [18, 19, 20] or in the relevant review papers that are cited throughout this chapter. We set the speed of light $c = 1$ and use the West Coast metric and the Einstein summation convention unless otherwise specified.

2.1 Cosmology from General Relativity

Cosmology has a rich history that intersects with philosophy, religion, and mythology as the branch of science primarily concerned with the origin, evolution, and eventual fate of the universe. However, the modern era of physical cosmology began with the formulation of the Einstein Field equations in the early 20th

century [21, 22] which are given below:

$$G_{\mu\nu} + \Lambda g_{\mu\nu} = 8\pi G\, T_{\mu\nu}, \tag{2.1}$$

where G is the gravitational constant, the energy momentum tensor $T_{\mu\nu}$ describes the energy (and thus matter) distribution of the universe, the metric tensor $g_{\mu\nu}$ encodes the geometrical properties of the smooth, four-dimensional manifold[1] we call spacetime on which all matter-energy exists and dynamical physics takes place, and the Einstein tensor $G_{\mu\nu}$ expresses the curvature of this manifold explicitly in terms of $g_{\mu\nu}$. The constant Λ is often referred to as the *cosmological constant* and allows for an intrinsic, non-zero energy density of space itself; we will return to this idea in Section 2.1.3. Briefly, Equation 2.1 explicitly links the energetic content of the universe to its curvature which describes gravity as an intrinsically geometric phenomena. As the famous adage coined by John Wheeler goes, "Spacetime tells matter how to move; matter tells spacetime how to curve" [23].

While this set of 10 independent, nonlinear partial differential equations have accurately described a variety of physical phenomena including the perihelion precession of Mercury [24], the increased deflection angle of starlight around the Sun as compared to Newtonian physics [25], and the existence of gravitational waves [26], unfortunately their complexity limits their practical applicability to many realistic systems. However, the full weight of evidence from astronomical observations by the early 20th century indicated that the universe was, on the largest scales, fairly uniform[2]. This is captured in what is known as *the cosmological principle*: At sufficiently large scales, the universe is spatially homogeneous and

[1] A *manifold* is a topological space that can have global curvature but locally resembles the flat, Euclidean space we commonly experience.

[2] While more recent observations have disputed this, it is a good enough approximation that it is nearly universally assumed for cosmological models. See [27] for an overview)

isotropic [28].

We can use the symmetries implied by the cosmological principle to greatly simplify the Einstein Field Equations. First we encode homogeneity and isotropy into the the metric, which is the well-known Friedmann–Lemaître–Robertson–Walker (FLRW) metric:

$$ds^2 = -dt^2 + a^2(t)\left[\frac{dr^2}{1-kr^2} + r^2(d\theta^2 + \sin^2\theta d\phi^2)\right], \tag{2.2}$$

where ds is a spacetime interval, r is a comoving radial coordinate, and k indicates the global curvature of the spatial hypersurface ($k = +1, 0, -1$ for a universe that is spherical, flat, or hyperbolic respectively). $a(t)$ is the *scale factor* of the universe at time t which describes how the physical separation between two objects at a fixed comoving distance changes over time; it is defined such that $a(0) = 1$ where the lookback time $t = 0$ corresponds to today. Robertson and Walker showed in the 1930's that this metric is the most general solution for an expanding universe that is both homogeneous and isotropic for every spacelike slice [29, 30].

With this metric in hand, the problem can be re-framed as finding the evolution of the scale factor a given assumptions about the curvature and constituents of the universe contained in the solutions to Equation (2.1). The solution is given by the Friedmann equations [31]:

$$H^2(t) = \left(\frac{\dot{a}(t)}{a(t)}\right)^2 = \frac{8\pi G}{3}\rho(t) + \frac{\Lambda}{3} - \frac{1}{k^2a^2(t)}, \tag{2.3}$$

$$\frac{\ddot{a}(t)}{a(t)} = -\frac{4\pi G}{3}\left(\rho(t) + 3p(t)\right) + \frac{\Lambda}{3}, \tag{2.4}$$

where $\rho(t)$ and $p(t)$ are the energy density and pressure of the universe which we model as a fluid, and where we introduced the Hubble parameter $H(t) \equiv \dot{a}/a$

which encapsulates the expansion history of the universe.

2.1.1 Density is Destiny

Equation (2.3) states that the expansion rate of the universe depends on its energy density, curvature, and (in principle) cosmological constant, while Equation (2.4) tells us that its acceleration is dependent on its density and pressure. We can solve these equations exactly for a *perfect fluid*[3] which has an equation of state given by

$$p(t) = w\rho(t) \tag{2.5}$$

where w is a dimensionless constant. If we then model the universe as a mixture of different perfect fluids ρ_i each with a corresponding w_i, we find that

$$\rho_i(t) \propto a(t)^{-3(1+w_i)}. \tag{2.6}$$

The value of w_i determines how the density contribution of a particular energetic component scales with $a(t)$. For non relativistic matter[4] (whether dark or baryonic), $w_m = 0$ and so it scales as a^{-3}; this matches our intuition as a simple decrease in the number density as the spatial volume expands. Radiation in the form of light or massive particles moving at relativistic speeds has $w_r = 1/3$ which gives a scaling of a^{-4}. The additional factor of a comes from the energy loss related to the redshifting of light or decrease in comoving speed of relativistic particles as space expands. Finally, a cosmological constant has the special property that $w_\Lambda = -1$ which leads to a contribution that does not scale with the expansion or size of the universe – hence the name. A visual representation of these scalings are shown in Figure 2.1.

[3] Which is isotropic by definition.
[4] Often called "dust".

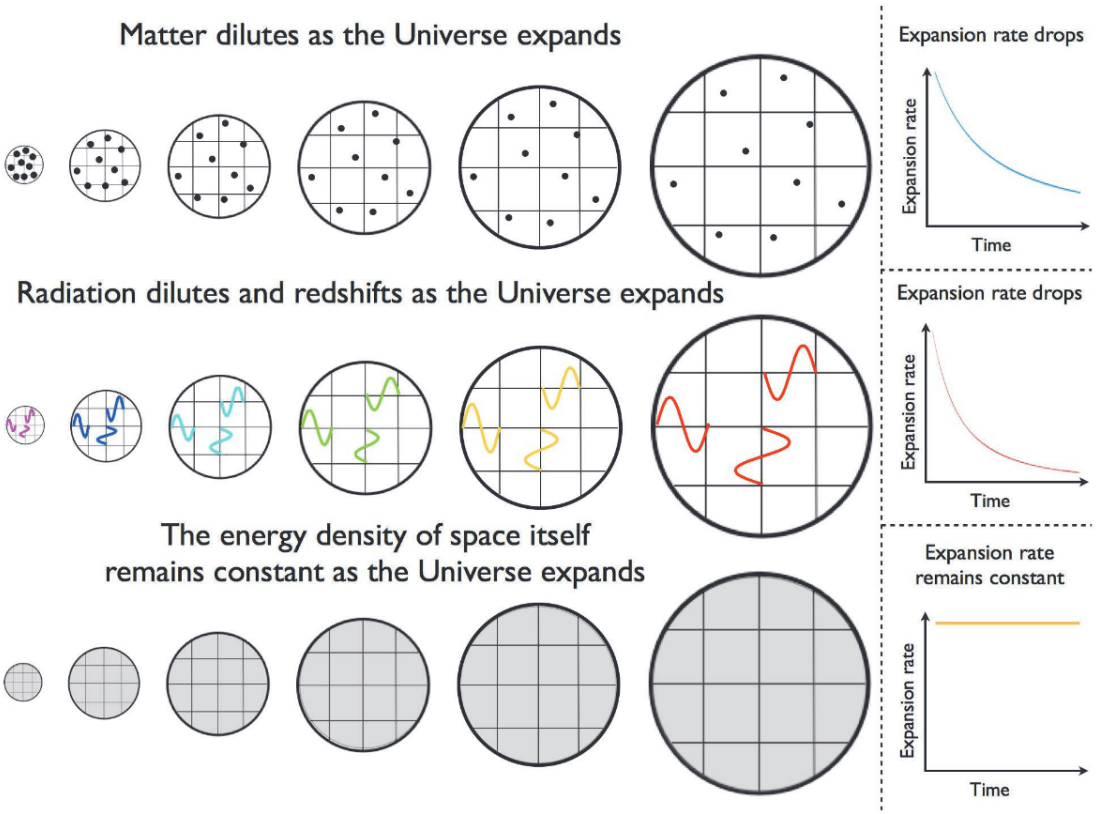

Figure 2.1: A graphical representation of how the energy density of non-relativistic matter, radiation, and a cosmological constant change as the universe expands. A plot of the expansion rate over time for a universe made of only each constituent is shown in the right column. While the matter density dilutes only from the expansion of space, the energy density of radiation falls faster as it is additionally redshifted (or slowed, if relativistic matter). In contrast, the vacuum energy of empty space from a cosmological constant remains fixed. Image taken from [32].

We can then model the total energy density $\rho(a(t))$ in terms of the energy mixture with appropriate scale factors as

$$\rho(a) = \rho_m a^{-3} + \rho_r a^{-4} + \rho_\Lambda. \tag{2.7}$$

Rescaling the density components in the following way using critical density ρ_c at the current epoch ($t = 0$):

$$\begin{aligned} \rho_{c,0} &= \frac{3H_0^2}{8\pi G}, \\ \Omega_{i,0} &= \frac{\rho_{i,0}}{\rho_{c,0}}; \quad i \in m, r, \\ \Omega_k &= -\frac{k}{H_0^2} \\ \Omega_\Lambda &= \frac{\Lambda}{3H_0^2}, \end{aligned} \tag{2.8}$$

where H_0 is similarly the current value of the Hubble parameter, and recognizing that $\Omega_k(t) = 1 - \Omega(t)$, we can combine Equation (2.7) with (2.3) to arrive at the remarkable result

$$\frac{H(t)}{H_0} = \left[\Omega_{r,0}\, a^{-4}(t) + \Omega_{m,0}\, a^{-3}(t) + (1 - \Omega_0) a^{-2}(t) + \Omega_{\Lambda,0}\right]^{1/2}. \tag{2.9}$$

In other words: For a homogeneous and isotropic universe filled with a perfect fluid mixture, we can completely capture it's expansion history simply by measuring the current expansion rate H_0 along with the current energy density of each energetic component! It is from this equation that we often hear the claim *density is destiny*. Figure 2.2 shows how different combinations of these density parameters lead to universes with very different properties, and overplots constraints on these parameters from measurements in our universe.

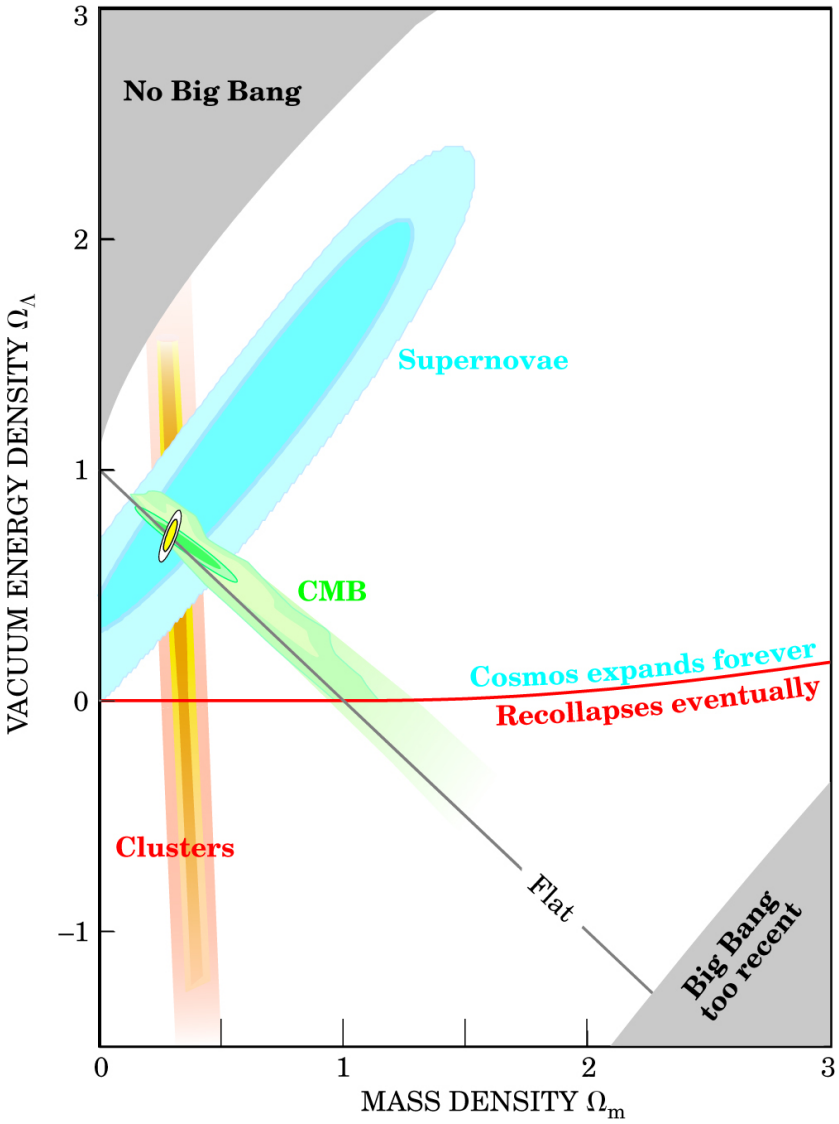

Figure 2.2: A plot showing how different combinations of the matter density Ω_m and vacuum density Ω_Λ as measured today lead to different universes as governed by Equation (2.9). As the contribution due to radiation in the current epoch is extremely small, only the effect of $\Omega_k = (1 - \Omega_0)$ is shown. The constraints of these parameters circa 2003 from measurements of supernovae, galaxy clusters, and the cosmic microwave background (CMB) are overplotted. Figure is taken from [33].

2.1.2 Current Constraints and the Hubble Tension

Our best estimates of these density parameters have traditionally come not from the local universe but from from the cosmic microwave background (CMB), which is the nearly uniform[5] background radiation from $\sim 380,000$ years after the big bang that we observe in all directions on the sky. As light was coupled to the hot, ionized matter before the universe had cooled enough to form neutral hydrogen, called the epoch of recombination, the temperature fluctuations we observe in the CMB correspond to fluctuations in the underlying matter density of the universe. The exact shape and amplitude of the power spectrum of these fluctuations is dependent on the various density parameters Ω_i (in addition to a few others such as scalar spectral index n_s and optical depth τ), which we have constrained very precisely with space-based telescopes such as the Cosmic Background Explorer (COBE; [34]), the Wilkinson Microwave Anisotropy Probe (WMAP; [35]), and the Planck telescope [36]. The latest Planck constraints from [1], which make a few assumptions such as a flat universe and cosmological constant, describe a universe with $H_0 = 67.3 \pm 0.6$ (km/s)/Mpc, $\Omega_m \approx 0.32$ and $\Omega_\Lambda \approx 0.68$, with Ω_m further split into its baryonic and dark components by $\Omega_b \approx 0.05$ and $\Omega_d \approx 0.27$ respectively[6]. This remarkable result offers significant evidence that the ordinary matter we interact with only accounts for less than 1/5th of the total mass and only $\sim 5\%$ of the total energy in the universe. It is the Planck results for these density parameters that are most often quoted and are the basis for Figure 1.1.

While the CMB is an ideal measurement of the state of the early universe as it consists of relatively simple physics, it is not particularly sensitive to the expansion history of the universe as the signal originates from very brief period of time. To

[5] With temperature fluctuations on the order of $\Delta T/\langle T \rangle \sim 10^{-4}$.

[6] The density values listed here are approximate as it is the product $\Omega_i h^2$ that is actually constrained, where $h = H_0/100$.

test if the universe can be accurately described by this fairly simple model of non-relativistic (or "cold") dark matter and a cosmological constant Λ, known as the Λ-Cold Dark Matter (ΛCDM) model, we must test if the parameter constraints from the CMB are consistent with alternative measurements at different epochs in the history of the universe. This is traditionally done through the extragalactic *distance ladder* which is a set of measurement techniques to estimate the physical distance to galaxies in the local universe – particularly with variable luminosity Cepheid stars and Type 1a supernovae. If accurate distances can be measured, then the current value of the Hubble constant H_0 is simply given by Hubble's Law [37]:

$$H_0 = \frac{v}{d} \tag{2.10}$$

where v and d are the recession velocity and proper distance to the galaxy respectively. As the measurement precision of these estimates have increased with better photometric calibration and systematics modeling, this late-time estimate for H_0 has converged to $\sim 73.2 \pm 1.3$ (km/s)/Mpc; a tension of over 4σ with Planck estimates from the CMB [38]. While this discrepancy, known as the *Hubble tension* [7], has been observed for nearly a decade, only in the past few years have the statistical uncertainties decreased sufficiently to confidently conclude that there may be something wrong with the ΛCDM model.

2.1.3 Extensions to ΛCDM

While the resolution to the Hubble tension could be due to underestimated or unmodeled systematics in the numerous, independent measurements, a more exciting possibility is that this tension hints at new physics such as modifications to general relativity or the presence of a new scalar field (see [7] for a review of each). In addition, the lack of a well-understood physical mechanism to produce

the magnitude of dark energy that we observe means that there is no *a priori* reason to expect a cosmological constant or static equation of state. The simplest such models are characterized by an equation of state where $w_\Lambda \neq -1$ which would allow the contribution by dark energy to change over time while still inducing an accelerating expansion (as long as $w_\Lambda < -1/3$). Alternatively, the universe could instead be filled with a dynamic dark energy with a time-dependent equation of state whose simplest parameterization is given by

$$w_\Lambda(a) = w_0 + (1-a)w_a, \tag{2.11}$$

where w_0 is the value of w in the current epoch and w_a encodes how it evolves linearly with $a(t)$. Then for late-time measurements where the contribution from radiation is negligible, and assuming $\Omega_k = 0$, we can rewrite Equation (2.9) as

$$\frac{H(a)}{H_0} = \left[\Omega_m a^{-3} + (1-\Omega_m)a^{-3(1+w_0+w_a)}e^{-3w_a(1-a)}\right]^{1/2}. \tag{2.12}$$

In either case, we can leverage measurements of the expansion rate $H(a)$ and density parameters Ω_i at different moments in the history of the universe to better understand how the universe has evolved and constrain what kinds of mechanisms can produce such evolution. If even these extended models, known as wCDM, cannot explain more complete and precise measurements of the expansion history, then more radical changes to our understanding of the universe may be required such as alternative theories of gravity that extend general relativity.

2.1.4 Cosmological Redshift and Distance Measures

Up to this point, we have parameterized everything in terms of the look-back time t (or implicitly so through $a(t)$) which is defined such that $a = 0$ at the

Big Bang. Unfortunately, t is not directly observable. However, Equation 2.10 suggests that we can estimate the elapsed time between two spacetime events by measuring how the wavelength of light emitted by one source expands with space while it travels to the second. This factor z is called the *redshift* and is given by

$$1 + z = \frac{\lambda_{\text{obs}}}{\lambda_{\text{emit}}}, \tag{2.13}$$

where λ_{obs} and λ_{emit} are the observed and emitted wavelengths respectively. The redshift for sources whose electromagnetic spectrum contains distinct features such as well-known absorption or emission lines can then be accurately estimated.

Using the geodesic equation for a photon traveling through the universe with a FLRW metric, it can be shown that the redshift is related to the scale factor in the following way:

$$a = (1 + z)^{-1}, \tag{2.14}$$

where z is defined to be relative to the present epoch. While in practice there are additional contributions to z such as the relative peculiar velocities of galaxies due to local gravitational infall instead of the expansion of space, for all but the closest galaxies it is dominated by the cosmological redshift. From this we can express the expansion history in terms of z:

$$\frac{H(z)}{H_0(z)} = \left[\Omega_{r,0}\,(1+z)^4 + \Omega_{m,0}\,(1+z)^3) + \Omega_k(1+z^2) + \Omega_{\Lambda,0}\right]^{1/2}. \tag{2.15}$$

Defining $E(z) = H(z)/H_0$ as the dimensionless Hubble parameter and $D_H = c/H_0$ as the Hubble distance, this leads to a redshift-distance relation of

$$\chi(z) = D_H \int_{z_1}^{z_2} \frac{dz}{E(z)}, \tag{2.16}$$

where χ is the *comoving* distance between observers at z_1 and z_2 and scales with the expansion of the universe. This means that the change in χ for two observers whose only relative motion is due to the expansion of space (or the "Hubble flow") will be zero. While in principle Equation 2.16 allows us to calculate the distance to far-away galaxies given an assumed cosmology, conversely we can constrain cosmological parameters by measuring the physical distances to objects along with their redshifts and thus the expansion history.

In a similar fashion, we can define the *transverse comoving distance* at a given z as

$$D_M(z) = \begin{cases} \frac{D_H}{\sqrt{\Omega_k}} \sinh\left(\frac{\sqrt{\Omega_k}\chi(z)}{D_H}\right) & : \Omega_k > 0 \\ \chi(z) & : \Omega_k = 0 \\ \frac{D_H}{\sqrt{|\Omega_k|}} \sin\left(\frac{\sqrt{\Omega_k}\chi(z)}{D_H}\right) & : \Omega_k < 0 \end{cases}, \tag{2.17}$$

which is used to measure the distance $D_M \cdot \delta\theta$ between two sources at the same redshift and angular separation $\delta\theta$. Another distance measure we will find useful is the *angular diameter distance* which is defined to be the ratio of an object's transverse physical size to its angular size:

$$D_A = \frac{D_M(z)}{1+z}. \tag{2.18}$$

Interestingly, D_A does not monotonically increase with z but instead peaks around $z \sim 1$; this means that objects further away than this distance will actually appear larger to us in angular size [39]. Finally, we can now parameterize the look-back time t in terms of z:

$$t = D_H \int \frac{dz}{(1+z)E(z)}. \tag{2.19}$$

Summary

It is worth summarizing how we got here. Combining the Einstein Field Equations with the cosmological principle leads to the FLRW metric and corresponding Friedmann equations. Under the assumption of a perfect fluid, we can get exact solutions that show the expansion rate of the universe is dependent on a small handful of energy density parameters: radiation, matter (both baryonic and dark), curvature (which is likely zero), and dark energy (whether dynamic or a cosmological constant). We have precise estimates of these parameters from measurements of the early universe with the CMB, but there is disagreement in these values when compared to constraints from measurements of the local universe. The resolution of this tension may come from better characterization of measurement systematics or from new physics, both of which provide motivation to make ever more precise cosmological measurements at a variety of epochs.

2.2 Galaxy Clustering and the Growth of Large Scale Structure

The near uniformity of the matter density of the early universe is believed to have originated from an exponential expansion of spacetime in an inflationary epoch during the first $\sim 10^{-32}$ seconds after the big bang [40, 41, 42]. The expansion by over 60 e-foldings (e^{60}) smoothed out large-scale irregularities in the density field and any non-zero local curvature. This extreme burst of expansion in such a short time resolves both the fine-tuning issues of why our universe happens to have a measured curvature so close to zero, known as the flatness problem [43], and why causally-disconnected regions are homogeneous, known as the horizon problem [44]. In essence, inflation sets near-universal initial conditions across the

universe for structures to begin to grow through gravitational interactions.

The evolution of the small density perturbations remaining after inflation to the current epoch carry significant cosmological constraining power. We can define the initial fluctuation field δ as

$$\delta = \frac{\rho - \overline{\rho}}{\overline{\rho}} \tag{2.20}$$

where ρ is the matter density field and $\overline{\rho}$ is the mean density of the universe at that time. ΛCDM predicts a hierarchical formation of structure where overdense regions with $\delta > 0$ pull in surrounding matter which may collapse into viralized objects, while regions with $\delta < 0$ are underdensities and may form large voids. The linear growth of these density fluctuations is conventionally captured in the normalization of the linear matter power spectrum on (comoving) scales of 8 megaparsecs (Mpc), called σ_8, which sets the scale of the fluctuations in the early universe. Larger values of σ_8 indicate larger initial perturbations and a faster growth of structure.

The dynamics of structure formation have no analytical solution once the fluctuations are beyond the linear regime when $\delta \sim 1$, but in an expanding universe an idealized spherical collapse model [45, 46] predicts that perturbations larger than the critical density $\delta_c = 1.686$ will form dark matter halos (for a typical cosmology). The large gravitational potential well of these halos attract the baryonic gas surrounding them and provide the conditions for stellar and galactic formation in their dense centers. Over billions of years the virialized halos interact with one another to form even larger structures such as galaxy clusters and the filaments that connect them, culminating in the cosmic web of structure that we see today.

As dark matter only interacts with baryonic matter gravitationally[7], our ob-

[7]There are many dark matter models that *do* allow for other interactions such as weakly

servations cannot access the dark matter halos that contain most of the matter in these structures. We must instead infer their distribution based upon the distribution of the luminous galaxies that we *can* see scattered across the sky. In order to capture this cosmic signal, the past few decades has seen the advent of wide-field galaxy surveys that catalog the positions and properties of up to hundreds of millions of galaxies to precisely measure this statistical self-clustering as a function of time, or in practice redshift.

2.2.1 2-point statistics

The most common way to characterize the clustering of galaxies in modern cosmology is the two-point correlation function (2PCF). This function $\xi(\chi)$ relates the probability dP that a source is located within a volume element dV at comoving distance χ away from a randomly chosen object:

$$dP = n\,(1 + \xi(\chi))\,dV, \tag{2.21}$$

where n is the mean source density in the observed field [48]. As the radial separation to distant galaxies is a notoriously difficult quantity to measure, it is typical in photometric surveys to instead look at the angular 2PCF $w(\theta)$:

$$dP = \mathcal{N}\,(1 + w(\theta))\,d\Omega, \tag{2.22}$$

which is interpreted in the same way except for a projected source density with mean $\mathcal{N}$ in annular regions of radius θ and thickness $d\Omega$.

In essence, the 2PCFs $\xi(\chi)$ and $w(\theta)$ measure the excess probability of finding

interacting massive particles (WIMPs; [47]), but there has yet to be any evidence confirming such models.

a galaxy separated by another galaxy at various separation distances as compared to a random field. This can be seen more clearly in a typical estimator for $w(\theta)$, such as the one proposed in [49]:

$$1 + w(\theta) = \left(\frac{n_R}{n_D}\right) \frac{DD(\theta)}{DR(\theta)}, \tag{2.23}$$

where $DD(\theta)$ is the weighted number of pair counts of galaxies in a given angular θ bin and $DR(\theta)$ is a similar weighted count of galaxy pairs but between the data and a generated random field of the sources. Here n_R/n_D is the ratio of the mean source density of the random to the real catalog. In practice, the Landy-Szalay (LS) estimator $w_{LS}(\theta)$ introduced in [50]:

$$w_{LS}(\theta) = \left(\frac{n_R}{n}\right)^2 \frac{DD(\theta)}{RR(\theta)} - 2\left(\frac{n_R}{n_D}\right) \frac{DR(\theta)}{RR(\theta)} + 1, \tag{2.24}$$

is commonly used as it optimizes the statistical error and accounts for edge effects for samples that contain complicated masks. The LS estimator is unbiased in the limit of infinite random points, and for most modern measurements the size of the generated random source realizations are much larger than the size of the data.

Importantly, however, this class of clustering estimators does not account for any clustering signal introduced by the selection function of these sources; systematic effects arising from variations in observing conditions on the sky such as incorrect background estimation can couple to the detection probability of objects, and biases in the photometric measurements of their properties can impact their selection into the sample. There have been many attempts to mitigate this problem by re-weighting galaxies according to their local observing conditions or instead imprinting these biases onto the random field itself (e.g. "organized randoms" [51]), but most methodologies depend on providing templates for each

systematic effect which are necessarily not complete. We discuss an approach to this problem in much greater detail and a solution without the use of templates using `Balrog` in Chapter 4.

It is typical to ignore small-scale variations in the source field where the physical modeling is far more difficult due to astrophysical effects such as radiative and kinetic feedback processes. In the case of large angular separations, we pixelate the projected source galaxy density field $n(\hat{\boldsymbol{n}})$ into a galaxy fluctuation field $\delta_g(\hat{\boldsymbol{n}})$:

$$\delta_g(\hat{\boldsymbol{n}}) = \left(\frac{n(\hat{\boldsymbol{n}})}{\overline{n}}\right) - 1 \tag{2.25}$$

where $\overline{n}$ is the mean density in the observed region and $\hat{\boldsymbol{n}}$ represents the position of a particular pixel. We can then express the angular correlation function $w(\theta)$ on these scales as

$$w(\theta) = \langle \delta_g(\hat{\boldsymbol{n}}) \delta_g(\hat{\boldsymbol{n}} + \theta) \rangle, \tag{2.26}$$

where $\langle\rangle$ denotes an ensemble average over pairs of pixels with angular separation $\theta = \cos^{-1}(\hat{\boldsymbol{n}}_1 \cdot \hat{\boldsymbol{n}}_2)$ as long as θ is sufficiently larger than the pixel size.

Finally, in many measurements it is more common to constrain the angular power spectrum $P(k)$ which is related to $w(\theta)$ through a Fourier transform of $w(\theta)$ in spherical coordinates:

$$\mathcal{P}_\ell = 2\pi\mathcal{N} \int_{-1}^{1} w(\theta) P_\ell(\theta) d\cos\theta, \tag{2.27}$$

where P_ℓ is the Legendre polynomial of index ℓ.

2.2.2 Photometric Redshifts

To constrain the evolution of $w(\theta)$ over time, *photometric*[8] galaxy surveys typically split their sources into tomographic redshift bins of various sizes, or assign a probabilistic redshift bin distribution to each source (e.g. [52]). We can then index w by the the bin indices i, j for the relevant fluctuation fields in the following way:

$$w^{ij}(\theta) = \langle \delta_g^i(\hat{\boldsymbol{n}}) \delta_g^j(\hat{\boldsymbol{n}} + \theta) \rangle, \tag{2.28}$$

where $i = j$ corresponds to the *auto-correlation* of the fluctuation field δ_i while $i \neq j$ corresponds to the *cross-correlation* of the fluctuation fields δ_g^i and δ_g^j. On sufficiently large scales, we can express an individual projected fluctuation field $\delta_g(\hat{\boldsymbol{n}})$ as

$$\delta_g(\hat{\boldsymbol{n}}) = \int \phi(z) \delta(\hat{\boldsymbol{n}}, z)\, dz \tag{2.29}$$

where δ is the 3-dimensional galaxy fluctuation field and $\phi(z)$ is the *radial selection function* [53]. This function characterizes the probability of a galaxy at a true redshift of z being included in the sample used for the estimate of $w(\theta)$. If surveys could make their sample cuts on the true redshifts, then this $\phi(\theta)$ would be simply

$$\phi(z) = \frac{dN_g}{dz} W(z). \tag{2.30}$$

Here dN_g/dz is the true number of galaxies per unit redshift and $W(z)$ is a window function that encodes the selection criteria of the sample including quality cuts (e.g. masking, flags), photometric cuts (e.g. signal-to-noise (S/N), magnitude, color), and the tomographic redshift binning.

[8] In contrast to *spectroscopic* surveys, which have robust redshift estimates for individual sources.

As the true redshift z is not accessible, we can instead express $\phi(z)$ as

$$\phi(z) = \frac{dN_g}{dz} \int P(z|z_p) W(z_p)\, dz_p, \tag{2.31}$$

where z_p is the estimated *photometric redshift* of an object, $P(z|z_p)$ is the conditional probability of the object having a true redshift z given it's estimated z_p, and $W(z_p)$ is now the photometric redshift window function. We can then update Equation (2.28) to be

$$\begin{aligned} w^{ij}(\theta) &= \langle \delta_g^i(\hat{\boldsymbol{n}}_1) \delta_g^j(\hat{\boldsymbol{n}}_2) \rangle & (2.32) \\ &= \int_{\Delta z^i} \phi^i(z_1)\, dz_1 \int_{\Delta z^j} \phi^j(z_2) \langle \delta(\hat{\boldsymbol{n}}_1, z_1) \delta(\hat{\boldsymbol{n}}_2, z_2) \rangle\, dz_2 & (2.33) \\ &= \int_{\Delta z^i} \phi^i(z_1)\, dz_1 \int_{\Delta z^j} \phi^j(z_2)\, \xi(\chi(z_1), \chi(z_2), \theta)\, dz_2, & (2.34) \end{aligned}$$

where ϕ^i is now indexed by the redshift bin Δz^i. The sensitivity of $w(\theta)$ to the expansion history of the universe is now seen clearly in the comoving distance $\chi(z)$.

$P(z|z_p)$ and $W(z_p)$ are extremely difficult to estimate in practice due to the many subtle systematic errors that enter in the transfer between a source's true properties and those determined by a survey's detector and measurement pipeline, including how this modulation varies across the sky with different observing conditions. The sample sizes of previous analyses were usually small enough that statistical errors dominated over these systematic biases and Gaussian photometric errors for properties like magnitude and color were common such as in [52]. However, more accurate estimates of the selection and transfer properties of sources in galaxy samples are needed for more robust calibration of the impact of photometric redshift estimation on the cosmic clustering signal contained in $w(\theta)$. The application of `Balrog` to characterize these effects in the context of the DES

Y3 source galaxy sample is described in detail in Chapter 6.

2.2.3 Galaxy Bias and the Connection to Dark Matter

While we expect galaxies to be good tracers of the underlying matter distribution as they form in the peaks of the dark matter field, the different properties and self-interactions of baryonic matter leads to a density evolution that is only partially coupled to the dark matter field [54]. At a minimum, it is reasonable to expect that the amplitude and shape of the clustering signal for dark matter halos is not the same as the clustering of galaxies. It is then crucial to accurately model the joint probability characterizing the connection between galaxy properties and the halos they reside in for understanding galaxy formation, the inference of cosmological parameters from galaxy surveys, and distinguishing between various dark matter models.

Unfortunately, the connection between galaxies and their dark matter halos is extremely complex with many unresolved questions (see [55] for a recent review). On sufficiently large scales, the effects of complex astrophysical interactions such as gas cooling, star formation and feedback from supernovae on the shape of the 2PCF are negligible and the signal is dominated by the clustering of galaxies *in different halos* rather than the clustering of galaxies *in the same halo*. This distinction is often characterized by splitting the 2PCF into the 2-halo and 1-halo terms respectively:

$$\xi(\chi) = \xi_{1h}(\chi) + \xi_{2h}(\chi). \tag{2.35}$$

Most current galaxy surveys implement scale cuts on χ (or in practice θ) to only measure the 2-halo term in the linear regime where the bias between the clustering signal of the dark matter halos and the galaxies that fill them is scale-

independent:

$$b(z) = \left(\frac{\xi_{gal}\left(\chi(z)\right)}{\xi_{dm}\left(\chi(z)\right)} \right)^{1/2}, \tag{2.36}$$

where b is called the *galaxy bias*[9] which evolves over time, or equivalently redshift. Then under these assumptions, we can update Equation (2.34) to be

$$w^{ij}(\theta) = \int_{\Delta z^i} b(z_1)\phi^i(z_1)\, dz_1 \int_{\Delta z^j} b(z_2)\phi^j(z_2)\, \xi(\chi(z_1), \chi(z_2), \theta)\, dz_2, \tag{2.37}$$

which now includes both the effects of photometric redshift calibration uncertainties and the bias from imperfect galaxy tracers. While galaxy clustering is a powerful tool for probing the evolution of the primordial density perturbations into the cosmic structures that we see today, the degeneracy between the cosmological parameters and the galaxy bias in their ability to set the scale of these fluctuations often requires additional constraints from other observational probes to break this degeneracy.

2.3 Weak Gravitational Lensing

Instead of using the spatial clustering of luminous matter to trace the hidden dark matter field, we can probe the total matter distribution of the universe more directly by measuring the (usually) subtle deflections of light emanating from distant galaxies as it travels through intervening mass structures on the way to our telescopes. This distortion is called *gravitational lensing*, and results from the principle that photons travel along null geodesics[10] in spacetime. As the local spacetime curvature is non-zero in the presence of inhomogeneous matter such as

[9] Or often just *bias*, which can add significant confusion given the numerous biases in any discussion of galaxy surveys.

[10] This is often described as light traveling along a path between spacetime events that minimizes the elapsed time, but technically it is a path that is stationary in time.

galaxies and dark matter halos, the resulting spacetime geodesic that a photon travels on will also be curved. This phenomena was famously used as strong evidence in support of general relativity after observations during the solar eclipse on May 29, 1919 measured the distortion in the positions of stars near the sun's surface in close agreement with Einstein's predictions [56].

The results of this distortion can be dramatic, stretching compact galaxy profiles into large arcs, Einstein rings, or even into multiple distinct images. These are examples of *strong* gravitational lensing and can be used to study the mass and substructure of large galaxy clusters[11] as well as constrain the Hubble parameter $H(z)$ by measuring the time delay between flux measurements in each image (see [57] for a review). Most matter fields are not dense enough to produce these effects and instead slightly perturb light profiles in a linear regime called *weak* lensing. While the small shearing and magnification of each galaxy shape is far harder to detect than brilliant arcs and rings, the effect is present for *all* sources and thus can be used to estimate the mass density across the sky.

The most crucial feature of gravitational lensing in the context of cosmology is that the deflection angle is not sensitive to the type of mass producing the gravitational field – only the amplitude and shape of the matter distribution. This makes lensing a direct probe of the underlying matter density field and does not require difficult modeling of the galaxy-halo connection or assumptions about galaxy bias[12]. In addition, the distortion we observe depends on the integrated line-of-sight mass between the source and the telescope which probes mass structures not only at different radial distances but thus also at different epochs in the expansion history of the universe. It is for these reasons that the weak lensing

[11] Which are the largest virialized structures in the universe, and confusingly *not* the same concept as galaxy clustering.

[12] Though mass estimation from lensing comes with its own theoretical biases, such as the mass-sheet degeneracy [58].

measurements of galaxies in different redshift bins, called cosmic tomography, has become an essential measurement in all modern and upcoming galaxy surveys (see [59, 60, 61, 62] for a few recent examples).

There are however numerous practical complications in using lensing as a cosmological probe. In particular, the lensing distortion for the vast majority of galaxy profiles is dominated by the intrinsic shape of the object; in most cases by a factor of 100 or more [63]. The presence of this *shape noise* requires a statistical measurement to average out the random intrinsic shapes and capture the residual, correlated distortion induced by the light from galaxies traveling through the same cosmic structures. As the largest modern galaxy surveys now measure the shapes of hundreds of millions of galaxies, the mean measurements have become so precise that otherwise relatively small systematics in the modeling of the point-spread function (PSF) [63], photometric shape calibration [64], blending of sources [65], and unwanted stellar contamination [63] can significantly bias the resulting cosmological constraints. Accurately accounting for these systematic effects is crucial for the continued success of galaxy survey, which we will return to after briefly introducing this important cosmological probe.

2.3.1 Gravitational Lensing Formalism

Here we summarize some of the most important results from a formal treatment of gravitational lens systems, particularly focusing on the portions most relevant to galaxy survey observations. A far more complete treatment is given in [66] which guides much of this summary. For the simplest scenario of a point mass M, general relativity predicts a deflection angle $\hat{\alpha}$ exactly twice that predicted by Newtonian gravity [67] to be

$$\hat{\alpha} = \frac{4GM}{c^2\xi} \tag{2.38}$$

where G is the gravitational constant, ξ is the projected distance from the source to the lens mass known as the impact parameter[13], and where we have chosen to explicitly show the dependence on c for this section. As the mass lens has infinitesimal width by definition, we can represent the gravitational lens system as a source with angular extent β, observed extent θ, and deflection angle $\hat{\alpha}$ in Figure 2.3. This estimate holds as long as ξ is much larger than the Schwarzschild radius of the lens given by $R_s = 2GMc^{-2}$ which implies that $\hat{\alpha} << 1$ and thus is safely in the weak lensing regime.

Under the assumption of a sufficiently weak gravitational field, the Einstein field equations can be safely linearized and we can express the deflection angle for a more complex lensing mass distribution as the sum (or integral) of the individual lensing contributions:

$$\hat{\boldsymbol{\alpha}}(\boldsymbol{\xi}) = \frac{4G}{c^2} \sum dm(\xi_1', \xi_2', r_3') \frac{\boldsymbol{\xi} - \boldsymbol{\xi'}}{|\boldsymbol{\xi} - \boldsymbol{\xi'}|^2} \tag{2.39}$$

$$= \frac{4G}{c^2} \int d^2\xi' \int dr_3' \, \rho(\xi_1', \xi_2', r_3') \frac{\boldsymbol{\xi} - \boldsymbol{\xi'}}{|\boldsymbol{\xi} - \boldsymbol{\xi'}|^2}, \tag{2.40}$$

where ρ is the three-dimensional mass density of the lens, r_3 is the radial distance from the lens plane, and $\boldsymbol{\xi}$ is now a two-dimensional vector on the lens plane. This procedure is analogous to using the Born approximation in quantum mechanics [68]. We can then define the *surface mass density* $\Sigma(\boldsymbol{\xi})$ as

$$\Sigma(\boldsymbol{\xi}) = \int dr_3 \, \rho(\xi_1, \xi_2, r_3), \tag{2.41}$$

which is the lens mass density projected onto the lens plane. Using this definition,

[13] This is an unfortunate convention due to the dual use of ξ as the impact parameter *and* the 2PCF.

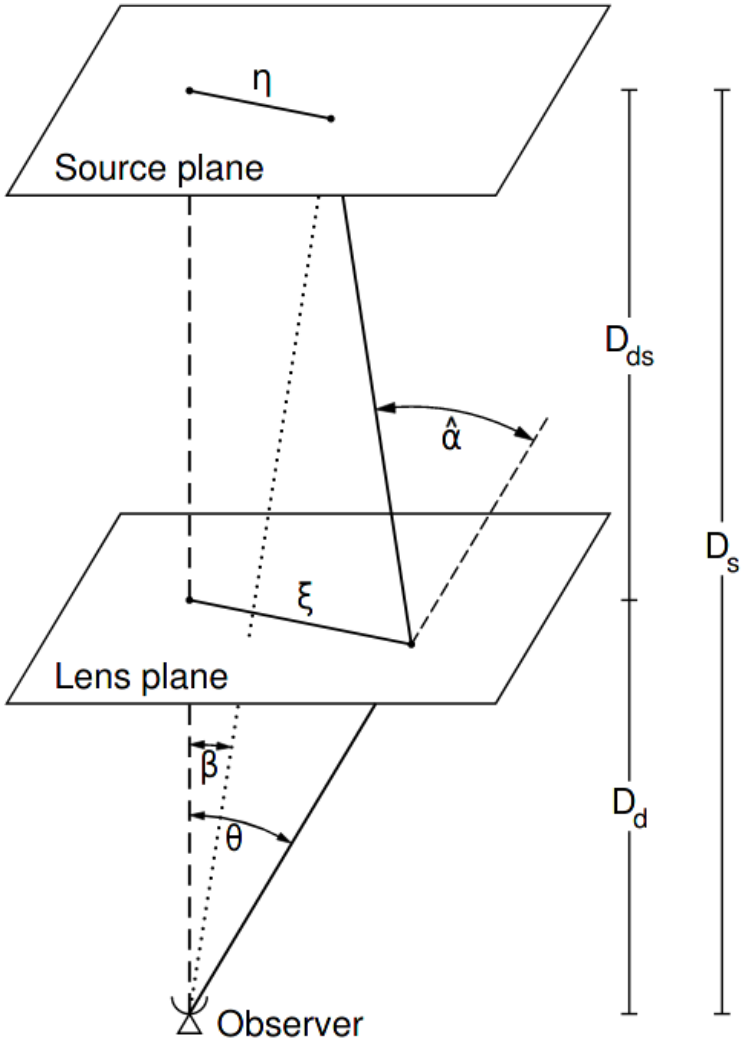

Figure 2.3: A diagram of a typical gravitational lens system for a point mass or when using the thin-lens approximation, taken from [66]. β is the angular position of a photon in the source plane, θ is the distorted angular position in the lens plane, ξ is the impact parameter, and α is the deflection angle. The relevant distance scales are shown on the right, with D_d defined as the distance from the observer to the lens plane, D_s as the distance from the observer to the source plane, and D_{ds} as the distance between the source and lens planes.

$\hat{\alpha}$ is then given by

$$\hat{\boldsymbol{\alpha}}(\boldsymbol{\xi}) = \frac{4G}{c^2}\int d^2\xi' \Sigma(\boldsymbol{\xi}) \frac{\boldsymbol{\xi} - \boldsymbol{\xi'}}{|\boldsymbol{\xi} - \boldsymbol{\xi'}|^2}. \tag{2.42}$$

This expression for $\hat{\boldsymbol{\alpha}}$ is a valid approximation as long as the deflection of the light ray from a straight path is small compared the scale on which the mass distribution changes.

We can use this expression for $\hat{\boldsymbol{\alpha}}$ to relate the true position of a source to the observed position on the sky after lensing. This is given by the lens equation

$$\boldsymbol{\beta} = \boldsymbol{\theta} - \frac{D_{\mathrm{ds}}}{D}\hat{\boldsymbol{\alpha}}(D_{\mathrm{d}}\boldsymbol{\theta}) \equiv \boldsymbol{\theta} - \boldsymbol{\alpha}(\boldsymbol{\theta}), \tag{2.43}$$

where $\boldsymbol{\beta}$, $\boldsymbol{\theta}$, and the distance measures are all defined in the same way as Figure 2.3 and the quantity $\boldsymbol{\alpha}(\boldsymbol{\theta})$ is defined to be the scaled deflection angle in relation to $\hat{\boldsymbol{\alpha}}(\boldsymbol{\xi})$. It is possible for Equation (2.43) to permit multiple solutions for fixed $\boldsymbol{\beta}$ which corresponds to the multiple images of strong lensing. This is often quantified by using the dimensionless surface mass density $\kappa(\boldsymbol{\theta})$ called the *convergence field* defined as

$$\kappa(\boldsymbol{\theta}) = \frac{\Sigma(D_{\mathrm{d}}\boldsymbol{\theta})}{\Sigma_{\mathrm{cr}}}; \quad \Sigma_{\mathrm{cr}} = \frac{c^2}{4\pi G}\frac{D_{\mathrm{s}}}{D_{\mathrm{d}}D_{\mathrm{ds}}}, \tag{2.44}$$

where Σ_{cr} is the critical surface mass density. A source located at a point in the convergence field where $\kappa > 1$ will result in multiple images or, in very symmetric mass distributions, an Einstein ring. The ratio of the distances included in Σ_{cr} encodes the efficiency of the lens system, being minimized (and thus the lensing effect is maximized) at $D_{\mathrm{s}} = D_{\mathrm{ds}}$. This matches our intuition that a lens is most effective halfway between an observer and a source.

Using the convergence field, we can now express the scaled version of Equation (2.42) as

$$\boldsymbol{\alpha}(\boldsymbol{\theta}) = \frac{1}{\pi}\int d^2\,\theta' \kappa(\boldsymbol{\theta'}) \frac{\boldsymbol{\theta} - \boldsymbol{\theta'}}{|\boldsymbol{\theta} - \boldsymbol{\theta'}|^2}. \tag{2.45}$$

In this form, it is suggestive that $\boldsymbol{\alpha}(\boldsymbol{\theta})$ can instead be written as the gradient of a scalar field $\psi(\boldsymbol{\theta})$:

$$\boldsymbol{\alpha}(\boldsymbol{\theta}) = \nabla\psi(\boldsymbol{\theta}) \tag{2.46}$$

where

$$\psi(\boldsymbol{\theta}) = \frac{1}{\pi}\int d^2\theta'\,\kappa(\boldsymbol{\theta'})\ln|\boldsymbol{\theta}-\boldsymbol{\theta'}|. \tag{2.47}$$

$\psi(\boldsymbol{\theta})$ is called the *deflection potential* and is analogous to a Newtonian gravitational potential and satisfies the Poisson equation $\nabla^2\psi(\boldsymbol{\theta}) = 2\kappa(\boldsymbol{\theta})$.

2.3.2 Shear and Magnification

In principle, the distorted shape of an extended source is determined by solving equation (2.43) for all points in the surface brightness distribution $I(\boldsymbol{\beta})$. Liouville's theorem ensures that the total surface brightness is conserved, which gives

$$I(\boldsymbol{\theta}) = I^{(s)}(\boldsymbol{\beta}(\boldsymbol{\theta})) \tag{2.48}$$

where $I^{(s)}$ is the surface brightness density of the object in the source plane. For sources with angular size much smaller than the scale on which $\psi(\boldsymbol{\theta})$ changes, we can locally linearize the lens equation at $\boldsymbol{\theta_0}$ to be

$$\boldsymbol{\beta}-\boldsymbol{\beta_0} = \mathcal{A}(\boldsymbol{\theta_0})\cdot(\boldsymbol{\theta}-\boldsymbol{\theta_0}), \tag{2.49}$$

where $\boldsymbol{\beta_0}\equiv\boldsymbol{\beta}(\boldsymbol{\theta_0})$ and the Jacobian of the lensing transformation $\mathcal{A}$ is known as the *distortion matrix*:

$$\mathcal{A}(\boldsymbol{\theta}) \equiv \frac{\partial\boldsymbol{\beta}}{\partial\boldsymbol{\theta}} = \left(\delta_{ij} - \frac{\partial^2\phi(\boldsymbol{\theta})}{\partial\theta_i\theta_j}\right) = \begin{pmatrix} 1-\kappa-\gamma_1 & -\gamma_2 \\ -\gamma_2 & 1-\kappa+\gamma_1 \end{pmatrix}, \tag{2.50}$$

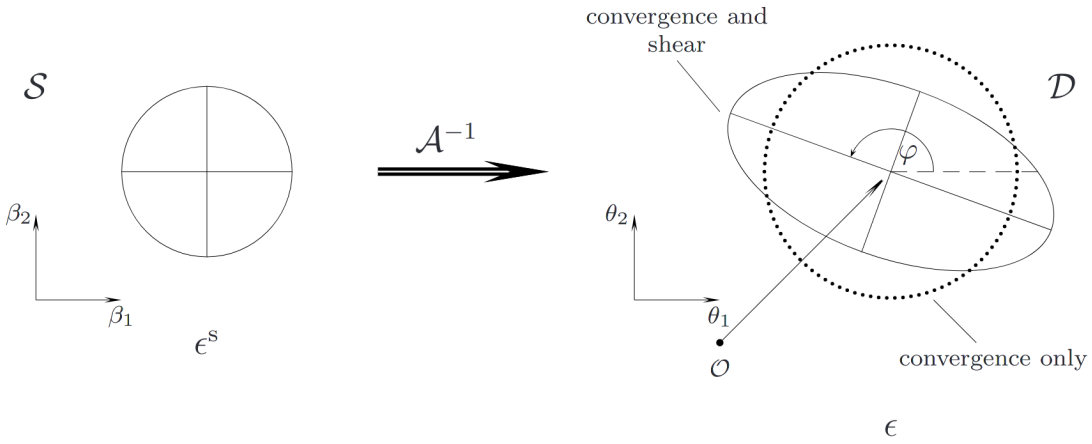

Figure 2.4: The weak lensing transformation of a circular source, shown on the left, to a measured ellipse governed by the distortion matrix $\mathcal{A}$. The solid lines are the profile contour while the dotted line corresponds to the magnified profile in the absence of shear. Image credit: M. Bradac.

where we have introduced the complex lensing *shear* $\gamma \equiv \gamma_1 + i\gamma_2 = |\gamma|e^{2i\theta}$[14]. With this approximation, Equation (2.48) becomes

$$I(\boldsymbol{\theta}) = I^{(s)}\left(\boldsymbol{\theta_0} + \mathcal{A}(\boldsymbol{\theta_0}) \cdot (\boldsymbol{\theta} - \boldsymbol{\theta_0})\right). \tag{2.51}$$

This equation distorts a circular source profile into an ellipse, with a magnification factor μ given by

$$\mu = \frac{1}{\det \mathcal{A}} = \frac{1}{(1-\kappa)^2 - |\gamma|^2}, \tag{2.52}$$

and a stretch along the semi-major and semi-minor axes given respectively by

$$a = \frac{R}{1-\kappa-|\gamma|}; \quad b = \frac{R}{1-\kappa+|\gamma|}, \tag{2.53}$$

where R is the radius of the circular source profile. A visual representation of this transformation is shown in Figure 2.4.

[14]The factor of 2 in the complex phase comes from the fact that an ellipse transforms as a spinor.

If all galaxies were intrinsically round, then we could precisely measure the lensing distortion for each object and make high-resolution maps of the mass density across the sky. In reality, the intrinsic shapes of galaxies dominates the measurement and any inference of the local matter field requires the statistical averaging of many sources. In addition, the small values of κ and γ in the weak lensing regime make it very difficult to accurately disentangle the distinct effects on individual sources. For this reason we define the *reduced shear* $g = |g|e^{2i\theta}$ to be

$$g \equiv \frac{\gamma}{1-\kappa}. \tag{2.54}$$

as it is the main observable we can detect with photometric surveys. This results in the distortion matrix having the particularly convenient form

$$\mathcal{A}(\boldsymbol{\theta}) = (1-\kappa)\begin{pmatrix} 1-g_1 & -g_2 \\ -g_2 & 1+g_1 \end{pmatrix}, \tag{2.55}$$

along with a straightforward way to estimate $|g|$ from the axis ratio of a lensed circular source:

$$|g| = \frac{1-b/a}{2+b/a}. \tag{2.56}$$

2.3.3 Measuring Shapes and Shear

The intrinsic, non-circular light profiles of galaxies can be quite complex and are often not well estimated by an ellipse. To map the relation between the intrinsic and observed profiles in terms of g, we need a generalized ellipticity for an arbitrary image shape. This is most commonly done in terms of the second

brightness moments of the profile:

$$Q_{ij} = \frac{\int d^2\theta\, w[I(\boldsymbol{\theta})](\theta_i - \overline{\theta_i})(\theta_j - \overline{\theta_j})}{\int d^2\theta\, w[I(\boldsymbol{\theta})]}; \quad i,j \in \{1,2\}, \tag{2.57}$$

where $\overline{\theta_i}$ is the first moment of the profile along angular dimension i and w is an appropriately chosen weight function [69]. The trace of Q measures the size of the image, while the off-diagonal elements encode the elliptical properties.

From this definition we can define a measured complex ellipticity $\epsilon = |\epsilon| e^{2i\theta}$ given by

$$\epsilon \equiv \frac{Q_{11} - Q_{22} + 2iQ_{12}}{Q_{11} + Q_{22} + 2(Q_{11}Q_{22} - Q_{12}^2)^{1/2}}. \tag{2.58}$$

As the measured moment matrix Q is related to the source moments $Q^{(s)}$ by the distortion matrix [70]

$$Q^{(s)} = \mathcal{A} Q \mathcal{A}^T, \tag{2.59}$$

this leads to the following equation relating ϵ to the similarly defined intrinsic source ellipticity $\epsilon^{(s)}$:

$$\epsilon = \begin{cases} \dfrac{\epsilon_s + g}{1 + g^* \epsilon^{(s)}} & |g| <= 1 \\ \dfrac{1 + g\epsilon^{(s)*}}{\epsilon^{(s)*} + g^*} & |g| > 1, \end{cases} \tag{2.60}$$

where * denotes the complex conjugate. Assuming that the intrinsic orientation of galaxies is random (which is not always an appropriate assumption due to physical correlations resulting from the formation history of a cosmic structure like a galaxy cluster or filament; see [71] for a detailed reveiw), then the expectation value of the measured ellipticity implied from Equation (2.60) by averaging over the intrinsic source distribution is

$$\langle \epsilon \rangle = \begin{cases} g & |g| <= 1 \\ 1/g^* & |g| > 1 \end{cases}, \tag{2.61}$$

where in the weak lensing limit of $\kappa, \gamma << 1$ we have that

$$\gamma \approx g \approx \langle \epsilon \rangle. \tag{2.62}$$

This remarkable result shows that, in principle, the measurement of the reduced shear provides an unbiased, though noisy, estimate of the local shear with noise set by the intrinsic ellipticity dispersion

$$\sigma_\epsilon = \sqrt{\langle \epsilon^{(s)} \epsilon^{(s)*} \rangle}. \tag{2.63}$$

This motivates the measurement of many source shapes in each region of the sky with galaxy surveys where the accuracy of the estimate depends on the local number density which is a function of the survey depth.

2.3.4 Shear Calibration Biases

Even if galaxy surveys are able to measure the shapes of sufficient sources to constrain the matter density field to the desired precision – in addition to accurately modeling physical effects such as intrinsic alignment and systematics related to photometric redshift estimation and selection effects – there will inevitably be biases in the calibration of the shape and thus shear measurements. In the weak lensing limit where we expect the ensemble ellipticity measurement to respond linearly to the average reduced shear estimate, the various contributions to the *shear calibration bias* are usually captured in the form

$$\langle \epsilon \rangle \approx (1 + m)\langle g \rangle + c, \tag{2.64}$$

where m and c are the multiplicative and additive shear biases respectively, which

may change depending on the tomographic redshift bin. The additive biases largely result from measurement errors such as detector defects [72], brighter-fatter effect [73], finite sampling from pixelization [74], and PSF asymmetries or modeling errors [75] that introduce orientation asymmetries in the image plane. The multiplicative biases are generally more difficult to characterize as, for many contributions, they are intrinsic to the ensemble properties of the galaxy sample which requires either prior knowledge on the properties of a much deeper sample or robust empirical calibration for accurate estimation.

Characterizing these nuisance parameters to high precision is vital for the success of weak lensing measurements from surveys when the measured signal g introduces only a few percent change in the axis ratio of a source, with requirements on m as stringent as $|m| < 10^{-3}$ [76]. Examples of the projected percent degradation in estimated cosmological parameter uncertainty for a variety of the most important cosmological parameters as a function of the size of the prior on m for two surveys are shown in Figure 2.5. These figures highlight the magnitude of the problem: a 1% shear calibration bias would correspond to $\sim 50\%$ increase in the errorbars on Ω_m, σ_8, and w for modern surveys like DES, and $\sim 100\%$ increase for upcoming surveys such as LSST!

Many surveys rely on generative image simulations with a known input source ellipticity distribution and applied shear to calibrate these biases (see [65, 77] for recent examples). However, having to explicitly identify and model each systematic effect in the simulations makes the calibration sensitive to any inaccurate modeling choices (called *model-misspecification bias*) and to any unidentified systematic contributions. More general approaches to handle these calibration biases have been proposed. The `Metacalibration` algorithm [64, 78] self-calibrates the multiplicative bias of a given survey by measuring the direct single-object *shear*

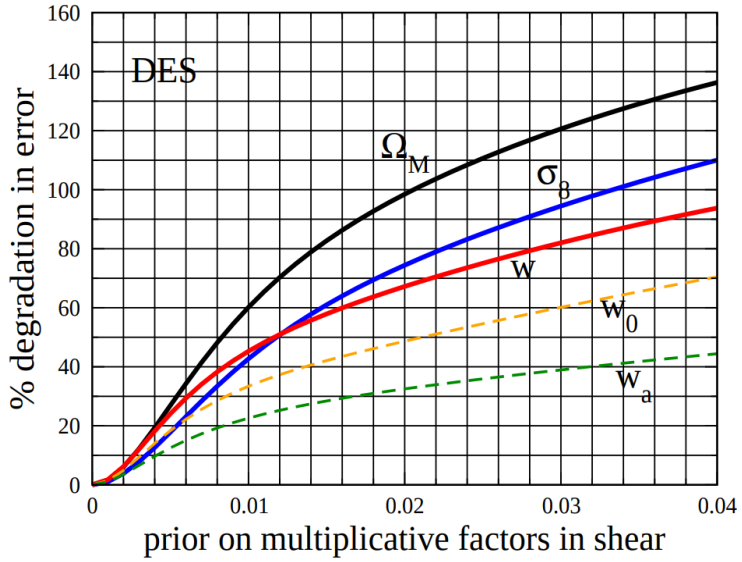

(a)

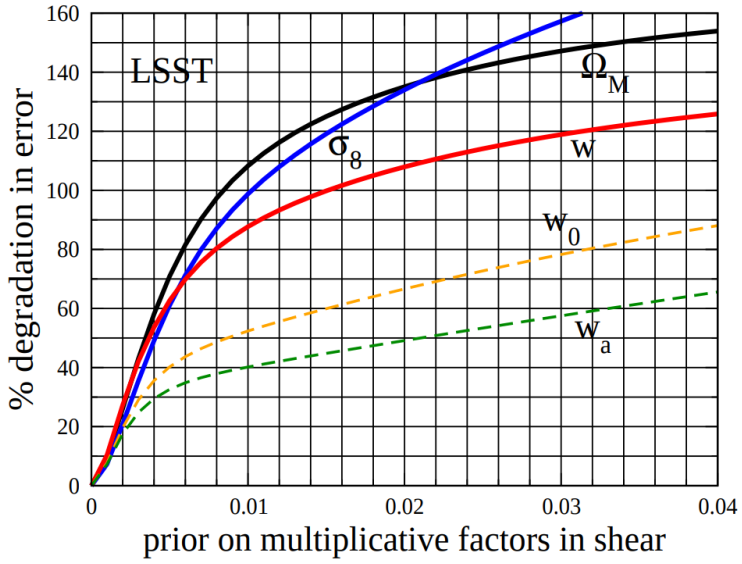

(b)

Figure 2.5: The percent degradation in marginalized errors for a few of the most relevant cosmological parameters measured by galaxy surveys as a function of the width of the prior on the multiplicative shear bias m. These projections are made for (a) DES and (b) LSST. Figures taken from [76].

response of each galaxy observation

$$\boldsymbol{R} \equiv \frac{\partial \boldsymbol{\epsilon}}{\partial \boldsymbol{g}}\Big|_{g=0} = \begin{pmatrix} \partial\epsilon_1/\partial g_1 & \partial\epsilon_2/\partial g_1 \\ \partial\epsilon_1/\partial g_2 & \partial\epsilon_2/\partial g_2 \end{pmatrix}\Bigg|_{g=0}, \tag{2.65}$$

which in practice is determined by remeasuring each galaxy after applying independent shears in order to compute a finite-difference central derivative. The use of the real, observed images mitigates the errors due to the unknown distribution of true galaxy morphologies and inherits effects present in the real data such as image artifacts, redshift-dependent morphological features, and certain selection effects. An update to this methodology called Metadetection also accounts for detection-dependent shear biases resulting from the blends of multiple sources at potentially different redshifts [79], though at the high computational cost of producing multiple versions of each galaxy sample that cannot be matched to one another.

An alternative approach called Bayesian Fourier Domain (BFD) [80, 81] obviates the need for accurate point-estimates of ellipticity by not measuring shapes or fitting morphological models to light profiles at all, instead directly predicting the probability $P(\boldsymbol{D}_i|g)$ that the image data $\boldsymbol{D}_i$ of source i has reduced shear g using a fully rigorous Bayesian treatment. This estimate works by comparing the observed image data to an unsheared "template" galaxy population from deeper observations used as a prior, which are nearly noiseless by comparison. In practice $\boldsymbol{D}_i$ is compressed into a set of intensity moments in the Fourier space of the image that roughly correspond to physical quantities such as the total flux, shape, size, and concentration. This approach is very similar to the `LENSFIT` methodology [82] but directly predicts shear rather than shape, reducing the multiplicative shear bias of the methodology by nearly two orders of magnitude. However, there are

still many difficulties in accurately calibrating the methodology without the use of image simulations; we present an example of how `Balrog` can be used to correct the covariance matrix of the BFD moments in the presence of noise contributions from undetected sources in Section 6.3.

2.3.5 Shear Correlation Functions

With accurate estimates of the shear of individual galaxies, we can locally average over many galaxies to capture the statistical correlations in the shears as a function of scale to infer the presence of large-scale cosmic mass structures[15]. The composite line-of-sight lensing distortion from these structures is called *cosmic shear*. The traditional observable is the same 2PCF described in Section 2.2.1 (though more ambitious techniques using machine learning to extract non-Gaussian information have been proposed, such as [83]). For a pair of galaxies with angular separation direction ϕ, we can define the tangential and cross-components of the shear γ_+ and $\gamma_\times$ respectively as

$$\gamma_+ = -\mathrm{Re}(\gamma e^{-2i\phi}); \qquad \gamma_\times = -\mathrm{Im}(\gamma e^{-2i\phi}), \tag{2.66}$$

where γ_+ is the component of the shear perpendicular to $\hat{\phi}$ and $\gamma_\times$ is the component offset by 45 deg. As shear has two components, there are three possible correlation functions that can be defined:

$$\xi_{++}(\theta) = \langle \gamma_+(\hat{\boldsymbol{n}})\gamma_+(\hat{\boldsymbol{n}}+\theta)\rangle, \tag{2.67}$$

$$\xi_{\times\times}(\theta) = \langle \gamma_\times(\hat{\boldsymbol{n}})\gamma_\times(\hat{\boldsymbol{n}}+\theta)\rangle, \tag{2.68}$$

$$\xi_{+\times}(\theta) = \langle \gamma_+(\hat{\boldsymbol{n}})\gamma_\times(\hat{\boldsymbol{n}}+\theta)\rangle, \tag{2.69}$$

[15] Ignoring in this section the effects of intrinsic alignment and randoms with intrinsic clustering due to spatially-dependent systematics for brevity; see [71].

where $\hat{\boldsymbol{n}}$ and θ are once again the position of the first source on the sky and the angular separation to the second. The information in the first two functions is most usefully expressed as

$$\xi_{\pm}(\theta) = \xi_{+}(\theta) \pm \xi_{\times}(\theta), \tag{2.70}$$

while cross-correlation $\xi_{+\times}$ is symmetric in its arguments and is not sensitive to lensing, which makes its measurement a useful test for systematic errors.

Weak gravitational lensing through cosmic shear provides a powerful cosmological probe sensitive to the total matter density of the universe without assumptions about the connection between dark matter and luminous galaxies. The intrinsically weak nature of the signal requires a statistical measurement in a similar fashion to galaxy clustering, but the resulting constraints are sensitive to very different sysetmatic biases and degeneracies with respect to the desired cosmological parameters. This suggests that their combined constraints are more powerful than their individual measurements; we return to this idea in Section 3.3.1.

Chapter 3

The Dark Energy Survey

The majority of the work in this dissertation relies on observations and data products from the Dark Energy Survey (DES), an optical and near-infrared photometric sky survey that has mapped hundreds of millions of galaxies and thousands of supernovae (SN) in the southern sky. The observing goals of DES are diverse, and include the study of trans-Neptunian objects such as the hypothetical Planet Nine [84, 85, 86], discovery of new ultra-faint Milky Way satellite galaxies and stellar streams [87, 88], the evolution of galaxy properties over time [89, 90, 91], and follow-up observations of optical counterparts to gravitational wave events[1] [92, 93, 94] (see [95] for an overview of measurements beyond cosmology). However, the primary aim of the survey outlined by the original 2005 proposal in [11] is to measure the dark energy equation of state and other cosmological parameters to high precision using four complimentary probes: the statistical clustering of galaxies, cosmic shear, the abundance of massive galaxy clusters, and distance measurements from Type Ia SN. Due to the vast number of measured galaxies and SN that can be used in the likelihood analysis, the final cosmological constraints

[1] While not technically part of the *survey* goals, a new DES working group was created in response to the emergence of multi-messenger signals from gravitational waves that provide a new "standard siren" measurements for independent constraints of the Hubble constant.

for many parameters of interest are projected to have uncertainties of only a few percent, even in the presence of moderate systematics [96].

DES is comprised of a collaboration of more than 600 scientists based in over 25 research institutions who have contributed to all aspects of the survey including building the main camera, conducting observations, processing data products, and analyzing the data across 11 science working groups (WG) in an attempt to provide the most precise cosmological constraints yet from a galaxy survey. DES is one of many ongoing optical galaxy surveys but is uniquely situated in its compromise of moderately large survey area (over 3 times the size of the Kilo-Degree Survey (KiDS; [97]) and the Hyper Suprime-Cam survey (HSC; [98]) but a fourth as large as the Sloan Digital Sky Survey (SDSS; [99])) while retaining considerable depth (nearly 2 magnitudes deeper than SDSS, though $\sim$0.5 and 2 magnitudes shallower than KiDS and HSC respectively). We begin by discussing the survey strategy in Section 3.1 and the complex process of converting the image observations into source catalogs for science measurements in 3.2. We then describe how the various DES probes are combined to constrain cosmological models and end by presenting the results for the first year of observations in Section 3.3.

3.1 Survey Strategy

DES is simultaneously a wide-field (WF) and time-domain survey. It accomplishes this by imaging a contiguous 5,000 deg^2 in the southern hemisphere across five distinct broadband filters ($grizY$) in up to 10 overlapping, dithered exposures per band, while regularly revisiting a much smaller 27 deg^2 area of sky hundreds of times at much higher cadence. This allows the survey to provide high-quality imaging of hundreds of millions of faint galaxies across one eighth of the total sky

to a median depth of $i \sim 23.8$ mag[2] while also detecting thousands of SN through difference imaging. The inclusion of both sets of observables enables joint cosmological constraints using a common set of measurement calibrations, systematics modeling, and parameter marginalization which provides a consistently validated (and blinded) analysis for comparisons to external measurements [101]. In addition, the SN fields offer a limited sample of much deeper observations to help calibrate the photometric properties and redshifts of the WF sample; this is discussed in much greater detail in Chapters 4 and 6.

The full DES footprint for both the WF and SN fields in relation to the Milky Way and the Large and Small Magellanic clouds (LMC/SMC) is shown in Figure 3.1. The irregular footprint shape is chosen to balance a number of competing requirements including imaging the sky most directly overhead the telescope to minimize the airmass while avoiding local structures like the Milky Way disk and the LMC/SMC. In addition, the footprint was extended at lower latitudes and along the celestial equator to maximize the synergies between complimentary experiments such as the South Pole Telescope (SPT) and SDSS. The overlap between DES and these other photometric and spectroscopic surveys are shown in Figure 3.2.

3.1.1 Observations with DECam and ObsTac

DES observations were taken with the 570 megapixel Dark Energy Camera (DECam; [103]) mounted on the prime focus of the 4m Victor Blanco telescope at the Cerro Tololo Inter-American Observatory (CTIO) in Chile from August to February over six[3] years (2013-2019) and 577 full-night equivalents [104, 105, 106].

[2]For a 1.95″ diameter aperture at S/N=10; see [100].

[3]The original proposal called for five years of observations, but an additional half-year was added after significant time was lost due to a particularly bad El Niño in the 2015/2016 season [104].

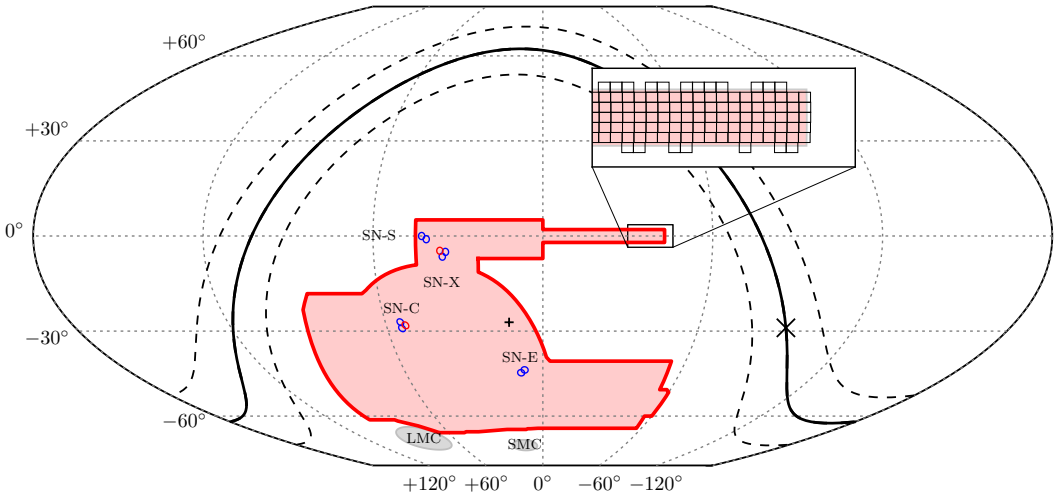

Figure 3.1: An equal-area McBryde-Thomas flat-polar quartic projection of the DES footprint in celestial equatorial coordinates. The 5,000 deg^2 WF survey is in the shaded region, while the eight shallow and two deep SN fields are indicated by blue and red circles respectively. The positions of the LMC and SMC are shown at the bottom of the footprint, along with the extent of the Milky Way disk in between the dashed lines. The inset shows a simplified version of the tiling of the WF footprint from individual focal-plane observations. Figure taken from [102].

DECam was designed and built by the DES collaboration with strict design requirements to ensure excellent image quality with low readout noise, high sensitivity to red and near-infrared colors, and an angular resolution of 0.263″ per pixel, offering one of the largest field-of-views (FOV) of any ground-based optical or infrared imaging surveys at 3 deg^2 [107]. The imager, as seen in Figure 3.3a, is composed of 74 individual charge-coupled devices (CCDs) in a hexagonal pattern, 62[4] of which are 2048×4096 pixel^2 science CCDs for data collection with the remaining 2048×2048 pixel^2 CCDs used for guiding, focusing, and alignment of the images. WF images are typically 90s exposures with a $\sim$ 30s readout time that is processed while the telescope slews to the next observation. SN exposures are significantly longer, up to 400s depending on the field. Each image is taken through

[4]CCDs 2, 31, and 61 had partial or total failures for most of the survey, resulting in an effective 59.5 or 60.5 science CCDs depending on the year.

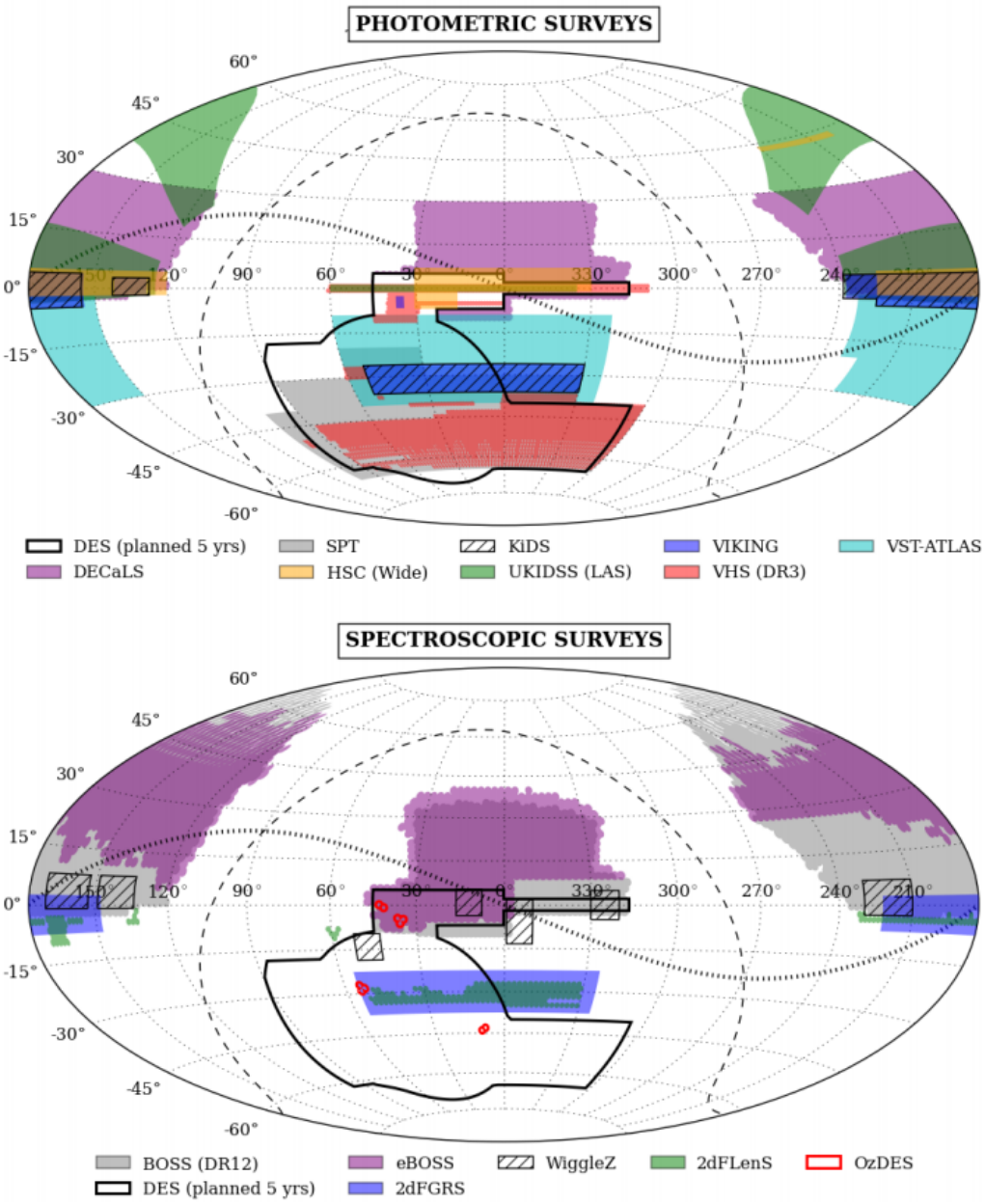

Figure 3.2: A footprint comparison of DES (outlined in black) compared to various photometric surveys on top and spectroscopic surveys on bottom. A Hammer projection in equatorial coordinates is used, with the dashed and dotted lines indicating the Galactic plane and the ecliptic plane respectively. Many features of the DES footprint, such as the extended "arm" to cover the SDSS Stripe 82 on the celestial equator, are explicitly incorporated to take advantage of potential calibration studies and joint constraints from other surveys. Taken from [95].

a bandpass filter corresponding to frequencies between 400 nm and 1080 nm. The DECam bandpass filter response is shown for the $grizY$ bands in Figure 3.3b.

The choice of telescope pointing at a given time was made by the Observing Tactician (ObsTac) algorithm [108]. Each decision was made through a complex decision tree that includes information about the observational conditions (e.g. the sky brightness and atmospheric seeing during the exposure), the relative position of the telescope compared to the celestial plane (e.g. accounting for the season and relative airmass), and survey progress (e.g. which fields had the least number of exposures). ObsTac also automatically handled the balancing of the WF vs. SN observations, ensuring that each pointing in the SN fields was observed in each band at least once every seven days. While multiple DES observers were present at all times in addition to telescope operations staff, the automated pointings provided by ObsTac ensured that the allocated observing nights were used optimally with minimal downtime.

3.1.2 Image Evaluation

The fidelity of the survey images was quantified by comparing the observing conditions of each exposure to historical values typical at CTIO. In particular, the PSF, sky background, and atmospheric transmission were combined into a single figure of merit t_{eff} which expresses the ratio of the actual exposure time compared to the expected time necessary to achieve the same S/N under "fiducial" conditions [109, 102]. The exact expression for t_{eff} is given by

$$t_{eff} = \left(\frac{FWHM_{fid}}{FWHM}\right)^2 \left(\frac{B_{fid}}{B}\right) F_{trans}, \tag{3.1}$$

where $FWHM_{fid}$ and B_{fid} are the fiducial PSF full width at half maximum (FWHM) and sky background respectively, $FWHM$ and B are the correspond-

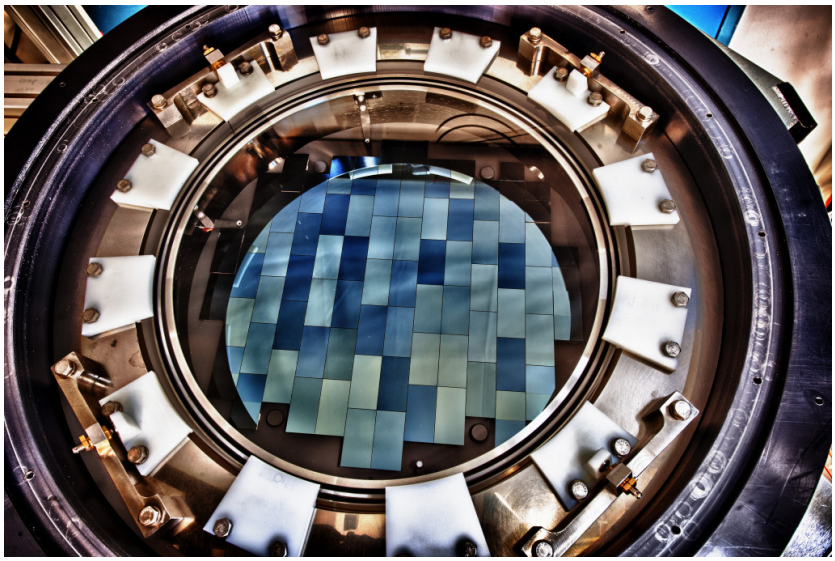

(a)

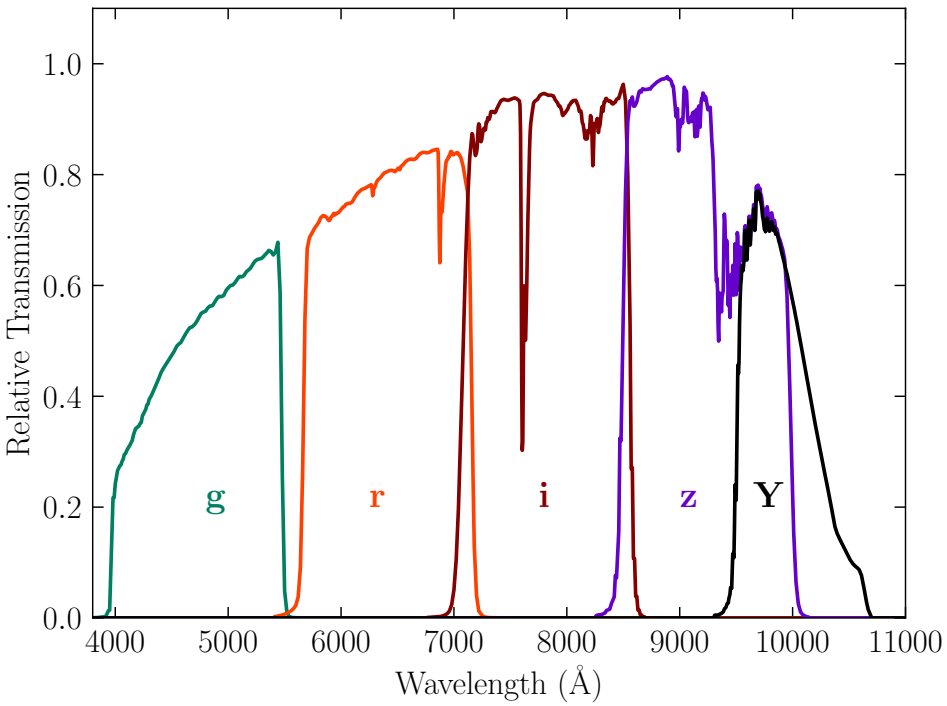

(b)

Figure 3.3: (a) A picture of the DECam imager with the CCDs visible. (b) The composite atmospheric and instrumental transmission response for the *grizY* bandpass filters.

Filter	$FWHM_{fid}$ (arcsec)	B_{fid} (electrons s^{-1})	Minimum t_{eff}	$FWHM_{max}$ (arcsec)
g	0.9927	1.05	0.2	1.765
r	0.9369	2.66	0.3	1.666
i	0.9000	7.87	0.3	1.600
z	0.8685	16.51	0.3	1.544
Y	0.8550	14.56	0.2	1.520

Table 3.1: The fiducial values for the PSF $FWHM$ and sky brightness B for each band, as well as the limiting values for t_{eff} and $FWHM$ used in the First Cut image evaluation for for WF images. Table reproduced from [102].

ing measured quantities, and F_{trans} is the atmospheric transmission relative to a typically clear night. By definition, $t_{eff} \equiv 1$ under nominal conditions.

While t_{eff} is usually the most stringent requirement in the acceptance of an exposure, there are additional requirements made for WF exposures including a maximum PSF FWHM. These requirements are summarized in Table 3.1. When ObsTac estimated the PSF FWHM to be sufficiently large, it reverted to observations of the SN fields that had not been observed in at least four nights. For more details, see the description of the *First Cut* image evaluation in [102].

3.2 From Pixels to Catalogs

Nearly half a million total science and calibration exposures, corresponding to $\sim$ 250 terabytes of raw image data, produced over 76,000 calibrated WF DECam images that passed the basic quality cuts described in Section 3.1.2. These data must be compressed into source catalogs of stars and galaxies for the creation of science samples for the cosmological likelihood analysis. The images are processed and archived by the Dark Energy Survey Data Management (DESDM; [110]) pipeline, operating from the the National Center for Supercomputing Applications (NCSA) at the University of Illinois at Urbana-Champaign. Each of

the calibration steps applied, algorithms used, and modeling choices made during the transfer between image data and source catalogs are susceptible to potential biases in the detection and measurement of the resulting science catalogs. While the DES image processing pipeline is too complex to fully describe here (see [102]), a basic understanding of the data flow is necessary for the work done in this thesis. Therefore we provide a brief overview of the most important steps for the WF survey here and describe additional details of a few components when relevant for `Balrog` in Chapter 4. A schematic of this process is shown in Figure 3.4.

3.2.1 Single-Epoch Processing

Preprocessing

All raw exposures require various calibrations before being used to create the First Cut images described in the next section. These include standard photometric calibration procedures such as bias frames, dome flats, and scattered light maps [111] in addition to corrections due to detector effects such as amplifier cross-talk between the CCD amplifiers [112], residual "tree rings" defects due to resistivity variations in the CCD silicon [72], and the "brighter-fatter" effect [73, 113]. Nonlinear pixel responses are accounted for and bad pixel masks (BPM) are created for each image. Finally, a model for the sky background is derived to detrend the exposures [114]. The raw pixel values RAW are combined with these corrections to produce the calibrated values CAL in the following way:

$$\mathrm{CAL} = \frac{\mathrm{BF}(\mathrm{LIN}(\mathrm{RAW\text{-}BIAS}) \times \mathrm{GAIN})}{\mathrm{FLAT}}, \tag{3.2}$$

where BF is the brighter-fatter correction, LIN is the linearization factor, GAIN is an amplifier-specific conversion from photo-electrons to digital counts, and BIAS

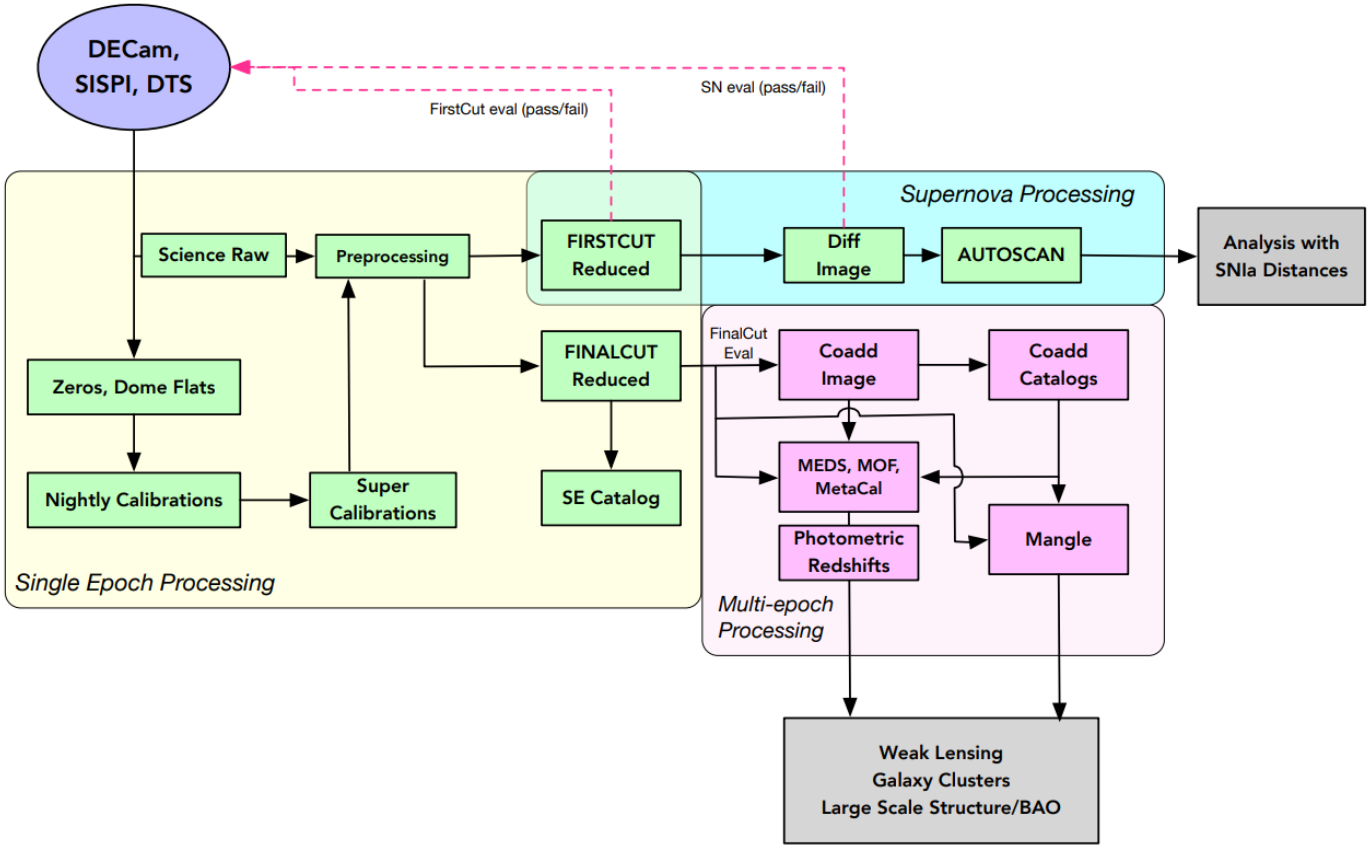

Figure 3.4: A schematic view of the DES image processing pipeline. Raw science images are combined with calibration corrections (bias image, dome flats, etc.) to produce a First Cut image for initial evaluation as described in Section 3.1.2. More sophisticated photometric calibration is used for the Final Cut images from which the the coadd images are constructed. These coadds are the basis of all multi-epoch measurements made for the science catalogs. Figure taken from [102].

and FLAT are the corrections from the bias and flat frames respectively.

First Cut

The evaluation of DECam exposures must happen quickly so that their pointing can be added back into the ObsTac queue if they are rejected. This motivated a simplified processing stack called *First Cut* that is fast enough to evaluate images within a few hours of acquisition. This procedure was not static and was updated throughout an observing season as improvements were available. In addition to the preprocessing calibrations described above, the First Cut processing calculates an initial astrometric solution using Software for Calibrating AstroMetry and Photometry (`SCAMP`; [115]) and single-epoch source catalog using Source Extractor (`SExtractor`; [116]). These products are not used in the creation of the WF science catalogs, but are useful for matching to reference stars and catalogs for the initial photometric calibration and PSF modeling with the tool PSFEx [116]. A more complete image mask is then created which accounts for saturated pixels, satellite trails, and cosmic rays. With calibrations made and PSFs estimated for each image, the exposures are then accepted as part of the survey data or rejected for re-imaging as described in 3.1.2

Final Cut

The final, uniform processing of each WF exposure for a given processing campaign is called *Final Cut*. In practice this is often very similar to the First Cut processing, but includes improved software updates and super-calibration images that are based off of multiple nights of calibration frames for increased statistical power. Significant changes are usually present when entering a new internal release campaign (e.g. Y1, Y3, Y6) when all exposures up to that point are remeasured

with the latest measurement software needed for the desired precision of the next cosmological analysis. The largest individual change in the Final Cut processing is the use of the Forward Global Calibration Method (FGCM) [117] for sophisticated photometric calibration that does not rely on traditional standard stars. This method forward models contributions to the spatial and time dependencies of the image zeropoints from the instrumental response and atmospheric extinction (called *gray* corrections), in addition to corrections dependent on the spectral energy distribution (SED) of individual sources (called *chromatic* corrections). This rigorous approach leads to a stable photometric calibration over many years of observations of order 1%.

3.2.2 Multi-Epoch Processing

Coaddition

The DES science catalogs are based on composite *coadds* of the single-epoch exposures to produce deeper images and extract fainter, more distant sources from the images. This is needed for making measurements at higher redshift which is vital for constraining the dark energy equation of state and detecting any potential evolution of w_Λ. To simplify the procedure, the footprint is divided into 10k×10k pixel^2 squares called *tiles* corresponding to 0.73×0.73 deg^2. There is at least 1″ overlap between adjacent tiles that increases significantly when approaching the southern celestial pole. The coadd image of a tile in each band is composed of every CCD image that intersects the tile area, meaning that single-epoch images can contain data in multiple tiles.

Combining the individual exposures requires a consistent astrometric solution that is achieved by recalculating all relevant exposure solutions simultaneously. This also minimizes the width of the coadded PSF, though this is rarely used for

model fits in science catalogs due to discontinuities across the coadd along the input CCD edges. The SWARP tool [118] then resamples (or "warps") the pixels of the input images into the pixels of the coadd projection. This resampling takes into account the different image zeropoints, weight maps, and masks to optimally weight the input pixels and linearly interpolates over pixels flagged from the BPM or satellite trails.

Source Detection

In addition to individual coadd images for $grizY$, a composite[5] riz coadd is made for a detection image that incorporates flux information from multiple bands. This allows for detection of sources that are above the detection threshold in some bands but not in others. The g and Y bands are excluded from the detection image as they are generally noisier or have large or irregular PSFs that would degrade the detection image. This is not a significant problem for cosmological measurements in DES as they are primarily focused on redder objects [102].

All science catalogs are comprised of sources detected by `SExtractor` in the riz detection image with a local threshold of S/N$\sim$10. The measurements of these sources by `SExtractor` are made in dual image mode, which defines the location of the object based upon its location in the detection image but measures its photometric properties in the single-band coadd images. The set of measured properties include flags, positional values, aperture photometry, and limited model-fitted quantities based upon the local PSF. In addition, a basic star/galaxy classifier called `SPREAD_MODEL` is computed which is the basis for more sophisticated classifiers.

[5]This composite coadd is created using a `CHI-MEAN` combination of the riz coadds, which minimizes discontinuities between regions with different numbers of exposures [119].

Photometric Model Fitting

While `SExtractor` provides various photometric estimates of source properties such as their flux, shape, and size, their measurements are done on the coadd images which results in correlated noise properties and a PSF that is discontinuous across a tile. This is a major problem for cosmological probes that require precise measurements on galaxy properties; particularly cosmic shear which depends critically on the measurement of galaxy shapes to better than 1%. In addition, a sub-optimal PSF estimate will increase the blending rate of sources which dilutes the clustering signal, broadens the ellipticity distribution of affected galaxy by over 10% [120], and can even dominate the shear multiplicative bias [121].

Instead, the photometry of DES sources in science samples use the joint fit of pixel data from all available single-epoch images without significant masking. This allows for the use of local PSF estimates that do not have to be interpolated across multiple CCDs. This process begins with the creation of Multi Epoch Data Structures (MEDS; [122]) that contain single-epoch image cutouts, weight maps, masks, segmentation maps, background estimates, PSF estimates, and image metadata such as the zeropoint for each source in a tile. The size of each cutout is determined by rounding up the `SExtractor` `FLUX_RADIUS` to the nearest multiple of 16[6]. The MEDS files are then passed to a suite of measurement codes that utilize the single-epoch information for more robust estimates.

The primary photometric measurements of the survey are done by the software `ngmix`[7] [123], which simultaneously fits a light profile model to the *griz* bands and all epochs of a given source. The model is convolved with the local PSF in each cutout and a total χ^2 sum is evaluated for the model across all images. The model

[6] The evaluation of this cutout size can have dramatic effects on the recovered photometry of sources; see Section 5.3.3.

[7] https://github.com/esheldon/ngmix

parameters are varied until an estimate of the maximum likelihood is found, with convergence defined to be when flux did not change by more than 1 in 10^3 and morphological parameters by 1 in 10^6. In practice, `ngmix` uses Gaussian mixture model approximations to the chosen profiles (hence the name) given in [124] for significantly faster convolutions with the (also Gaussian mixture approximated) PSFs.

Most fits by `ngmix` are based on a Sérsic profile introduced in [125], where the intensity I for a round source at radius r is given by

$$I(r) \propto \exp\left[-\left(\frac{r}{r_0}\right)^n\right]. \tag{3.3}$$

Here r_0 is the half-light radius and n is the Sérsic index that controls the degree of curvature in the profile. For a fixed n, a typical `ngmix` elliptical profile has six parameters defining the centroid position, ellipticity shape parameters, size, and flux. To account for the diversity of galaxy morphologies with different values for n, DES adopted a *composite model*[8] (CModel, or `cm`) from SDSS which is a linear combination of an exponential disk $M_{\rm exp}$ with $n = 1$ and a bulge described by a de Vaucouleurs' profile [126] with $n = 4$:

$$M_{\rm tot} = f_{\rm dev} M_{\rm dev} + (1 - f_{\rm dev}) M_{\rm exp}, \tag{3.4}$$

where $f_{\rm dev}$, also called `fracdev`, is the relative flux ratio between the bulge and disk components. As freely fitting the galaxy model in this way was unstable, in practice each component was fit separately and then followed by fitting for the optimal value of $f_{\rm dev}$. Finally, this value of `fracdev` (along with the relative scale size) is fixed for a new fit where the centroid, total size, and fluxes are free

[8] https://www.sdss.org/dr12/algorithms/magnitudes/#cmodel

parameters. Only the flux is allowed to vary between bands.

Each profile measurement is performed twice with different methods for dealing with blending effects from the proximity of nearby sources. The first, introduced in [127] for Y1, is called multi-epoch, multi-band, multi-object fitting (MOF). This procedure first identifies groups of nearby sources using a friends-of-friends (FOF) algorithm and performs an initial fit to each object as described above after subtracting the light of neighbors using the überseg algorithm [122]. This process is repeated iteratively using the previous MOF fit until the model of each source in the FOF group converges simultaneously, or after a maximum of 15 iterations. A simpler version of this fitting procedure called single-object fitting (SOF) was introduced in Y3 that masked rather than modeled the light of other sources in the FOF group which was significantly faster, led to less failures, and had negligible impact on the overall photometric performance [128]. While SOF is now the default photometry used for most non-lensing samples in Y3, measurements in the most dense fields such as those relevant for galaxy clusters still use MOF for the more robust deblending procedure [129, 12].

The source sample for the DES weak lensing analysis uses measurements from `Metacalibration` instead of MOF or SOF for its photometry as shear biases resulting from sample cuts on these quantities can be controlled for as described in [64, 130] and Section 2.3.4. The `Metacalibration` measurements are also based on `ngmix` which incorporates the same multi-epoch fitting procedure, but a simple 2D Gaussian profile is used in place of more complex models such as CModel. This simplification is made for computational considerations as each source must be measured a total of five times: four measurements to measure the differential shear response, and an unsheared measurement for the baseline Gaussian photometry. In addition, while `Metacalibration` deconvolves the original images by the full

PSF solution, it reconvolves by a Gaussian approximation to the PSF for the four sheared images. Despite a Gaussian being a poor fit to the DES PSF, [78] demonstrated that the measured shear response accounts for any mismatch between the real PSF and the used fitted model sufficiently for the precision required by DES. While measurements are made simultaneously in *griz*, in Y3 only the *riz* bands were used in cosmological analyses as there were known issues in the estimation of the *g* band PSF due to galaxy contamination in the stellar calibration population and systematic effects related to differential chromatic refraction [75]. Further implementation details for `Metacalibration` applied to DES data in Y1 and Y3 are described in [130, 131] respectively.

A few additional measurements are made at this stage such as the BFD moments (introduced in Section 2.3.4) and various point-estimates for the photometric redshifts of sources using Bayesian Photometric Redshift estimation (BPZ; [132, 52]), Directional Neighborhood Fitting (DNF; [133]), and the mixture of machine learning-based techniques in `ANNz2` [134]. The most relevant redshift estimation for this work is done separately for the weak lensing source sample (see [135]) and is described in detail in Section 6.1, along with the crucial role that `Balrog` plays in its calibration.

3.2.3 The GOLD Catalog

Most of the previous photometric measurements are collated into a single science catalog called the GOLD catalog (see [127, 128] for Y1 and Y3 respectively). This data set serves as a common basis for most WF measurements and provides additional extensive validation, value-added quantities, and ancillary data products for the cosmological analyses. A few of the most important components include: (1) a set of quality control and positional masking flags to allow elimination

Release	Area ($\deg^2$)	Depth (i band)	Nb. Objects (million)	Uniformity (mmag)	Reference
SV GOLD	∼250	23.68	25	<15	[138]
Y1 GOLD	1786	23.29	137	<15	[127]
DR1	5186	23.33	399	<7	[137]
Y3 GOLD	4946	23.34	388	<3	[128]
DR2	4913	23.80	691	<2.5	[100]

Table 3.2: DES data releases along with a few of their associated properties. The quoted i band depth corresponds to S/N=10 in 1.95″diameter apertures. The approximate area coverage *decreases* slightly for the latest two releases due to more stringent requirements on image quality and the fractional area required for coadded tile images. All releases are made public at https://des.ncsa.illinois.edu/. Reproduced from [128], with additional data from [100].

of sources that had photometric fitting errors, are near bright stars or extended foreground objects, or lie outside of the survey footprint, (2) an updated photometric calibration of source fluxes that improves survey uniformity by accounting for interstellar extinction and improved per-object chromatic corrections, (3) a set of star-galaxy classifiers dependent on object morphology, and (4) a set of survey property maps[9] that quantify the spatial variation of various quantities such as the depth, mean PSF size, sky brightness, and stellar density across the footprint. The property maps in particular are important for traditional approaches to mitigating systematics due to survey properties that are correlated with cosmic signals such as the fluctuations in the galaxy density field [136]; examples for three of the property maps of the Y3 data are shown in Figure 3.5. Table 3.2 summarizes some of the most important properties of each GOLD release (in addition to the two public data releases (DR1 and DR2; [137, 100])) such as the surveyed sky area, i band depth, number of objects detected, and photometric uniformity.

[9]Often called "systematics maps", this is misleading; while the observing properties may *correlate* with the systematics of a cosmological measurement, there is no guarantee that these maps contain the necessary information to correct for them.

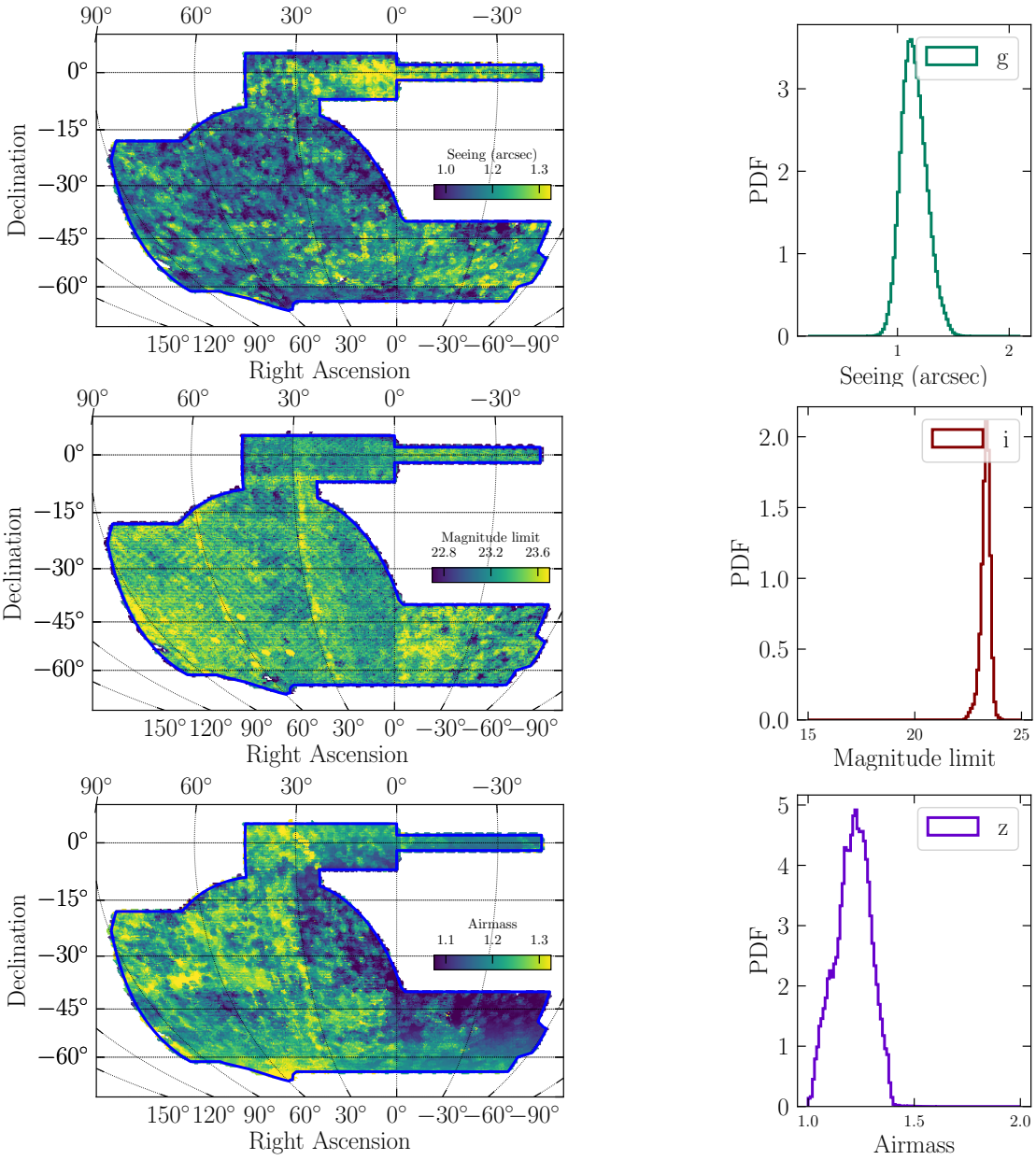

Figure 3.5: The sky maps and histograms for the spatial variation of the g band seeing, i band depth, and z band airmass across the DES footprint. These are just three of the many survey property maps compiled by DES that also include the mean sky brightness, exposure time, zeropoint corrections, and stellar density. Taken from [128].

3.3 Cosmology from DES

As discussed in Chapters 1 and 2, the elements of a cosmological model such as the abundance of dark matter or evolution of dark energy impacts cosmic signals in two key ways: (1) the changing geometry of the universe through the dependence of the comoving distance on the Hubble parameter $H(z)$, and (2) the acceleration (due to dark matter) or suppression (due to dark energy) of the growth of cosmic structures. Any individual observational probe is sensitive to these cosmic signals in different ways, and each have their own degeneracies with model nuisance parameters or measurement systematics that can mimic the signal being measured. These degeneracies can be broken by considering the joint likelihood of the measurements from multiple probes which motivates the survey design as described in Section 3.1. While such joint constraints can be done by combining different experiments in an attempt to remove correlations between systematics, making each measurement with the same data set standardizes the blinding and validation procedures as well as providing a robust cross-check on more traditional joint analyses.

3.3.1 3×2pt Analysis

One of the most powerful ways DES combines cosmological constraints is in what is called the 3×2pt analysis. As the primary measurements of galaxy clustering and cosmic shear described in Sections 2.2 and 2.3 respectively are both based on 2PCFs, we can combine this information into three distinct two-point functions: (1) the auto-correlation of galaxy positions (galaxy clustering), (2) the auto-correlation of galaxy shears (cosmic shear), and (3) the cross-correlation between galaxy positions and their shears (galaxy-galaxy lensing). This combination is particularly constraining as the complimentary information in each probe

breaks the degeneracy between galaxy bias and cosmological parameters, as well as allows for the joint fit to internally solve for other important systematics such as the estimation of photometric redshifts and intrinsic alignment. This method for increasing constraining power and the mitigation of biases is of critical importance as the fiducial DES 3×2pt likelihood models contain 20 astrophysical and measurement systematic nuisance parameters that must be marginalized over [139].

The clustering signal is measured on a sample of foreground *lens* galaxies, from which the induced shear on background *source* galaxies is captured in the cosmic shear signal. Each sample has separate tomographic binning and photometric redshift estimates which allows for measurements of the galaxy-galaxy lensing signal of source galaxies in source bin i by lens galaxies in lens bin j. Each of these measurements are compared to model predictions that are similar to those discussed in Chapter 2 but with substantially more detailed corrections to account for subtle measurement systematics (see [136, 60, 140] for the details of the Y1 clustering, cosmic shear, and galaxy-galaxy lensing measurements respectively, and [141] for details on the theoretical modeling for each). The best-fit model is determined by generating Markov Chain Monte Carlo (MCMC) samples of the posterior distribution using a Gaussian likelihood whose covariance matrix is computed in [141] and with prior distributions on the model parameters defined in [139].

3.3.2 Y1 Cosmological Constraints

The DES Y1 cosmological constraints from 3×2pt were unblinded in July of 2017 and described in [139]. The constraints for Ω_m, w, and S_8[10] after marginaliza-

[10] $S_8 = \sigma_8(\Omega_m/0.3)^{1/2}$ is variant of σ_8 that is more directly constrained by DES measurements.

tion over all other parameters is shown in Figure 3.6. The constraints from only cosmic shear (in green) and from clustering plus galaxy-galaxy lensing (in red) are significantly less constrained than the joint analysis (in blue) which demonstrates the power of the combined approach. While these initial results provide a marginalized constraint of $w = -0.82^{+0.21}_{-0.20}$, the Bayes factor analysis in [139] suggests that ΛCDM is slightly favored over wCDM from these data. A similar result of $w = -0.80^{+0.09}_{-0.11}$ was found in [101] after combining this 3×2pt analysis with DES measurements of the first three years of SN [142] and baryon acoustic oscillations (BAO) [143] measurements. Intriguingly, joint constraints of DES 3×2pt with the CMB and external measurements of SN and BAO resulted in $w = -1.00^{+0.05}_{-0.04}$; exactly the expected value of a cosmological constant.

However, the most stringent test of ΛCDM is to compare the DES constraints to those from the CMB to see if the same cosmological model adequately fits early and late-time measurements of the universe. This comparison for Y1 is shown in Figure 3.7 for Ω_m and S_8. While the peaks of each distribution are offset by more than 1σ and visually hint at a possible tension, the more quantitative analysis of the full 26-dimensional parameter space in [139] found "substantial" evidence of consistency on the Jeffreys scale [144]. While the statistical power of this sample was not sufficient to robustly demonstrate a tension between the measurements, the much larger Y3 analysis may include enough sources to decrease the contour sizes such that a statistical tension is undeniable. This makes the enormous task of characterizing the numerous measurement systematics of the survey of vital importance to ensure that any measured tension is of physical origin hinting at new physics and not due to insufficiently understood or characterized biases.

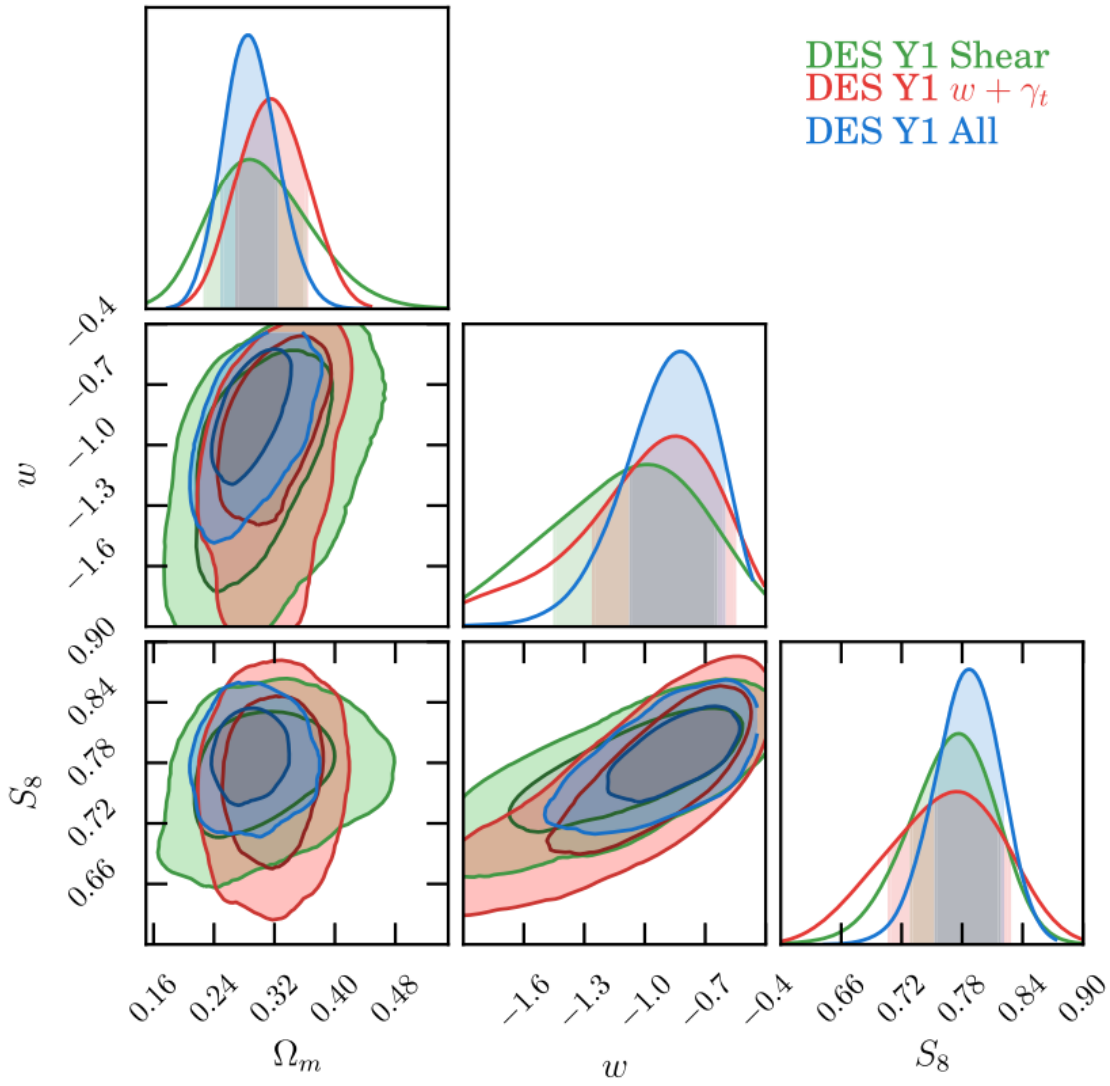

Figure 3.6: The marginalized constraints on three of the cosmological parameters considered in the DES Y1 wCDM model: Ω_m, w, and S_8. The constraints from only cosmic shear are shown in green, the combined angular clustering and galaxy-galaxy lensing constraints are in red, and the combined 3×2pt constraints are in blue. Contours represent the one and two σ confidence regions. Taken from [139].

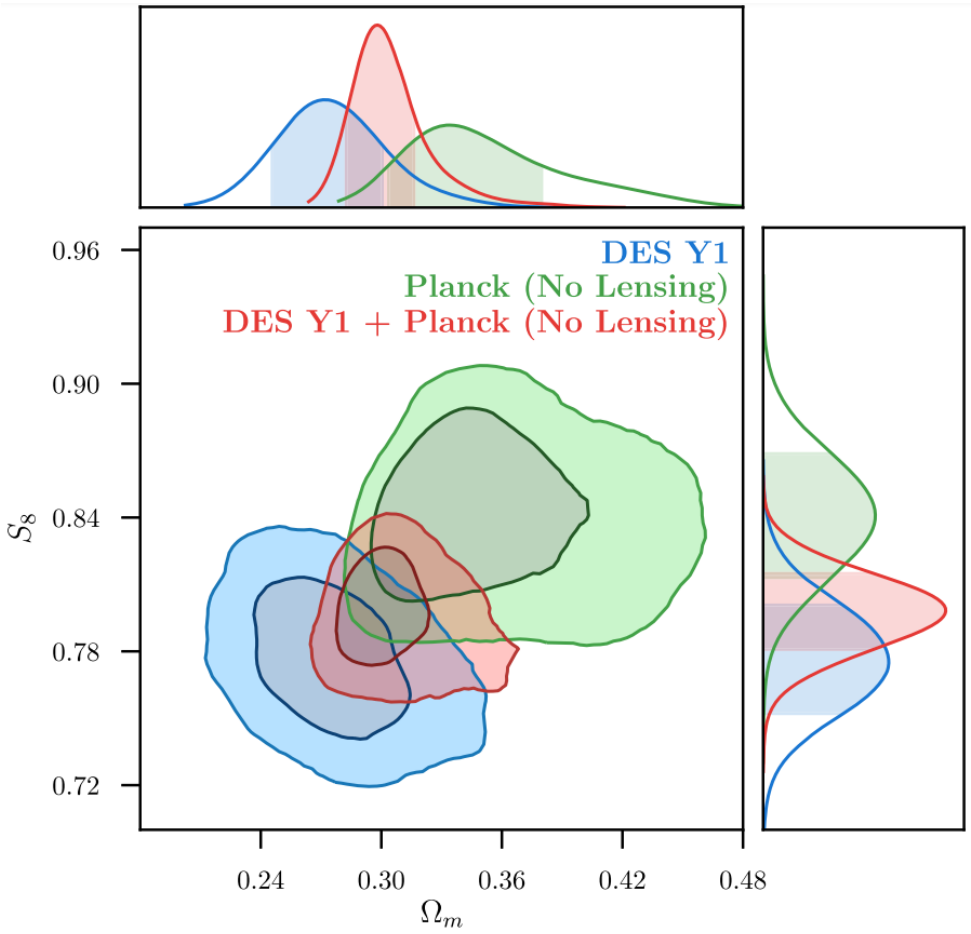

Figure 3.7: A comparison of the marginalized ΛCDM constraints Ω_m and S_8 from DES Y1 in blue versus the equivalent constraints from Planck without external lensing constraints in green. The combined constraints are shown in red. Contours represent the one and two σ confidence regions. Taken from [139].

Part II

No Galaxy Left Behind:

Systematics Control with `Balrog`

Chapter 4

Measuring the DES Transfer Function with Balrog

Part I of this dissertation has demonstrated how wide-field imaging surveys such as DES have revolutionized modern astronomy and provided some of the tightest constraints on the cosmological models that describe our universe. For the largest surveys, the resulting constraints have become so precise that percent-level spatial variations in the survey's depth can cause biases that are now beginning to dominate over the statistical errors (see for instance [76, 145, 146, 147, 148]). Small biases – as small as one part in 10^4 in some cases – in the measurements of sizes, shapes, and fluxes of sources can have similarly important impact on the science results [149]. The remainder of this dissertation aims to create a general solution to this problem with a framework called `Balrog`, and to carefully characterize the photometric measurement systematics present in the first three years (Y3) of DES data to be used in the calibration of the Y3 cosmological results. Much of the material in the following two chapters was first presented in [150] on which I am the lead author.

4.1 Introduction

As first discussed in Chapter 1, the cumulative effect of the many selection effects and measurement biases of an astronomical survey is captured by its *transfer function*. This function maps how the photometric properties of astronomical sources are distorted by real physical processes such as interstellar extinction or by our imperfect measurements at every step from detector calibration to object catalog creation. As most cosmological measurements from survey data are based on the same processed images and source catalogs, this mapping is crucial for accurately estimating the true cosmic signals imprinted on the sky such as the spatial clustering of galaxies (see [151, 152, 136] for a few examples) and weak lensing of galaxy light profiles by the intervening matter field (similarly, see [153, 154, 60]).

Unfortunately, many of these effects are in practice difficult to characterize or even identify. For example, the object catalogs derived from survey images are produced by a complex process: Calibration, detection, measurement, and validation involve a number of nonlinear transformations, thresholds applied to noisy quantities, and post-facto cuts made on the basis of human judgment. Despite significant efforts to explicitly characterize some of these effects in the past (see [155] and [156] for the DES and LSST pipelines respectively), this complexity makes each contribution to the transfer function extremely difficult to model – and even small errors in the estimated survey completeness can substantially bias measurements such as the amplitude of galaxy clustering or important calibration efforts like the photometric redshift inference of weak lensing samples [157, 149, 158, 159].

Simulating the survey data from scratch can accurately capture some, but not all, of this complexity. Spatial variations in the effective survey completeness depend not just on the observing conditions but also on the ensemble properties of the stars and galaxies being studied. Systematic errors in the sky background esti-

mation and biases in the measurements of galaxy and stellar properties can couple to fluctuations in the galaxy density field leading to a completeness that depends on the signal being measured. Finally, there is a wide variety of non-astrophysical features that can affect the measurement quality and completeness such as artificial satellite trails, pixel saturation, or the diffraction spikes of bright stars. Not only are these effects difficult to model or simulate at high fidelity, but attempts to do so can introduce model-misspecification bias which can underestimate the true uncertainty in the downstream fitted photometric parameters [160, 161].

In contrast, injecting artificial sources directly into the real images can naturally capture many of these effects. Synthetic objects added to the real data automatically inherit the background and noise in the images as well as the biases arising from measurement in proximity to their real counterparts. Injecting realistic star and galaxy populations, convolving their light profiles with an accurate model for the point-spread function (PSF), and applying accurate models for effects not directly probed (such as Galactic reddening and variable atmospheric transparency) results in a population of simulated sources that inherits the same completeness variations and measurement biases as the real data. Mock catalogs made in this way can be used to discover, diagnose, and derive corrections for systematic errors and selection biases at high precision.

Injection simulations of this kind have been used for limited calibration studies of detection efficiency and photometric calibration in the presence of realistic noise and crowded fields since at least the mid-1980's [162, 163, 164], not long after the widespread adoption of charge-coupled devices (CCDs) in astronomical imaging. There is a rich history of mixing real and synthetic data to estimate the detection efficiency of an apparatus in hybrid Monte Carlo techniques commonly used in particle physics measurements [165], and recently there have been examples to

improve blinding procedures for rare events such as embedding fake gravitational wave signals ("hardware injections") into the Laser Interferometer Gravitational-wave Observatory (LIGO; [166]) data and similarly "salting" the data taken by the Large Underground Xenon (LUX; [167]) experiment with artificial events to test the robustness of their detection pipelines and guard against confirmation bias ([168, 169] respectively).

However, generating full-scale mocks via injection is computationally demanding for a modern wide-field (WF) galaxy survey. The injection simulations described in [17] for the early releases of DES data did not attempt to pass the injected galaxies through every part of the measurement process, opting to inject only onto the coadd images. The SynPipe package [170] has been used to examine measurement biases for the HSC pipeline and includes single-epoch processing, but only on a very small fraction of the survey's available imaging. The `Obiwan` tool developed to model completeness variations for the Dark Energy Spectroscopic Instrument (DESI: [171]) has also has incorporated single-epoch processing but focuses only on the emission-line galaxies that are the primary DESI targets [172] which reduced its utility for general diagnostics discovery. Despite injection pipelines having shown great promise, the difficulty in distinguishing intrinsic methodological uncertainties in their sampling of the transfer function from actual measurement biases (in addition to the extremely high computational cost) have until now kept them from being used to directly calibrate cosmological analyses and instead largely relegated them to compelling but ultimately unapplied proof of concept measurements.

This rest of this chapter describes the generation of the `Balrog` injection simulations for the first three years of DES data (referred to as Y3), covering a randomly selected 20% of the total Y3 footprint. Sources drawn from DECam

[103] measurements of the DES Deep Fields (DF) [173] are self-consistently added to the single-epoch DES images which are then coadded and processed through the full detection and measurement pipeline. This extensive simulation and reduction effort allows us to characterize, in detail, the selection and measurement biases of DES photometric and morphological measurements as well as the variation of those functions across the survey footprint. In addition, using an input catalog with measurements from the same filters as the data resolves many of the issues in capturing the same photometric distributions as real DES objects seen in [17] – particularly for color. The resulting catalogs generally follow completeness and measurement bias variations in DES catalogs to high accuracy, with mean color biases of a few millimagnitudes and number density fluctuations varying with survey properties within 1% for a typical cosmology sample; this will be demonstrated in Chapter 5.

As the measurement pipelines for the DES DF and WF data are complex and quite technical, so too are parts of the next two chapters. However, we also motivate interesting science cases for the presented response catalogs for both calibration and direct measurement purposes including the photometric redshift calibration of weak lensing samples, magnification effects on lens samples, and the impact of undetected sources on image noise. For those more interested in using `Balrog` for potential science applications or as a general diagnostic tool, this is discussed in detail in Chapters 5 and 6.

This chapter is organized as follows: In Section 4.2 we introduce the significantly updated `Balrog` pipeline which now emulates more of the DES measurement stack, including the completely new injection framework for source embedding into single-epoch images in Section 4.2.2 and the validation of the pipeline in idealized conditions in Section 4.2.3. Section 4.3 describes the injection sam-

ples and methodological choices for the Y3 `Balrog` simulations including a new scheme for handling ambiguous matches. This will be followed by Chapter 5 where we compare the recovered `Balrog` samples to the fiducial Y3 object catalog (Y3 GOLD; [128]), as well as present the photometric response of the main star and galaxy samples. We leave a more detailed discussion of the implications of our results, methodological limitations, and future directions for Chapter 7, after describing a few of the most important applications of `Balrog` to key DES Y3 science analyses in Chapter 6.

4.2 The `Balrog` Pipeline

`Balrog` was first introduced in [17] as a software package[1] that injects synthetic astronomical source profiles into existing DES coadd images to capture realistic selection effects and measurement biases for the Science Verification (SV) and Year 1 (Y1) analyses. However, as the precision of the subsequent DES cosmological analyses has increased, so too has the need for even more robust systematics control and more precise characterization of the survey transfer function. The main limitations of the original methodology were that (1) injections into the coadd rather than single-epoch images skip many important aspects of the measurement pipeline whose effects we want to capture, and (2) the injected objects were drawn from fitted templates to sources in the space-based Cosmological Evolution Survey (COSMOS: [174]) rather than measurements consistent with DECam filters which introduced discrepancies in the recovered colors. While the latter is solved by using the new Y3 DF catalog [173], the former required significant additional complexity in the simulation framework to consistently inject objects across all exposures and bands.

[1] https://github.com/emhuff/Balrog

To address this, we have developed a completely new software framework that is described and validated in the remainder of this section. An overview of the Y3 `Balrog` process is shown in Figure 4.1, with simplified summaries of the DF and Y3+`Balrog` measurement pipelines. Briefly, we use the significantly deeper DECam measurements of sources in the DES DF as a realistic ensemble of low-noise objects to inject into the Y3 calibrated single-epoch images. We then rerun the DES measurement pipeline on the injected images to produce new object catalogs that contain the `Balrog` injections. Finally, we match the resulting catalogs to truth tables containing the injection positions to provide a mapping of DF truth to WF measured properties.

All astronomical image injection pipelines such as `Balrog` have two distinct elements: emulation of a survey's measurement pipeline and source injection into the processed images. As our methodology for the former is intrinsically specific to DES while the latter is a fairly generic problem, development on the new Y3 `Balrog` was split into the two corresponding pieces discussed in detail in Sections 4.2.1 and 4.2.2 below.

4.2.1 DESDM Pipeline Emulation

The DES survey data are processed through a set of pipelines by the DES Data Management team (DESDM) which perform basic astronomical image processing as well as applying state-of-the-art galaxy fitting, PSF estimation, and shear measurement codes. The standard processing steps applied to the DES Y3 data are described in detail in [102] and summarized in Section 4.2. Ideally, to ensure that identical codes and versions were used at each stage of processing, one would implement `Balrog` as part of the standard data reduction. However, this was not an option for DES Y3 as the updated `Balrog` methodology did not exist

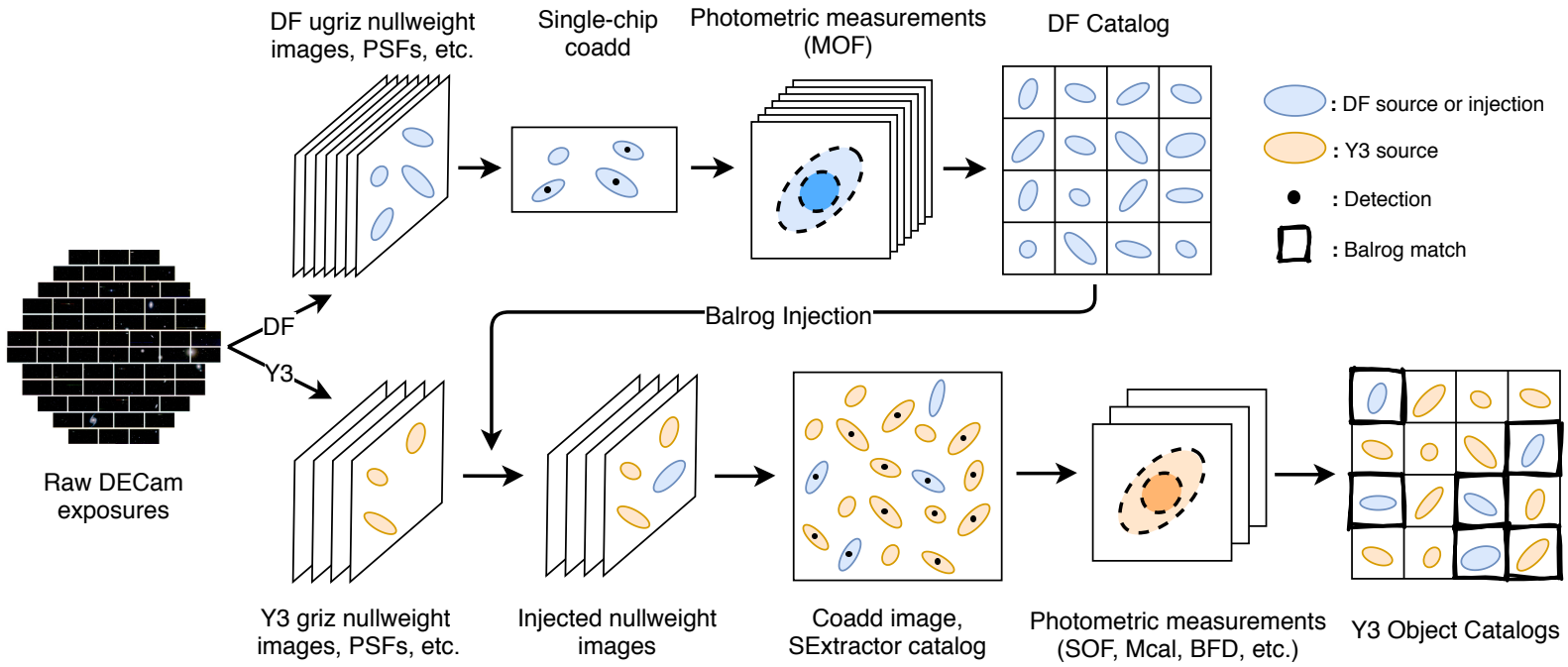

Figure 4.1: A high-level overview of how the Deep Fields (DF) and Y3 image processing pipelines interact to create the `Balrog` catalogs. The raw DECam exposures are used as the basis for both tracts, with the much deeper DF data being represented by the larger image stacks. The DF exposures are not dithered and thus single-CCD coadds are created in place of the much larger Y3 coadds. Measurements of the DF objects constitute the injection catalog which are added to the Y3 null-weight images directly. Afterwards, the injected null-weight images are processed in a nearly identical way to the real images including coaddition, detection, and photometric measurements. Finally, we match the output object catalog to truth tables containing the injected positions. As all sources are remeasured, there is some ambiguity in the matching; this is discussed further in Section 4.3.5.

until after the Y3 data were completely processed (this is now true for a future Year 6 (Y6) `Balrog` analysis as well). Therefore it was necessary to replicate the DESDM processing pipeline stack as closely as possible. While this usually amounted to calling the relevant codes and scripts with identical configurations and software stack components, sometimes minor changes were required due to differences in computing environments or practical considerations such as processing time. These differences will be noted whenever relevant.

A modular design for the measurement pipeline[2] was chosen both for ease of testing and for the ability to do non-standard production runs (see Chapter 6 for examples). The individual `Balrog` processing stages for a single DES coadd tile ($44' \times 44'$) are as follows:

(1) **Database query & null-weighting** – Find all single-epoch *immasked* (the DES designation for flattened, sky subtracted, and masked) images in the *griz* bands that overlap the given DES Y3 tile. Download all exposures, PSFs, photometric and astrometric solutions from the DESDM Y3 processing archive. A masking process called "null-weighting" is applied to these immasked images which sets weights of pixels with certain flagged features (e.g. cosmic rays) to 0. These null-weight images are the starting point of the later injection step.

(2) **Base coaddition & detection** – Remake the tile coadds from the single-epoch exposures with no objects injected using `SWarp` [118] and the detection catalogs with `SExtractor` [116]. Construct Multi-Epoch Data Structure (MEDS; [122]) files with cutouts of the coadd and single-epoch images used for additional photometric measurement codes. This allows us to cross-check our measured catalogs with Y3 GOLD to ensure that we recover the same

[2] https://github.com/kuropat/DES_Balrog_pipeline

detections and base photometry, as well as easily investigate proximity effects on the injections. Can be skipped to save processing time if desired.

(3) **Injection** – Consistently add input objects in all relevant exposures and bands using the local PSF model in each exposure with corrections to the flux from the image zeropoints and local extinction – along with any other desired modifications such as an applied shear or magnification. This is discussed in detail in Section 4.2.2.

(4) **Coaddition & detection** – Same as (2) but with the injected null-weight images. The resulting photometric catalogs contain existing real objects, injections, new spurious detections, and blends between the two.

(5) **Single-Object Fitting (SOF)** – Fit a composite bulge + disk model that is the sum of an exponential and a de Vaucouleurs profile (CModel) to every source, while masking nearby sources.

(6) **Multi-Object Fitting (MOF)** – Fit sources with CModel, but group nearby detections into friends-of-friends (FOF) groups that have all of their properties fit iteratively to account for proximity effects. Only available for some `Balrog` runs due to its computational expense.

(7) **Metacalibration** – Fit a simple Gaussian profile to detections and then re-measure after applying four artificial shears [78]. This is useful for the creation of weak lensing samples where correcting for shear-dependent systematics is more important than absolute flux calibration [64].

(8) **Gaussian APerture (GAp) fluxes** – Fit a robust, scale-length-independent alternative to model-fitted photometry. Object flux is calculated within a

Gaussian-weighted aperture with full-width at half-maximum (FWHM) of 4″. Described further in Section 4.3.5.

(9) **Bayesian Fourier Domain (BFD)** – Estimate the shear of sources without explicitly fitting a shape using the methodology described in [80]. Available only for a few specialized runs.

(10) **Match and compute GOLD value-adds** – Match input injections to output detections while accounting for ambiguous matches (see Section 4.3.5). Merge truth and measured table quantities. Compute Y3 GOLD value-added quantities including flags, object classifiers, masks, and magnitude corrections (though only the dereddening component is used for `Balrog` magnitude corrections; see below).

The resulting photometric catalogs of measured `Balrog` sources can then be used to measure the DES wide-field response to various input quantities or used directly as randoms with realistic selection effects (see [17] and [172] for examples). In addition, an "injection catalog" is created which contains information for all injected sources, detected or not, for investigations of detection and completeness properties. The emulation steps (3) through (10) can be repeated for multiple injection realizations of a given tile to obtain sufficient sampling for the needed science case. However, as discussed in Section 4.3, for Y3 analyses we opted for a single realization with relatively high injection density due to the large computational cost of each realization.

Differences from the DESDM Pipeline

While `Balrog` strives to emulate the DESDM pipeline from null-weight images to science catalogs at high fidelity, there are some discrepancies due to practical limitations. The most significant are:

- **Reuse of existing single-epoch images, PSF models, photometric zeropoints, and World Coordinate System (WCS):** The injected fluxes of sources from the input catalog are modified only to account for an image's photometric zeropoint and the local extinction. Due to this we do not recalculate the photometric and astrometric calibrations or PSF estimate for any exposures which have additional objects added to them; the Y3 DESDM solution is carried forward unchanged. This means that we cannot probe the individual systematic error contributions of steps in the DESDM pipeline before this stage, such as biases in the PSF modeling or image detrending.

- **Incomplete `SExtractor` parameter list:** We chose to measure only a subset of the Y3 `SExtractor` parameters that were anticipated to be important for downstream analyses in order to save processing time. In particular, we did not compute any model-fitted magnitudes including `MAG_PSF` which is needed for the WAVG quantities described in [102]. Ultimately, the overall time saved was small and we plan to save all `SExtractor` quantities for future runs.

- **MOF is skipped for the cosmology sample:** While MOF photometry is available for the Y3 GOLD catalog, most Y3 cosmological analyses use the variant SOF which skips the multi-object deblending step in favor of masking neighbors. This approach is significantly faster, fails less often, and has negligible impact in photometric performance (E. Sheldon, private communication). As MOF is not needed for Y3 cosmology calibration and contributed roughly a quarter of all `Balrog` runtime (see Table 4.2), we elected to skip this step for the main samples.

- **Zeropoint and chromatic corrections are not applied:** The Y3 photometric calibration introduces new chromatic corrections that achieve subpercent uniformity in magnitude by accounting for differences in response arising from varying observing conditions and differences in object SEDs (see [128]). However, the mean Y3 GOLD chromatic corrections are significantly below 1 millimagnitude (mmag) for all but g band (0.45 mmag). As this is a subdominant effect that requires significant computation to correct in each injection realization, we do not account for these corrections before injecting into images. In addition, the SED-independent "gray" corrections that account for variations in sky transparency and instrumentation issues like shutter timing errors were not accounted for in the injection zeropoints. This was not intentional and will be included in all future `Balrog` runs. However, these corrections are also quite small, with the mean absolute Y3 GOLD gray zeropoint correction below 1 mmag for all bands except for z band (1.2 mmag). As we do not modulate the truth fluxes with these corrections during injection, it is not necessary to apply these corrections *after* measurement either.

- **Partial GOLD Catalog Creation**: Due to the staged approach in the creation of Y3 GOLD with value-added products being incorporated as they were being developed, the exact same procedure for compiling the `Balrog` catalog could not be followed strictly as it would have produced an unnecessary and severe overhead in the production time. Scripts that approximately replicate this process were provided by DESDM, though they only reproduce the columns that were deemed to be most relevant to Y3 key science goals. Slight modifications had to be made to quantities such as `FLAGS_GOLD` and the object classifier `EXTENDED_CLASS_SOF` where the required MOF columns

were not available; these differences are mentioned when relevant throughout this dissertation.

While not technically a difference in the *pipeline* emulation itself, we note here that PSF models used for injections (PSFEx; [116]) were found to be slightly too large in [130] for bright stars in Y1 due to the brighter-fatter effect (see [73]). However, we still used PSFEx for our injection PSFs as the new Y3 PIFF PSF model described in [175] was not yet implemented into the `GalSim` configuration structure that was required for our injection design, which is discussed below.

4.2.2 Injection Framework

As mentioned in the beginning of this section, incorporating single-epoch injection into `Balrog` required a new software design to handle the significant increase in simulation complexity beyond what was done in [17] for the SV and Y1 analyses. Development on the injection framework was partitioned into its own software package[3] as the injection step is fairly generic and of potential interest to other analyses outside of DES Y3 projects – as well as upcoming Stage IV dark energy experiments such as LSST. Briefly, our injection framework maps high-level simulation choices into individual object and image-level details consistent between all single-epoch images for the simulation toolkit `GalSim` [176] to process. With this design, `Balrog` automatically inherits much of the modularity, diverse run options, and extensive validation of `GalSim`. A schematic overview of the injection process is shown in Figure 4.2. The remainder of this section will quickly summarize the most relevant aspects of each step; we leave a more detailed description of the implementation details as well as a description of the most important user options for this new software package in Appendix A.

[3] https://github.com/sweverett/Balrog-GalSim

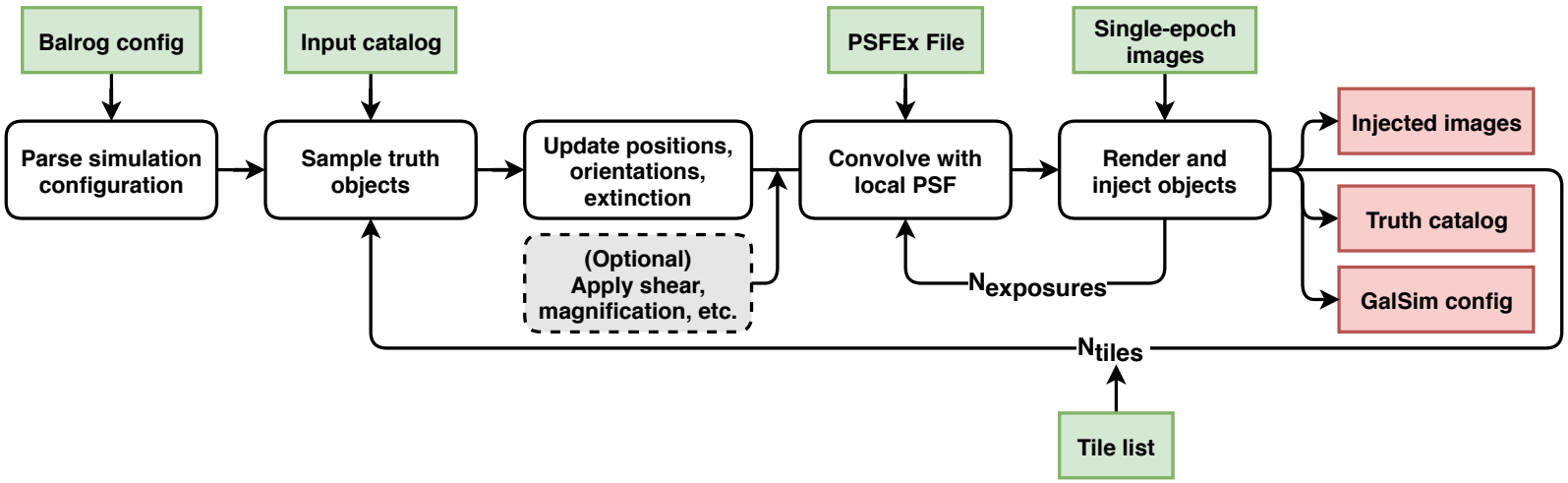

Figure 4.2: High-level overview of the injection processing for a single realization. Green boxes are inputs to the injection framework while red boxes are outputs. The length of each loop is determined by the number of exposures and tiles considered in the full simulation. While the main runs used for Y3 cosmology calibration modify only the position, orientation, and flux normalization of the truth inputs, there are many optional transformations that can be applied such as a constant shear or magnification. The main output of our injection package is a multi-document configuration file with detailed injection specifications that is then executed by `GalSim`, with each step being executed in the physically correct order. Additional realizations replicate all steps, other than the initial configuration parsing, and produce unique outputs.

Injection Configuration

The `Balrog` configuration serves as the foundation for the final, much larger `GalSim` configuration file produced for each tile by the injection pipeline which follows the `GalSim` configuration conventions that are extensively documented[4]. Global simulation parameters that apply to all injections are defined here such as the input object type(s) (see §A.2), position sampling method, injection density, and number of injection realizations. During injection processing, the requisite simulation details needed to inject the sampled input objects consistently across the relevant survey images are appended to this file to create a multi-document `GalSim` configuration file with each document corresponding to a single CCD exposure. An example configuration that was used for the two main cosmology runs is given in §A.4.

Input Sample and Object Profiles

While any native `GalSim` input type can be used for the simulations, most `Balrog` runs sample objects from an existing catalog with parametric properties that describe the flux and morphology of each source. The photometric measurements of the DF catalog, as well as most measurements in Y3 DES WF science catalogs, are based on Gaussian mixture model fits to various profiles by `ngmix`[5] introduced in [123] and most recently updated in [128]. Each profile parameterization is converted to a sum of `GalSim Gaussian` objects that represent the Gaussians components used in the original fit. `Balrog` can currently inject the following `ngmix` model types: a single Gaussian (`gauss`), a composite model (CModel; `cm`) first introduced in SDSS[6] which is a linear combination of an ex-

[4] https://github.com/GalSim-developers/GalSim/wiki/Config-Documentation
[5] https://github.com/esheldon/ngmix
[6] And described in Section 3.2.2

ponential disk and a central bulge described by a de Vaucouleurs' profile [126], and a slightly simpler CModel with fixed size ratio between the two components (`bdf`, for Bulge-Disk with Fixed scale ratio). In DES Y3, the DF measurements use `bdf` profiles while the WF uses `cm`.

See §A.2 for all provided custom input types, including the option to inject the "postage stamp" image cutouts of objects in MEDS files. While using the actual images of DF sources rather than parametric fits to their profiles would be a more accurate representation of the true distribution of galaxy properties and morphologies, there are significant added complexities due to adding artificial noise from stamps with larger associated PSFs than the injection image and ensuring stamp and mask fidelity of the full DF catalog; these issues are discussed in detail in Chapter 7.

Updating Truth Properties and Optional Transformations

Measurements of the transfer function with `Balrog` require truth tables that compile the properties of injected objects. For injections that are based off of real sources, some of these object properties are modified to fit the needs of the simulation such as the positions, orientations, and fluxes. The updated source properties either replace their original columns in the output truth catalogs or are appended as new columns. Object fluxes are scaled to account for interstellar extinction and to match the photometric zeropoint of each single-epoch injection image. Additional transformations such as a constant shear or magnification factor can be applied depending on the desired science case (see Section 6.2 for an example using magnification in Y3).

The position sampling of injections depends on the desired science case; uniform sampling naturally allows for `Balrog` objects to be used directly as randoms

for galaxy clustering calibration, but overlapping `Balrog` injections can artificially inflate the inferred blending rate. Alternatively, a hexagonal lattice is more appropriate for a perturbative sampling of the transfer function at a given position, but this embeds an unrealistic (though correctable) clustering signal at small scales. The available options are described in §A.3 and the trade-offs are discussed in more detail in Section 4.3.4.

PSF Convolution

The PSF used for each object is determined by the local single-epoch PSFEx solution at the injection position. Simpler PSF models are also allowed for testing purposes but not recommended for science runs.

Object Rendering and Injection

All of the previous simulation choices are ultimately encoded in a detailed configuration file that is structured to be read by `GalSim`. This design was chosen over explicit use of the software's Python API as the configs facilitate easily reproducible simulations and allow for runs that are identical except for minor modifications such as an added constant magnification factor. Each transformation from truth property to pixel value is automatically handled by `GalSim` processing in the physically correct order. After an object stamp is rendered (including Poisson noise from the new source), its pixels are summed with the initial image while ignoring any part of the profile that may go off image. Rarely a profile will require an extremely large grid for the fast Fourier transform (FFT) during PSF convolution and exceed available memory. To avoid this, we set a maximum grid length of 16,384 pix^{-1} (or $\sim 63,000$ arcsec^{-1} for DES) per side and skip objects that exceed this limit. While the injection framework was designed

with flexibility in mind for uses outside of the Y3 cosmology science goals (and even DES itself), there are currently some assumptions made about the structure of the input data to emulate DES Y3 that we plan on generalizing in upcoming releases.

4.2.3 Pipeline Validation

As `Balrog` is a non-generative, or discriminative, model of the transfer function, it is difficult to disentangle any intrinsic errors in the input sample or survey pipeline emulation from actual systematic effects we are trying to characterize – particularly since `Balrog` was run independently of DESDM processing for Y3. Therefore a series of increasingly complex test runs were completed in order to validate both the injection and emulation steps and characterize the pipeline fidelity at a detailed level. We initially ran `Balrog` with the injection step turned off to confirm that we recovered identical detection and photometry catalogs as Y3 GOLD when carefully accounting for the same random seeds in the fitters that were used in nominal Y3 processing. Once this was achieved, we verified that the injected profiles of objects drawn onto blank images matched single-object renderings made independently of the pipeline.

We then ran a series of tests where we ignored the existing survey image data during injection except for the estimated residual local sky background that is automatically subtracted from the exposures later in the pipeline. Objects were placed on a sparse grid to limit proximity effects from other injections with two types of noise depending on the run – either only Poisson noise for the injections or Poisson in addition to low levels of zero-mean Gaussian background sky noise. These blank image runs became progressively more complex as we added the features used in the main science runs described in Section 4.3 and acted as a

form of regression testing[7].

These tests are relevant for more than pipeline validation; effects from methodological choices can also be identified and quantified while working in a simplified environment. As an example, the runs with only Poisson noise indicated that there were two subgroups of objects with statistically significant differences in magnitude response – one was well calibrated, the other with a mean offset of $\sim$7.5 mmag too faint in each of *griz*. This was ultimately discovered to be a result of different priors used for the parameter that measures the relative flux ratio between the de Vaucouleurs and exponential component, `fracdev`, for the `ngmix` profile type used to fit DF objects (`bdf`) and the one used to fit wide-field measurements (`cm`). A series of plots that show the difference in input vs. measured `fracdev` and examples of its downstream effect on the recovered magnitude and color responses for this test are shown in Figure 4.3.

The impact of the different `fracdev` fits on the magnitude response can be seen clearly in Figure 4.3d, where the difference in measured vs. true i band magnitude as a function of injected magnitude is colored by the response in `fracdev` for a single tile. As the difference in profile definition between `cm` and `bdf` is largely due to fitting stability and has little to do with the true distribution of galaxy properties, this effectively puts a lower bound on the accuracy of the mean magnitude response that we are able to measure with `Balrog` when using the DF sample as inputs at around 3 mmag. Importantly, however, the effect is nearly identical in each of the *griz* bands and has negligible impact in the recovery of colors, as seen in Figure 4.3c. This example highlights some of the difficulties in choosing a "truth" definition for injections based on model fits and the importance of carefully testing the impacts of model assumptions.

[7]These tests are performed by setting the field `inj_objs_only` to `True` in the configuration file along with the `noise` field set to either `BKG` or `BKG+SKY`, though this mode of testing is only available for the provided `Balrog` image class, not `AddOn`. See Appendix A for further details.

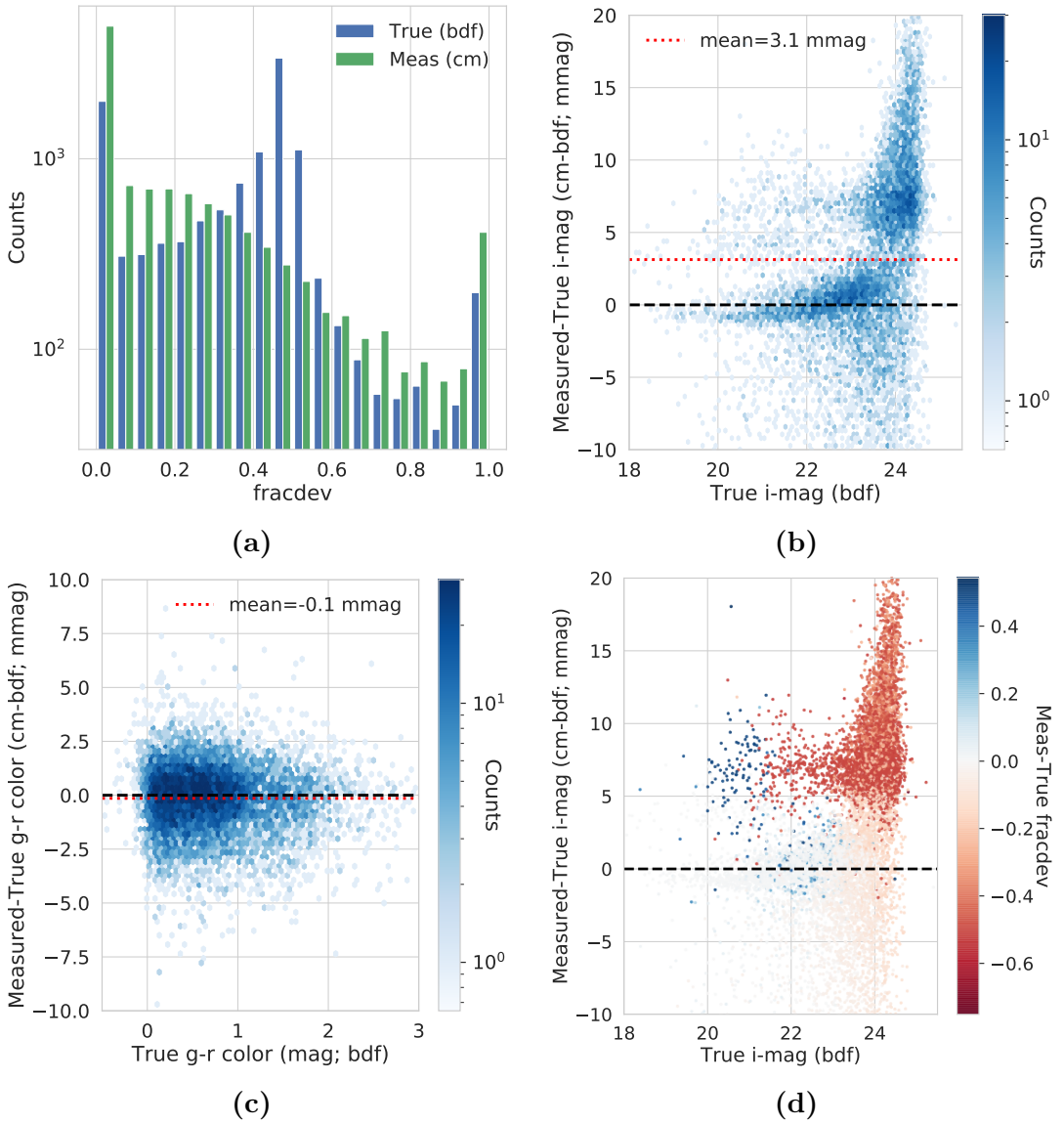

Figure 4.3: A series of plots highlighting aspects of the noiseless blank image test described in Section 4.2.3. (a) The difference in input `bdf_fracdev` vs measured `cm_fracdev` for detected objects. The additional peak at 0.5 for `bdf_fracdev` is a result of the slightly different model definition. (b) The i band magnitude response of these objects, where there are clearly two different populations. (c) The $g-r$ color response for these objects. The bias in recovered magnitude is nearly identical in $griz$ and so does not translate to the recovered colors. The mean color response for $g-r$, $r-i$, and $i-z$ is 0.1, 0.3, and 0.2 mmag respectively. (d) The biased magnitude population is a result of injections with input `bdf_fracdev`$\sim$0.5 scattering to 0 or 1 to match the expected `cm_fracdev` prior.

The final version of the blank image test was performed with identical input and configuration to that used to produce the fiducial Y3 catalogs across 200 tiles which contain over 2.3 million injections and 1.6 million detections. Zero-mean Gaussian background noise was applied to the blank images with variance set to the corresponding CCD `SKYVAR` value. The resulting object responses allow us to characterize the baseline performance of the photometric pipeline in ideal (though overly simplistic) conditions which in turn may provide lower limits on the intrinsic uncertainty in our sampling of the DES transfer function. The mean and median difference in recovered versus injected magnitude for *griz* is plotted in Figure 4.4. The vertical bars correspond to the mean of the standard deviations of *griz* magnitude responses in each truth magnitude bin, centered at the mean magnitude response.

The medians are extremely well calibrated, with only $g < 18.5$ and $22.5 < z < 23$ off by more than 5 mmag, or 0.45%, through 23rd magnitude where selection effects near the detection threshold become significant. The mean responses are consistently biased towards larger recovered flux on the bright end by $\sim$15 mmag due to the asymmetric tendency of SOF to measure the sizes of bright, extended objects to be too large in the presence of neighbors; this is a real effect seen in the main data runs and is discussed in greater detail in Section 5.3.1. Such biases are not seen in isolated SOF measurements of similar objects (E. Sheldon, private communication) and appear in this test as it was inefficient to use a grid size large enough to keep all other grid injections outside the MEDS stamps of the largest injections. This effect also keeps the magnitude error from decreasing as the intrinsic brightness increases as one would naively expect. While the magnitude bias induced by the difference in the `cm` vs. `bdf` profile definition is present in this measurement, it is negligible compared to proximity biases for extended sources

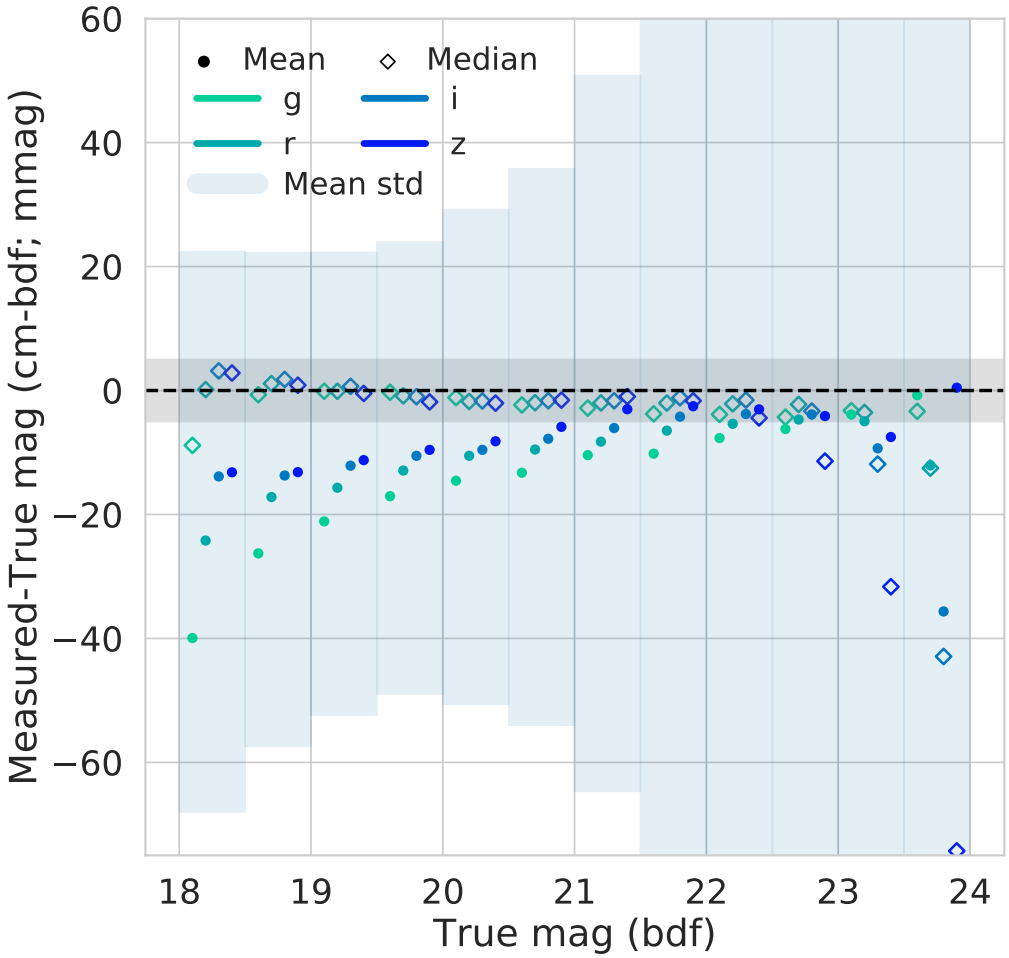

Figure 4.4: The mean (solid circle) and median (hollow diamond) difference in measured vs. injected magnitude (<Δmag>) as a function of input magnitude for the final blank image runs with zero-mean Gaussian background noise. The vertical bars correspond to the mean of the standard deviations of *griz* magnitude responses in each truth magnitude bin, centered at the mean magnitude response. The vertical bars represent the average of the standard deviations of *griz* magnitude responses in each bin of size 0.5 magnitudes, centered at the mean magnitude response. The overall calibration is excellent, with the median response less than 5 mmag in all bins except for $g < 18.5$ and $22.5 < z < 23$. We expect significant biases past magnitude 23 due to selection effects near the detection threshold. The mean responses show some bias however – particularly on the bright end. As discussed in the text, this is due to an asymmetric tendency for SOF to measure the fluxes of bright, extended galaxies to be too large when neighbors are contained in the object's MEDS stamps. The errors in <Δmag> do not substantially decrease past input magnitudes of 20 for the same reason.

and selection effects present in the noisier images.

Importantly, there is no significant band-dependence in the median magnitude responses where the recovered sample is complete, with a typical spread in median *griz* biases of ∼3 mmag for truth magnitudes ranging from 18.5 to 22 with no characteristic shape or distribution systematics. While there is a detectable band-dependence in the mean magnitude responses, it is nearly eliminated when binned in signal-to-noise (S/N) instead of magnitude to account for differences in sky noise.

4.3 `Balrog` in DES Year 3

We describe here the injection samples, pipeline settings, and matching choices used to create the Y3 `Balrog` data products for the photometric performance characterization presented in Chapter 5 and downstream science calibrations described in Chapter 6. For Y3, we ran `Balrog` several times with different configurations for various validation and science cases. These runs are tabulated in Table 4.1 which lists the following quantities: the run name, the number of simulated tiles, the total number of injected objects, the fraction of detected objects, the spacing between injections, and the magnitude limit used for sampling. As detection in DES is based on a composite *riz* detection coadd, we emulate the detection magnitude by averaging the dereddened *riz* fluxes of the injections.

The main runs used for cosmological analyses are called `Run2`[8] and `Run2a`. The former samples the transfer function across 1,544 randomly chosen tiles (of the 10,338 Y3 tiles) to a detection magnitude limit of 25.4. This limit was chosen to capture DF objects that had at least a 1% chance of being detected as measured

[8]The designation `Run1` was used for an earlier set of simulations that used an inferior DF catalog.

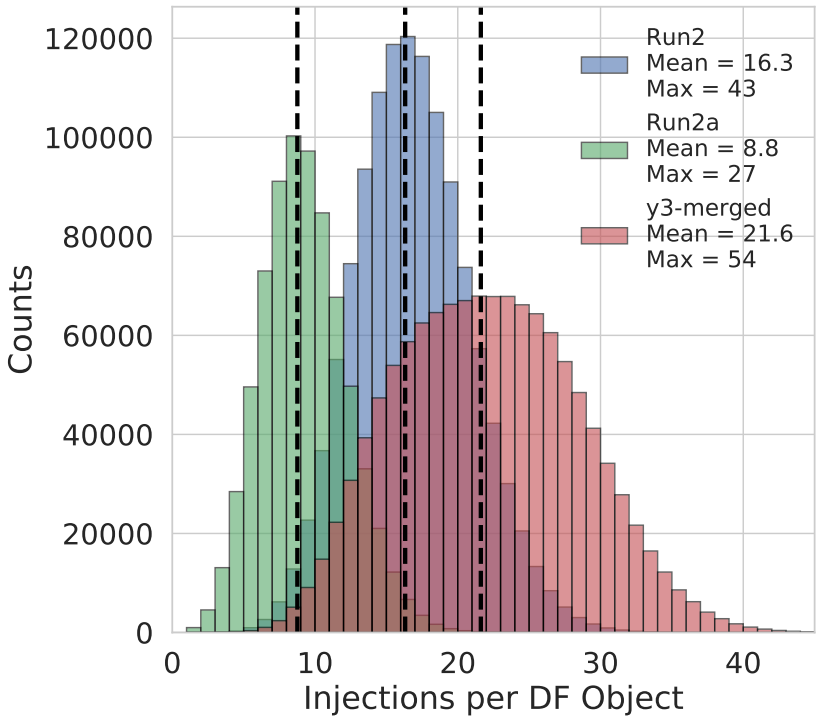

Figure 4.5: The number of injections per unique DF object for `Run2` in blue, `Run2a` in green, and their combination `y3-merged` in red. The mean number of injections per run is shown with dashed vertical lines and is stated along with the maximum number of injection realizations. `Run2` is composed of 1,544 tiles vs. only 497 for `Run2a`, but has a larger input catalog to sample due to the more conservative composite *riz* detection magnitude of 25.4 vs. 24.5 for `Run2a`. The resulting combination is no longer a Poisson distribution but this can be accounted for in downstream analyses by weighting by the column `injection_counts`. The typical `Balrog` object in `y3-merged` has just over 20 unique injection realizations across the sampled footprint.

Run Name	Tiles	N Det	Det-Frac	Lim	Spacing	Notes
`grid-test`	200	1.6 M	0.702	24.5	20″	Blank images with noise
`noiseless-grid`	196	2.6 M	0.997	24.5	20″	Above, but without noise
`Run2`	1544	7.4 M	0.369	25.4	20″	Main run, deepest
`Run2a`	497	3.9 M	0.600	24.5	20″	Main run, shallower
`Run2-mag`	155	0.8 M	0.463	25.4	20″	2% magnification
`Run2a-mag`	497	3.9 M	0.607	24.5	20″	2% magnification
`clusters`	901	39.9 M	0.930	23.0	10″	Tiles containing clusters
`blank-sky`	88	–	—	—	20″	Injected zero-flux objects

Table 4.1: A list of Y3 Balrog runs and associated parameters: the number of tiles sampled, the number of total detections (N Det), the detection fraction (Det-Frac), the composite *riz* detection magnitude limit (Lim), and injection lattice spacing.

from a 200 tile test run. `Run2a` was a supplemental run at a shallower limiting magnitude of 24.5 across 497 tiles to increase the fraction of recovered injections for analyses that needed a larger total sample. These runs are combined for the fiducial `Balrog` catalogs `y3-merged` and `y3-stars` which are described in upcoming sections. The distributions of the number of injection realizations per input object for these runs are shown in Figure 4.5, and the spatial distribution of these tiles are shown compared to the full DES footprint in Figure 4.6. `Run2-mag` and `Run2a-mag` are identical to the above runs except for a constant added magnification of $\mu = 0.02$; these are described in more detail in Section 6.2. The `grid-test` and `noiseless-grid-test` runs were used for the validation tests shown in 4.2.3. The `blank-sky` and `clusters` runs were conducted separately from the main cosmology runs in order to facilitate two of the science cases discussed in Sections 6.3 and 6.4 respectively.

The processing was done on a dedicated compute cluster at Fermilab, "DE-grid", consisting of 3000 cores with 6-8GB RAM per core available. The typical core and memory provisioning along with wall-clock running times for each stage of the pipeline are given in Table 4.2. MOF is not used for the fiducial Y3 cosmology

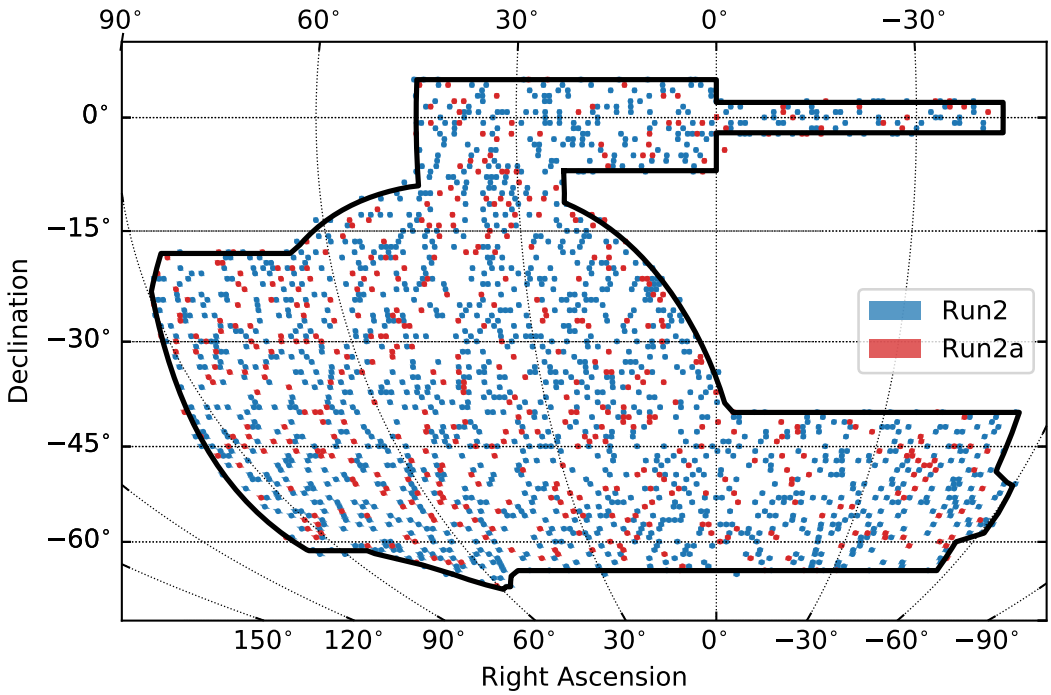

Figure 4.6: The spatial distribution of randomly sampled DES tiles used for `Balrog` injections. 1,544 `Run2` and 497 `Run2a` tiles are shown in blue and red respectively. The outline of the DES footprint is shown in black. Some tiles are outside of the enclosed area due to observations that overlap the footprint edge.

analyses and so is excluded for `Run2` and `Run2a` – along with their corresponding magnification runs. We include the estimated computational cost to show the difficulty in scaling this methodology to full footprint coverage and WF density – we discuss this more in Chapter 7. All output measurement catalogs were archived including the MEDS cutout images of detected objects; the injected single-epoch images and resulting coadds were only saved for validation runs.

A few additional post-processing steps were required to match changes made to the Y3 object catalogs after the fiducial GOLD catalog creation. These consisted of a correction to the Metacalibration S/N column, redefining the `size_ratio` quantity from `mcal_T_r / psfrec_T` to `mcal_T_r / mcal_Tpsf`, and adding a shear weight to each of the Metacalibration measurements described in 6.1.

Stage	Cores	RAM	Clocktime
Database Query	1	64 GB	2.0 hr
Base Coaddition/Detection/MEDS	4	64 GB	3.0 hr
Injection	16	64 GB	3.0 hr
Coaddition/Detection/MEDS	4	64 GB	5.0 hr
MOF*	32	256 GB	6.5 hr
SOF	16	64 GB	1.5 hr
Metacalibration	8	320 GB	2.5 hr
Match/Merge/Flag	2	512 GB	1 hr
Total/tile	16-32	64-512 GB	$18 - 24.5$ hr/tile

Table 4.2: Approximate `Balrog` stage run times and memory allocations per tile. *As MOF is not used in the fiducial Y3 cosmology analysis, this step was only run for `Run1` due to the long clocktime. The two total reported clocktimes are with MOF excluded or included in the pipeline emulation respectively.

4.3.1 Input Deep Field Catalog for y3-merged

The majority of Y3 `Balrog` analyses use injections drawn from DECam measurements of objects in the DF described in [173]. In brief, this catalog of nearly 3 million sources is assembled from hundreds of repeated exposures of three DES supernovae (SN) fields and the COSMOS field. The corresponding deep single-CCD coadds have S/N of $\sim\sqrt{10}$ times their WF counterparts and thus provide a good sample of low-noise sources to draw from for explorations of systematics in the WF measurements. There are multiple versions of the DF catalogs that provide trade-offs in the average seeing quality vs. the maximum depth. In Y3 `Balrog`, we use `COADD_TRUTH` as it strikes a balance between using observations with 10 times the mean WF exposure time while ensuring that the composite DF FWHM be no worse than the median single-epoch FWHM in the WF for each of the injection bands.

We emphasize that we are not injecting the actual *images* of DF galaxies but instead take the MOF `ngmix` parameterized model fit to each detection and gen-

erate an idealized galaxy profile based on those model parameters (with added Poissonian noise). The injection framework described in Section 4.2 is capable of injecting the MEDS stamps directly which in principle would account for additional diversity in galaxy morphologies and eliminate any model bias compared to the true distribution of galaxy properties. However, this requires extensive validation of the DF stamps before injection and introduces additional complications due to image masks and added noise for injections into CCDs with better seeing than the DF composite image. We plan to revisit these issues for `Balrog` in the Y6 methodology.

The DF catalog is comprised of model fits that are very similar to the WF CModel with two major differences: the two components (bulge + disk) are fit simultaneously rather than separately, and the ratio of the size of each component, `TdByTe`, is fixed to be 1. While this was chosen for increased fitting stability for the fainter DF sources, fixing the relative bulge-disk size ratio reduces the total number of free parameters in the model by one and significantly changes the distribution in the relative flux fraction `fracdev` (recall Section 4.2.3 for how this impacts the corresponding recovered CModel photometry in idealized conditions). Ultimately, any photometry can be used for the injection truth as long as it is an unbiased estimate of the real distribution of object properties. The `bdf` profile will be used for all Y6 DES source fitting and for Y6 `Balrog` – avoiding the small systematic difference in magnitudes between `cm` and `bdf`.

DF Object Extinction

The DF catalog has detailed photometric corrections to the fluxes including for extinction as described in [173]. However, these corrections were not yet ready when `Balrog` began the cosmology runs. Thus in order to accurately account

for variations in DF extinction, as well as extinction variations among tiles in the Y3 survey footprint, we enacted the following procedure to deredden the DF input objects and then re-extinct them by an appropriate amount in the injection WF tile: For the DF objects, we sample the extinction maps described in [177] at five points (center and corners) in each input DF CCD (of size $9' \times 18'$) and record the average of the 5 E(B-V) values. We also record the five-point average of E(B-V) for the larger (size $44' \times 44'$) WF tiles. During injection, we deredden each object by the DF recorded value for its CCD of origin and apply the mean extinction value for the WF injection tile. This chip and tile-level correction is simple to implement and distorts the overall magnitude and color distribution of the DF galaxy sample from the cosmic average only slightly. However, we plan on implementing per-object extinction corrections in the Y6 methodology. The used dereddening and extinction values are preserved in the injection truth tables for later flux and magnitude corrections to enable consistent comparisons between true and measured quantities.

4.3.2 Input Star Sample for y3-stars

While the majority ($\sim$90%)[9] of the injections are sources (both stars and galaxies) from the DES DF, $\sim$10% of injections are simulated stars. In addition to characterizing the photometric response of stars in DES with nearly no galaxy contamination (see Section 5.2), the `y3-stars` sample is useful for quantifying the baseline performance of the DESDM pipeline for the simplest morphologies. This allows us to isolate the more complex model fitting issues for the heterogeneous `y3-merged` sample.

The morphologies are modeled as pure delta (δ) functions convolved with the

[9]Most tiles were run with a 9-1 ratio between input catalogs, but the first 152 tiles of `Run2` were run with an 8-2 ratio.

local PSFEx solution used during injection. The magnitude and color distributions are based on the local stellar population in each of the 10,338 tiles in the Y3 footprint. For example, areas of the survey with higher stellar density near the galactic plane received more bright stars than areas toward the south galactic pole in the center of the footprint. To represent color distributions fainter than the WF limit of $i{\sim}24$, the color distribution near $i{\sim}24$ was extended by two magnitudes to $i{\sim}26$ using models of the Galactic disk and halo [178]. The simulated star catalog has already been corrected for extinction, so no other preprocessing is required. The measurement pipeline has no knowledge of the difference in input star/galaxy classification and returns the same CModel fits as `y3-merged`.

4.3.3 Object Classification and Differences in Measurement Likelihood

While we expect `y3-merged` and `y3-stars` will be used for calibration of DES galaxy and stellar systematics respectively, there are additional star injections in `y3-merged` as it draws from all sources in the DF that pass quality cuts. Sources in the DF catalog have been classified with a k-nearest neighbor algorithm[10] trained on a subset of objects that have near-infrared (NIR) data from the UltraVISTA survey ([173, 179]). The classifier's stellar sample is not perfectly complete from magnitudes $18 < i < 24$ (an average of 93%), but its mean weighted purity is greater than 98% over the same range. The requirement of successful detection and measured photometry for all $ugrizJHK$ bands reduces the total number of objects with classification by 44.5%. The cut `NearestNeighbor_class=2` selects this star sample while `NearestNeighbor_class=1` will select the classified galaxies. The DF stars are not used in the analysis of the Y3 stellar photometric performance in

[10]This classifier was added after the `Balrog` runs completed, and so is not included as one of the truth columns. It has to be matched to the relevant Y3 DF catalogs.

this paper but are available if a larger sample is required for a given science case. However, we do use these classifications when estimating the galaxy contamination in Y3 stellar samples in Section 5.4.

We note that there is a subtle difference in the measurement likelihoods corresponding to each sample. The likelihood of the δ-sample, $\mathcal{L}^{\delta}_{\rm star}$, assumes perfect classification knowledge and is given by

$$\mathcal{L}^{\delta}_{\rm star} = p(\boldsymbol{\theta}_{\rm meas},\, c_{\rm meas}|\boldsymbol{\theta}_{\rm true},\, c_{\rm true}{=}{\rm star}) \tag{4.1}$$

$$= p(\boldsymbol{\theta}_{\rm meas},\, c_{\rm meas}|\boldsymbol{\theta}_{\rm true}), \tag{4.2}$$

where $\boldsymbol{\theta}_{\rm meas}$ and $\boldsymbol{\theta}_{\rm true}$ are the measured and true objects' photometric parameters and $c_{\rm meas}$ and $c_{\rm true}$ are the corresponding object classifications. Alternatively, the likelihood of the DF star sample, $\mathcal{L}^{\rm DF}_{\rm star}$, accounts for the uncertainty in the truth classification:

$$\mathcal{L}^{\rm DF}_{\rm star} = p(\boldsymbol{\theta}_{\rm meas},\, c_{\rm meas}|\boldsymbol{\theta}_{\rm true},\, c_{\rm true}). \tag{4.3}$$

This becomes particularly relevant if one wants to combine results from Sections 5.2 and 5.3 for modeling errors of the composite sample. The needed conditional probabilities that capture the stellar efficiency and galaxy contamination of `y3-merged` can be derived from the results in Section 5.4.

4.3.4 Sample Selection & Injection Strategy

While in principle we would randomly sample from all sources in the DF, there are some methodological and practical considerations that led to the following conservative cuts:

```
      flags = 0
AND   mask_flags = 0
AND   in_VHS_footprint
AND   bdf_T < 100
AND   bdf_flux / bdf_flux_err > -3
AND   bdf_det_mag < {25.4, 24.5}
```

First, we eliminate any objects flagged with model fitting errors or in manually masked regions. We also require injections be from regions with external observations in the near-infrared (IR) as these IR bands are critical for the photometric redshift calibration (see 6.1). We restrict the characteristic size of the injections (`bdf_T`) to be less than 100 arcsec^2 (corresponding to $\sim$10 arcsec) to reduce the rate of `Balrog-Balrog` blends and proximity effects on the injection grid – though this selection may result in slightly over-sampling large, highly-elliptical galaxies. In addition, this choice may be in conflict with other potential science cases such as measuring the detection efficiency and photometric response of low-surface-brightness (LSB) galaxies [180]. Next, we remove objects with flux to error ratios of less than -3 in any band; this cut was needed after inspection of the DF catalog showed that there was an excess of objects with extremely negative flux values compared to WF measurements (though `ngmix` fluxes are clipped below 10^{-3} when computing magnitudes).

Finally, we apply a detection magnitude limit of 25.4 to limit the time spent on injections that have almost no chance of being detected while still using a source catalog that is $\sim$2 magnitudes deeper than WF. As described in the beginning of Section 4.3, this limit was derived from the mean dereddened *riz* `bdf_flux` of injections that had at least a 1% chance of being detected during a 200 tile test of `Run2`. We do not consider the flux in g in this calculation as it is not used in the detection image in DESDM processing. The `Run2a` limit of 24.5 was chosen

based based on requirements for the lens magnification measurement detailed in [181] (and described further in Section 6.2). After making this selection, the DF injection catalogs used in `Run2` and `Run2a` have just over 1.23 million and 746,000 objects respectively.

The star catalog was sampled to its full depth of 27th magnitude in g at a fraction of 10% of the total objects injected into `Run2a` and (most) `Run2` tiles. No additional cuts were made. Since the relative contribution of Galactic stars to the total object count peaks at about 21st magnitude in a standard Y3 tile, these injections do not dominate the faint end of the distribution.

Choosing the injection density per realization is a trade-off between increasing the statistical power of the catalogs, reducing the rate of `Balrog-Balrog` blends, and reaching the desired footprint coverage given available computational resources. Ideally, we would measure the response of a single source added to DES images for a high number of realizations. As this is unfeasible we instead add objects on a hexagonal lattice with $20''$ spacing using a `MixedGrid` (see §A.3) for a single realization, corresponding to a density of $\sim$7.8 objects per arcmin^2 (or about 40% of the total Y3 density).

We can achieve a much higher injection density than that used in [17] as we do not randomly sample the positions which greatly reduces the self blending rate of injections. This is crucial as running a single `Balrog` tile realization in Y3 takes $\sim$40 times longer than in SV and Y1 due to the increased complexity of the injection framework and additional photometric measurements. While this does in principle limit the ability to use `Balrog` injections as randoms to measure clustering signals on scales at and below the grid size, this is currently well below the scale cuts of order $10'$ used in the Y3 analysis. In addition, we note that `Balrog` can still be used for studies of samples with intrinsic clustering by sub-

sampling the full catalog of grid injections to match the desired clustering signal.

However, this relatively high density could have significant implications for a non-local deblender like the one used in MOF. In early testing, we found that this level of injection density can sometimes lead to nearly all objects in a tile becoming a single MOF FOF group. Such non-local effects are less relevant for SOF except in cases where blends of other nearby injections with large, real sources may change how the masking of the blend is handled (or for extremely large injections that would be captured in the MEDS cutout of other injections, which is why we cut on the injection size). Dealing with non-local contributions to the measurement likelihood may be an important consideration for Y6 as the object detection threshold is lower and proximity effects are more of a concern.

4.3.5 Blending and Ambiguous Matches

An important caveat in using an object injection pipeline like `Balrog` is that there is often inherent ambiguity in the matching of the new object catalogs to the injections. Remeasurement on the injection images changes the number of detections and catalog ID assignments in unpredictable ways, and light profiles that were previously considered distinct detections can be blended together into single objects. While we will show that the fraction of ambiguous cases is relatively small at our injection density in DES images ($<1.5\%$) and can in principle be removed for our photometric tests, this ignores the increased shear noise and root mean square (RMS) of the measured ellipticity distribution for these objects which may be a dominant systematic for weak lensing measurements in deeper surveys like LSST [120]. In addition, highly non-linear detection and photometry algorithms can often respond in unexpected ways to perturbations (particularly deblenders that are intrinsically non-local) which can lead to additional spurious

detections and splitting of objects. As a rule: *Any matched catalog from an injection pipeline has made assumptions about ambiguous matches and blending!* For these reasons, we save the full remeasured photometry catalogs so that different matching procedures can be applied depending on the desired science case. This is distinct from the approach in [17] which ran remeasurement in `SExtractor`'s association mode near injection positions.

However, it is useful to have a standard catalog sample with consistent matching for downstream cosmological analyses. Unless otherwise specified, Y3 analyses using `Balrog` catalogs use a catalog which applied the following matching prescription: We define the *antecedent* of any blend as the "brightest" of the individual objects that contributes to it by some metric. Each blend thus comprises a noisy version of the antecedent as well as the non-detection of all other contributors to the blend. This approach gives a consistent and complete assignment of detection, non-detection, and antecedent to all objects of interest in the remeasured images and strikes the desired balance of including photometric scatter by blend contributors while excluding extreme outliers due to faint injections near existing bright objects. In addition, in the absence of measurement noise this scheme sets a maximum for the possible flux error of the antecedent in a two-object blend to be $|\Delta\text{mag}|\sim 0.75$; a factor of 2. An overview of how this scheme applies to the most common case of a two-object blend is shown in Figure 4.7.

The above prescription requires a brightness metric to determine the antecedent. We use the average of the dereddened Gaussian-weighted aperture (GAp) fluxes in each of the DES detection bands (riz). GAp fluxes are conceptually similar to GAaP fluxes described in [182] but instead measure the aperture flux for source profiles *before* convolution with the PSF. These fluxes are computed analytically from the MOF `bdf` fits to the DF injections and the SOF CModel fits

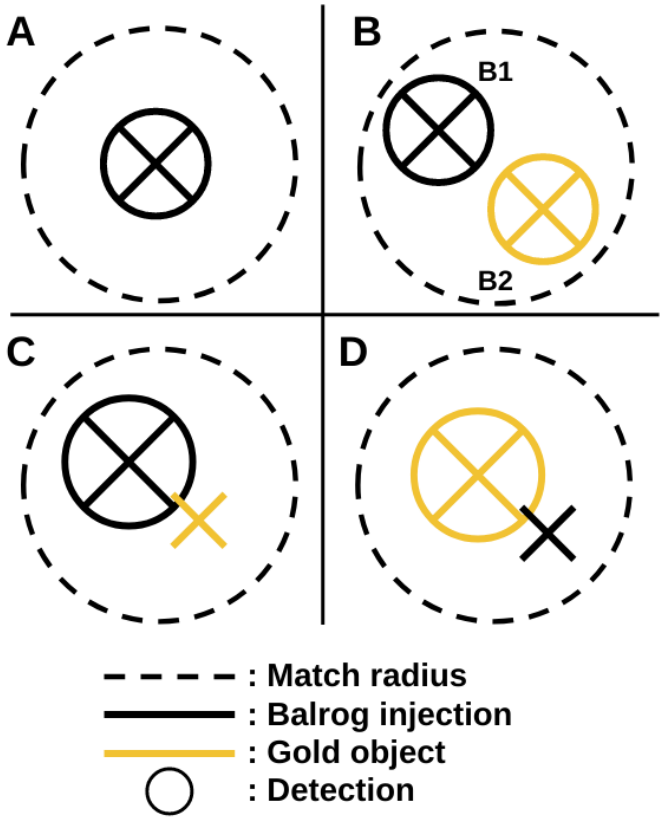

Figure 4.7: An overview of how ambiguous matches can arise in the case of a two-object blend. A black cross mark denotes the position of a `Balrog` injection while a gold cross mark denotes the position of a Y3 GOLD detection. A circled cross mark indicates a detection in the `Balrog` catalog while the dashed circle indicates the region inside of the search radius r_2. Case (A) is by far the most common and is unambiguously a `Balrog` injection. Case (B) has both the injection and the GOLD object detected within r_2 but is *extremely* rare; in this case we select the closer detection. Cases (C) and (D) are true blends where there is ambiguity in whether to classify it as a `Balrog` object with properties blended by the GOLD source or as a GOLD object that was blended by an injection. In this case we assign the object with the larger average *riz* GAp flux as the antecedent. Only Case (D) is removed from the `Balrog` catalogs when applying a `match_flag` cut.

to Y3 GOLD objects using a Gaussian weight function with FWHM of $4''$. This allows us to use an estimate derived from our best guess of the flux of the PSF-deconvolved profile near the relevant object centroids while discounting variations in measured flux due to morphological differences – particularly those arising from significant flux contributions from the wings of extended profiles. We use the average of the detection band δ fluxes for `y3-stars` since an equivalent GAp flux is not well defined. This difference only becomes relevant for the brightest star injections, though in these cases they are very likely to be the antecedent.

The matching procedure is implemented in two separate steps. First, the injection positions are matched to the closest object in the remeasured photometry catalogs within a search radius of $r_1 = 0.5''$. All objects that have a match are saved in the output `Balrog` catalogs and undergo the aforementioned post-processing steps. Afterwards, the output catalogs are matched against the Y3 GOLD catalog to compare the relative brightness of any existing detections within a second match radius r_2 for a series of radii from $0.5''$ to $2.0''$ in increments of $0.25''$. Over 96% of candidate objects have no GOLD sources within the search aperture and are unambiguously a `Balrog` injection[11]. Candidates that have an existing GOLD object within r_2 with mean riz GAp flux below their own are considered the antecedent and given a `match_flag_{r2}_asec=1` to indicate the presence of a nearby real source. Candidates that have a match within r_2 but have a smaller mean GAp flux than the existing object are assigned `match_flag_{r2}_asec=2` and are recommended to be cut from science analyses. We encode this information as a flag instead of cuts to the fiducial catalog to allow `Balrog` users more flexibility in choosing how to handle blending and ambiguous cases as needed. In this paper, we cut on `match_flag_1.5_asec < 2` as we found that only 0.1%

[11] In principle there can be rare exceptions to this such as new spurious detections very close to injection positions, but we do not consider that here.

and 0.5% of Y3 GOLD objects were separated at distances less than 1.5″ at i magnitudes of 21 and 22.5 respectively (or about 1.3-1.8 times the median PSF size depending on the band).

We show in Figure 4.8 the the difference between the recovered and injected GAp magnitude, $\Delta\text{mag}_{\text{gap}}$, for all recovered `Run2` objects for three choices of ambiguous matching cuts. In the left panel where no cut on ambiguous matches has been made, there is a long, asymmetric tail for negative $\Delta\text{mag}_{\text{gap}}$ where the recovered GAp flux is up to 10 magnitudes brighter than the input. While there can be extremely large magnitude responses to model-fitted photometry in crowded fields or extreme imaging conditions (see Section 5.3.3), we expect GAp magnitudes to be less sensitive to these failure modes and most large discrepancies to be due to ambiguous matches. This is indeed the case: In the following panels where a match flag with r_2 of 0.5″ and 1.5″ are used to create the sample, the worst GAp response outliers have been removed and the fraction of detections where $|\Delta\text{mag}_{\text{gap}}| > 1$ falls by 41% and 65% respectively. Some remaining scatter beyond $|\Delta\text{mag}_{\text{gap}}| = 0.75$ is expected even for an optimal r_2 due to ambient light in dense fields, blends with extended sources, and image artifacts, though the number of objects below $\Delta\text{mag}_{\text{gap}} = -1$ for the 1.5″ cut falls by over an order of magnitude for each bin of unit size.

With ambiguous matches dealt with, the `Balrog` catalogs are now ready to be used for diagnostics, photometric performance characterization, and measurement calibrations. We discuss the first two in the next chapter and summarize the most important applications for the DES Y3 cosmological analysis in Chapter 6.

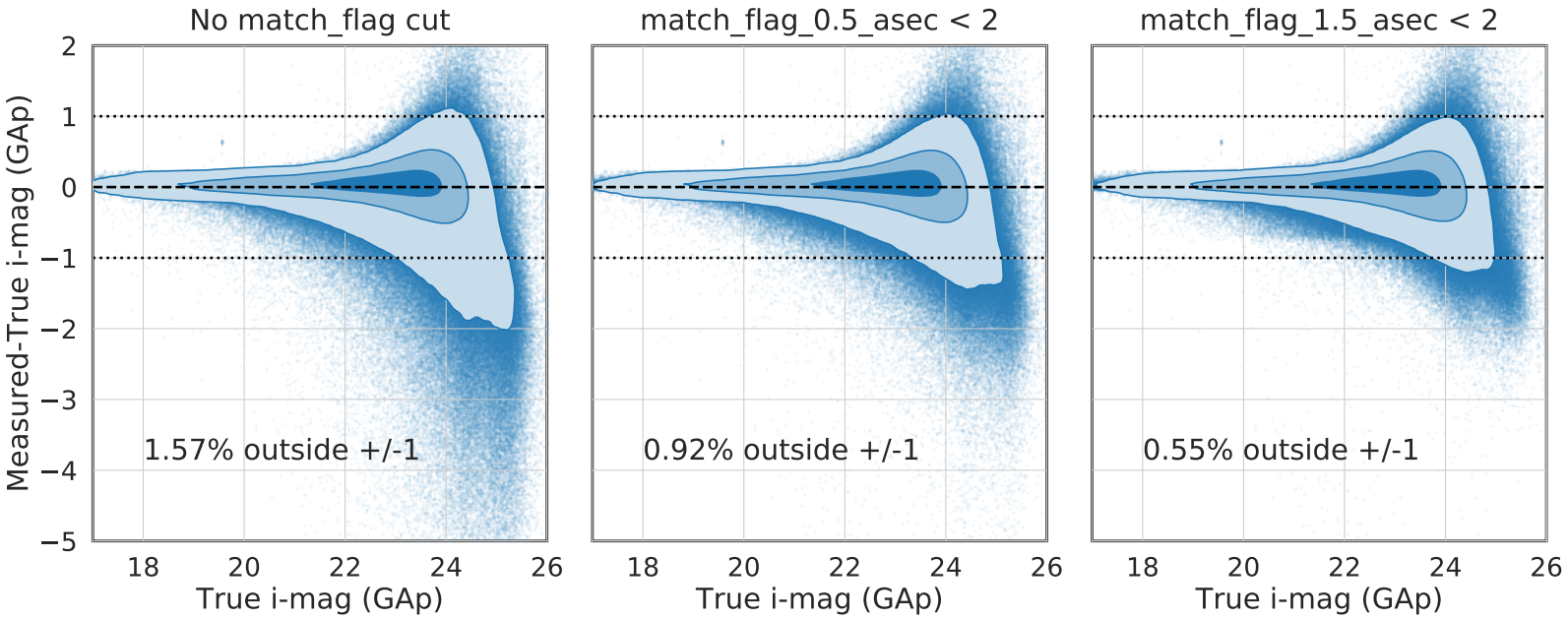

Figure 4.8: The effectiveness of our ambiguous matching scheme, illustrated by the difference in measured vs true i band GAp magnitude ($\Delta\text{mag}_{\text{gap}}$) as a function of input GAp magnitude for three ambiguous matching choices. The overplotted contours contain 39.3%, 86.5%, and 98.9% of the data volume, corresponding to the volume contained by the first three σ's of a 2D Gaussian distribution respectively. The percentage of detections outside of the dashed region denoting $|\Delta\text{mag}_{\text{gap}}| < 1$ for each choice is labeled in the bottom left of each panel. The left panel shows the $\Delta\text{mag}_{\text{gap}}$ response for `y3-merged` when no cut is made to handle ambiguous matches. The following two panels show the same distribution after cutting on the match flag using a r_2 of $0.5''$ and $1.5''$ respectively. The outlier tail significantly decreases in size as more ambiguous blends are accounted for, with nearly three times less objects outside of $|\Delta\text{mag}_{\text{gap}}| < 1$ when using the fiducial value of $r_2 = 1.5''$.

Chapter 5

Characterizing the Photometric Performance of DES Y3

Here we present the photometric performance of the DES Y3 science catalogs using the `Balrog` DF sample `y3-merged` along with the synthetic star sample `y3-stars`. While there are many photometric catalogs and science samples of interest for Y3, here we largely focus on the SOF CModel photometry of a basic Y3 GOLD sample [128] used as a starting point for more restrictive samples. Unless otherwise specified, the cuts for this sample are given by

```
    FLAGS_FOREGROUND = 0
AND FLAGS_BADREGIONS < 2
AND FLAGS_FOOTPRINT = 1
AND FLAGS_GOLD_SOF_ONLY < 2
AND EXTENDED_CLASS_SOF >= 0
AND MATCH_FLAG_1.5_ASEC < 2
```

along with any appropriate object classification cut which will be mentioned when relevant. Note that `FLAGS_GOLD_SOF_ONLY` is used in place of the typical `FLAGS_GOLD` as we are unable to compute the first bit flag without `y3-merged`

MOF runs. While ∼3.5% of Y3 GOLD objects have `FLAGS_GOLD=1`, no Y3 cosmology analyses currently use this flag bit due to the use of SOF or Metacalibration photometry in favor of MOF. Additional samples for a few interesting `Balrog` applications are discussed in more detail in Chapter 6.

We begin by examining how representative the `Balrog` catalog properties are compared to Y3 GOLD in Section 5.1, including a detailed look at how the number density fluctuations of both samples vary with respect to survey property maps. We then show the magnitude and color responses of `y3-stars` and `y3-merged` along with a discussion of interesting photometric failure modes in Sections 5.2 and 5.3 respectively. We then end by characterizing the performance of the `EXTENDED_CLASS_SOF` star-galaxy separator, using the extremely pure `y3-stars` sample whenever possible. As it is not practical to plot the photometric responses of all quantities of interest, one-dimensional Gaussian summary statistics for many relevant parameters are provided in Appendix C.

5.1 Consistency with DES Data

Even without perfect emulation fidelity, we expect the measured `Balrog` property distributions to closely resemble DES catalogs if we are indeed sampling an adequately representative transfer function and input sample. We will broadly check this agreement at various steps along the measurement path: object detection, photometric properties, and correlations with survey systematics – along with how these differences impact a typical clustering signal measurement. As we are primarily interested in the consistency in the transfer function of galaxies for cosmology, we use the `y3-merged` sample throughout and mention any classification cuts when relevant.

5.1.1 Completeness

We begin with object detection. Of the nearly 26.5 million galaxies injected in `y3-merged`, just over 41.9% were detected during re-measurement after accounting for ambiguous matches. However, as this catalog is the merger of two runs with different magnitude limits, it is more accurate to say that 36.3% and 59.4% of objects were recovered for `Run2` and `Run2a` respectively. The fraction of injections contained in the fiducial sample drops to 14.4% and 44.2% after considering the basic flag and mask cuts described above. To simplify the comparison on the faint end we use only `Run2` for the following comparison as it is about a magnitude deeper.

The detection completeness of sources in *griz* for `Run2` (points) compared to Y3 GOLD objects in the X3 supernovae field (lines) is shown in Figure 5.1. The completeness is plotted as a function of reference magnitude; the injection magnitudes for `Balrog` and the DF measurements of objects in the X3 field for Y3 GOLD. As we are comparing the mean completeness of the `Balrog` sample across all `Run2` tiles to only a small region for Y3 GOLD, to make a fair comparison we estimate the uncertainty in the difference with 50 jacknife samples of the `Run2` footprint. Note that the inferred completeness is only robust until the forced magnitude limit cutoff of 25.4 indicated by the dashed vertical line; beyond this point, the sampled injection objects have inherited a selection bias that forces at least one of the other detection bands to be significantly brighter than the magnitude limit and thus is more likely to be detected.

Overall the completeness measurements are quite similar, with the only discrepancies greater than twice the estimated error occurring for the brightest g band magnitudes and the faintest i and z bin. The `Balrog` g band completeness dips on the bright end despite the very high S/N as g is not included in the com-

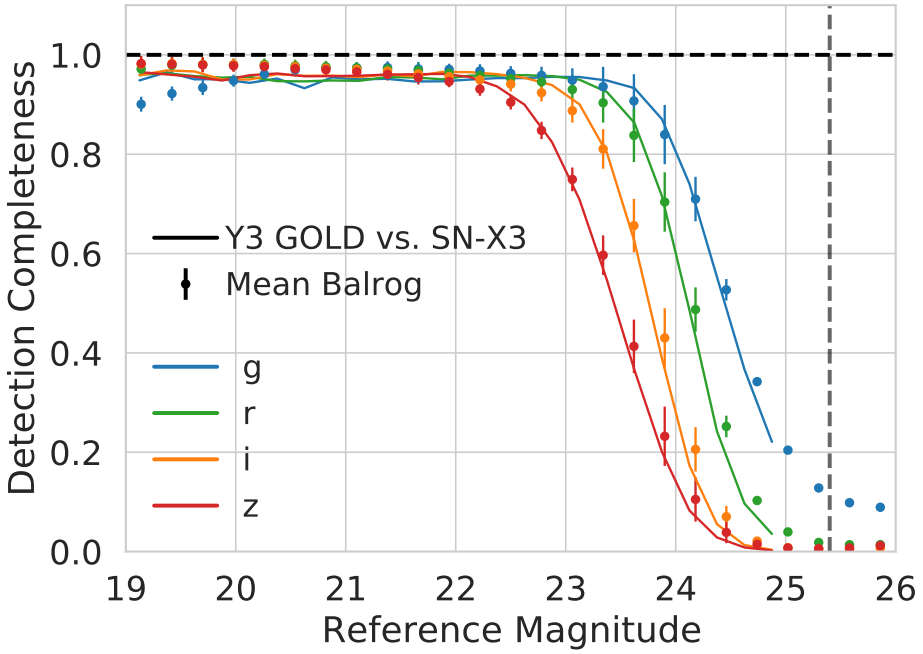

Figure 5.1: The fraction of objects recovered by band and input injection magnitude. Solid lines show completeness measurements comparing the wide and deep samples on the SN-X3 field as described in Section 5.2 of [128]. Points with error bars are the Balrog mean completeness measurements for the full sampled `Run2` footprint. Errors are the standard deviation of 50 jacknife samples of the sampled footprint, rescaled as appropriate for the area of the SN-X3 field. The dashed vertical line indicates the injection effective magnitude limit of 25.4.

posite detection magnitude image limit, and thus objects bright in g band but not in other bands are sometimes not detected. This is not seen as significantly in the Y3 GOLD sample which suggests that the input DF sample over represents these kinds of objects. It is more difficult to determine possible discrepancies past the detection threshold in each band without careful examination of both measurements, though their residuals are only marginally beyond 1-σ and could simply be statistical fluctuations. While it is encouraging to see similar detection properties between `Balrog` and the data, that alone is not enough to ensure sufficient similarity for science calibrations.

5.1.2 SOF Photometry

We can make similar comparisons of the measured photometry. Figure 5.2 compares the recovered `Balrog` SOF $griz$ magnitudes, $g-r$ and $r-i$ colors, and a few morphological parameters to Y3 GOLD after both samples have applied basic cuts. The comparison is in absolute counts with `Balrog` in blue and the mean of 100 GOLD bootstrap subsamples of identical size to the `y3-merged` sample in black. The standard deviation of the subsample counts in each bin are used to estimate the uncertainty, and the percent errors of the binned residuals are plotted below each distribution.

The distributions are qualitatively extremely similar in the most dense regions of parameter space for most quantities, with the most obvious discrepancies occurring in the low-density tails of the distributions. This is particularly noticeable for the magnitudes and colors. The relative residuals confirm this: While nearly all `Balrog` magnitude bins have fractional distribution differences below 5% of the mean Y3 GOLD sample from 18 to 24, the region of interest for most Y3 cosmological analyses, `Balrog` counts in magnitudes below 18 underestimate GOLD by 10 to 50% by magnitude 16. The colors are similar with the only discrepancy above 5% in the densest regions occurring at $1.3 < g - r < 1.5$, values typical of M-dwarf stars [183]. A few other notable discrepancies are that `Balrog` appears to underestimate the number of objects with ellipticities `cm_g_{1/2}`$\sim$0 and negative size parameter `cm_T` relative to the Y3 GOLD sample - both of which are again values typical of stars.

We stress that these binned residuals are still a largely qualitative check on the agreement between property distributions as they are very sensitive to sample selection. For example, the relative error in `cm_T`, `cm_g_1`, and `cm_g_2` near zero are all significantly smaller after applying the stellar cut `EXTENDED_CLASS_SOF`

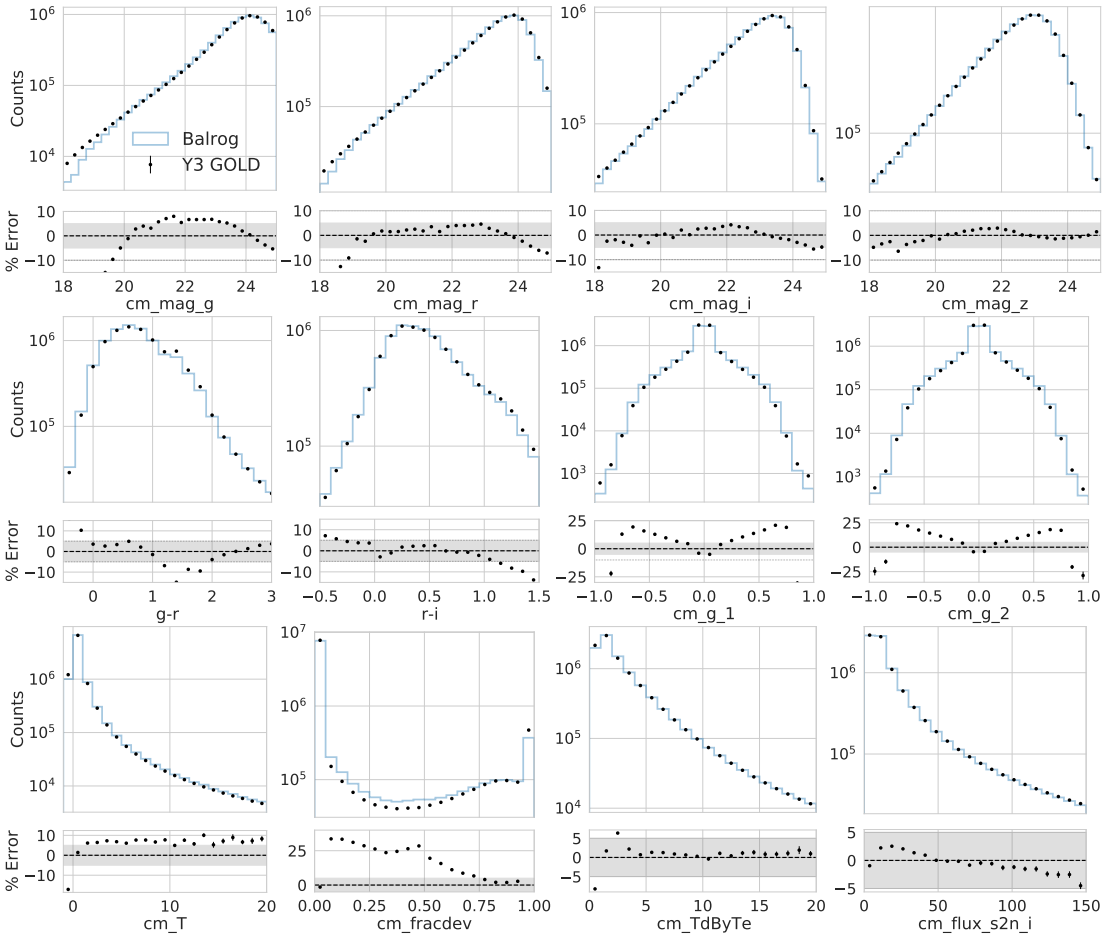

Figure 5.2: Comparison of the `y3-merged` sample (in blue) vs. Y3 GOLD (in black) for measured *griz* magnitudes, $g - r$ and $r - i$ color, shape parameters `cm_g_1` and `cm_g_2`, size `cm_T`, flux component ratio `cm_fracdev`, size component ratio `cm_TdByTe`, and i band S/N. Both samples have had the basic cuts applied as described in the beginning of the chapter. To compare the distributions, we resample Y3 GOLD with replacement to match the size of the `y3-merged` catalog 100 times and plot the mean and std of these bootstrap samples in black. The percent error of the binned residuals are shown below each distribution, which have been zoomed in to show the results of the most relevant regions. The region corresponding to +/-5% has been shaded in gray. When quantities do not have hard boundaries, we include at least the 2nd-97th percentiles of the values.

> 1 which indicates that the y3-merged sample does not capture the transfer properties of stars as well as galaxies. Yet the shape of these residuals often indicate important real differences. The change in residual sign near the detection threshold in each band indicates potential small differences in the effective depth of the samples, and the overabundance of `Balrog` objects with `cm_fracdev` near 0.5 reflects the effect of parameter priors not matching the true underlying distribution as discussed in section 4.2.3.

In addition, residuals consistent with zero even under the assumption of perfect emulation fidelity requires a completely representative input sample. There are many known reasons for why our input sample fails this requirement, a few of which we discuss here:

(i) The DF sample underestimates cosmic variance as it only uses objects from a tiny fraction of the sky, which is particularly a problem for the stellar population as its distribution varies across the sky much more strongly than galaxies.

(ii) The photometric pipeline used to make measurements of DF objects is not identical to the one used in the WF in order to deal with non-dithered observations, an increased blending rate, the large number of exposures per detection, and instabilities in the detection of very faint sources in the presence of diffuse emission (see [173]).

(iii) The morphological model fits to the DF objects are subtly different (`bdf` vs `cm`) which we have shown can introduce small biases in other parameters such as the magnitude.

(iv) CModel is not an appropriate photometric model for all objects in the sky.

There are simple practical limitations that contribute to these discrepancies as well, such as limiting the size and magnitude distribution of objects to reduce `Balrog`-`Balrog` blends and the computational time spent on injecting near certain non-detections. We discuss these issues more in Chapter 7.

5.1.3 Spatial Variation and Property Maps

While the overall similarities in the photometries are encouraging, what is most critical is how well `Balrog` reproduces the measurable signals used in cosmological analyses as well as correlations with spatially varying image conditions and survey properties. These systematic trends are particularly important when measuring the galaxy clustering signal where local observing conditions can imprint fluctuations in number density that are not cosmological in origin such as variations in seeing, depth, and sky brightness [184]. We now investigate the similarity of these systematic trends in `Balrog` and Y3 GOLD for a highly incomplete sample where the variation is more apparent, before looking at their contribution to the clustering signal itself for a cosmology-like sample in Section 5.1.4.

Figure 5.3 compares the number density of all `y3-merged` and Y3 GOLD galaxies with basic cuts as a function of survey property in overlapping HEALPix [185] pixels of `NSIDE=2048`, corresponding to an area of 2.95 arcmin^2. The survey properties are assigned from the Y3 HEALPix maps in [128] (based off the methodology in [127]) that have been rescaled[1] from a $N_{\rm side}$ of 4096 to 2048 to smooth out irregularities in the pixel occupation distribution due to the regular structure and lower density of `Balrog` sources. The uncertainty in number density was estimated by resampling the pixels used in each sample of equal size with replacement for 100 bootstrap samples. The distribution of the rescaled survey

[1]The map rescaling is done by averaging all non-empty pixels.

properties for the Y3 GOLD sample are plotted in the background in green to highlight typical property values.

With a few notable exceptions, the number density of the two samples match closely in both amplitude and shape. It is especially encouraging to see `Balrog` capturing the high frequency structure in the dependence of a few of the more complex trends such as the local sky brightness (`skybrite`) and airmass. The largest differences in recovered number density occur for extremely rare values of a few properties such as the quadrature sum of zeropoint uncertainties (`sig_zp`) and exposure time (`exp_time`) and are not particularly concerning. However, there are still some more serious unresolved discrepancies in amplitude – particularly in r band seeing and airmass. The same potential issues in input sample representativeness and photometric assumptions discussed previously apply to these measurements, but it is not immediately clear why these issues would manifest in a band-dependent fashion in seeing or why the largest discrepancies occur for an indirect parameter of the images like airmass. These differences may be indicative of features in the transfer function not currently captured by `Balrog` such as PSF modeling errors with unexpected chromatic effects or the unapplied injection zeropoint corrections. Such differences warrant further investigations in preparation for an improved Y6 `Balrog` methodology but do not themselves indicate insufficient consistency for a clustering measurement. We explore this further below.

5.1.4 Galaxy Clustering Systematics

Many of the core science cases of interest to cosmology involve measurements of galaxy clustering. To be useful in calibrations for this purpose, it is not enough that the number counts of `Balrog` and Y3 GOLD galaxies follow the same trends

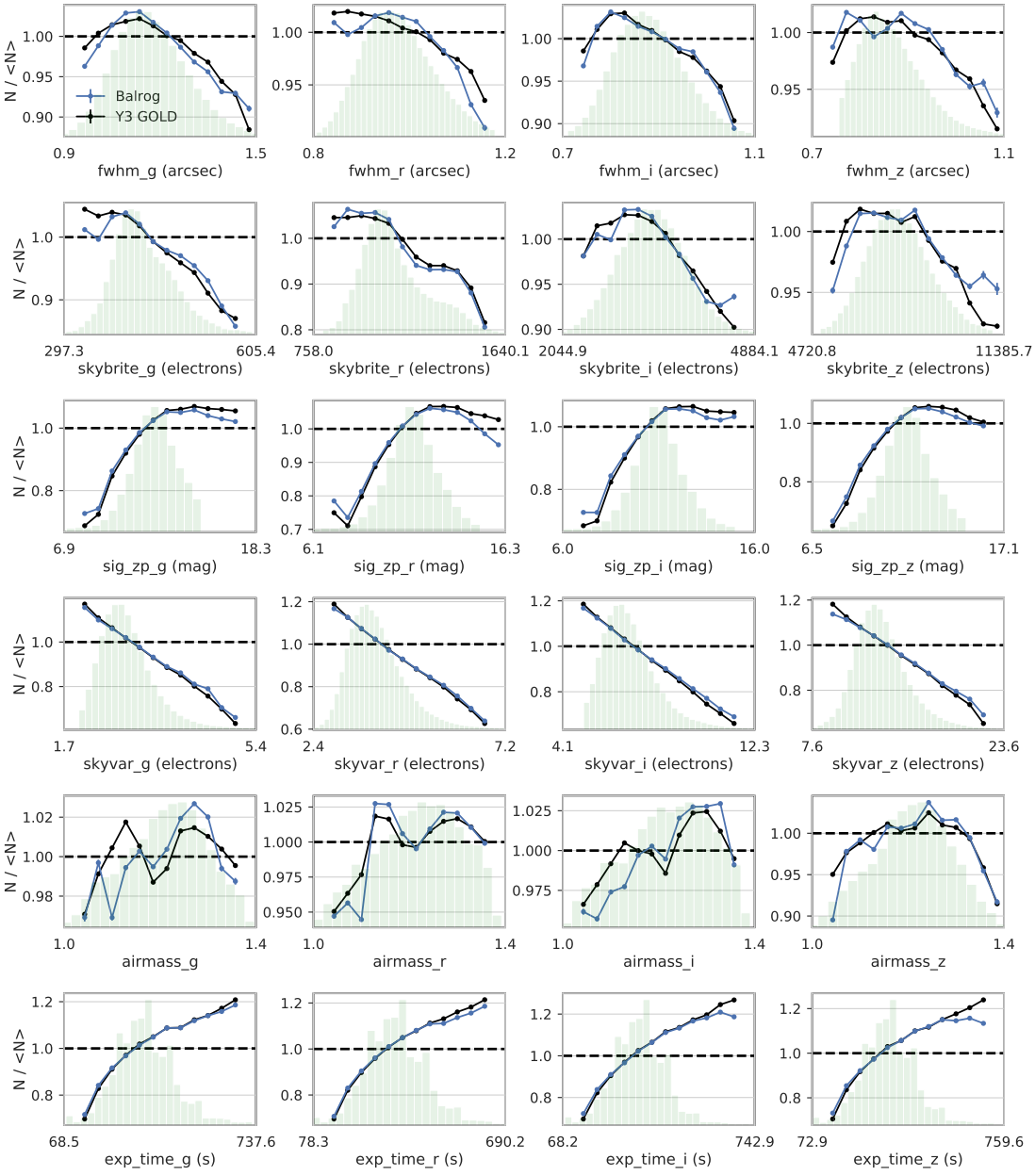

Figure 5.3: The trend in number density fluctuations $N/<N>$ as a function of various survey observing properties for the full (and highly incomplete) `Balrog`, in blue, and Y3 GOLD, in black, samples after basic cuts for overlapping HEALPix pixels of `NSIDE`=2048. The distribution of survey condition values for the rescaled Y3 GOLD map is displayed in the background in green to highlight typical values. The property maps are described in Table E.1 in [128], but we briefly defined them here in order from the top: the mean PSF size, the local sky brightness, the quadrature sum of the zeropoint uncertainties, the variance of the sky brightness, the airmass, and the exposure time.

with image properties like those shown in Figure 5.3. Where the systematic error is independent of the signal (as, for example, variations in the airmass and the true galaxy density on the sky are statistically independent of one another), the resulting variations in survey depth enter, to leading order, as additive systematic errors in the two-point statistics used for cosmology. Correcting for these observational systematics is critical for unbiased cosmological inference from clustering, and the ability to use `Balrog` as object randoms with realistic measurement biases – if it sufficiently captures the clustering fluctuations of the data – offers an ideal calibration method without using the data vector directly which avoids possible overfitting (see [17, 186, 187]). In addition, direct calibration with `Balrog` would eliminate the need to identify all sufficiently important survey property contributions at a desired precision (and avoid biases from any unidentified systematics) while potentially allowing for measurements on larger scales where the true signal is very small and the corrections have to be *extremely* accurate.

Here we estimate the approximate impact on the clustering signal due to systematic differences between `Balrog` and Y3 GOLD for a sample broadly similar to the MagLim science sample described in [188], where we cut both the Y3 GOLD and `Balrog` samples to $17.5 < i < 21.5$ in addition to the previous cuts. We make density maps based on each property map across the full Y3 GOLD footprint by interpolating the trends in `Balrog` and GOLD to fill in cells where we do not have injection samples. These maps are estimates of the MagLim galaxy number density fluctuations in Y3 if they could be completely described by the survey property in question[2]. We then estimate the angular power spectra of both interpolated maps for each survey property using the pseudo-C_ℓ estimation code PyMaster[3] [189]. These are then compared to the power spectra of the survey

[2]Where only regions with `Balrog` samples are used for the estimate.
[3]https://pypi.org/project/pymaster/

property maps themselves along with a typical nonlinear galaxy power spectrum at $z = 0.7$ computed with the `CAMB` [190] implementation of the nonlinear power spectrum described in [191]. Finally, we compute the differences in power from the interpolated `Balrog` and Y3 GOLD density maps as a fraction of the galaxy power spectrum at each ℓ-scale.

Results for the best (g band PSF FWHM) and worst (i band `sig_zp`) performing map are shown in Figure 5.4. Angular clustering systematics for the remaining survey properties, generated in the same way, are shown in Appendix B. For scales comparable to or smaller than the DECam focal plane (approximately $\ell > 200$), the difference between Y3 GOLD and `Balrog` is in all cases less than 1% of the typical amplitude of the angular clustering of galaxies (plotted in black). For some quantities, such as the g band PSF (shown in the top panel in Figure 5.4), the differences are several orders of magnitude smaller.

While the differences are small in absolute terms, or as compared to a realistic cosmological signal, the relative deviation between the simulated and real catalogs is in some cases quite large. It is difficult to disentangle the relative contribution to these differences from insufficient sampling across survey property values, issues in the input sample, or missing features in the sampled transfer function (such as the zeropoint corrections highlighted in Section 4.2.1). We discuss these issues further in Chapter 7. However, that the absolute additive contributions are well below 1% at most relevant scales for even a single realization of a 20% sampling of the footprint gives us confidence that injection simulations like `Balrog` will be crucial for systematics calibration of clustering measurements in Y6 and the next generation of galaxy surveys with even more ambitious precision goals.

Whether `Balrog` is sufficiently similar to Y3 data ultimately depends on the science case and desired measurement precision. In addition, the magnitude of

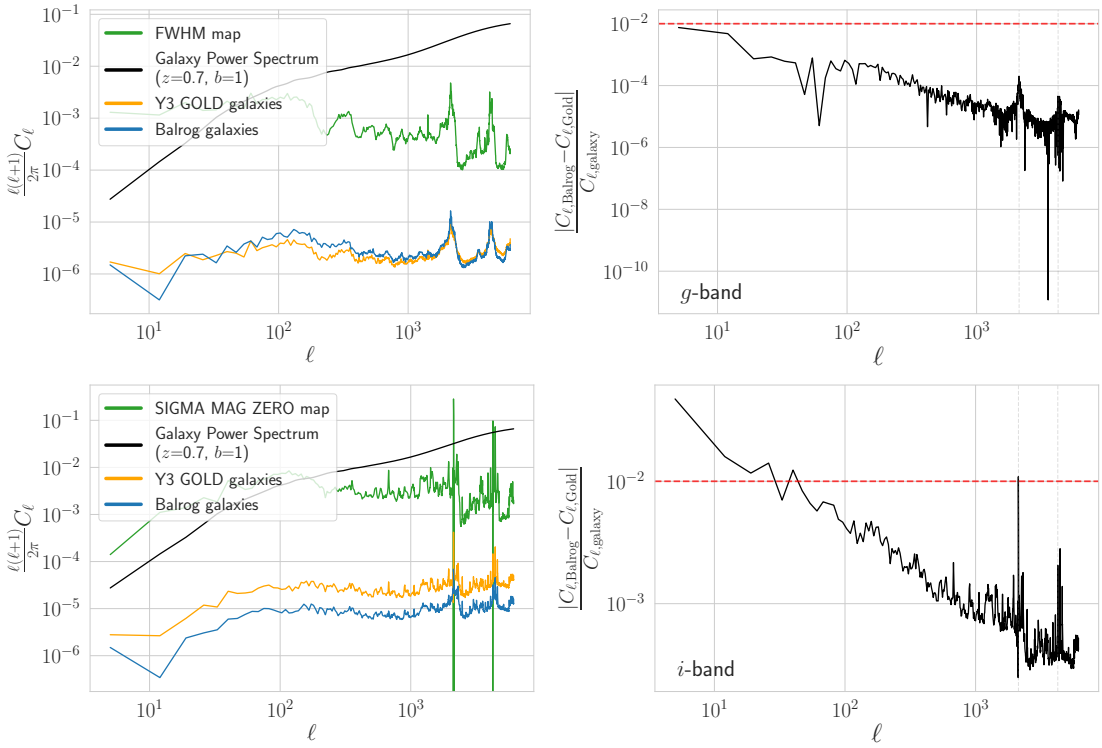

Figure 5.4: Examples of the survey property maps with the smallest (top row) and largest (bottom row) estimated additive systematic impact on the clustering signal from differences in number density between `Balrog` and Y3 GOLD. The left panels show the angular power spectrum of the noted survey property (in green) and the corresponding power spectra of the number densities of the `Balrog` (in blue) and Y3 GOLD (in gold) MagLim-like galaxies across the Y3 footprint using the interpolated trends described in Sections 5.1.3 and 5.1.4. The reference galaxy power spectrum in black is `CAMB`'s implementation of the nonlinear matter power spectrum described in [191], meant to represent a typical cosmological signal at $z = 0.7$ with linear galaxy bias parameter of 1. The right panels show the difference in power between Y3 GOLD and `Balrog` as a fraction of the fiducial cosmological power spectrum shown on the left. We draw a red dashed line indicating the 1% systematic error threshold as reference. Even in the worst case, we find that `Balrog` is able to capture the clustering amplitude due to variations in survey properties to better than 1% for $\ell > 50$ (corresponding to $\theta > \sim 3.5$) deg. Equivalent plots for many other survey property maps in all *griz* bands are shown in Appendix B.

discrepancies can depend strongly on the choice of sample cuts - particularly for those effects related to star-galaxy separation and magnitude limits. However, we find that `Balrog` captures a significant amount of the variation in number density as a function of observing conditions even for *extremely* incomplete samples, and achieves systematics control of well under 1% for the clustering measurement of a typical cosmology sample. For an additional example of how to estimate the contribution of the intrinsic uncertainty in the `Balrog` methodology to the Y3 photometric redshift calibration error budget for source galaxies, see [135].

5.2 Photometric performance of y3-stars

As discussed in 4.3.2, the injections in `y3-stars` consist of pure delta functions convolved with the local PSFEx solution. The extremely high purity of this star sample with realistic transfer properties is unique to injection pipelines such as `Balrog` where we have truth information about the underlying object classification in addition to its photometry - which is not always the case for galaxy samples (discussed further in Section 5.3). This eliminates the need for a traditional star-galaxy separation metric like `EXTENDED_CLASS_SOF` and (nearly) removes any bias resulting from misclassified objects, though we still cut on `EXTENDED_CLASS_SOF` $<= 1$ to match what is done to create stellar samples in Y3 GOLD. The only contaminants in the main star sample come from ambiguous matches which is why we still cut on `match_flag_1.5_asec` < 2. This eliminated 1.9% of detections for this sample. Here we focus on the photometric performance and leave the discussion on stellar completeness and galaxy contamination in Section 5.4. We remind the reader that this sample probes a subtly different measurement likelihood than that of `y3-merged` as we have knowledge of the underlying object classification, as described in 4.3.3.

While the underlying morphology of stellar profiles is not well described by a Sérsic model, we still use the SOF CModel fits for the stellar sample as there was a systematic calibration offset in the PSF model photometry used in Y3 measurements on the data. This has been corrected for Y6 processing but leaves us without a reliable PSF photometry for our response measurements. However, ultimately this has only a small impact on the recovered photometry for sources smaller than the PSF as these objects are fit with a `cm_T` size near 0 – effectively eliminating the Sérsic components.

5.2.1 SOF CModel Magnitudes

The difference in recovered CModel magnitude compared to input magnitude Δmag_δ as a function of input magnitude for *griz* is shown in Figure 5.5. Density contours are plotted on top of the scatter with percentiles equivalent to the first three sigmas of a 2D Gaussian distribution, corresponding to 39.3%, 86.5%, and 98.9% of the total data volume. The mean response bias $<\Delta\text{mag}_\delta>$, median response $\widetilde{\Delta\text{mag}}_\delta$, and scatter $\sigma_{\text{mag}_\delta}$ in truth magnitude bins of size 0.25 magnitudes are over-potted in black bars. These summary statistics provide estimates for the statistical precision and accuracy of the SOF magnitudes, though we stress that the underlying distributions are not Gaussian. These are compared to the mean reported SOF error in the bin indicated by the dashed white curve which do not attempt to account for systematic effects.

The overall calibration of CModel for the stellar sample is quite good, with $<\Delta\text{mag}_\delta>$ and $\widetilde{\Delta\text{mag}}_\delta$ ranging from 1-10 mmag (or 0.1-0.9%) across all bands up to an input magnitude of 20 and between 2-15 mmag (0.2-1.4%) for $20 <\Delta\text{mag}_\delta< 22$ except for the final two z band bins. $<\Delta\text{mag}_\delta>$ stays under 1.5% for each band in all bins where the number of objects are increasing (input magnitudes

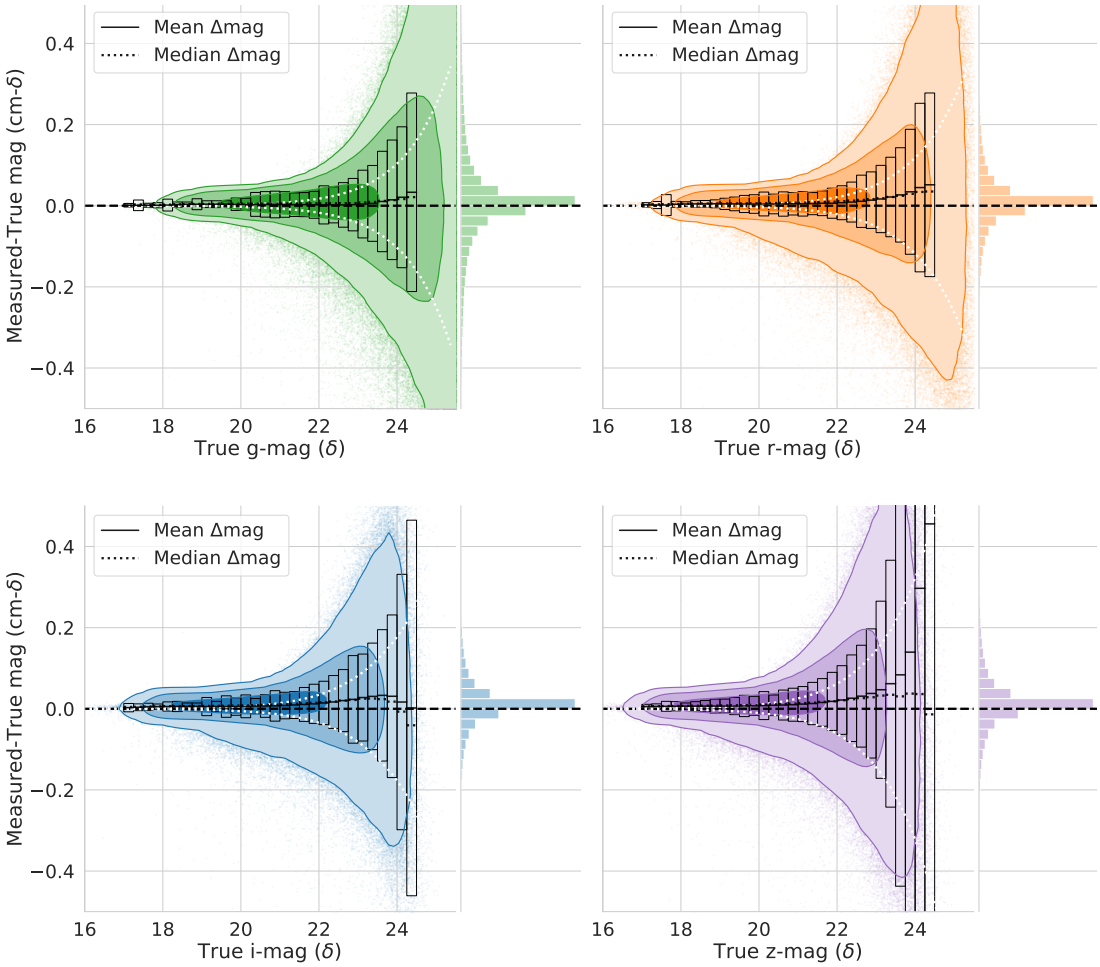

Figure 5.5: The distribution of differences in recovered *griz* SOF CModel magnitude vs the injected δ-magnitude (Δmag_δ) as a function of input magnitude for the `y3-stars` sample. The density is overplotted where the contour lines correspond to the percentiles of the first three sigmas of a 2D Gaussian, containing 39.2%, 86.5%, and 98.9% of the data volume respectively. The mean (solid), median (dotted), and standard deviation of the magnitude responses in bins of size 0.25 magnitude are shown in the overlaid black bars. These are compared to the reported SOF CModel errors by the dashed white lines which do not attempt to account for systematic effects. The marginal distributions of Δmag_δ are included to highlight the small relative volume of the outlier tails.

of 23.5, 22.5, 22, and 22 respectively) except for the final z band bin which is $\sim$1.7%. The responses are a bit higher than the quoted 3 mmag uniformity of Y3 GOLD stars when compared to the Gaia star catalog ([128, 192]), though the Y3 GOLD uniformity was measured only with respect to Gaia's G band which we find to have the best photometric performance (differences of 0.5-6 mmag) over the quoted magnitude range. The Y3 GOLD measurement used a restricted $0.5 < g - i < 1.5$ color range as well which eliminates the worst outliers that we still consider here. In addition, the larger discrepancies found here could be the result of the CModel model-misspecification bias discussed previously.

The response bias and scatter increase significantly after these points due to competing systematic effects as the sample becomes progressively more incomplete, with the mean responses rising to $\sim 1.5-3\%$ as they approach the detection threshold in each band. Small sample sizes and strong selection effects lead to $<\Delta\text{mag}_\delta>$ and $\widetilde{\Delta\text{mag}}_\delta$ biases of $\sim$4% for g and r by 24th magnitude, while the biases of the much shallower i and z rise significantly to over 10%. At the median coadd magnitude limits quoted in Table 2 of [128] of 24.3, 23.0, 22.6, and 22.2 (corresponding to a S/N of 10), the mean $griz$ biases are measured to be 3.0%, 4.1%, 2.5%, and 2.2% respectively. The complete set of values for all binned summary statics are included in Table C.1. While the underlying measurement likelihood of these objects is non-Gaussian, the morphological simplicity of stars results in these summary statistics qualitatively capturing the response features well when complete. We will return to this point in Section 5.3 where the situation is significantly more complicated.

There is evidence of a small band dependence in both the accuracy and precision of the magnitude response. This is most evident when comparing g band, where Δmag_δ is never above 5 mmag (0.5%) too faint below an input magnitude

of 23.25, to the z band Δmag_δ which is exclusively above 5 mmag too faint over the same interval. Unlike the blank image tests in Section 4.2.3, the $\widetilde{\Delta\text{mag}_\delta}$ values for each band in a bin have a distinct, monotonically increasing shape with the spread between the bands consistently 5-10 mmag brighter than injection magnitudes of 21. However, this effect is much less pronounced when binned by the measured S/N in each band where the detection significance and local sky background is taken into account. Binned in this way, $\widetilde{\Delta\text{mag}_\delta}$ is nearly identical for i and z bands for S/N greater than 20 while g and r are consistently offset by at least 5 and 2 mmag respectively. As this band-dependent response in $\widetilde{\Delta\text{mag}_\delta}$ was not present in the blank image tests, it may suggest issues in the real image calibration such as the estimation of sky background which we discuss more in Sections 5.3 and 6.3.

5.2.2 SOF CModel Colors

Of primary interest is the accuracy of the recovered colors due to their importance for photometric calibration, star-galaxy separation, photometric redshift estimation, and the study of Milky Way structure. We plot the difference in measured SOF CModel $g-r$, $r-i$, and $i-z$ color vs. input color with respect to the input color in Figure 5.6. The contours and summary statistics are computed in the same way as the magnitudes, though with a bin size of 100 mmag for $g-r$ and $r-i$ and 50 mmag for $i-z$. The color calibration for this sample is excellent. For the three colors examined here, the median color difference $\widetilde{\Delta\text{c}_\delta}$ is never greater than 5 mmag (0.5%) from injected color of -0.25 to 1.25 and is most commonly less than 3 mmag (0.3%). Beyond 1.25, $\widetilde{\Delta\text{c}_\delta}$ grows to a maximum of 25 mmag (2.3%) too blue for $g-r$ while for $r-i$ it never exceeds an absolute difference of over 3 mmag. The mean responses vary significantly due to extremely long scatter tails

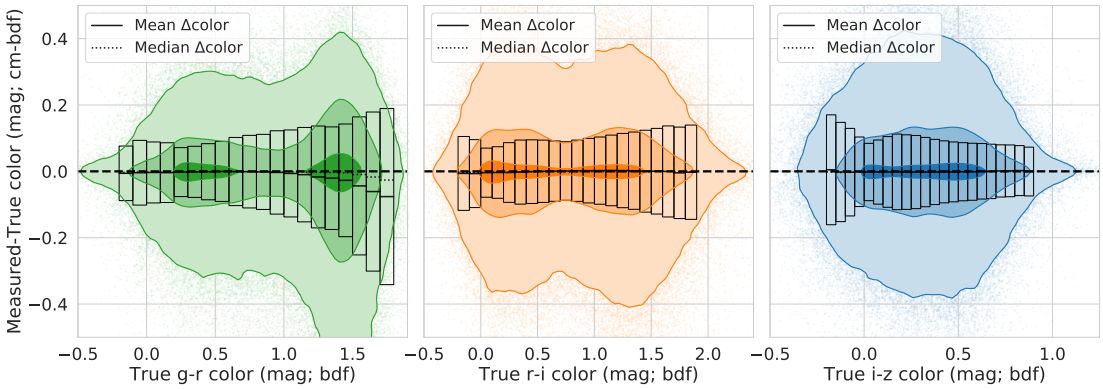

Figure 5.6: The distribution of differences in measured SOF CModel $g-r$, $r-i$, and $i-z$ color vs. the injected δ-color (Δc_δ) as a function of input color for the `y3-stars` sample. The density is overplotted where the contour lines correspond to the percentiles of the first three sigmas of a 2D Gaussian, containing 39.2%, 86.5%, and 98.9% of the data volume respectively. The mean (solid), median (dotted), and standard deviation of the magnitude responses in bins of size 100 mmag magnitude for $g-r$ and $r-i$ and 50 mmag for $i-z$ are shown in the overlaid black bars.

in both directions from the magnitude difference and are less reliable estimators of the overall performance in this case. However, they tend to be within a factor of two of the medians except for $g-r$ which increases in absolute size dramatically after 0.75 due to the long tail as can be seen in the figure. The full set of summary statistics are shown in Table C.1. Notably we do not find evidence of a systematic chromatic response in CModel color.

Next we compare the color-color diagrams for $g-r$ vs $r-i$ and $r-i$ vs $i-z$ for the input and recovered samples in Figure 5.7. As expected, the recovered injected colors have broader distributions due to the inherited WF noise as well as moderately large magnitude scatter near the detection threshold. However, the broadening is concentrated outside of the 1-σ contours where the agreement is extremely similar.

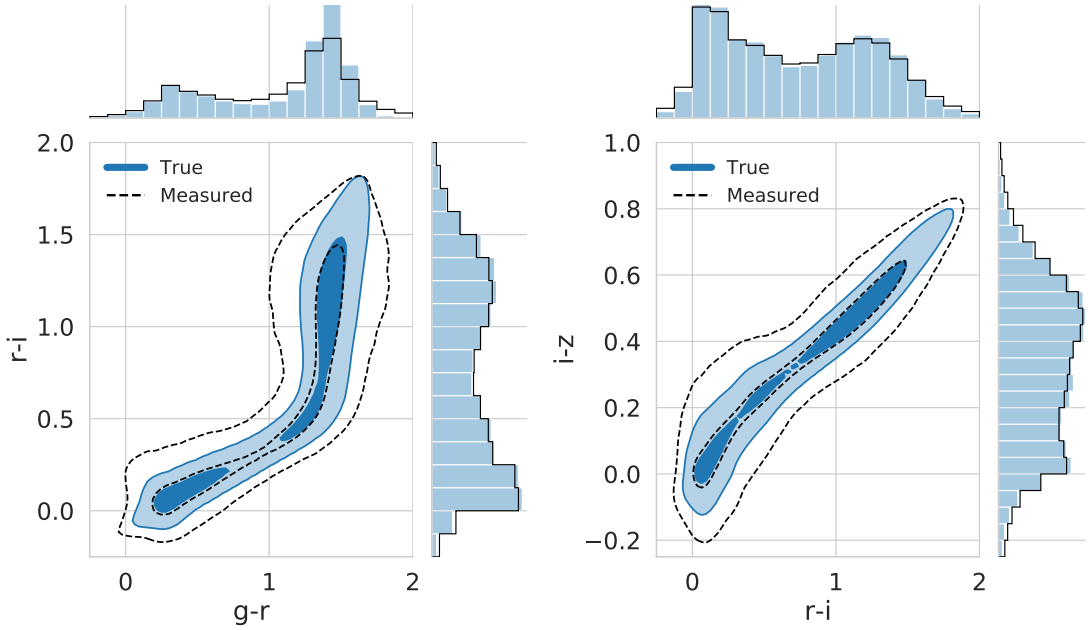

Figure 5.7: The $g - r$ vs. $r - i$ and $r - i$ vs. $i - z$ color-color distributions for the input colors in blue and measured colors in black. The density contour lines correspond to the percentiles of the first two sigmas of a 2D Gaussian, containing 39.2% and 86.5% of the total data volume respectively. The marginal distributions are included for comparison.

5.3 Photometric Performance of y3-merged

Unlike the synthetic δ star sample, `y3-merged` objects are sampled from fits to real sources contained in the DES DF. Thus not only are the properties of these injections far more diverse, but we do not have perfect knowledge of their true classification. However, we anticipate that most uses of this `Balrog` sample will be to calibrate galaxy samples used in cosmology analyses. In these cases, we do not care about the true classification as we want to capture the same contamination fraction as the data. For this reason we apply the cut `EXTENDED_CLASS_SOF > 1` and leave questions of star contamination to Section 5.4. Removing ambiguous matches with the cut `match_flag_1.5_asec < 2` decreased the sample by just under 1.5%.

There are numerous photometries and parameters whose response can be explored with this sample. We restrict ourselves largely to SOF CModel colors, magnitudes, and sizes here for brevity but find similar results for Metacalibration. As with `y3-stars`, we include summary statistics of the tabular results in Appendix C.

5.3.1 SOF CModel Magnitudes

We compare the difference in recovered SOF CModel magnitude vs. true DF magnitude $\Delta\text{mag}_{\text{DF}}$ as a function of input magnitude for *griz* bands in Figure 5.8. As with `y3-stars`, we characterize the photometric performance of `y3-merged` measured galaxies with the summary statistics $<\Delta\text{mag}_{\text{DF}}>$, $\widetilde{\Delta\text{mag}}_{\text{DF}}$, and $\sigma_{\text{mag}_{\text{DF}}}$ in bins of truth magnitude overplotted in black bars. Unsurprisingly, the overall scatter in magnitude response for this sample is significantly larger than for the pure stellar injections due to the rich variety of injected morphologies and issues with blending of extended sources. The measured $\sigma_{\text{mag}_{\text{DF}}}$'s reflect this by being an

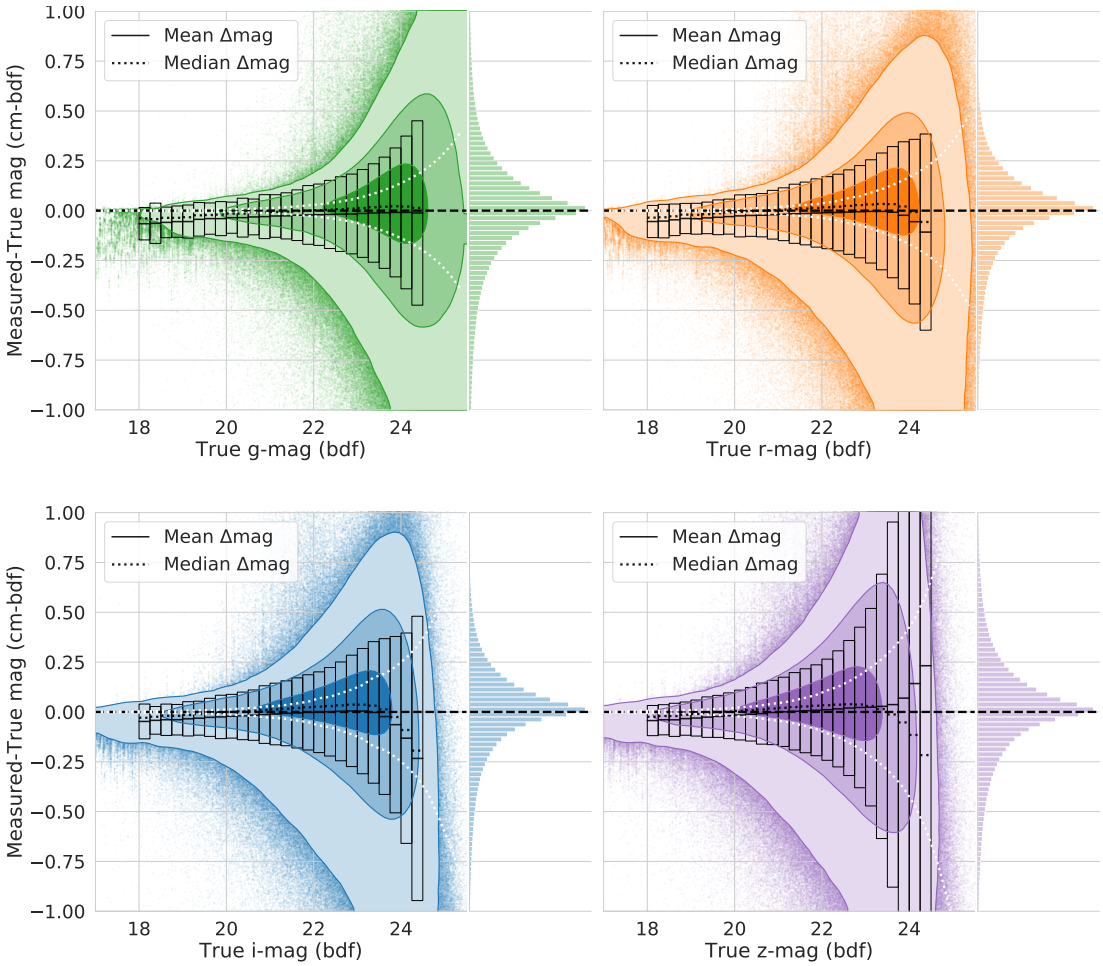

Figure 5.8: The distribution of differences in recovered *griz* SOF CModel magnitude vs the injected DF magnitude ($\Delta\text{mag}_{\text{DF}}$) as a function of input magnitude for the `y3-merged` sample. The density is overplotted where the contour lines correspond to the percentiles of the first three sigmas of a 2D Gaussian, containing 39.2%, 86.5%, and 98.9% of the data volume respectively. The mean (solid), median (dotted), and standard deviation of the magnitude responses in bins of size 0.25 magnitude are shown in the overlaid black bars. These are compared to the reported SOF CModel errors by the dashed white lines which do not attempt to account for systematic effects. The marginal distributions of $\Delta\text{mag}_{\delta}$ are included to highlight the small relative volume of the outlier tails.

average of over 4 times larger than the corresponding $\sigma_{\mathrm{mag}_\delta}$ distribution over the same magnitude range, with the ratio reaching as high as 9 for very bright objects. We then expect the mean response bias $<\Delta\mathrm{mag}_{\mathrm{DF}}>$ to be larger as well, but their behaviour is more interesting than the stellar sample. On the bright end below 19th magnitude, the 50th-99th percentile of objects are detected within 30 mmag (or 2.7%) of truth but there is a clear asymmetric preference for the recovered flux to be too large for the remaining objects.

This result is driven by a sizeable fraction of bright, extended injections that are commonly blended with existing Y3 GOLD galaxies and are subsequently measured to have far too large of a size. The measured fluxes of these objects vary significantly depending on local conditions and create visible vertical lines in the response scatter due to their many injection realizations and relatively small population of objects with true magnitude less than 19. Image cutouts for a set of these objects along with the 50th and 95th percentiles of their measured CModel flux profiles are shown in Figure 5.9 – in addition to a more compact, typical injection at the same input magnitude that does not suffer from proximity effects or blending. These examples of large magnitude responses correlated with measured size errors are the first hint of a systematic issue with SOF fits in crowded fields that we investigate in more detail in Section 5.3.3.

As in the `y3-stars` sample, we detect a relatively small but clear band dependence in the mean and median responses. For all input magnitude bins brighter than 23 where the sample is nearly complete, there is a monotonic increase in the mean and median response in *griz* with absolute spread of ∼16 mmag, or about 1.4% difference between g and z. This effect was hinted at in the response of the pure stellar sample but is far more evident here. This chromatic response is diluted but not eliminated when binning in measured S/N rather than input

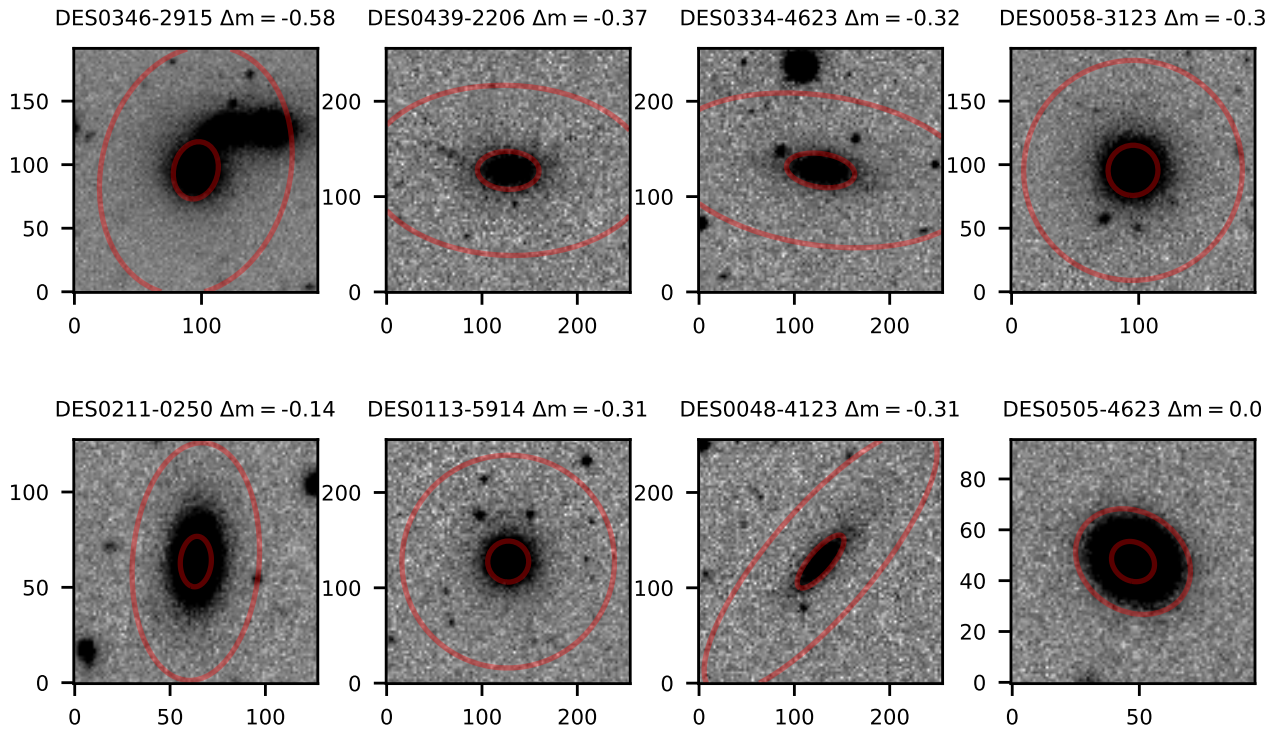

Figure 5.9: A few examples of injections that contribute to the long scatter tail in magnitude response of bright `y3-merged` objects due to blending of extended DF injections discussed in Section 5.3.1. Each injection had a true g band magnitude between 17 and 19, and we include the tilename and magnitude response Δm at the top of each panel. The red lines correspond to the 50th and 95th percentile flux contours of the *measured* profile. The extended profiles of these injections cause the MEDS image cutout size to be relatively large which increases the probability of including real neighbors in the MEDS stamp. This in turn can cause SOF to significantly overestimate the `cm_T` size and thus a much larger Δm than one would naively expect for objects with these bright magnitudes. The final panel shows a typical bright but compact object that is very well calibrated for comparison. The stretch in each panel runs from $-3\sigma_{\rm sky}$to$+10\sigma_{\rm sky}$.

magnitude, with $\widetilde{\Delta \mathrm{mag}_{\mathrm{DF}}}$ no longer strictly monotonic and with a typical spread of 4-5 mmag for riz bands but 10-20 mmag when including g band for S/N greater than 20.

We believe this chromatic effect is due to a systematic overestimation of the true sky background level in DES (and thus `Balrog`-injected) images. The `SExtractor` sky mode estimator is somewhat susceptible to the presence of neighboring objects in its sky annulus, especially in moderately to highly crowded fields. A mode estimate for the background appropriately allows for the fact that there will be background sources, detections, and undetected sources which is particularly important in the presence of many sources [164]. As a precise mode estimation was once computationally impractical, traditional codes such as `SExtractor` have in practice used a Pearson-style mode estimator $\mathrm{Mode}_{\mathrm{est}} = 2.5 \cdot \mathrm{Median} - 1.5 \cdot \mathrm{Mean}$ for background estimation. This can result in a slight bias in overestimating the background which becomes larger as the field becomes more crowded and in the neighborhood of bright stars with extended wings (E. Bertin, private communication).

This sky overestimation results in too faint a measurement of a galaxy's true magnitude and the effect is stronger when there is more sky noise per object signal. The fact that the sky is more crowded as one moves from bluer (g, r) to redder (i, z) bands could lead to the chromatic effect described above. That the scale of this effect is lessened by binning objects of similar S/N across bands together supports this conclusion. Note that these offsets are computed with dereddened magnitudes, which has the effect of enhancing the chromatic offset in g band compared to the redder bands. Additionally, [193] analyzed the noise properties of DES images and found that there was a slight positive bias induced in the sky noise level due to faint unresolved sources in the field of essentially all

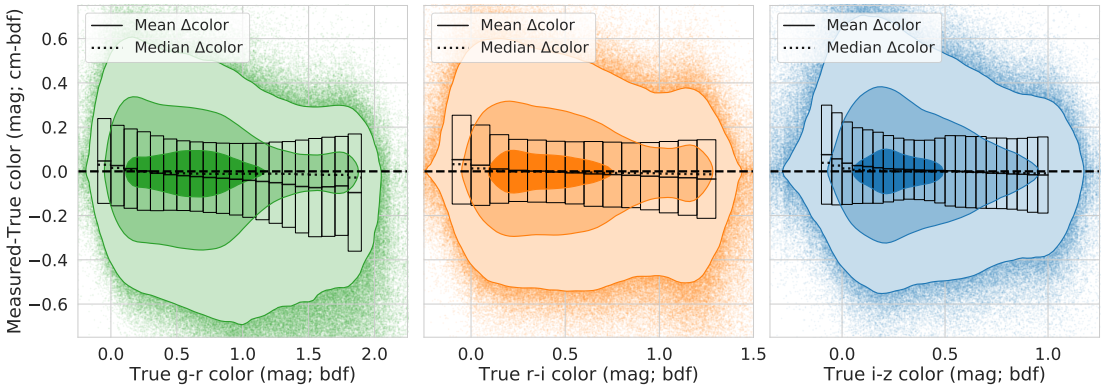

Figure 5.10: The distribution of differences in measured SOF CModel $g-r$, $r-i$, and $i-z$ color vs. the injected DF color ($\Delta c_{\rm DF}$) as a function of input color for the `y3-merged` sample. The density is overplotted where the contour lines correspond to the percentiles of the first three sigmas of a 2D Gaussian, containing 39.2%, 86.5%, and 98.9% of the data volume respectively. The mean (solid), median (dotted), and standard deviation of the magnitude responses in bins of size 100 mmag magnitude for $g-r$ and $r-i$ and 50 mmag for $i-z$ are shown in the overlaid black bars.

images (see Section 6.3 for more details). The sign of this effect, while smaller, has the same trend and was found to only be significant for riz bands. We plan to investigate this further for the Y6 `Balrog` analysis and potentially propose additional magnitude corrections to account for this effect.

5.3.2 SOF CModel Colors

Next we investigate the color response of `y3-merged` objects in Figure 5.10, where we plot the difference in measured SOF CModel $g-r$, $r-i$, and $i-z$ colors vs the injected DF colors $\Delta c_{\rm DF}$ against the input colors. The density contours and overplotted summary statistics are defined in the same way as the previous plots. While the color response scatter is significantly larger than in `y3-stars`, the overall calibration is still excellent and with less extreme outlier tails than in the individual magnitude responses. The behaviour of the summary statistics is slightly more complex but we find that the median color response $\widetilde{\Delta c}_{\rm DF}$ is typically

$\sim$3 mmag (0.3%) too faint from -0.25 to 0 and $\sim$1-11 mmag too bright between 0 and 1.0 for all three colors. The responses are much noisier outside of these regions due to much smaller sample sizes. $\widetilde{\Delta c}_{DF}$ tends to be $\sim$15-25 mmag (1.4-2.2%) too faint below 0.25 and 15-25 mmag too bright beyond 1.0 for all colors (though a bit worse for $r-i$, reaching 12% too bright near 1.5) while $<\Delta c_{DF}>$ differences are about three times as large as $\widetilde{\Delta c}_{DF}$ in the same direction depending on the color and bin. As with the stellar injections, individual $<\Delta c_{DF}>$ and $\widetilde{\Delta c}_{DF}$ bin values can vary significantly due to long scatter tails and we find no evidence of a systematic chromatic response in CModel color. The full color response is summarized in Table C.4.

5.3.3 Catastrophic Model Fitting

While Figure 5.8 shows that the vast majority of magnitude responses are well calibrated and are typically much less than Δmag_{DF} of 0.5, it ignores the very long tail of up-scattered outliers that are far larger than the measured photometric errors would predict. The responses of these outliers from blends and catastrophic photometry failures can be over an order of magnitude larger than those previously discussed as shown for i band in Figure 5.11 where the contours from Figure 5.8 are overlaid in white.

Here the true complexity of even a small slice of the transfer function is revealed: The many competing effects are often in opposition, with biases in the opposite direction of long, asymmetric tails that vary as a function of truth magnitude in a complex way. Simple Gaussian summary statistics like $<\Delta mag_{DF}>$ and $\sigma_{mag_{DF}}$ are not able to appropriately capture the magnitude of these features and we argue that the `Balrog` samples themselves (or at least higher fidelity forms of data compression) should be used for most cosmological analyses that need accu-

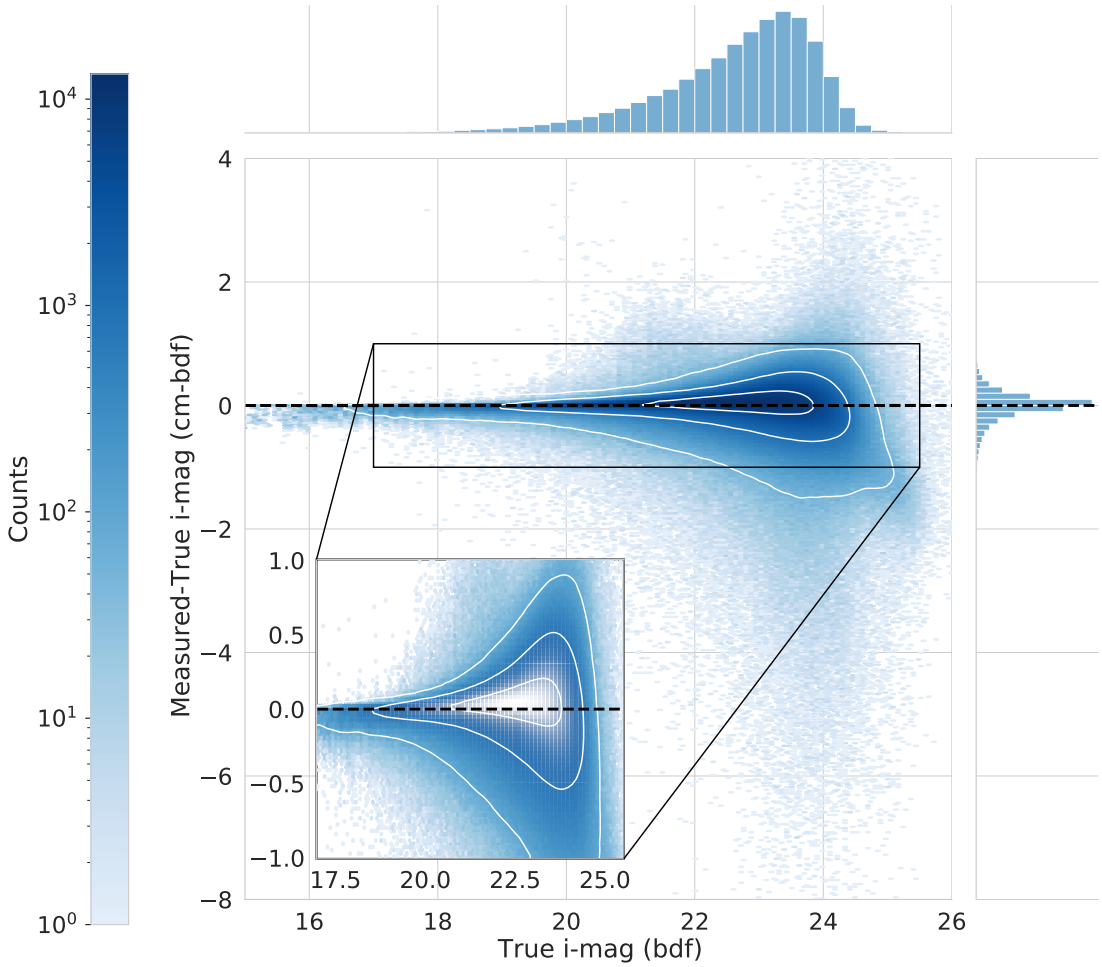

Figure 5.11: The distribution of differences in recovered i band SOF CModel magnitude vs the injected DF magnitude ($\Delta\text{mag}_{\text{DF}}$) as a function of input magnitude. The inset corresponds to the i band panel in Figure 5.8 where the density contours still contain 39.2%, 86.5%, and 98.9% of the data volume respectively. While most of the density is captured in the inset, it misses many of the rich features of the full magnitude response – particularly the long outlier tail of injections measured to have magnitudes up to 10 greater than truth.

rate photometric error modeling. Examples of how the full richness of the transfer function can be used in photometric redshift calibration and the magnification of lens samples are given in Sections 6.1 and 6.2 respectively.

However, it is reasonable to be skeptical of magnitude responses of $\Delta\text{mag}_{\text{DF}}\sim$2-8 (a factor of 6-1,600 in flux!) by supposedly well-calibrated photometry pipelines. To demonstrate what is causing these extremely large differences in recovered flux, we show in Figure 5.12 a set of injections of the same DF object with r band magnitude of 21.42 into eight different WF tiles where the red lines correspond to the 50th and 95th percentile flux contours. In most cases the true magnitude is recovered within the reported errors of a few percent. However, in four instances there is at least one nearby object contained in the MEDS cutout image that interferes with SOF's ability to provide a reliable fit due to either an excess of masked pixels in the cutout or residual light unassociated with the injection. The result is a fitted characteristic size `cm_T` which is much greater than its actual size. For this particular injection, the true size of the object (after deconvolution with the PSF) corresponds to a scale length of $0.77''$. Yet in the four cases with nearby sources the fitted size of the object is at least $1''$, resulting in a flux measurement which is significantly greater than that of the input true flux. In the worst case for tile DES0346-5248, the target object is by chance injected near a very bright pair of merging galaxies and is fitted with a scale length of over $17''$ resulting flux 2.32 magnitudes brighter than the input DF value.

These photometric measurement failures correlated with errors in measured `cm_T` can be even more dramatic. In Figure 5.13 we show eight examples of catastrophic fitting failures due to crowded fields, nearby bright stars, and unflagged image artifacts. These rare but real environments lead to `Balrog` magnitude responses from 5 to even 7 magnitudes brighter than the injected truth. We em-

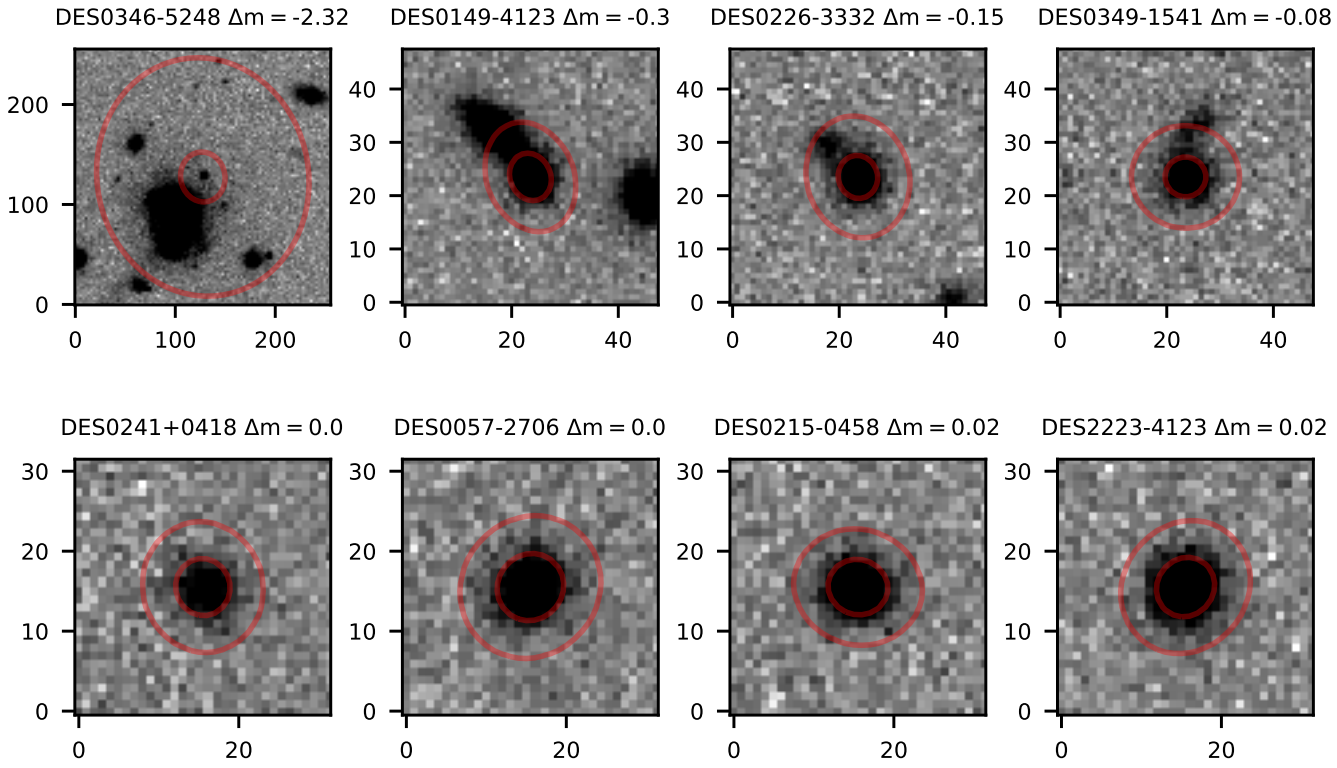

Figure 5.12: The MEDS image cutouts for a few injection realizations of the same DF object with true r-magnitude of 21.42 in eight distinct WF tiles (`bal_id` of 10034605248852). The red contours give the 50% and 95% enclosed light apertures for the injected object as modeled in each tile. The magnitude response Δm is listed next to each tile name, with the cutouts ordered by the magnitude response. Not all cutouts are the same size, as the box size expands based on the initial `SExtractor FLUX_RADIUS` measurement. The true scale length of the object (after PSF deconvolution) is $0.77''$. The fitted profile for the object on tile DES0149-4123 is $1.0''$ and while that on tile DES0346-5248 is an unrealistic $17''$, leading to an overestimate of the object flux. The stretch in each panel runs from $-3\sigma_{\rm sky}$to$+10\sigma_{\rm sky}$.

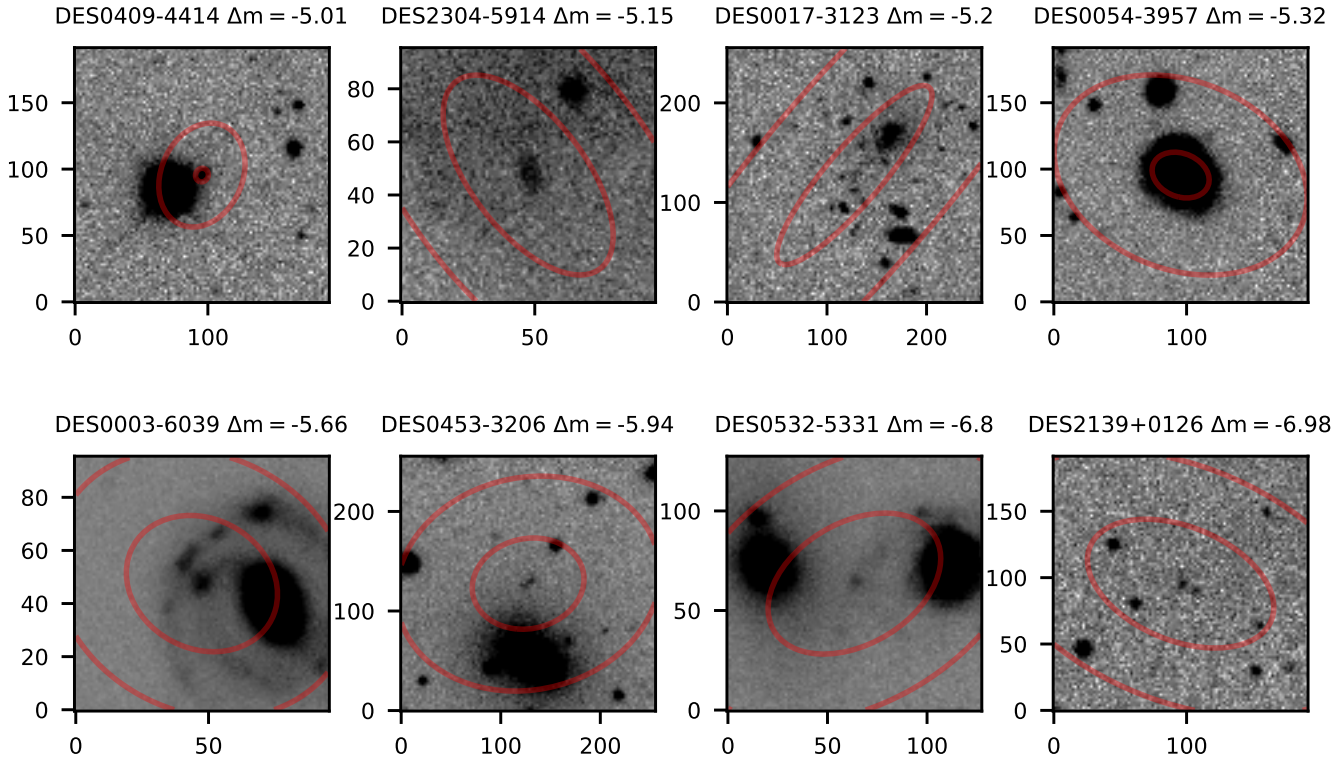

Figure 5.13: The MEDS image cutouts for eight `Balrog` objects with extremely large differences between the measured and injected magnitude Δm. The red lines correspond to the 50th and 95th percentile flux contours of the measured profile. These injections happened to be placed in regions of rapidly varying sky brightness, in the spiral arm of a large spiral galaxy, in a rich cluster, near a stellar diffraction spike, in between two extended galaxies, or simply in crowded fields. In all cases the fitted size is far too large for the source, which in turn leads to an overestimate of the object's flux. This processed is discussed in detail in Section 5.3.3. The stretch in each panel runs from $-3\sigma_{\rm sky}$to$+10\sigma_{\rm sky}$.

phasize that all of these objects pass the basic Y3 GOLD science catalog quality cuts described in the beginning of the chapter.

While the exact causal relationship between complex local environments and extreme magnitude errors requires further analysis, preliminary investigations suggest the following: In crowded fields or areas with unusual image features or artifacts, the `SExtractor` `FLUX_RADIUS` (which defines a circle that contains half of the total corresponding `FLUX_AUTO` value) can get artificially inflated in size as compared to what it would return for an object in an isolated environment. As a source's MEDS cutout image size is rounded up to the next integer multiple of 16, this leads to a MEDS stamp that is significantly larger than what is needed to fit the relevant flux profile in question. This leaves large areas of the stamp with masked pixels when fit with SOF as the algorithm masks rather than models the light of other detected sources within the cutout. The resulting CModel fits then preferentially overestimate `cm_T` for this subpopulation which can greatly increase the inferred flux for a given surface brightness measurement - though we defer investigations into the exact details of the scale and frequency of this effect for a future analysis.

Even without a complete understanding of the underlying cause, the correlation between $\Delta\text{mag}_{\text{DF}}$ and Δ`T` is evident as can be seen in Figure 5.14. Here we have plotted the full i band magnitude response of `y3-merged` but colored individual responses by the absolute difference in measured `cm_T` vs. input `bdf_T`. The vast majority of injections with truth i-magnitude below 23 with very small $\Delta\text{mag}_{\text{DF}}$ responses have `T` differences much less than 1 which are colored blue. Bright objects with responses substantially below the zero line have moderately large errors in recovered `T` as we discussed in Section 5.3.1, while fainter injections with enormous magnitude errors have correspondingly large errors in `T` – reaching

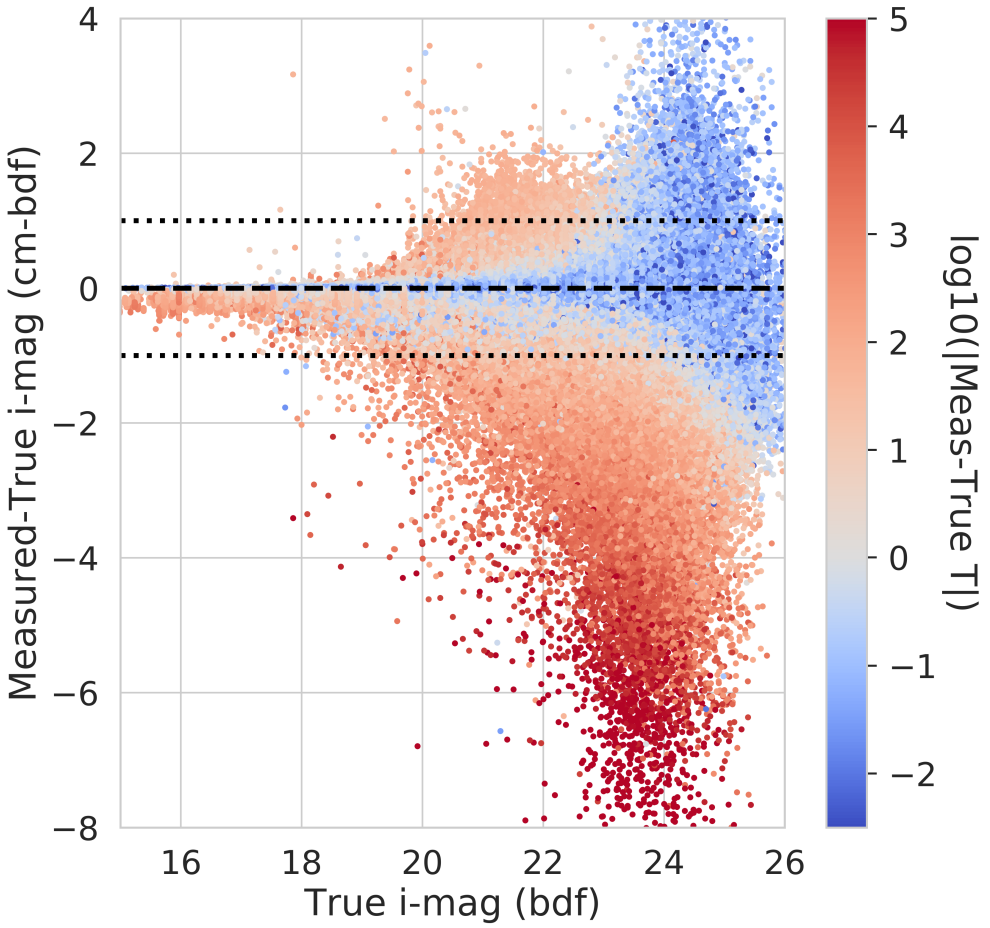

Figure 5.14: The full i band magnitude response $\Delta\text{mag}_{\text{DF}}$ for `y3-merged` shown in Figure 5.11 but now colored by the logarithmic absolute error in recovered size parameter `cm_T` vs input size `bdf_T`. The response scatter is largely correlated by error in recovered size; injections with small $\Delta\text{mag}_{\text{DF}}$ values typically have small errors in recovered `T` as well (in blue), while nearly all of the extreme magnitude outliers have correspondingly large size errors. The correlation is less strong past the detection threshold at $i{\sim}23$ where other systematic effects increase in importance.

as high as the parameter prior limit of 10^6 arcsec^2 (or scale length of $\sim 10^3$ arcsec). The situation is more complicated near and past the detection threshold, about 23rd magnitude in i band, where additional systematic effects become important.

Model fitting photometry codes are complex, nonlinear, and sometimes non-local algorithms that can have unexpected consequences – particularly for low S/N measurements, crowded fields, or when image artifacts are not appropriately weighted or masked. The journey from pixels to catalogs can at times be chaotic, and our modeling of photometric uncertainties should reflect this.

5.3.4 Scatter from Ambiguous Matches

Despite the efforts described in Section 4.3.5 there will always be some ambiguity in the matching to injected sources that can introduce large, non-physical scatter. To check this, we visually inspected hundreds of the MEDS stamps of `Balrog` objects whose absolute magnitude response was greater than 2 – and in particular the set of objects with large $\Delta \mathrm{mag}_{\mathrm{DF}}$ whose size errors were small. There were a few isolated instances of ambiguous matches where a faint injection landed in the very center of an extremely bright Y3 star whose GAp flux measurement failed. These can easily be accounted for by adapting our ambiguous matching algorithm to reject `Balrog` injections near objects with flagged GAp fluxes but this was not discovered in time to update the catalogs used in downstream measurements. However, this issue has negligible impact as we estimate only a few hundred instances in the total `y3-merged` sample.

5.4 Star-Galaxy Separation

We use the δ injections of `y3-stars` to estimate the stellar efficiency (or true positive rate) and the classified DF sources in `y3-merged` for the contamination rate (or false discovery rate) for the `Balrog` star sample as a function of injection magnitude in Figure 5.15a. The solid, dashed, and dotted lines represent the fraction of objects classified as less than or equal to an `EXTENDED_CLASS_SOF` value of 0, 1, or 2 respectively. While `y3-merged` is required to estimate the contamination rate in order to have a realistic relative ratio between star and galaxy counts, we use the `y3-stars` sample to compute the efficiency as its truth classifications are nearly noiseless and the measurement does not need any external information about galaxy contaminants. We find that the stars are correctly classified (`EXTENDED_CLASS_SOF` $<=$ 1) over 95% of the time below an i band magnitude of 21.75 and 80% of the time below magnitude 22.75 before dipping to 70% efficiency near the detection threshold at $i\sim$23. The stellar efficiency quickly drops to below 50% beyond 23rd magnitude. The efficiency of high confidence stars (`EXTENDED_CLASS_SOF` $==$ 0) follows a similar trend but reaches the previously quoted values about 0.5 magnitudes earlier. Alternatively, the rate of DF galaxies misclassified as stars stays below 10% until 22nd magnitude where there is a sharp increase until the detection limit where at low S/N it is extremely difficult to differentiate between classifications. However, we again note that the stellar efficiency measurement is less noisy due to the higher degree of confidence in accurate classification compared to the DF sample.

We make equivalent measurements for the galaxy efficiency and contamination in Figure 5.15b where the solid, dashed, and dotted lines now correspond to the fraction of objects classified as greater than or equal to `EXTENDED_CLASS_SOF` values of 1, 2, and 3. Here we must use sources in `y3-merged` exclusively as

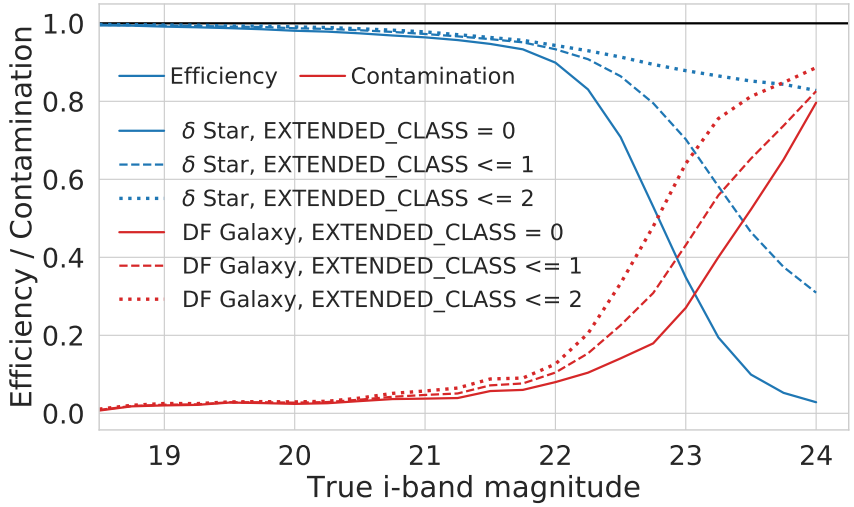

(a) Star Selection

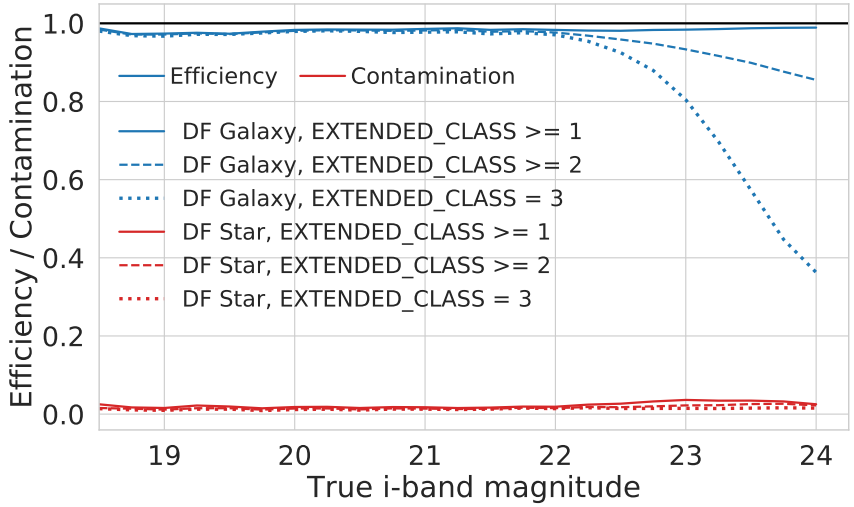

(b) Galaxy Selection

Figure 5.15: The efficiency (in blue) and contamination (in red) of the `Balrog` stellar sample (a) and galaxy sample (b). We use the δ injections of `y3-stars` as our population of true stars for (a) as it is a nearly pure sample, with only ambiguous matches as potential contaminates. We use the DF injections classified as galaxies from the DF k-nearest neighbor (knn) classifier described in Section 4.3.3 as our true galaxy sample which has intrinsic uncertainty as detailed in [173]. For (b), we cannot use the δ injections as the contamination measurement requires a realistic ratio of galaxy and stars sources in the sample so we instead use the classified DF stars. Each line corresponds to the fraction of objects above or below the noted `EXTENDED_CLASS_SOF` threshold value. We do not expect the galaxy efficiency to be 100% even at magnitudes where complete due to small impurities DF knn classifier.

the ratio between stars in the δ sample and galaxies in the DF sample is not realistic as required by a contamination estimate. The efficiency is slightly lower than the stars on the bright end due to impurities in the DF knn classifier but is quite close to 100% below 22nd magnitude. The efficiency of high-confidence galaxies (`EXTENDED_CLASS_SOF` == 3) decreases sharply near the detection limit, but over 85% of DF galaxies with assigned classifications are correctly identified (`EXTENDED_CLASS_SOF` >= 2) down to 24th magnitude in i band. The contamination rate of stars into the galaxy sample is consistently $\sim$2% until 22nd magnitude where it rises slightly to 4% at a magnitude of 23. This low level of contamination is largely due to the relatively small number of stars compared to galaxies at these magnitudes and is consistent with the findings quoted in [128]. A table of the `Balrog` classification (or "confusion") matrix as a function of input magnitude is provided in Table C.5.

Chapter 6

Applications of Balrog to DES Y3 Analyses

While estimating photometric uncertainties, completeness, and outlier rates of DES measurements is extremely valuable on its own as a diagnostic and systematics discovery tool, the real power of injection pipelines will be their direct use for calibrating cosmological measurements. The high computational cost of this latest iteration of `Balrog` at such high emulation fidelity has significantly reduced the relative size of the injection catalog compared to the data, which currently limits our ability to use `Balrog` for the most ambitious measurements such as their direct use as randoms for galaxy positions and shapes in two-point analyses. We discuss this and potential resolutions to this problem in Chapter 7. However, there is still a rich set of measurements that can be made with even a partial sampling of the survey footprint that can make a significant impact on the resulting cosmological constraints from DES.

We now present some of the most important applications of the Y3 `Balrog` catalogs, particularly those that are relevant for the DES Y3 cosmology analysis. Each of the following sections correspond to either a submitted publication or one

that is at an advanced stage, on which I am a contributing author. We begin with the photometric redshift calibration of weak lensing source galaxies in Section 6.1 and a measurement of the effect of magnification on lens galaxy samples in Section 6.2. We then present the discovery of an additional noise component in Y3 images from undetected sources in Section 6.3 which results in increased variance of BFD parameters and over-subtraction of the background by DESDM software. We then highlight some of the ongoing work to use `Balrog` for measurements of selection effects in galaxy clusters in Section 6.4. To our knowledge, this is the first time an object injection pipeline has been used for any of the following measurements or played such a critical role in the calibration of a galaxy survey's cosmological constraints. We anticipate that such tools will be even more critical for systematics control in DES Y6 and upcoming surveys.

6.1 Photometric Redshift Calibration

Chief among the applications of `Balrog` in Y3 is facilitating a novel inference method for the photometric redshift calibration of weak lensing samples. As discussed in Chapters 2 and 3, measuring the distances of sources in photometric galaxy surveys is extremely difficult without spectroscopic measurements. In their absence, the distances are usually inferred instead from noisy photometric properties such as magnitude and color. The large uncertainties in the estimated redshifts z are handled by placing sources in fairly large tomographic bins and estimating the redshift distribution $n(z)$ of each bin. Accurately characterizing each $n(z)$ is one of the most crucial components of the likelihood analysis, and remains one of the most dominant sources of uncertainty in cosmological inference from photometric surveys [76]. In the rest of this section, we summarize the measurement of DES Y3 redshifts for the source sample described in [135] and, in

particular, the key role `Balrog` plays in facilitating the calibration.

The DES Y3 photometric redshift inference scheme uses multiple, independent analyses to jointly constrain the redshift distribution of the weak lensing source sample:

- **Self-Organized Map $p(z)$ (SOMPZ)** which leverages the deep, multi-band observations of sources in the DES DF to measure the density of galaxies in "cells" of a projected $ugrizJHK_s$ color space and map how these densities change in the projection of the noisier, lower-dimensional riz color space as measured on the WF. This approach uses the DF as an intermediary between WF measurements and spectroscopic redshift samples to break degeneracies in redshift-color space and greatly reduce sample variance, shot noise, and survey selection effects when an accurate estimate of the survey transfer function is available [194, 135]. It is for this reason that `Balrog` with the DF as the injection catalog plays a central role in calibrating the method.

- **Clustering redshifts** that constrain the distances to source galaxies from their angular clustering compared to a reference sample in narrow redshift slices [195, 196, 197]. The basis of this method is that the amplitude of the angular 2PCF is proportional to the fraction of source galaxies in proximity to the reference sample.

- **Shear ratios** which compare the galaxy-galaxy lensing signal of different source bins behind each lens bin on small scales [198, 199]. These ratios are sensitive to the mean lens efficiency of each source bin as compared to that of the lens bin, which is dependent on their respective $n(z)$'s.

The variance of the resulting ensemble of redshift distributions encodes the

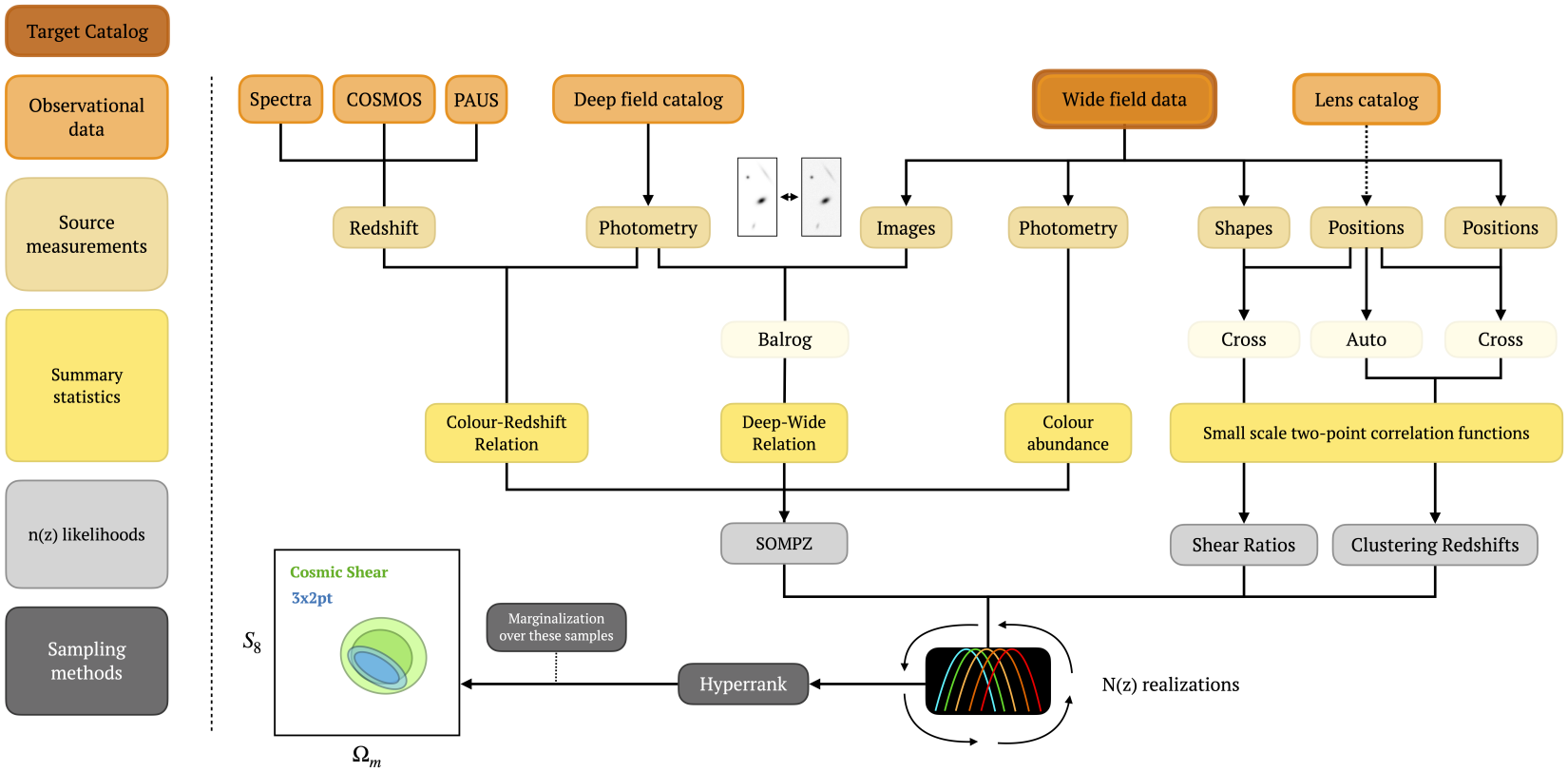

Figure 6.1: A flowchart that illustrates the photometric redshift calibration scheme of the weak lensing source sample. The three $n(z)$ likelihood functions from SOMPZ, clustering redshifts, and shear ratios are displayed in light gray. Multi-band color information from the DF is critical for the calibration of SOMPZ, and the mapping between this information and their WF realizations is captured by `Balrog`. Taken from [135].

the uncertainties on the estimated $n(z)$'s from multiple aspects of the data, and are marginalized over in the Y3 cosmological likelihood Markov chains using the `HYPERRANK` algorithm [200]. As clustering redshifts and shear ratio measurements are derived from small-scale information and do not utilize color, their derived constraints are complementary to SOMPZ and are largely independent of cosmological signals on larger scales. An overview of the weak lensing redshift distribution calibration scheme is shown in Figure 6.1.

6.1.1 SOMPZ Methodology

Extracting the redshift information from a deep, high-dimensional color space sample with at least partial spectroscopic measurements to estimate the redshift of a WF galaxy requires marginalizing over the properties of the deep sample and the measurement likelihood of the observed properties [194]. The probability for a particular galaxy to have a redshift of z conditioned on observed WF properties $\hat{\boldsymbol{x}}$, covariance matrix $\hat{\boldsymbol{\Sigma}}$, and selection function $\hat{s}$ is then given by

$$p(z|\hat{\boldsymbol{x}}, \hat{\boldsymbol{\Sigma}}, \hat{s}) = \int d\boldsymbol{x}\, p(z|\boldsymbol{x}, \hat{\boldsymbol{x}}, \hat{\boldsymbol{\Sigma}}, \hat{s}) p(\boldsymbol{x}|\hat{\boldsymbol{x}}, \hat{\boldsymbol{\Sigma}}, \hat{s}), \tag{6.1}$$

where $\boldsymbol{x}$ are the corresponding properties of the DF sample. As the large dimensionality of the integral in Equation 6.1 makes it unfeasible to directly estimate, the SOMPZ methodology first introduced in [194] and updated for DES Y3 in [135] discretizes the smooth color-magnitude space spanned by $\boldsymbol{x}$ and $\hat{\boldsymbol{x}}$ into categories c and $\hat{c}$ called galaxy *phenotypes*. While there are many non-unique ways to create a mapping of color-magnitude space to phenotypes, these analyses used an unsupervised machine learning algorithm to produce a Self-Organizing Map (SOM; [201]) as it provides a low, (typically) two-dimensional representation of the data which makes interpolation and visualization much easier to facilitate.

With this scheme, Equation 6.1 greatly simplifies to[1]

$$p(z|\hat{c},\hat{s}) = \sum_c p(z|c,\hat{c},\hat{s})p(c|\hat{c},\hat{s}) \tag{6.2}$$

$$\approx \sum_c p(z|c,\hat{s})p(c|\hat{c},\hat{s})p(\hat{c},\hat{s}), \tag{6.3}$$

where in the last line we have assumed that the $p(z)$ for galaxies assigned to a given deep photometric cell c is not sensitive to the noisy wide photometry of that galaxy. Each of the terms in this last equation are estimated from different galaxy samples:

(i) $p(\hat{c}|\hat{s})$ is the probability of a particular WF color-magnitude, as computed from the weak lensing source sample (described in Section 6.1.2).

(ii) $p(c|\hat{c},\hat{s})$ is the measurement likelihood of observing a DF galaxy with color-magnitude c with equivalent WF measurements of $\hat{c}$, including detection probability. This is a narrow slice of the full transfer function measured by `Balrog`. While this could be estimated simply from deep and wide photometric measurements of the DF sample, `Balrog` samples this probability over multiple injection realizations and over significantly more observing conditions across the footprint.

(iii) $p(z|c,\hat{s})$ is the redshift probability conditional on a given DF color-magnitude derived from the subset of the DF with reliable redshift estimates from spectroscopic measurements.

We can make this correspondence more explicit by rearranging Equation (6.3)

[1] We ignore the tomographic binning here for simplicity; see [135] for details.

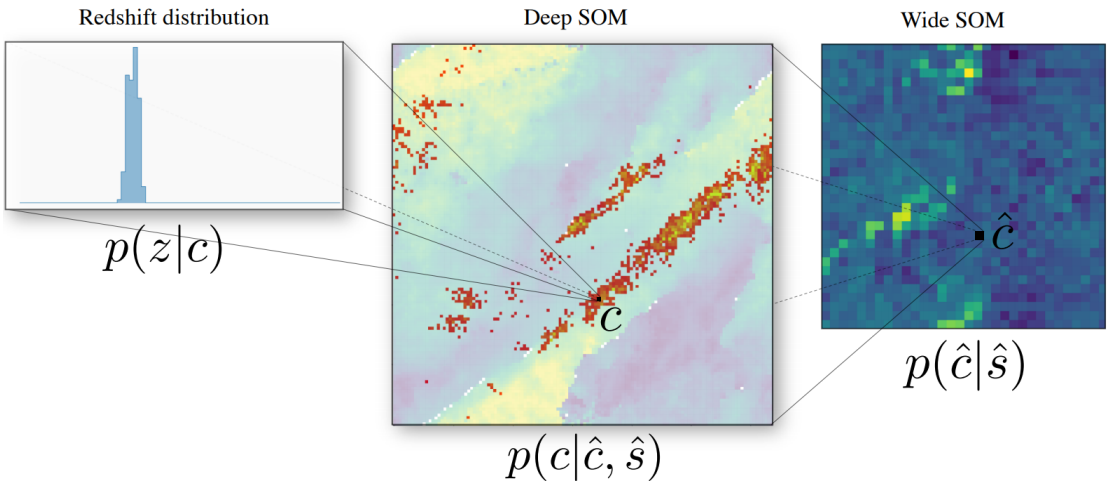

Figure 6.2: A high-level overview of the SOMPZ method. A galaxy measured by DES is assigned to the cell $\hat{c}$ in the wide SOM after training. Observations of galaxies in $\hat{c}$ can come from a variety of deep SOM cells c which is captured by the `Balrog` transfer function. Each deep cell has a corresponding redshift distribution $p(z|c)$ measured from the deep, spectroscopic sample. Taken from [194].

using the relation $p(c|\hat{c},\hat{s}) = p(c,\hat{c}|\hat{s})/p(\hat{c}|\hat{s})$:

$$p(z|\hat{c},\hat{s}) \approx \sum_c \underbrace{p(z|c)}_{\text{Redshift}} \underbrace{p(c)}_{\text{Deep}} \underbrace{\frac{p(c,\hat{c})}{p(c)p(\hat{c})}}_{\texttt{Balrog}} \underbrace{p(\hat{c})}_{\text{Wide}}, \tag{6.4}$$

where we have dropped the conditioning on $\hat{s}$ for clarity. A simple visual representation of this process is shown in Figure 6.2, with a more detailed view of how each of the probability terms in Equation (6.3) are connected in the inference methodology shown in Figure 6.3.

As originally shown in [194], we can extract information from the DES DF to break degeneracies in the measured riz color-redshift relation if we have accurate estimates of the corresponding WF properties of the DF sources. In this inference method, `Balrog` plays the essential role of determining the likelihood of a given deep, many-band color to be observed at a given region of noisier color-magnitude space in DES measurements at Y3 depth. This allows us to rigorously separate

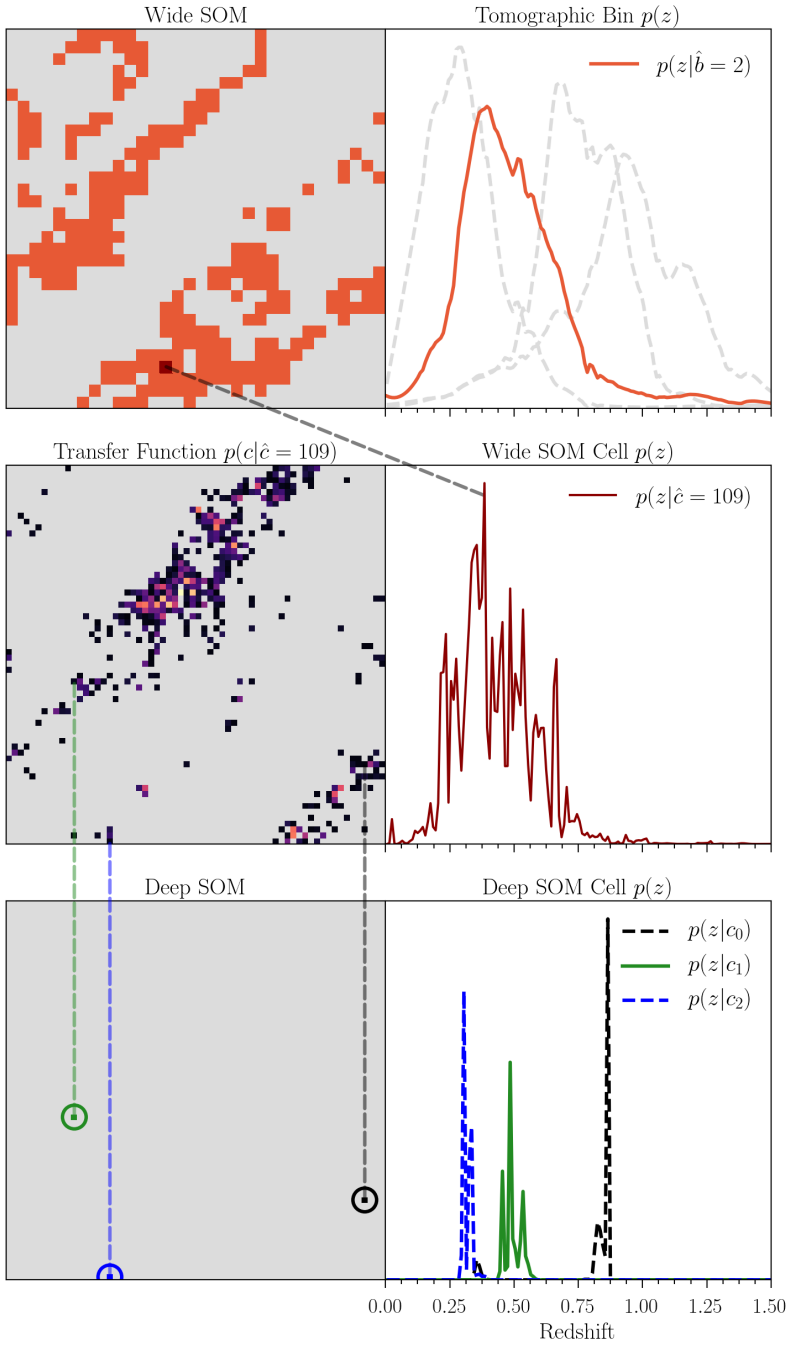

Figure 6.3: A more detailed look at how each probabilistic term in the SOMPZ inference methodology is connected, using the Y3 data. The top row shows the WF SOM cells assigned to the second bin. Galaxies in each cell $\hat{c}$ in this SOM have come from a different distribution of deep SOM cells c with weight determined by `Balrog` as shown in the middle row. The bottom row highlights the individual redshift distributions for three of these cells. Taken from [135].

the contributions from measurement noise to the true color-redshift relation when estimating the ensemble photometric redshift distribution of the lensing source sample.

The transfer function sampled by `Balrog` serves to correctly weight the well-constrained redshift distribution $p(z|c)$ of each deep SOM cell according to the probability of detecting those galaxies. As the SOM cells $\hat{c}$ are determined by Metacalibration magnitude and color, the `Balrog` samples are key to generating a distribution of observed Metacalibration magnitudes for each injected DF galaxy. In addition to breaking degeneracies in the color-redshift relation, `Balrog`, by virtue of enabling this scheme, facilitates avoiding otherwise prohibitive selection biases resulting from the use of spectroscopic redshifts for weak lensing redshift calibrations (see, e.g. [202]) because it uses spectroscopic redshifts only of galaxies for which 8 bands of DES DF photometry provide relatively well-constrained $p(z)$.

6.1.2 Sample Selection

The weak lensing source sample for DES Y3 measurements is presented in [131] and is a subset of the larger GOLD catalog described in [128] and Chapter 3. It consists of just over 100 million objects with photometry and shapes measured by `Metacalibration` in riz[2]. A number of the selections made in addition to the fiducial GOLD cuts were motivated by achieving a more homogeneous photometric catalog and accurate redshift distributions. These additional cuts are the following:

[2]Only the riz Metacalibration fluxes are used when defining the tomographic bins for the source sample, due to PSF issues in the g band [75].

$$
\begin{aligned}
& 15 < \texttt{MCAL\_MAG\_R} < 26 \\
\texttt{AND} \quad & 18 < \texttt{MCAL\_MAG\_I} < 23.5 \\
\texttt{AND} \quad & 15 < \texttt{MCAL\_MAG\_Z} < 26 \\
\texttt{AND} \quad & -1.5 < \texttt{MCAL\_MAG\_R} - \texttt{MCAL\_MAG\_I} < 4 \\
\texttt{AND} \quad & -4 < \texttt{MCAL\_MAG\_I} - \texttt{MCAL\_MAG\_Z} < 1.5.
\end{aligned}
$$

The bright-end limits on the riz magnitudes remove bright, nearby foreground galaxies and some stars that were incorrectly classified. The faint-end cuts exclude regions of the COSMOS-30 sample where the photometric redshifts were found to be more biased [203], and the last two cuts remove sources with unphysical colors that are likely artifacts or catastrophic photometry failures.

6.1.3 Characterization of Uncertainty Contributions

There are many sources of uncertainty in this method of estimating redshift distributions from galaxy photometry. The primary set of contributions examined in [135] include (i) sample variance, (ii) shot noise, (iii) biases in the redshifts of the used spectroscopic sample, (iv) photometric calibration uncertainty in the measurements of the 8-band colors of DF galaxies, (v) biases resulting from the SOMPZ methodological choices, and (vi) biases from any discrepancies between `Balrog` and the true transfer function. We will examine only the final source of uncertainty here.

The probability of observing a galaxy with wide properties $\hat{c}$ given true deep properties c depends on the observing conditions of the local field. As `Balrog` only samples about 20% of the footprint, we use the combined sample to calibrate the mean correction to each $n(z)$ across the footprint. One way to test the robustness of this estimate is to bootstrap the `Balrog` galaxies by their injected position in the WF. The validation work in [135] subdivided the full catalog into 100 subsamples

Uncertainty	Bin 1	Bin 2	Bin 3	Bin 4
Shot Noise & Sample Variance	0.006	0.005	0.004	0.006
Redshift Sample Uncertainty	0.003	0.004	0.006	0.006
Photometric Calibration Uncertainty	0.010	0.005	0.002	0.002
Inherent SOMPZ Method Uncertainty	0.003	0.003	0.002	0.002
`Balrog` Uncertainty	<0.001	<0.001	<0.001	<0.001

Table 6.1: The approximate error contributions to the mean redshift of each tomographic bin for a variety of components in the SOMPZ methodology. The sample variance of the DF was found to be the largest contributor to the overall uncertainty, while the choice of redshift sample became equally important at large redshifts. In comparison, intrinsic errors in the `Balrog` methodology were found to be negligible and their effect on $\overline{z}$ was not modeled in the final analysis. Values come from Table 2 in [102].

using a k-means clustering algorithm[3] and drew an equal number of subsamples with replacement to recompute the mean transfer function and re-estimate each $n(z)$ with SOMPZ. This process is repeated 1,000 times to compute the dispersion in the mean redshift $\sigma_{\overline{z}}$. The value of $\sigma_{\overline{z}}$ was found to be less than 10^{-3} in each tomographic bin, which is negligible compared to the other estimated sources of uncertainty which are displayed in Table 6.1.

A second test was performed to compare the transfer function using `Balrog` versus using the sample of position-matched sources that are present in both the DES DF and WF. While the `Balrog` measurement is preferred as it probes multiple realizations of each DF galaxy across a variety of observing conditions, we can test if their predicted mean redshift in each bin is reasonably in agreement as an additional validation check. The dispersion in mean redshift $\sigma_{\overline{z}}$ is again computed for this matched WF-DF sample, though it is not directly comparable to the results of the previous test as `Balrog` sources are injected at one-fifth the density of the WF. The comparison can be made with a WF-DF sample that is a comparable number of objects over five times the area, or the same area with

[3] https://github.com/esheldon/kmeans_radec

one-fifth of the number of sources. The former was chosen in [135] which yields a lower limit on the uncertainty from variable observing conditions.

The absolute difference between the mean redshifts $\Delta\overline{z}$ predicted by each transfer function was found to be the following:

$$(\Delta\overline{z} \pm \sigma_{\overline{z}}) \times 10^{-3} = [-2.8 \pm 1.8; \quad 3.6 \pm 1.4; \quad 3.1 \pm 1.4; \quad 8.2 \pm 4.8]. \tag{6.5}$$

The differences are within $\sim 2\sigma_{\overline{z}}$ and were deemed sufficiently consistent as $\sigma_{\overline{z}}$ is a lower limit of the expected variance due to spatially varying observing conditions.

6.1.4 Results

In the first application of this inference scheme to real data, [135] derived constraints on the redshift distributions of the DES Y3 weak lensing source sample from SOMPZ alone and from combined constraints with clustering redshifts and shear ratios; these are both shown in Figure 6.4. These ensemble redshift distributions define a full probability function over each $p(z)$ bin. The recovered distributions from SOMPZ alone are not always smooth functions of z due to the chosen likelihood model, but are smoothed by the inclusion of clustering redshift information. This demonstrates the value in combining independent constraints, as the clustering redshifts are significantly less sensitive to biases in the spectroscopic sample. The shear ratio constraints enter the ensemble distributions by shifting the mean redshift of each bin.

In addition to helping facilitate the calibration of one of the most important systematics in the DES 3×2pt likelihood analysis, it is notable that the intrinsic uncertainty in `Balrog`'s estimation of the transfer function is a negligible contributor to the overall error budget with an uncertainty on the mean redshift in each tomographic bin of $\sigma_{\overline{z}} < 10^{-3}$. This is a significant accomplishment as `Balrog`

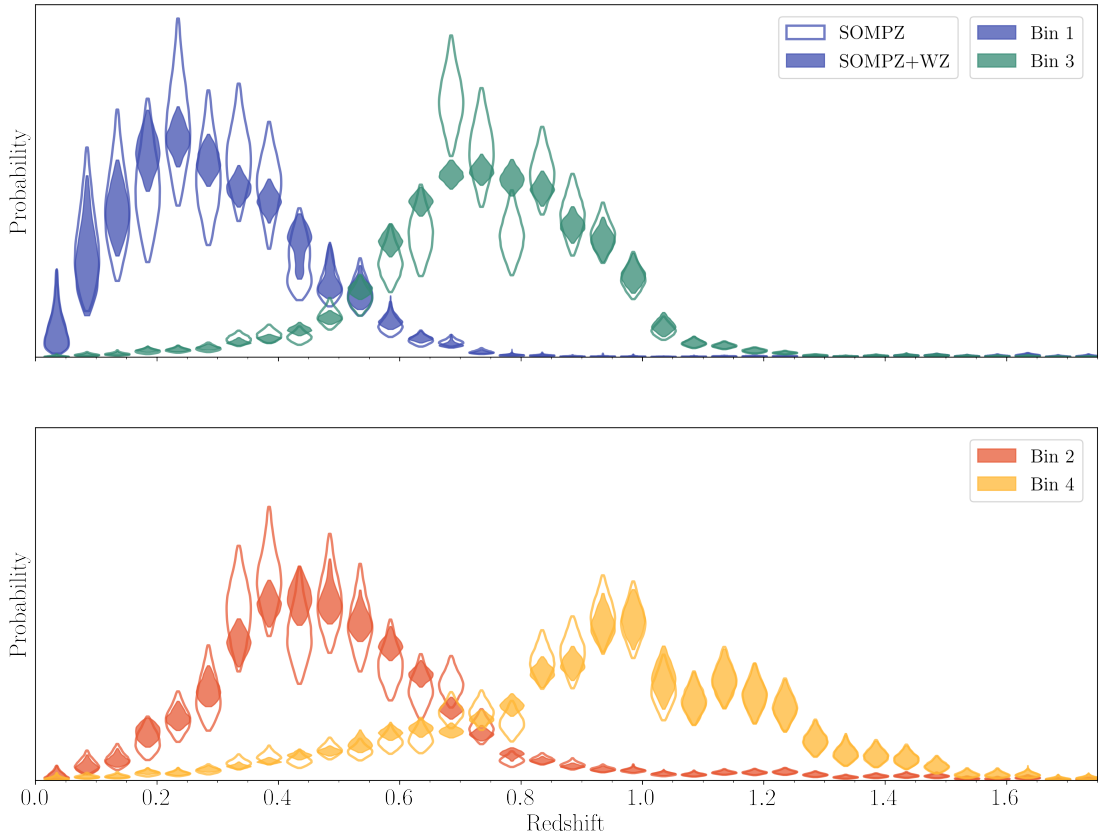

Figure 6.4: A violin plot showing the ensemble of redshift distributions for the four tomographic bins of the DES Y3 weak lensing source sample. The open contours show the constraints from SOMPZ alone, while the filled contours are combined with clustering redshifts (WZ). Each violin symbol visualizes the 95% confidence region for the probability that a source galaxy is designated in the corresponding tomographic bin and redshift value. Measurements from shear ratios enter as shifts on the mean redshift of the distributions. The decreased probability of galaxies near $z \sim 0.75$ in SOMPZ-only is the result of cosmic variance; an imprint of a large-scale structure in in the COSMOS field. This feature disappears when using complimentary information from WZ. Taken from [135].

was able to decrease the systematic bias in the photometric redshift estimates without contributing a novel source of intrinsic systematic uncertainty in its sampling of the transfer function, which was not obviously the case a priori. The use of `Balrog` in photometric calibration can be further leveraged in future analyses by incorporating positional-dependent selection effects θ in the used measurement likelihood $p(c|\hat{c}, \hat{s}, \theta)$. Further details on this methodology are given in [135].

6.2 Lens Magnification

As discussed in Section 3.3.1, galaxy clustering and galaxy-galaxy lensing are powerful tools in the DES 3×2pt analysis for estimating the underlying matter density field and large-scale galaxy bias. These constraints are based upon measuring the auto-correlation of lens galaxy positions or by cross-correlating the positions of foreground lens galaxies to the shapes of background source galaxies respectively, and thus are particularly sensitive to any systematic that affects source detection. One such bias that we consider here is the effect of lensing magnification on the detection and binning of galaxies in the lens sample. This section is a partial summary of the work presented in [181], which is an upcoming paper describing the measurement of lens magnification in the two DES Y3 galaxy samples used in the 3×2pt analysis. This measurement includes the novel use of an injection pipeline such as `Balrog` to directly calibrate this magnification effect in the measured 2PCF. While the methodology is now fixed, the presented results are preliminary.

6.2.1 Methodology

Weak gravitational lensing distorts the appearance of galaxies on the sky parameterized by the shear γ and convergence κ which is captured in the distortion matrix $\mathcal{A}$. As shown in Section 2.3, the magnification μ is simply the inverse of the determinant of $\mathcal{A}$:

$$\mu = \frac{1}{\det\mathcal{A}} = \frac{1}{(1-\kappa)^2 - |\gamma|^2} \approx \frac{1}{1-2\kappa} \approx 1 + 2\kappa, \tag{6.6}$$

in the weak lensing regime where $\gamma, \kappa << 1$. Magnification impacts the observed galaxy density fluctuation field $\delta_g^{\rm obs}$ through two competing effects: (i) a geometric suppression factor resulting from the the increased sky area for a fixed set of detections, and (ii) a boost in detection efficiency of faint sources – due to the increased profile area and preservation of surface brightness – which increases the local number density. The latter can also result in sources much brighter than the detection threshold changing tomographic bins when the photometric redshift is not well constrained (such as in a flux-limited sample; see Section 6.2.2).

Whether the geometric suppression or boost in detection efficiency dominates the effect on the clustering signal depends on the slope of the intrinsic flux distribution of the sample, in addition to more subtle morphological selection effects (which we ignore for the moment but will return to soon). We can quantify this by expressing the overdensity in the clustering signal due to magnification $\delta_g^{\rm mag}$ in terms of the ratio of the observed number density $n^{\rm obs}$ to the intrinsic density $n^{\rm int}$:

$$\delta_g^{\rm mag}(\hat{\boldsymbol{n}}, z, F_\mu) = \frac{n^{\rm obs}(\hat{\boldsymbol{n}}, z, F_\mu)}{n^{\rm int}(\hat{\boldsymbol{n}}, z, F_\mu)} - 1 \tag{6.7}$$

where $\hat{\boldsymbol{n}}$ is the position on the sky, z is the redshift (or tomographic bin), and F_μ is the effective flux cut after magnification (see [66, 204, 187] for more details).

The two magnification effects enter this formalism in the scaling of $F_\mu = \mu F_0$ for a given source of intrinsic flux F_0, and locally reducing the intrinsic number density by a factor of μ:

$$n^{\rm obs}(\hat{\boldsymbol{n}}, z, F_\mu) = \frac{1}{\mu(\hat{\boldsymbol{n}})} n^{\rm int}(\hat{\boldsymbol{n}}, z, F_0/\mu(\hat{\boldsymbol{n}})). \tag{6.8}$$

We can then express Equation 6.7 as

$$\delta_g^{\rm mag}(\hat{\boldsymbol{n}}, z, F_\mu) = \frac{1}{\mu(\hat{\boldsymbol{n}})} \frac{n^{\rm int}(\hat{\boldsymbol{n}}, z, F_0/\mu(\hat{\boldsymbol{n}}))}{n^{\rm int}(\hat{\boldsymbol{n}}, z, F_0)} - 1. \tag{6.9}$$

Dropping the explicit dependence on redshift and position for simplicity and using the approximation in Equation (6.6) to express μ in terms of the convergence κ, we have that

$$\delta_g^{\rm mag}(F_\mu) \approx (1 - 2\kappa) \frac{n^{\rm int}\left([1 - 2\kappa]F_0\right)}{n^{\rm int}(F_0)} - 1. \tag{6.10}$$

Using the parameterization of

$$n^{\rm obs} = A \left(\frac{F\mu}{F_*}\right)^{\alpha(F_\mu)}, \tag{6.11}$$

where A and F_* are constant parameters and α is the slope of the intrinsic flux distribution as a function of the flux limit F_μ, [205, 187] showed that we can update Equation 6.10 to be

$$\delta_g^{\rm mag}(F_\mu) \approx 2\left[\alpha(m_\mu) - 1\right]\kappa, \tag{6.12}$$

where $\delta_g^{\rm mag}$ and α are now parameterized in terms of the limiting magnitude m_μ:

$$\alpha(m_\mu) = 2.5 \frac{d}{dm_\mu} \left(\log_{10} n^{\rm obs}(m_\mu)\right). \tag{6.13}$$

Equation (6.12) is only correct in the idealized case of a sample defined by a simple flux limit (which is not always desired; see Section 6.2.2) with no additional selection biases such as how magnification affects shape. A simple variation of this model is to empirically measure the proportionality constant between $\delta_g^{\rm mag}$ and κ without an explicit model for $\alpha(m_\mu)$:

$$\delta_g^{\rm mag}(z) = C(z)\kappa \tag{6.14}$$

$$\delta_g^{\rm mag}(z) = \left[C_{\rm sample}(z) + C_{\rm area}\right]\kappa, \tag{6.15}$$

where $C_{\rm area} = -2$ by inspection of Equation 6.12 and $C_{\rm sample}$ is a constant to be determined for each redshift bin. Then for an intrinsic density fluctuation field $\delta_g^{\rm int}$, it will be related to the observed field $\delta_g^{\rm obs}$ by

$$\delta_g^{\rm obs}(z) = \delta_g^{\rm int}(z) + \delta_g^{\rm mag}(z) \tag{6.16}$$

$$= \delta_g^{\rm int}(z) + \left[C_{\rm sample}(z) + C_{\rm area}\right]\kappa, \tag{6.17}$$

and the corresponding galaxy clustering and galaxy-galaxy lensing 2PCFs will be modified as

$$\langle \delta_g^{\rm obs}\delta_g^{\rm obs}\rangle = \langle \delta_g^{\rm int}\delta_g^{\rm int}\rangle + C^2\langle\kappa\kappa\rangle + 2C\langle\delta_g^{\rm int}\kappa\rangle, \tag{6.18}$$

and[4]

$$\langle \delta_g^{\rm obs}\gamma\rangle = \langle \delta_g^{\rm int}\gamma\rangle + C\langle\kappa\gamma\rangle = \langle \delta_g^{\rm int}\gamma\rangle + C\langle\kappa\kappa_s\rangle \tag{6.19}$$

respectively, where we suppressed the dependence on z and introduced κ_s as the local convergence at source galaxy positions as $\gamma \propto \kappa_s$ in the weak lensing limit and their auto-correlation is easier to estimate.

[4]There are additional correction terms due to intrinsic alignment which we ignore here for clarity.

6.2.2 Lens Samples

This methodology is applied to two different samples of lens galaxies in DES Y3: REDMAGIC[5] and MAGLIM, each of which are briefly described below.

(i) **redMaGiC** was intended to be the fiducial lens sample used in Y3 3×2pt. This sample of galaxies is selected by running the REDMAGIC algorithm described [206] on the Y3 GOLD catalog, which selects luminous red galaxies (LRGs) from the magnitude-color-redshift relation for red-sequence galaxy clusters [207, 208]. The sample is defined by an input luminosity threshold $L_{\rm min}$ and a nearly constant comoving density, and is designed to create a sample of LRGs with minimal photometric redshift errors. In Y3, the REDMAGIC magic sample is split into five tomographic bins with bin edges defined at $z = [0.15, 0.35, 0.50, 0.65, 0.80, 0.90]$. The first three bins comprise the *high-density sample* with a luminosity threshold of $L_{\rm min} > 0.5L_*$, while the last two bins are called the *high-luminosity sample* with $L_{\rm min} > 1.0L_*$. In addition, the following sample cuts were made:

$$\begin{aligned} & \texttt{FLAGS\_GOLD} < 8 \\ \texttt{AND}\quad & \texttt{EXTENDED\_CLASS} >= 2 \\ \texttt{AND}\quad & \texttt{CHISQ} < \texttt{CHISQ\_MAX} \\ \texttt{AND}\quad & 0.15 < \texttt{ZREDMAGIC} < 0.9, \end{aligned}$$

where `CHISQ` is the χ^2 of the REDMAGIC template fit and `ZREDMAGIC` is the photometric redshift estimate made by REDMAGIC as described in [206]. The corresponding max χ^2 cuts depend on the tomographic bin.

(ii) **MagLim** is an alternative lens sample that optimizes the amount of cosmological information extracted for wCDM constraints from the data whose

[5]Which stands for red sequence Matched-filter Galaxy Catalog.

primary selection is based on a flux-limited sample [188]. The resulting sample is ~ 3.5 larger than redMaGiC which significantly reduces shot noise, but at a cost of redshift distributions that are $\sim 30\%$ wider due to the less homogeneous galaxy properties. The MagLim sample is split into six tomographic bins with edges defined to be $z = [0.20, 0.40, 0.55, 0.70, 0.85, 0.95, 1.05]$. Unlike redMaGiC, all selections are based off of columns in GOLD. The magnitude cut is made on the i band and depends linearly on redshift: $\text{mag}_i < 4 \times z_{\text{phot}} + 18$, where z_{phot} is the photometric redshift estimate of each source by the DNF algorithm [133]. All of the cuts are listed below:

$$
\begin{aligned}
& \texttt{FLAGS\_GOLD} < 1 \\
\texttt{AND} \quad & \texttt{EXTENDED\_CLASS} == 3 \\
\texttt{AND} \quad & \texttt{SOF\_CM\_MAG\_CORRECTED\_I} < 4 \times \texttt{DNF\_ZMEAN\_SOF} + 18 \\
\texttt{AND} \quad & \texttt{SOF\_CM\_MAG\_CORRECTED\_I} > 17.5 \\
\texttt{AND} \quad & 0.2 < \texttt{DNF\_ZMEAN\_SOF} < 1.05
\end{aligned}
$$

In addition, an angular mask defined on a pixelated `HEALPix` map is applied that only includes pixels with fractional coverage of at least 80% and with deep enough photometry that both lens samples are expected to have sufficiently uniform selection in all redshift bins. The sample of source galaxies lensed by these lens samples is identical to the one described in Section 6.1.2.

6.2.3 Estimating the Magnification Bias

The formalism described above requires an empirical estimate of C_{sample} for each tomographic redshift bin. For a given convergence field $\kappa(\hat{\boldsymbol{n}})$, we can combine Equations 6.7 and 6.14 to get

$$1 + [C_{\text{sample}} + C_{\text{area}}]\,\kappa = \frac{n^{\text{obs}}(F_0, \kappa)}{n^{\text{int}}(F_0)}, \tag{6.20}$$

where we have introduced the notation

$$n^{\rm obs}(F,\kappa) = (1-2\kappa)n^{\rm int}\left([1-2\kappa]F_0\right), \tag{6.21}$$

using the result in Equation 6.8.

Now considering the same convergence field with a small, uniform added convergence $\delta\kappa$, we have that

$$1 + \left[C_{\rm sample} + C_{\rm area}\right](\kappa + \delta\kappa) = \frac{n^{\rm obs}(F_0, \kappa+\delta\kappa)}{n^{\rm int}(F_0)}. \tag{6.22}$$

The difference between Equations 6.20 and 6.22 then gives

$$\left[C_{\rm sample} + C_{\rm area}\right]\delta\kappa = \frac{n^{\rm obs}(F_0, \kappa+\delta\kappa) - n^{\rm obs}(F_0, \kappa)}{n^{\rm int}(F_0)}. \tag{6.23}$$

In principle, this would suggest that estimators for $C_{\rm sample}$ would involve fitting measurements of the right-hand side of Equation 6.23 as a function of $\delta\kappa$ and subtracting $C_{\rm area} = -2$ from the slope. However, in practice most simulation and data estimates do not account for the changing solid angle on the sky and thus are not sensitive to the contribution by $C_{\rm area}\delta\kappa$. This leads to the following estimator:

$$C_{\rm sample} = \frac{n^{\rm obs}(F_0, \kappa+\delta\kappa) - n^{\rm obs}(F_0, \kappa)}{\delta\kappa \cdot n^{\rm int}(F_0)}. \tag{6.24}$$

We now discuss three different methods of estimating $C_{\rm sample}$ from this Equation below.

Estimating the Bias With `Balrog`

Equation 6.24 motivates measuring $C_{\rm sample}$ directly as the response of the recovered number density signal in the presence of a small applied convergence $\delta\kappa$.

`Balrog` is the ideal way to measure this response, as it captures all of the typical selection effects on the detection efficiency of the lens sample (due to variable observing conditions, image artifacts, etc.) that are convolved with the magnification bias by repeating the fiducial `Balrog` simulations with identical configuration and input with the only difference being an applied small, constant magnification factor. This procedure is outlined below:

1) Run a supplemental `Balrog` simulation over a subset of WF tiles with an input DF catalog that has a less conservative (i.e. brighter) flux limit cut. This is needed to increase the statistical power of the measurement as only a very small fraction of injections in `Run2` will be classified as redMaGiC galaxies. The lens sample is generally much brighter than the source sample, so precisely capturing the transfer properties of very low detection probability objects is less important for this measurement than for the photometric redshift calibration of source galaxies in Section 6.1. This was the motivation for `Run2a` in Chapter 4.

2) Use the produced `GalSim` configuration files from `Run2a` as the input for an addition run called `Run2a-mag` with the only change being an added line to magnify all injections by $\mu = 1.02$, corresponding to a $\delta\kappa \sim 0.01$. All other aspects of the simulations such as the input sample, injection positions, and image noise are identical.

3) Apply the redMaGiC and MagLim sample selections to both the "intrinsic" `Run2a` (label i) and "observed" `Run2a-mag` (label o). This results in four relevant observables for each redshift bin:

   (a) N_i: The number of `Balrog` galaxies in the intrinsic, $\kappa = 0$ run for each sample.

(b) N_o: The number of `Balrog` galaxies after applying a constant magnification factor to each injection.

(c) $N_{i\bar{o}}$: The number of galaxies in the intrinsic `Balrog` sample but not in the magnified sample.

(d) $N_{\bar{i}o}$: The number of galaxies in the magnified sample that were not in the intrinsic sample.

While ideally $N_{i\bar{o}} = 0$, Chapter 4 shows that the complex detection and measurement process can lead to some sources dropping out of the samples even for small perturbations in the images. This quantity contributes to the uncertainty in our estimate of C_{sample}.

The estimator for C_{sample} given by Equation (6.24) is then

$$C_{\text{sample}}^{\texttt{Balrog}} = \frac{N_o - N_i}{\delta\kappa \cdot N_i}. \tag{6.25}$$

Assuming each of the observables are independent draws from a Poissonian distribution, the uncertainty in $C_{\text{sample}}^{\texttt{Balrog}}$ is given by

$$\sigma_{C_{\text{sample}}^{\texttt{Balrog}}} = C_{\text{sample}}^{\texttt{Balrog}} \sqrt{\frac{N_{o\bar{i}} + N_{\bar{o}i}}{(N_o - N_i)^2} + \frac{1}{N_i} + \frac{2N_{\bar{o}i}}{(N_o - N_i)N_i}}. \tag{6.26}$$

In practice, this methodology was tested on a preliminary[6] `Balrog` run on over 1,000 tiles with a series of different flux limits on the composite riz detection magnitude ranging from 24 to the fiducial value of 25.4. Figure 6.5 shows how the estimated value of C_{sample} varied as a function of the corresponding magnitude limit. Ultimately, the composite flux limit corresponding to 24.5 magnitudes was chosen to balance increasing the recovered lens sample (a cut of nearly 40% of the

[6]Called `Run1`, which had an inferior DF catalog.

final DF sources) while not deviating from the fiducial estimate in a systematic direction or by more than 1σ in any redshift bin.

Direct Estimate from Flux Gradient

An alternative estimate of the magnification bias comes from the data itself. By adding a constant magnitude offset Δm to all objects in the sample,

$$\Delta m = -2.5 \log_{10}(1 + 2\delta\kappa), \tag{6.27}$$

for a small $\delta\kappa \sim 0.01$, we can repeat the sample selection on the updated magnitudes (assuming identical redshift binning) to estimate $C_{\text{sample}}^{\text{Data}}$ using Equation 6.24. In contrast to the estimator from `Balrog` described above, this approach ignores the contribution from all systematics other than magnification bias on object fluxes. The statistical uncertainty for this estimator is given by

$$\sigma_{C_{\text{sample}}^{\text{Data}}} = C_{\text{sample}}^{\text{Data}} \sqrt{\frac{1}{N_o - N_i} + \frac{1}{N_i}}. \tag{6.28}$$

Estimate from N-Body Simulations

The final estimate of the magnification bias in the Y3 data in [181] was done with the MICE and Buzzard N-Body simulations (See [209, 210, 211] and [212, 213] respectively). The local κ at each galaxy is computed through ray tracing, and the corresponding magnification factor is applied according to Equation (6.27). Samples are selected with and without this magnitude correction to compute $(N_o - N_i)/N_i$ in 10 equally spaced κ bins. These values are then fit with a line using a least squares fit to compute $C_{\text{sample}}^{\text{N-Body}}$ in each bin. Like the flux gradient estimator, this approach ignores systematic contributions other than magnification bias.

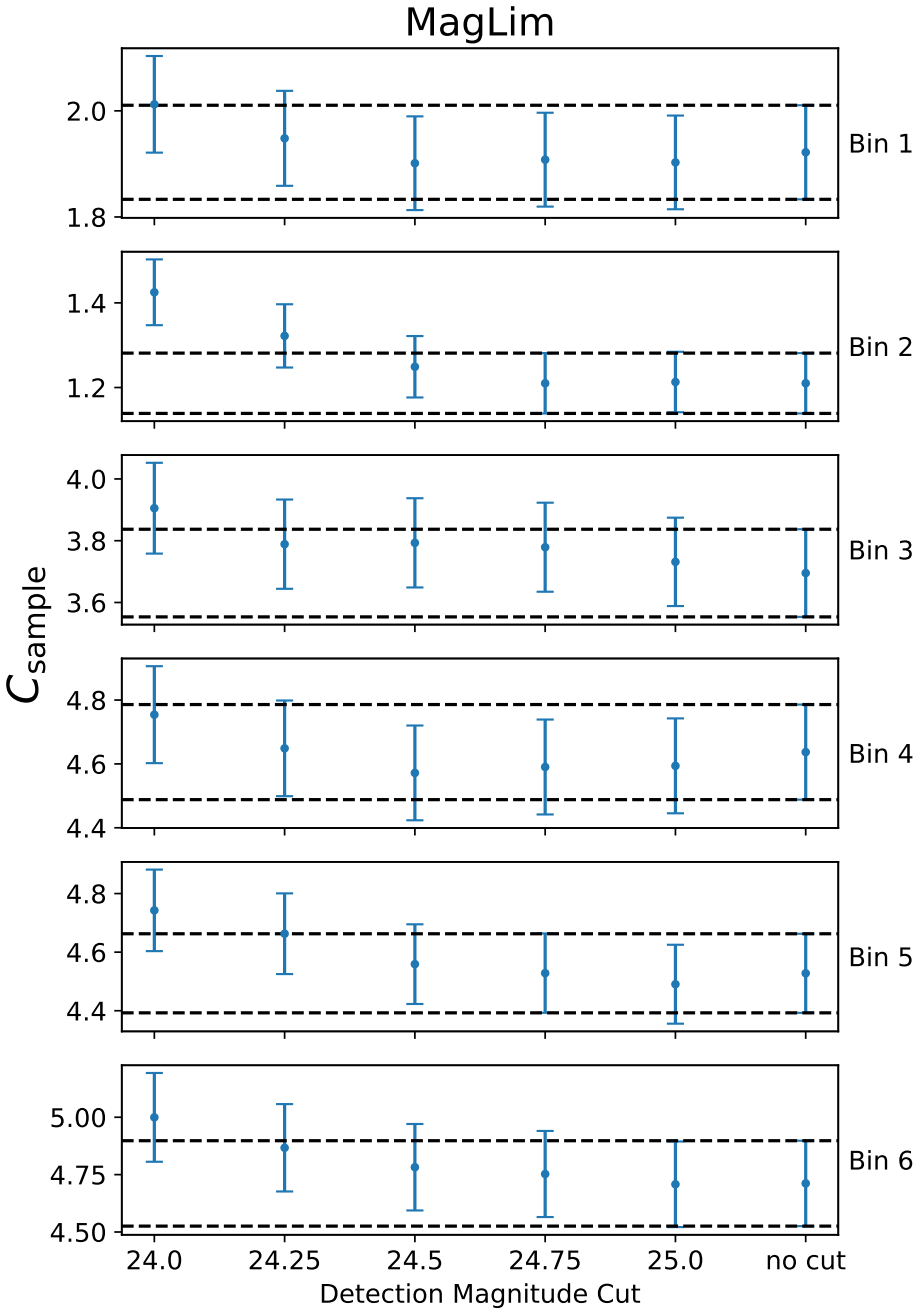

Figure 6.5: A preliminary measurement of C_{sample} for the MagLim sample for each redshift bin on `Balrog Run1` for a variety of flux-limited cuts on the composite riz detection flux used to select the input DF sample (where the shown bins are the corresponding detection magnitudes). The dashed lines correspond to the 1σ error bars on the measurement with no cuts. This result motivated the choice of 24.5 as the detection magnitude used for `Run2a`.

redMaGiC							
redshift	Balrog			Data direct method			Buzzard
	N_i	N_o	$C_{\text{sample}}^{\texttt{Balrog}}$	N_i	N_o	$C_{\text{sample}}^{\text{Data}}$	$C_{\text{sample}}^{\text{N-Body}}$
$0.15 < z < 0.35$	2291	2350	2.63 ± 1.491	337275	330243	2.08 ± 0.025	2.47 ± 0.753
$0.35 < z < 0.5$	4825	4776	-1.04 ± 1.009	583352	571551	2.02 ± 0.019	2.08 ± 0.287
$0.5 < z < 0.65$	6654	6698	0.67 ± 0.842	890701	872611	2.03 ± 0.015	1.99 ± 0.157
$0.65 < z < 0.8$	4100	4281	4.5 ± 0.999	457486	442302	3.32 ± 0.027	4.22 ± 0.259
$0.8 < z < 0.9$	4149	4309	3.93 ± 0.951	391329	377329	3.58 ± 0.031	4.35 ± 0.122

Table 6.2: Number counts and estimated C_{sample} values for the three estimation methods in the redMaGiC sample. Preliminary result from [181].

MagLim							
redshift	Balrog			Data direct method			MICE
	N_i	N_o	$C_{\text{sample}}^{\texttt{Balrog}}$	N_i	N_o	$C_{\text{sample}}^{\text{Data}}$	$C_{\text{sample}}^{\text{N-Body}}$
$0.2 < z < 0.4$	25997	26616	2.43 ± 0.264	2236473	2307562	3.18 ± 0.012	3.28 ± 0.091
$0.4 < z < 0.55$	18294	18706	2.3 ± 0.395	1599500	1665503	4.13 ± 0.016	4.09 ± 0.034
$0.55 < z < 0.7$	19194	19900	3.75 ± 0.375	1627413	1695311	4.17 ± 0.016	4.17 ± 0.04
$0.7 < z < 0.85$	25119	26089	3.94 ± 0.345	2175184	2273409	4.52 ± 0.015	4.5 ± 0.03
$0.85 < z < 0.95$	20652	21373	3.56 ± 0.435	1583686	1663140	5.02 ± 0.018	4.84 ± 0.023
$0.95 < z < 1.05$	17796	18661	4.96 ± 0.531	1494250	1571747	5.19 ± 0.019	5.04 ± 0.054

Table 6.3: Number counts and estimated C_{sample} values for the three estimation methods in the MagLim sample. Preliminary result from [181].

6.2.4 Results

Measurements of C_{sample} for all redMaGiC and MagLim redshfit bins using the above three methods are shown in Tables 6.2 and 6.3 respectively and visualized in Figure 6.6. The estimates from `Balrog` tend to be smaller than those from the alternative methods, particularly for $0.3 < z < 0.6$. These differences can be the result of any number of selection systematics such as stellar contamination, changes in photometric redshift binning, or differences in detection efficiency (e.g. changes in the blending rate and size estimates). The agreement between the different methods is much closer for a simple flux-limited sample with no redshift binning as shown in [150]. As the `Balrog` estimates account for these effects, they are chosen as the fiducial correction coefficients for the 3×2pt analysis.

The analysis in [181] studies the impact of the estimated magnification bias on the different aspects of the 3×2pt data vector and cosmological constraints for both simulations and the real data. They find that magnification has the

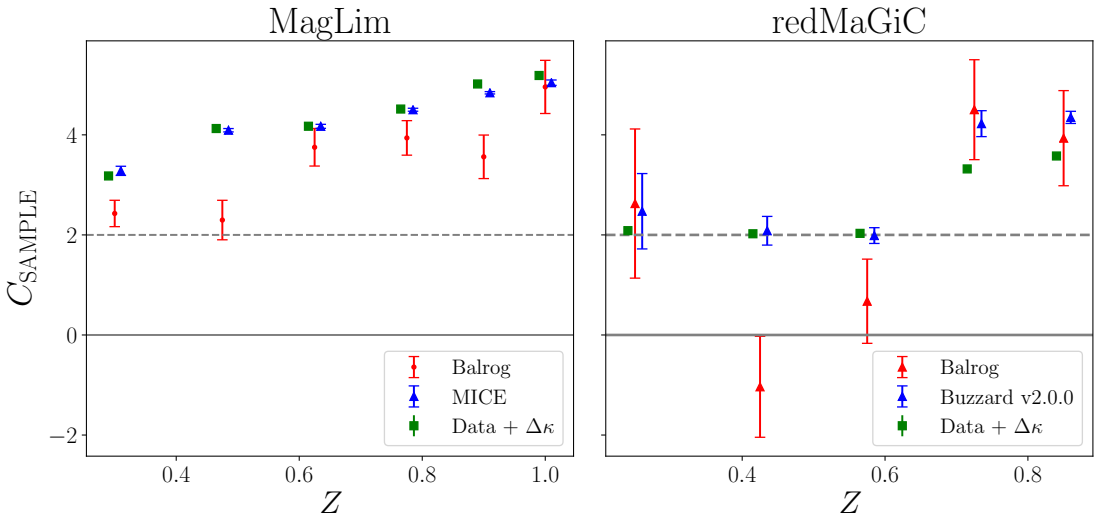

Figure 6.6: The estimated $C_{\rm sample}$ values for each lens sample derived from `Balrog`, a simple flux gradient measurement, and N-Body simulations (MICE for MagLim and Buzzard for redMaGiC). The solid black line corresponds to a zero magnification bias from the sample itself, while the dashed line represents a net zero magnification factor as $C_{\rm area} = -2$. Error bars are the corresponding 1σ statistical uncertainties of each method only. Preliminary result from [181].

largest impact on the galaxy-galaxy lensing signal of high-redshift source galaxies about the lens galaxies in the highest redshift lens bins. In the cosmological analysis, three priors for $C_{\rm sample}$ were tested: a flat prior from -4 to 12, a Gaussian prior centered at the `Balrog` estimate with size determined by the uncertainty estimate in Equation (6.26), and a "fixed" prior of a delta function at the measured `Balrog` values. The use of a flat prior slightly degraded the inferred cosmological constraints, but there was negligible difference between using a Gaussian and fixed prior; a fixed prior was recommended for the fiducial 3×2pt analysis.

While the cosmological constraints on the data are shown to be robust to choices of priors on $C_{\rm sample}$, the marginalized posterior constraints on $C_{\rm sample}$ when using a flat prior (i.e. letting the data inform the magnification bias instead of the above calibration) can be significantly different than than any of the three estimates described here – especially for the third MagLim redshift bin. Given

the good agreement in C_{sample} estimates for this bin between the different methods, this seems to suggest an unknown systematic in the data vector that is at least partially degenerate with the magnification signal. This is discussed in much greater detail in [214].

6.3 Noise from Undetected Sources

The cosmological constraining power from galaxy surveys is intrinsically tied to the precision of the photometric measurements of its sources and thus is sensitive to how well we can model the noise properties of the images where the measurements are made – particularly for weak lensing measurements. This is typically dominated by detector effects (discussed in Section 3.2.1), nuisance signals like cosmic rays or satellite trails that are masked or interpolated over, or by the Poissonian shot noise of the arriving photons from each source and the sky background. However, there are additional sources of noise that are less commonly accounted for.

One such contribution is from undetected sources (US) below the flux limit of the survey that add noise far above the mean background flux. While [215] found that the estimated impact of US on the shear bias of the IM3SHAPE estimator [216] would be below the statistical uncertainty of the DES Y1 weak lensing analysis [60], it will become an increasingly important effect for upcoming analyses, including Y3 and Y6, as the statistical errors shrink with far more source measurements. For a recent example, [217] estimates that US down to magnitudes of $\sim$ 28 will need to be considered for sufficient calibration of the shear bias for multiple methods in Euclid – including the combination of `SExtractor` with PSFEx that was used in Y1.

The remainder of this section summarizes the discovery of significant contribu-

tions by undetected sources in DES Y3 images to the measured variance of galaxy moments by the Bayesian Fourier Domain (BFD; [80], Section 2.3.4) method using a modified version of the new `Balrog` pipeline as first presented in [193]. In addition to computing a correction to the BFD covariance matrix to account for this effect, this work finds that the background sky noise in riz DES images is currently overestimated and is correlated with the local number density.

6.3.1 Review of Bayesian Fourier Domain

As introduced in Section 2.3.4, BFD is a principled, Bayesian shape measurement algorithm with estimated multiplicative shear bias of order $\sim 2 \times 10^{-3}$ in simple simulations for isolated galaxies [80, 81]. Rather than providing point-estimates for galaxy shapes, BFD estimates the shear directly from the images by comparing a set of chosen "moments" of the galaxy image in Fourier space to the corresponding moments of an unsheared prior population of (effectively) noiseless template galaxies. This removes the need for generative image simulations to calibrate shear bias. The galaxy moments are measured after accounting for the local PSF so that the mean result is, in principle, independent of the seeing. The seven BFD moments considered in [193] are defined to be:

$$M \equiv \begin{pmatrix} M_F \\ M_X \\ M_Y \\ M_R \\ M_1 \\ M_2 \\ M_C \end{pmatrix} = \int d^2\boldsymbol{k} \frac{\widetilde{I}(\boldsymbol{k})}{\widetilde{T}(\boldsymbol{k})} W(\boldsymbol{k}^2) F(\boldsymbol{k}); \quad F = \begin{pmatrix} 1 \\ k_x \\ k_y \\ k_x^2 + k_y^2 \\ k_x^2 - k_y^2 \\ 2k_x k_y \\ \left(k_x^2 + k_y^2\right)^2 \end{pmatrix}, \tag{6.29}$$

where $\widetilde{I}(k)$ is the Fourier transform of the galaxy image, $\widetilde{T}$ is the Fourier transform of the PSF, and $W(k^2)$ is a weight function to account for the finite extent of the

PSF. The M moments roughly correspond to, in order, the zeroth-order object flux M_F, first-order centroid position (M_X, M_Y), the second-order size M_R and shape (M_1, M_2), and a fourth-order concentration M_C. The centroid moments are measured first, with the remaining moments measured about that point. Importantly, the sky background level is assumed to be zero at this measurement stage which effects the estimation of only M_F; we return to this problem and an alternative sky subtraction in Section 6.3.2.

A fundamental assumption of BFD is that the pixel noise in the image cutouts is stationary[7] and that the probability distribution of the measured Fourier moments about their true value is a multivariate Gaussian with covariance given by

$$\Sigma_M^{ij} = \int d^2\boldsymbol{k} P_n(\boldsymbol{k}) \left| \frac{W(\boldsymbol{k}^2)}{\widetilde{T}(\boldsymbol{k})} \right|^2 F_i(\boldsymbol{k}) F_j(\boldsymbol{k}), \tag{6.30}$$

where $P_n(\boldsymbol{k})$ is the power spectrum of the noise. This assumption is valid for sky background and detector read noise but not for sources with significant shot noise – though these bright sources are rarely the objects of interest for weak lensing studies. We will find that one part of the noise contribution from US is stationary whose correction can simply be added to Σ_M, while another aspect is not. This is discussed further in Section 6.3.4.

6.3.2 Noise Tests with `Balrog`

Up until now, BFD shear estimates have been validated only against simulated data where the noise was constructed to be Gaussian and stationary. `Balrog` offers an ideal setting to test these assumptions in the presence of realistic image effects. The first test that was considered was to measure the *pull* distribution of each

[7]Meaning uniformly distributed in time and space.

moment, where the pull of an individual object is defined to be

$$\chi_M = \frac{M_D - M_T}{\sigma_M}, \tag{6.31}$$

where M_D and M_T are the measured and true BFD moment respectively with noise estimate σ_M. If the noise estimate from BFD is accurate, than we would expect the pull distribution to be Gaussian distributed with mean $\mu = 0$ and standard deviation $\sigma = 1$. A measured σ greater than one would indicate that the noise is being underestimated, while the opposite would be true for $\sigma < 1$. A similar test is to examine the distribution of χ^2_M which would follow a cumulative χ^2 distribution function (CDF) with one free parameter if the noise is well-modelled. For N moments, this can be generalized to

$$\chi^2_M = (\boldsymbol{M_D} - \boldsymbol{M_T})^T \Sigma_M^{-1} (\boldsymbol{M_D} - \boldsymbol{M_T}). \tag{6.32}$$

We ran 48 randomly-selected Y3 tiles of low-density `Balrog` with a limited set of measurement codes, including BFD, before the fiducial cosmology runs started to provide a sample to make the described measurements. The injection catalog was an early version of the one used in Chapter 4 and described in [173]. While this catalog had less validated object masking and photometric calibration, the resulting changes were small enough that they should not impact the conclusions of this work. These tests were made on a sample of recovered `Balrog` objects whose measured S/N was between 3-20 and had no detected neighbors within $5''$. This resulted in a sample of $\sim 300,000$ injections across all 48 tiles.

The results for four i band moments (first-order flux and third-order size/shape) of the pull distribution test for a single tile is shown in Figure 6.7. The widths of the distributions are generically greater than 1, indicating that the image noise

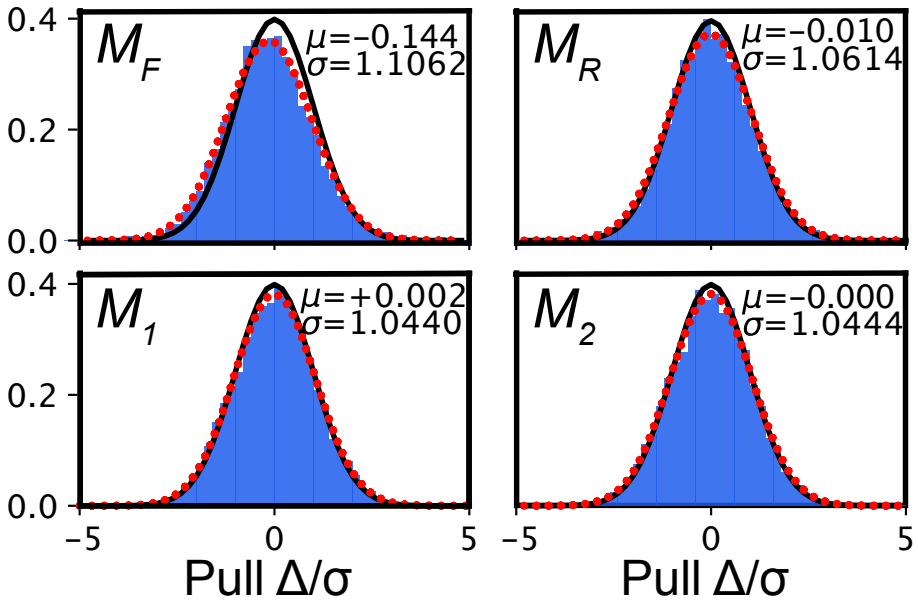

Figure 6.7: Histograms of the i band χ_M moments for the flux M_F, size M_R, and shape $M_{1/2}$ for the `Balrog` tile DES0332-3206. The fitted Gaussian curves are shown in the red dotted line compared to a unit Gaussian in solid black. Each histogram is composed of $\sim 7,000$ detected `Balrog` injections, corresponding to 1σ uncertainties on the mean and standard deviation of ~ 0.01 and ~ 0.008 respectively. Taken from [193].

is underestimated by BFD. This is found across all *griz* bands and tiles, with an overall 6-30% underestimate of the pixel variance. This is most significantly seen in the flux moment M_F but is present in the shape moments as well. Additionally, there is a significant (and unexpected) mean offset in the recovered flux moment of $\approx 0.13\sigma$, corresponding to an over-subtraction of the background noise and thus negative bias in the estimated M_F by BFD. The fitted values across all tiles are shown in Table 6.4.

Similar results were found in the χ^2_M test. In Figure 6.8 we show the CDF of χ^2_M for M_F and $\boldsymbol{M} = [M_F, M_R, M_1, M_2]$ for the same band and tile as Figure 6.7. In each case, the measured χ^2_M distribution is not consistent with a χ^2 distribution of the corresponding degrees of freedom (DOF), with an evident and systematic

moment	g		r		i		z	
	μ	σ	μ	σ	μ	σ	μ	σ
M_F								
shot	0.019	1.127	-0.016	1.136	-0.022	1.113	-0.019	1.098
shot+US	0.016	1.002	-0.015	1.026	-0.020	1.007	-0.018	1.013
M_R								
shot	0.029	1.068	0.017	1.074	-0.000	1.068	-0.003	1.062
shot+US	0.027	1.004	0.016	1.004	-0.000	0.998	-0.003	1.009
M_1								
shot	0.001	1.052	0.003	1.058	-0.002	1.046	-0.003	1.040
shot+US	0.001	1.019	0.003	1.026	-0.002	1.019	-0.003	1.019
M_2								
shot	-0.004	1.041	-0.001	1.055	-0.001	1.047	-0.005	1.030
shot+US	-0.004	1.011	-0.001	1.023	-0.001	1.022	-0.004	1.011

Table 6.4: The mean and standard deviation values for the pull distribution noise test, with "shot" denoting consideration of background Poisson noise and detector read noise only, while "shot+US" includes the measured US noise variance described in Section 6.3.3.

bias.

Further investigation was done to understand the mean offsets of the pull distributions in Figure 6.7. Figure 6.9 shows the fitted μ value for each of the 48 tiles as a function of the object density of the tile. The blue points show the mean μ of the Gaussian fit to the pull distribution of BDF flux moments for each tile as a function of object density where a clear correlation can be seen, particularly for the redder riz bands. This is consistent with the discussion in Section 5.3.1 that proposed a chromatic response in DES object magnitudes due to differences in sky noise and object density between the bands. We suspect that the over-subtraction is due to a combination of (i) residual light from large, bright galaxies, (ii) scattered light from bright stars, and (iii) errors in how `SExtractor` treats the US component of the background. The mean μ offsets from all tiles tiles are $\mu_g = 0.02$, $\mu_r = -0.08$, $\mu_i = -0.135$, and $\mu_z = -0.123$.

A correction for this effect was computed by estimating the local sky back-

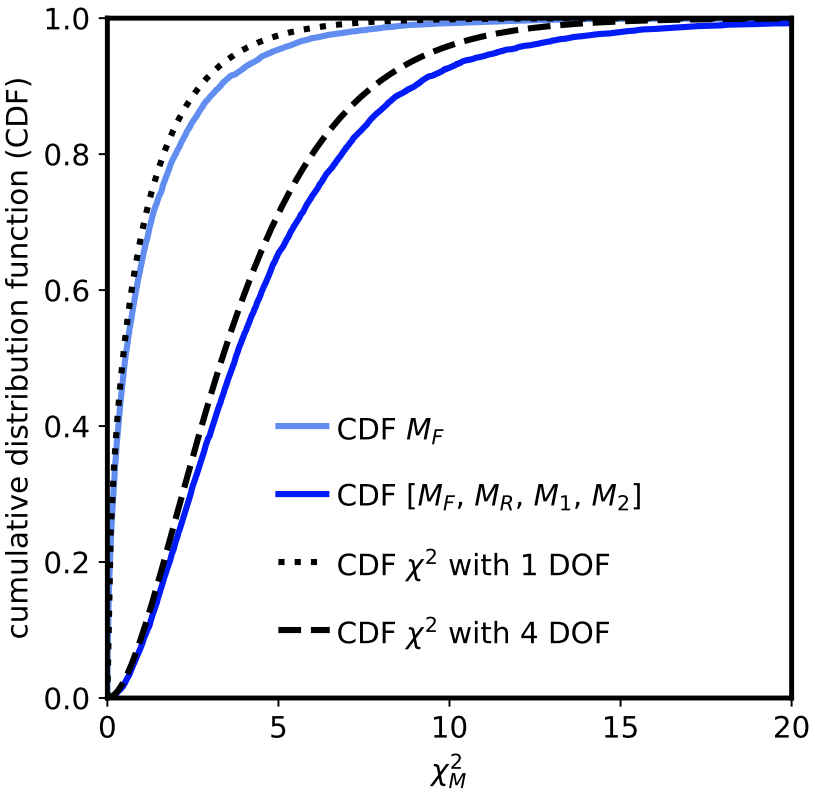

Figure 6.8: The CDF of χ_M for M_F in light blue and $\boldsymbol{M} = [M_F, M_R, M_1, M_2]$ in dark blue, as compared to the nominal χ^2 distributions of $N = 1, 4$ in dashed black lines. We find that $\langle \chi^2_M \rangle$=1.24 and 4.64 for N of 1 and 4 respectively, indicating an inconsistency with the hypothesis that the image noise is purely due to shot noise from the sky background and detector read noise. Taken from [193].

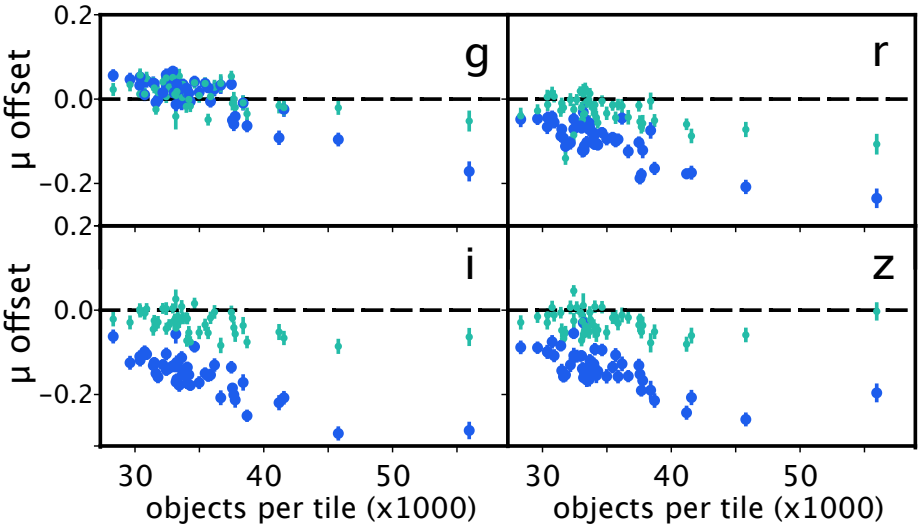

Figure 6.9: The Gaussian mean offset μ in the BFD flux moment pull distribution as a function of object density for the 48 used `Balrog` tiles in blue. The green points show the mean offset for the tiles after a local sky subtraction which mitigates the flux bias. While g band is relatively unaffected, the redder riz bands show statistically significant sky over-subtraction that is correlated with object density. Taken from [193].

ground in each galaxy postage stamp using a 2-pixel-wide window that scanned across the frame boundary. This value is then converted to an offset in the flux moment M_F and its contribution to the uncertainty is computed by subtracting this value from each pixel in the stamp. While this is sufficient for isolated sources, a more sophisticated correction would have to be done in the presence of blended sources. The updated flux moments are shown as the green points in Figure 6.9 and have values of $\mu_g = 0.019$, $\mu_r = -0.023,$, $\mu_i = -0.022,$, and $\mu_z = -0.025$. While this process contributes additional uncertainty to the M_F measurement, it reduces the mean sky error from 10-20% of the sky noise to only $\sim 2\%$.

6.3.3 Empty Sky Cross Power Spectra

In order to determine if the excess noise was due to US, a slight variant on the `Balrog` injection procedure was followed in which we injected zero-flux objects into 39 tiles at random positions and then made cutout postage stamps[8] of these random patches of sky. Stamps that had any overlap with detected sources as determined by the `SExtractor` segmentation map were discarded. The cross-power spectra of distinct exposures of the "ghost" injections in *griz* were then computed and averaged over each tile, which would yield zero signal if the noise is only Poisson or read noise as they cancel on average. This procedure isolates the contributions from US.

The 2D average of the cross-power spectra for a single tile is shown in the top panel of Figure 6.10. A clear detection of US noise is made in each band. To test that this signal is not an unaccounted for detector artifact, a similar measurement of the cross-spectra is made across *distinct* regions which is shown in the bottom panel of the figure. No signal is present, confirming an unaccounted for contribution that is localized to the position of each "ghost" injection.

This cross-spectra measurement clearly demonstrates the presence of US in the noise properties of the images but is inappropriate for computation of the BFD US-correction covariance matrix as it does not include corrections due to the PSF and small pixel shifts between the images. Instead, [193] measured the BFD moments of these empty patches directly. This empirical approach allows computed BFD moments to calibrate the moment covariance matrix on the survey images rather than relying on simulations of unknown fidelity, and naturally includes the contribution by US as a source of noise within the Bayesian calculation. The updated σ values for the χ_M test after this correction are compared to the original

[8] Of size 32×32 pixels, which is the minimum for DES object stamps.

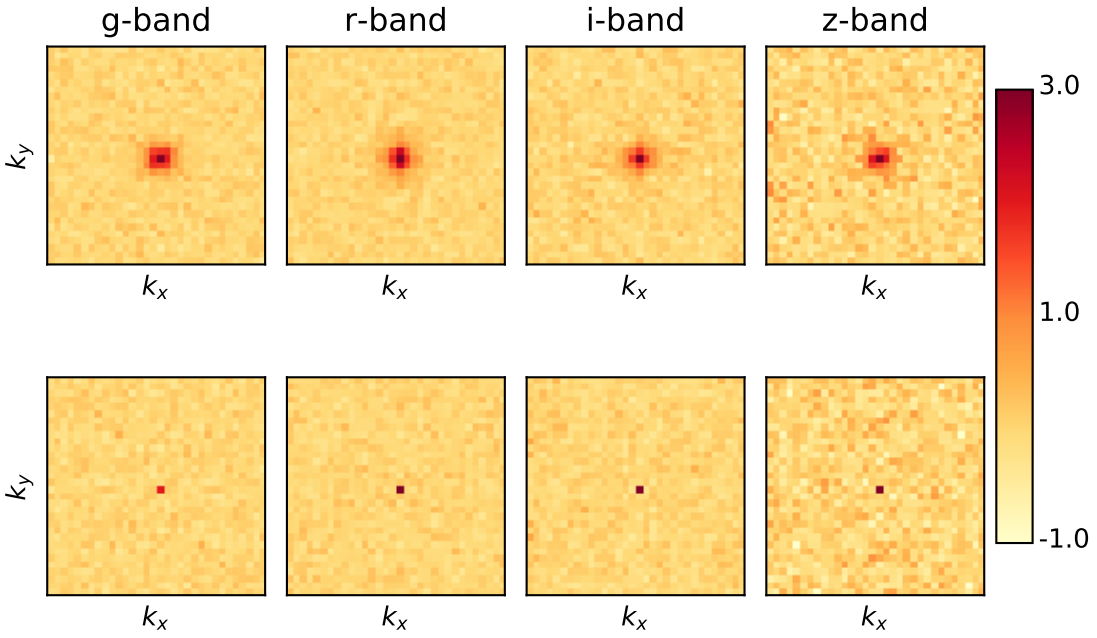

Figure 6.10: Top panel: The average of the 2D cross-spectra of all `Balrog` "ghost" injection cutouts across a single tile, normalized to the 99th percentile power in each band. As this measurement is made across many exposures, the sky background and detector read noise contributions cancel while the signal from US remains. Bottom panel: The same measurement as above, but for the cross-spectra of *distinct* regions of the tile. As expected, the signal from US vanishes. The residual value at $k = 0$ is due to the background estimation error discussed in Section 6.3.2. Taken from [193].

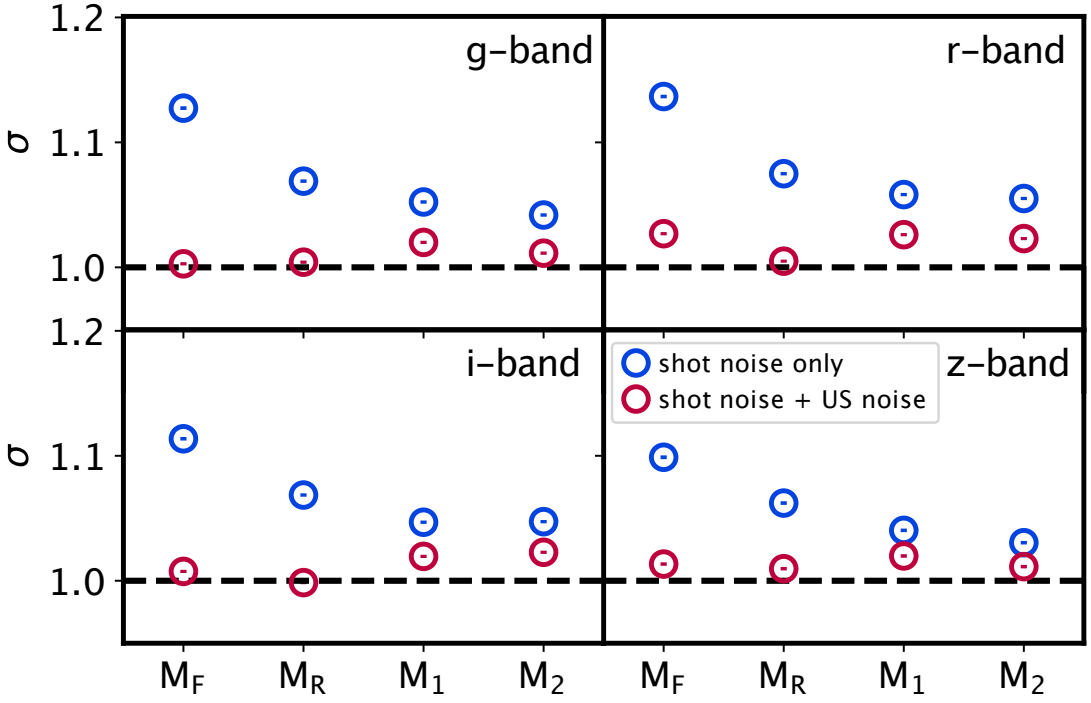

Figure 6.11: The fitted σ value of the χ_M distribution for four BFD moments using shot noise only in blue and with the US correction in red. These values come from measurements across all 48 `Balrog` tiles. The US correction leads to a far more consistent fit with the expected value of $\sigma = 1$. Taken from [193].

measurements in Figure 6.11.

6.3.4 Discussion of Results

Using `Balrog` for a suite of image tests of BFD measurements, [193] showed that US constitute a significant noise contribution to DES Y3 images; up to a $\sim$ 30% increase in variance for the flux moment. In addition, a clear over-subtraction of the sky background is detected in the *riz* bands which is consistent with the findings from Chapter 4. A variant of `Balrog` that injects "ghost" galaxies with zero flux was then used to grab randomly-selected patches of the single-epoch images from which a cross-spectra measurement confirmed the existence of US and formed the basis of a correction to the BFD covariance matrix. This

correction leads to a far more accurate estimation of image noise, as demonstrated in Figure 6.11.

While the measured noise due to undetected sources by `Balrog` is stationary by construction due to the uniform hexagonal lattice of injection positions (and thus uniformly distributed with respect to the detection population), this is not true in general. Galaxies tend to cluster around other bright galaxies, leading to two associated effects: (i) random projection US at different redshifts, and (ii) physically associated US at the same redshift. The first is captured by the presented measurement with `Balrog`, though it ignored secondary effects such as the extinction of US by the foreground objects and magnification bias. The second effect results in an excess of US around detections and breaks the assumption of stationarity. While [217] demonstrated that this can have a significant impact on the shear biases of photometric methods that are based on shape measurements, BFD naturally accounts for this effect as long as the template galaxy population is clustered in the same way as the target population. Thus no additional correction is in principle necessary, but this should be validated with further studies.

6.4 Photometric Response near Galaxy Clusters

Clusters of galaxies – especially rich, crowded clusters – are known to present additional obstacles in the accurate detection and characterization of cluster members. These member galaxies often have higher detection incompleteness and significant photometric biases because of the increased rate of proximity effects. Detected sources in or near galaxy clusters in the sky can be further biased because of blending with member galaxies or contamination from intra-cluster light [218]. To aid in studies of these difficult measurement biases and selection effects, a high-density `Balrog` run was performed targeting areas near rich galaxy clusters.

A sample of 900 tiles, each containing a galaxy cluster with optical richness[9] $\lambda > 35$, were injected with a similar DF galaxy sample as used in `y3-merged` at a lattice separation of $10''$ resulting in four times the injection density of the main cosmology runs. This higher injection density was needed to properly sample the effects of clusters on the transfer function as a function of radius from a cluster center given the number of tiles used[10]. Additionally, we used a more restrictive *riz* detection magnitude of 23 to increase the fraction of detected objects for this analysis.

The magnitude responses of the injected galaxies were measured as well as their distances to the center of the nearby clusters. The sample was further subdivided by the host cluster's richness, the measured object size `cm_T`, and the magnitude of the cluster's brightest cluster galaxy (BCG) to see how these parameters affect the magnitude bias of the added objects. Preliminary results of this analysis for clusters in a redshift range from 0.2 to 0.3 are shown in Figure 6.12. Unsurprisingly, the magnitude responses become more negatively biased closer to cluster centers where the complex environments make accurate photometric measurements difficult and faint sources are up-scattered by the abundant residual light. As the injections approach the center of a cluster, the median bias becomes increasingly negative indicating that the objects are measured to be progressively brighter than injected truth the closer they are to the BCG. Of the three properties examined, the measured object size appears to have the strongest influence over magnitude bias among the three quantities, though richer clusters also show larger $\Delta\mathrm{mag}_{\mathrm{DF}}$ responses. This preliminary result will be followed up in Masegian & Zhang et al. (in preparation) including a careful study of the detection efficiency

[9] See [129] for a description of the cluster mass-proxy richness and the DES cluster catalog.

[10] While this increases the probability of unwanted proximity effects from other `Balrog` injections, we estimate that the chances of two neighboring injections with `bdf_T` > 10 (or $\sim 3.3''$) in this run to be less than 0.25%.

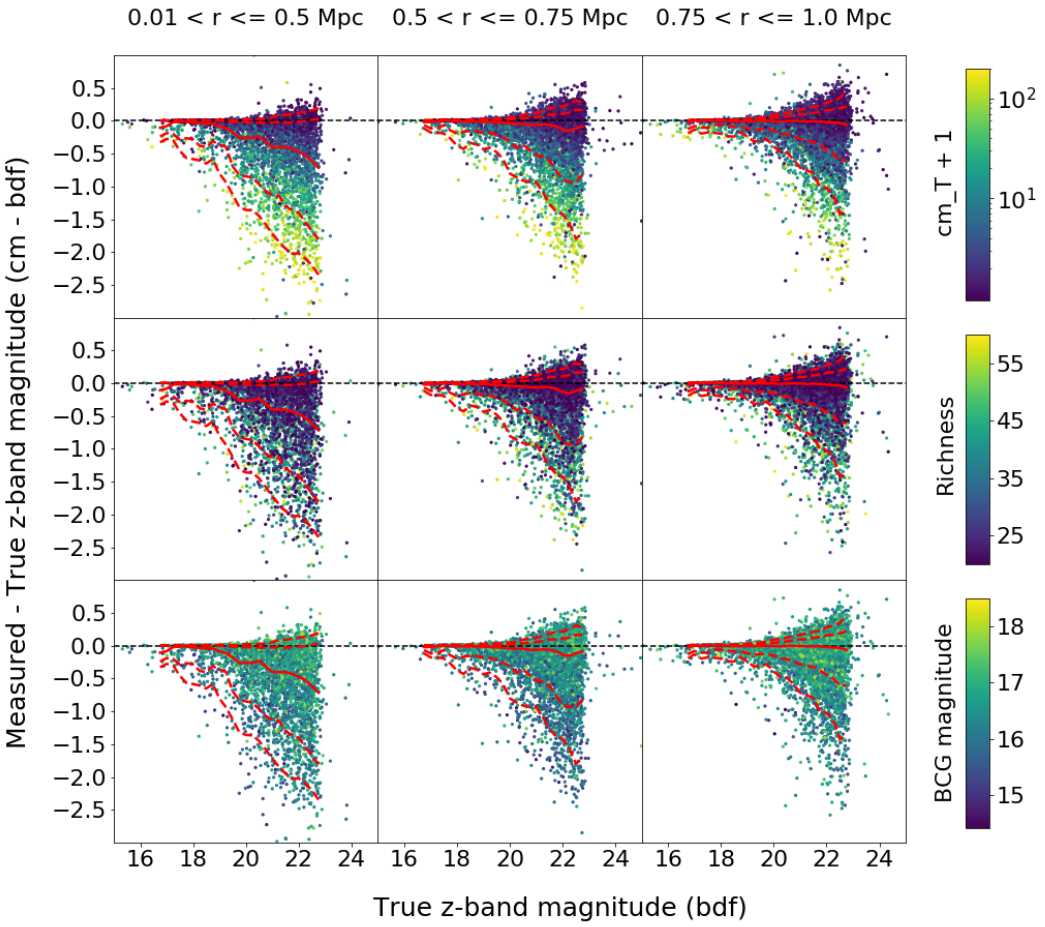

Figure 6.12: The difference in measured z band magnitude vs. the injected DF magnitude as a function of input magnitude for the high-density `clusters` run in a redshift range of 0.2 to 0.3. The three columns present the magnitude responses binned by their radial distances to nearby cluster centers as specified at the top of the columns. The three rows show the response bias colored by the measured object size `cm_T`, cluster richness λ, and the cluster BCG magnitude. The median response biases across the range of the injected magnitudes are displayed as solid red lines, with the first and second σ contours indicated by the dashed lines above and below. Taken from [150].

as a function of various parameters including radial distance.

We find a similar correlation between an object's measured size and magnitude response as seen in Section 5.3.3. The proximity effects that cause asymmetric overestimates of `cm_T` are amplified in the very crowded cluster environments, a trend that grows even stronger closer to the cluster centers. Correlation between magnitude bias and the other examined parameters, cluster richness and the BCG magnitude, is weaker but still present – particularly for richness. All correlations appear to bias the recovered magnitudes in the same direction and the scale of these effects increases as the injections approach cluster centers. Taken together, the proximity to cluster centers, cluster richness, and BCG brightness artificially increases the number of observed objects near clusters above a fixed brightness threshold which, in turn, can collectively bias cluster measurements from a corresponding increase in cluster member galaxies. We plan on accounting for these correlations in future DES cluster analyses.

Chapter 7

Conclusion

In this dissertation, we have presented the suite of DES Y3 `Balrog` simulations and resulting object catalogs used in downstream Y3 analyses. Like its Y1 predecessor, this current iteration of `Balrog` directly samples the DES transfer function by injecting an ensemble of realistic sources into real survey images to make precise measurements of the inherited systematic biases in the photometric response. However, the updated methodology (and entirely new coding framework) for Y3 `Balrog` makes significant strides beyond [17] in replicating many of the more complex features of the DESDM pipeline including the coaddition of single-epoch images and multi-epoch photometric measurements from SOF and Metacalibration in order to probe more aspects of the true measurement likelihood. In addition, we used a more realistic input sample based on the DES DF source catalog with observations using DECam filters which eliminated the need for template fitting to COSMOS galaxies and incorporated more cosmic variance in object properties. We also implemented a novel ambiguous matching scheme to capture many of the impacts of source blending while largely eliminating the contributions from undesired dropouts that happened to land on top of existing bright sources.

This effort culminated in tens of millions of Monte Carlo samples of the DES transfer function at high fidelity across 20% of the full DES footprint to Y3 depth, capturing systematic biases from more variations in observing conditions than any previous `Balrog` analysis. The improved methodology resulted in the injected objects matching Y3 GOLD photometric properties and capturing clustering systematics correlated with survey property maps to better than 1% accuracy for a typical cosmology sample on relevant scales. Additionally, we find that `Balrog` captures the clustering amplitudes of these systematics within a few percent for even *highly* incomplete samples – an encouraging first step for future analyses that wish to leverage more of our hard-earned photons.

We quantified the photometric responses of Balrog injections through the Y3 DESDM measurement pipeline, particularly for magnitudes, colors, and morphology. We find that the magnitudes of most injections are well calibrated until selection effects near the detection threshold become significant, although we have found a clear asymmetric bias for objects in crowded fields or near image artifacts to have moderately to severely overestimated sizes which correlate with large negative magnitude biases. These biases are fairly common for bright, extended objects and can become extremely large (up to $\Delta\mathrm{mag}_{\mathrm{DF}}{\sim}8$) at fainter magnitudes – though they constitute a much larger relative fraction of objects on the bright end. We demonstrated that these catastrophic photometry failures are real effects and often pass science cuts. We plan on exploring the causal relationship of this photometric failure mode further in a future analysis. While these magnitude response biases can cause significant discrepancies from more naive error estimates, fortunately their effect appears to have little impact on the recovered colors where we find typical median response biases of ∼1-3 mmag for stars and ∼5-10 mmag for galaxies in the densest regions of parameter space – an effective median color

calibration offset of less than 1%.

Finally, we discussed a few of the most important applications of the presented `Balrog` catalogs to the Y3 cosmology analysis and other DES science measurements. In particular, we provided a realistic measurement likelihood in the calibration of photometric redshifts of source galaxies to reduce systematic biases in one of the highest sources of uncertainty in the cosmological measurement without contributing any additional uncertainty to the overall error budget. Additionally, the use of modified `Balrog` runs facilitated the measurement of magnification bias on lens samples for more accurate cosmological constraints from galaxy clustering and galaxy-galaxy lensing measurements. Unexpected findings such as the noise contributions from undetected sources in DES images and sky over-subtraction in the *riz*-bands described, in addition to the moderate band-dependence in magnitude response and discovery of a new class of catastrophic photometry failures correlated with measured size, are indicative of the diagnostic power of object injection pipelines like `Balrog` in modern galaxy surveys.

7.1 Current Methodological Limitations and Future Directions

While this latest iteration of `Balrog` has made great advances in its ability to precisely quantify difficult measurement systematics, there remain many challenges to overcome if we are to reach the level of precision required by upcoming Stage IV surveys like LSST where the increased depth, pipeline complexity, and blending rate will otherwise limit the constraining power on cosmological parameters. Some of these challenges, such as properly accounting for per-object chromatic corrections at injection time or pushing the injection step further upstream

in the measurement pipeline to account for more systematic effects in the image calibration, are largely technical barriers that can be addressed with more development time. Our ambiguous matching scheme can be improved by incorporating pixel-level information on the overlap between injected and real sources similar to the blending parameter introduced in [170]. In addition, many of the complexities and additional development time needed for careful emulation of a survey's measurement pipeline can be nearly eliminated by having injection pipelines placed directly in the software stack of the fiducial data processing runs. While this was not possible in DES, this approach is now taken in HSC with `SynPipe` and planned for LSST. However, there are more fundamental barriers in leveraging injection pipelines to their full potential.

A primary challenge is increasing the representativeness of the input catalog. Using the DECam observations of sources in the DES DF as the basis for the input object photometry rectified many of the input sample issues described in [17] – particularly the discrepancy in recovered `Balrog` colors as compared to Y1 GOLD that arose from interpolating the spectral energy distribution (SED) of COSMOS galaxies to match DECam filters. However, Figure 5.2 shows that we have further work to do. While it is difficult to disentangle intrinsic errors in the emulation of the DESDM pipeline from the input sample representativeness, there are some clear avenues for improvement. The conceptually simplest is to sample a wider population of deep objects across more deep patches of sky in order to incorporate greater cosmic variance in the injection sample. However, these deep observations are very expensive which limits the practicality of this approach. It may be possible to combine with external deep datasets, though this comes at the expense of a return to SED interpolations to match DECam filters. In addition, more detailed studies of the difficult PSF modeling in the DF may yield a stellar

population more similar to the WF measurements and resolve some of the largest discrepancies between `Balrog` and Y3 GOLD for bright, PSF-like objects.

Another possibility is that the discrepancies between the recovered WF sample and Y3 GOLD are driven, at least in part, by the inability of CModel profiles to accurately capture the full diversity of galaxy morphologies. True galaxy profiles have many complex features such as spiral arms, star knots, and long asymmetric disruptions from mergers that we are not currently capturing with our DF injections. The most direct solution to this problem is to inject the MEDS image cutouts of the DF sources. We have already built the basic infrastructure to do so with `Balrog`, as described in §A.2, but there are new issues to consider. The image cutouts can include artifacts, excessive masking, truncated profiles of nearby objects, or even be blended with other sources. This may be rectified in the future by using machine learning methods such as non-negative matrix factorization or generative adversarial networks to handle the required pixel-level deblending of sources in the stamps (see [219] and [220] for examples respectively).

However, using the image cutouts directly would introduce undesired noise when injecting into single-epoch exposures that had better seeing conditions than the composite PSF of the single-chip DF coadd and remains an unresolved issue. In addition, precisely defining the "truth" properties of the stamps is less straightforward than for model fit injections. This will likely be handled by making accurate measurements of each relevant WF photometry type on the stamps which would eliminate inheriting non-physical parameter biases from small profile definition differences such as the resulting magnitude bias from differences in `fracdev` prior shown in Figure 4.3.

The most difficult challenge to overcome is the high computational cost of injection pipelines. The new single-epoch processing and additional photometric

measurements in Y3 `Balrog` has increased the total mean CPU time per recovered injection to ∼80 seconds; about 12 times greater than in [17]. This large increase in runtime is only at Y3 depth corresponding to ∼4-6 epochs per injection and made it unfeasible to directly calibrate many of the other key aspects of the Y3 cosmological analysis for which `Balrog` would otherwise be the ideal measurement tool. For example, to achieve the equivalent statistical precision on how the blending of galaxies at different redshifts effects the multiplicative shear bias as measured in [65], we estimate that we would have to run the equivalent of over a dozen `y3-merged` samples to sufficiently capture how an identical injection population responds to an input shear signal that varies with redshift. In addition, the original goal of using `Balrog` to directly calibrate the spatially-dependent measurement biases and completeness inhomogeneities in the galaxy clustering measurement as outlined in [17] would require many more injections than sources for the estimation of the angular correlation function; a daunting prospect in light of the ∼40% Y3 density achieved in this analysis. The situation will become significantly worse for much deeper surveys like LSST where we can expect hundreds of exposures for each object.

Perhaps even more consequential than the low number density realistically achievable, the high cost of running `Balrog` led to only a single injection realization across just 20% of the total footprint area. This limited the calibrations from `Balrog` in Y3 to either be based on mean measurements, such as those described in Chapter 6, or required a reduction in the considered footprint such as the clustering measurement presented in Section 5.1.4. While even the relatively low sampling of `y3-merged` was sufficient to capture systematics variations in the clustering amplitude to better than 1% for a MagLim-like sample in the overlap area, reaching this threshold (or beyond) for highly incomplete samples or for

accurate calibrations of large-scale fluctuations may require orders of magnitude more injections. Despite an expected significant increase in the total tiles sampled for Y6, achieving the many realizations of full footprint coverage required for the most ambitious `Balrog` measurements, such as providing realistic random properties for clustering and shear two-point measurements, will likely remain impractical without a dramatic increase in computational investment.

One promising solution that we plan to explore is the use of the `Balrog` samples as a training set for an emulator that predicts additional realizations conditional on the survey property maps. A somewhat similar approach is taken in [221] where they mitigate galaxy clustering systematics by producing "organized" random catalogs with fluctuations in number density imprinted from a SOM approach that trained on maps of the variations in KiDS observing properties. Using an injection catalog like `Balrog` directly as a training sample for this approach would leverage our very high fidelity measurements of the survey transfer function to include unknown systematics not fully captured by the identified survey properties. While still more computationally expensive than a machine learning-only approach, this will allow us to build an efficient way of creating accurate random samples tuned for the desired measurement without increasing the total survey pipeline computational cost by more than a factor of two. We plan to use the presented `Balrog` catalogs to gauge the accuracy and feasibility of this approach in an upcoming analysis.

This dissertation only scratches the surface in cosmological calibration potential and the identification of new systematics with injection pipelines such as `Balrog`. In particular, the combination of direct Monte Carlo sampling of the transfer function with an emulator to boost the total statistical power has the potential to facilitate many of the most difficult measurements in modern galaxy

surveys and lead us ever closer to a new era of accurate cosmology. It is clear that we have yet to dig too deep.

Appendix A

Injection Software

Here we describe a few of the most relevant configuration options when running the new injection framework introduced in Section 4.2.2, as well as templates for custom injection classes defined by the user for more advanced pipeline interfacing; see the code repository[1] for more details on running the simulations.

A.1 Injection Configuration

Configuration settings specific to a typical `Balrog` run have been wrapped into custom `GalSim` `image` and `stamp` types, both called `Balrog`:

- **`image: Balrog`** - This image type is required for a full `Balrog` run. It parses all novel configuration entries and defines how to add `GalSim` objects to an existing image with consistent noise properties. It also allows the `Balrog` framework to be run on blank images for testing.
- **`stamp: Balrog`** - An optional stamp type that allows `GalSim` to skip objects whose fast Fourier transform (FFT) grid sizes are extremely large and

[1] https://github.com/sweverett/Balrog-GalSim

can occasionally cause memory errors when using photometric model fits to DES DF objects.

We also provide a much simpler `image` class called `AddOn` which adds any simulated images onto an initial image without the full `Balrog` machinery. Some configuration details can also be set on the command-line call to `balrog_injection.py` for ease of use as long as they do not conflict with any settings in the configuration file.

A.2 Input Sample and Object Profiles

In principle any native `GalSim` input and object type can be used for injection. However, the object sampling, truth property updating, and truth catalog generation steps require knowledge about underlying structure of the input data (e.g. parametric models vs. image cutouts). We handle this ambiguity through the use of `BalInput` and `BalObject` parent classes that define the necessary implementation details to connect `GalSim` to `Balrog`. These classes can be used to register any needed injection types to `Balrog` including custom `GalSim` classes. Subclasses provided for injection types used in DES Y3 runs are described below:

- **`ngmixGalaxy`**: Described in Section 4.2.2. A sum of `GalSim Gaussian` objects that represent a Gaussian mixture model fit to a source by the measurement software `ngmix`. `Balrog` can currently inject the following `ngmix` profile model types: a single Gaussian (`gauss`), a composite model (`cm`) that combines an exponential disk with a de Vaucouleurs' profile, and a modified CModel with fixed size ratio between the two components (`bdf`). As `ngmix` allows for objects with negative size before convolution with a PSF, these

negative values are clipped to a small non-zero value (`T`=10^{-6}, corresponding to a size scale of $\sim 10^{-3}$ arcsec) to avoid rendering failures.

- **`DESStar`**: A synthetic star sample with realistic density and property distributions across the DES footprint was created to a depth of 27 magnitude in g. These objects are treated as delta functions convolved with the local PSF. These magnitudes are referenced as δ-mag in Chapter 5. Further details about this star catalog are described in Section 4.3.2.

- **`MEDSGalaxy`**: Single-epoch image cutouts of detected DES objects are stored in MEDS files for each band. These image cutouts can be used directly for injection after deconvolving with the original PSF solution and re-convolving with the local injection PSF.

`Balrog` can inject multiple object types in the same run by setting the `gal` field in the configuration as a `List` type; this is identical to `GalSim` configuration behaviour. The relative fraction of each injection type is then set in the `pos_sampling` field described below.

A.3 Updating Truth Properties and Optional Transformations

Most `Balrog` runs sample objects from an existing catalog. Some of the object properties are modified to fit the needs of the simulation such as the positions, orientations, and fluxes. Updates to positions and orientations are automatically applied to the output truth catalogs while flux corrections due to local extinction and zeropoint offsets are not, though we save the applied extinction factor.

Different behaviour for these quantities as well as any additional changes can be defined when creating the relevant `BalObject` subclass.

Position sampling is determined by the configuration parameter `pos_sampling` and can be set to `Uniform` for spherical random sampling or one of the following grid choices that are regularly-spaced in image space: `RectGrid` for a rectangular lattice, `HexGrid` for a hexagonal lattice, and `MixedGrid` for one of the previous grid choices that mixes multiple injection object types on the same grid with a set relative abundance `inj_frac`. The user has control over the grid spacing as well as whether to apply random translations and/or rotations of the grid for each tile in addition to random rotations of the object profiles themselves with `rotate_objs`.

In addition to flux scaling to match the zeropoint of each image, an additional extinction factor can be applied with the configuration option `extinct_objs`. If set, extinction factors in *griz* for each tile are loaded and applied to object fluxes. Incorporating more sophisticated per-object, SED-dependent extinction implementations based on the maps provided in [177] is planned for a future code release but are currently applied at the tile level. Any of the native `GalSim` noise models can be added to the injection stamps with the Poisson component ignoring the existing image pixel values as long as the `Balrog` (or `AddOn`) image type is used. Optional transformations such as a constant shear or magnification factor that are uniform across a tile can be added in the injection configuration with the same syntax as a typical `GalSim` configuration, while per-object effects need to be implemented into the relevant `BalObject` subclass.

A.4 Configuration Example

Here we show the high-level configuration settings used for `Balrog Run2` and `Run2a`, where capitalized quantities in {} refer to local file paths:

```
modules:
  - galsim.des,
  - injector,
  - ngmix_catalog,
  - des_star_catalog

input:
  des_star_catalog:
    base_dir: {INPUT_DIR}
    data_version: y3v02
    model_type: Model_16.5-26.5

  ngmix_catalog:
    catalog_type: bdf
    de_redden: True
    dir: {INPUT_DIR}
    file_name: {INPUT_FILENAME}
    t_max: 100

gal:
  type: List
  items:
  - # y3-merged DF injection
    type: ngmixGalaxy
  - # y3-stars delta-injection
    type: desStar

psf:
  type: DES_PSFEx

stamp:
  draw_method: no_pixel
  gsparams:
    maximum_fft_size: 16384
  type: Balrog

image:
  bands: griz
  extinct_objs: True
```

```
rotate_objs: True
n_realizations: 1
noise: {} # Turn on Poisson noise
nproc: 16
pos_sampling:
  des_star_catalog:
      type: MixedGrid
      inj_frac: 0.1
  ngmix_catalog
      type: MixedGrid
      grid_spacing: 20
      grid_type: HexGrid
      inj_frac: 0.9
      offset: Random
      rotate: Random
random_seed: {SEED}
run_name: {Run2/Run2a}
type: Balrog
version: y3v02
wcs:
  type: Fits
xsize: 2048
ysize: 4096
```

Appendix B

Angular Clustering Systematics

Section 5.1.4 introduced a method for translating the differences between the `Balrog` and Y3 GOLD catalogs into a predicted systematic error in the angular clustering of galaxies. We first choose a sample selection which is applied to both catalogs. We then measure the dependence of galaxy counts fluctuations in both selected `Balrog` and Y3 GOLD samples on several measured image quality indicators, as in Figure 5.3. Finally, for each data quality indicator, we interpolate the density fluctuation trends to the full survey area and estimate the angular clustering that these trends imply. As small systematic variations in the survey depth enter, to leading order, as additive power in the measured clustering signal, a comparison of the power we measure in these interpolated maps offers a direct estimate of the importance of any deviation between our injection catalogs and the real data.

Here we show the same maps as Figure 5.4 for six measured survey properties in all bands, for the $17.5 < i < 12.5$ sample selection meant to emulate the Y3 MagLim sample. With the exception of a negligible spike in power in a few of the `SIGMA_MAG_ZERO` maps, the measured systematic errors are less than 1% of the fiducial galaxy clustering signal (calculated as described in Figure 5.3) on scales below approximately 1° ($\ell > 180$).

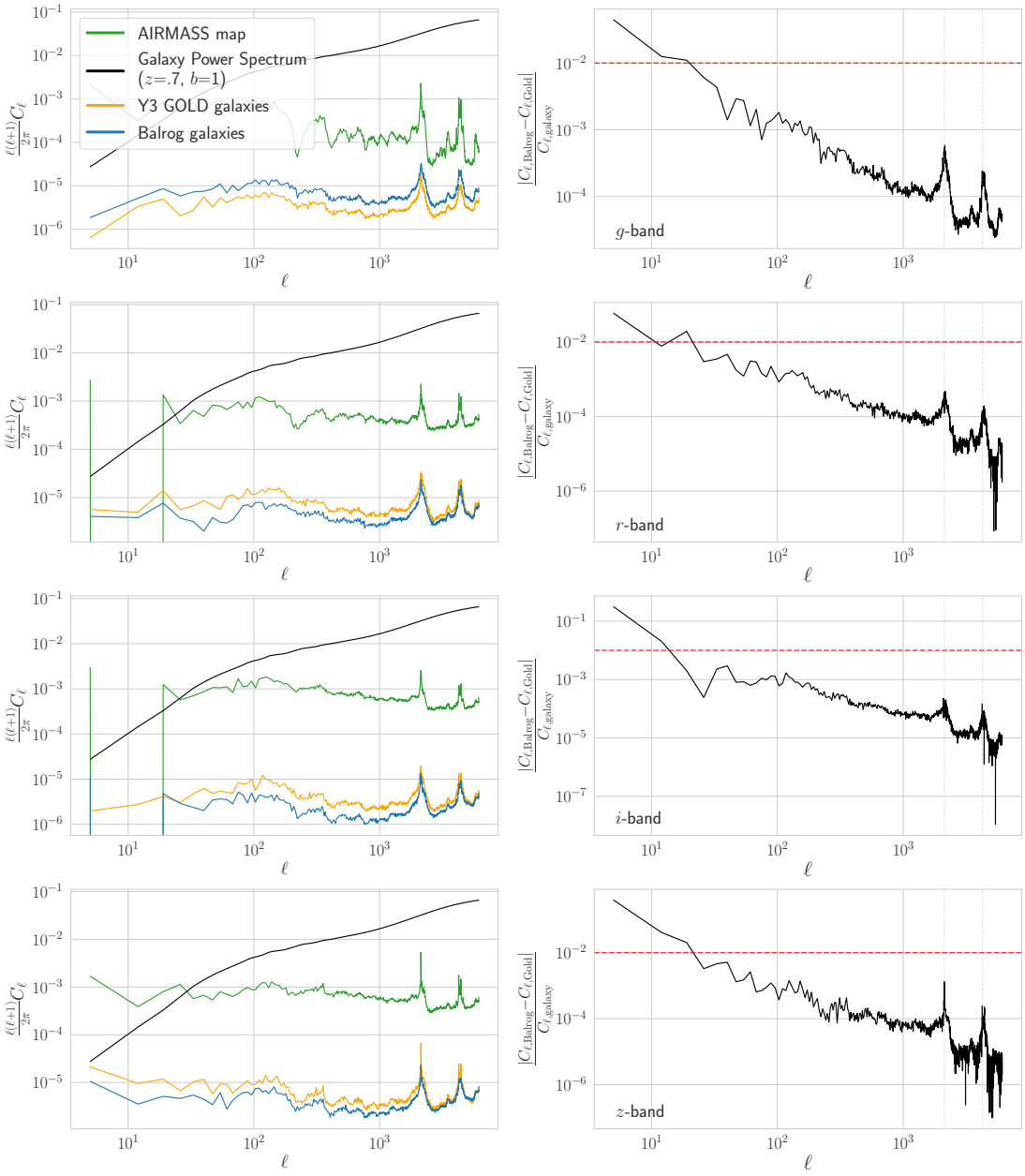

Figure B.1: Power spectra of the mean airmass, and associated interpolated `Balrog` and Y3 GOLD galaxy count variations, as in Figure 5.4. The left panels show the angular power spectrum of the noted survey property (in green) and the corresponding power spectra of the number densities of the `Balrog` (in blue) and Y3 GOLD (in gold) MagLim-like galaxies across the Y3 footprint. The reference galaxy power spectrum in black represents a typical cosmological signal at $z = 0.7$ with linear galaxy bias parameter of 1. The right panels show the difference in power between Y3 GOLD and `Balrog` as a fraction of the fiducial cosmological power spectrum shown on the left.

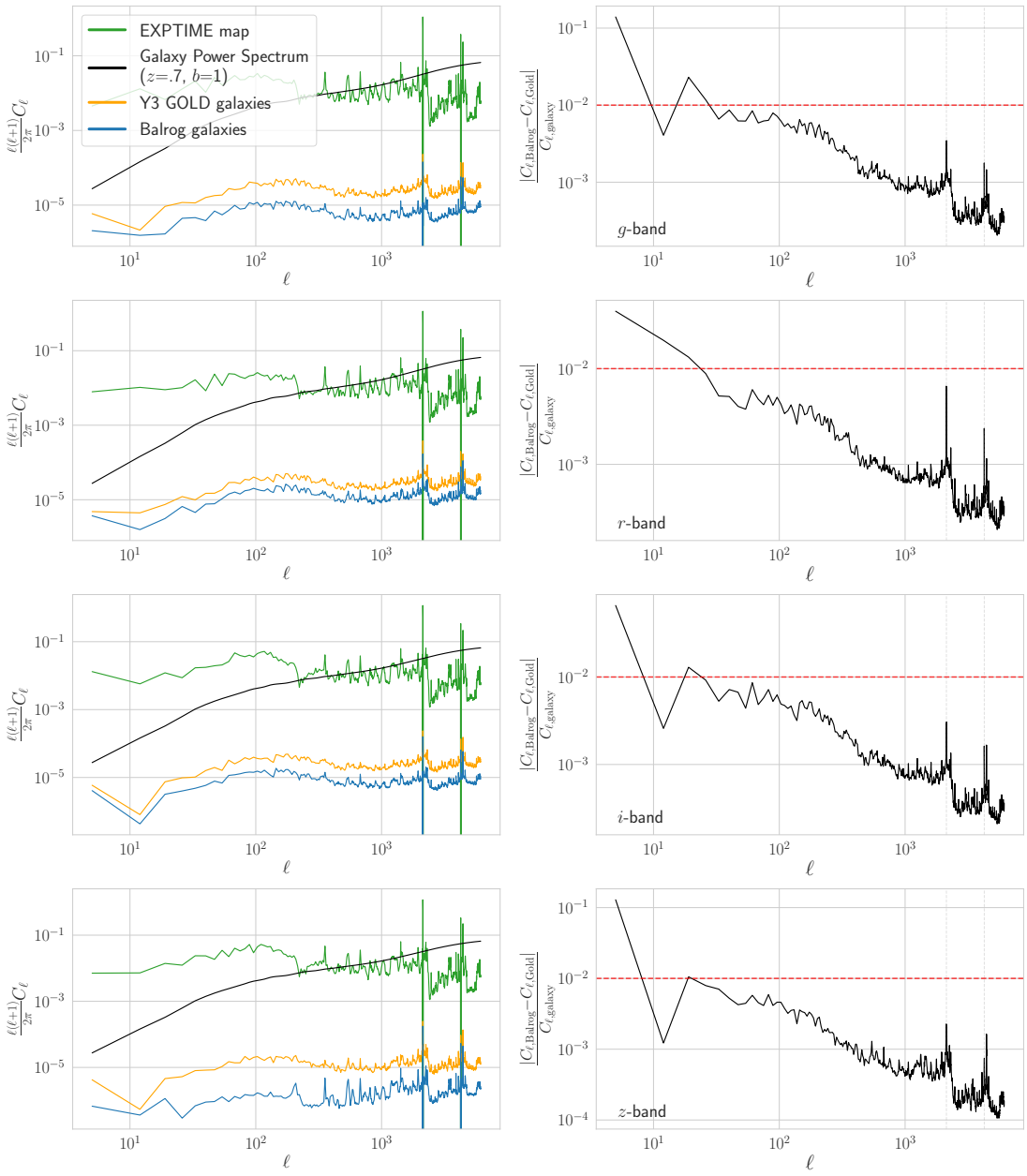

Figure B.2: Power spectra of the mean exposure time, and associated interpolated `Balrog` and Y3 GOLD galaxy count variations, as in Figure 5.4. The left panels show the angular power spectrum of the noted survey property (in green) and the corresponding power spectra of the number densities of the `Balrog` (in blue) and Y3 GOLD (in gold) MagLim-like galaxies across the Y3 footprint. The reference galaxy power spectrum in black represents a typical cosmological signal at $z = 0.7$ with linear galaxy bias parameter of 1. The right panels show the difference in power between Y3 GOLD and `Balrog` as a fraction of the fiducial cosmological power spectrum shown on the left.

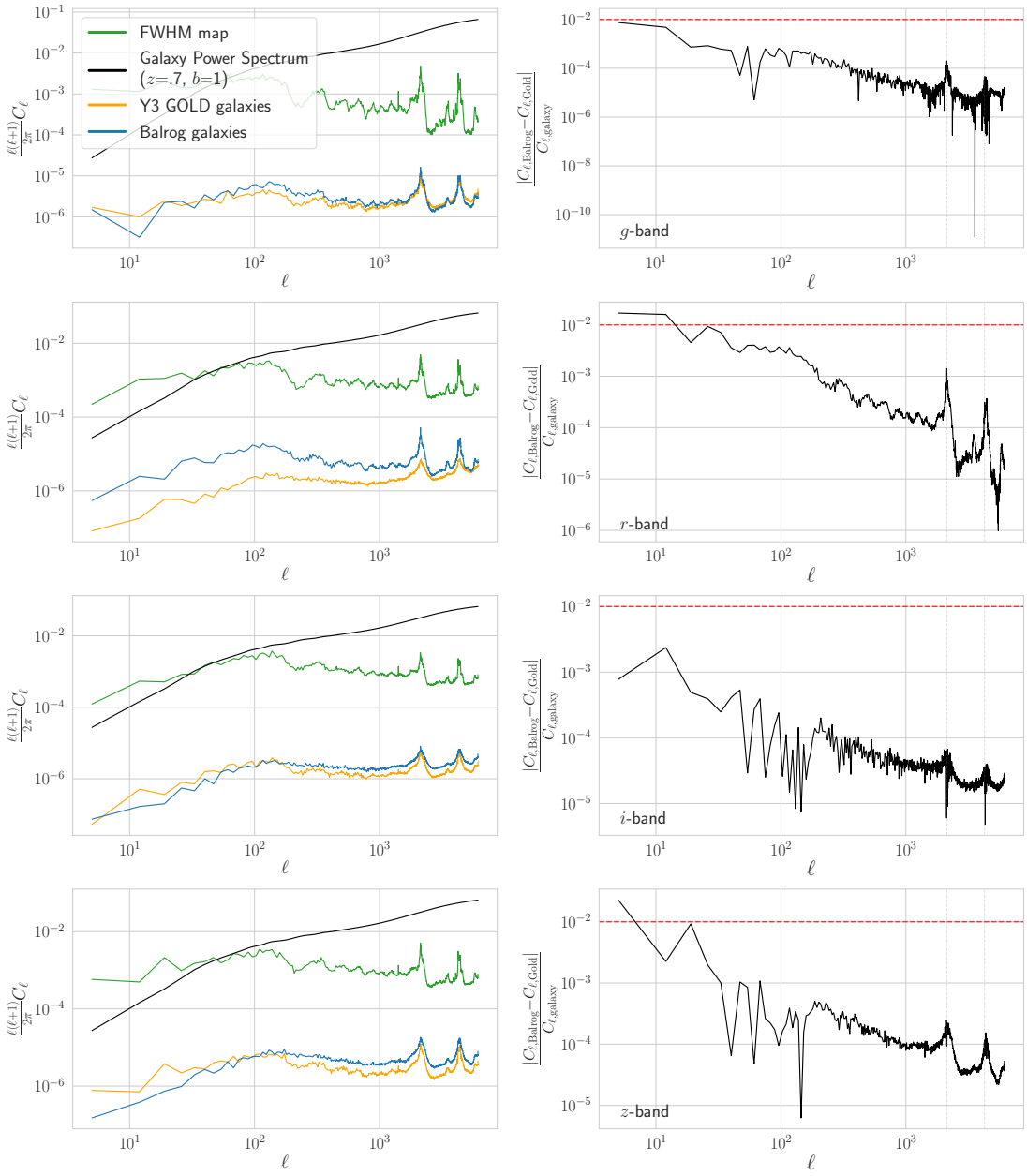

Figure B.3: Power spectra of the mean PSF FWHM, and associated interpolated `Balrog` and Y3 GOLD galaxy count variations, as in Figure 5.4. The left panels show the angular power spectrum of the noted survey property (in green) and the corresponding power spectra of the number densities of the `Balrog` (in blue) and Y3 GOLD (in gold) MagLim-like galaxies across the Y3 footprint. The reference galaxy power spectrum in black represents a typical cosmological signal at $z = 0.7$ with linear galaxy bias parameter of 1. The right panels show the difference in power between Y3 GOLD and `Balrog` as a fraction of the fiducial cosmological power spectrum shown on the left.

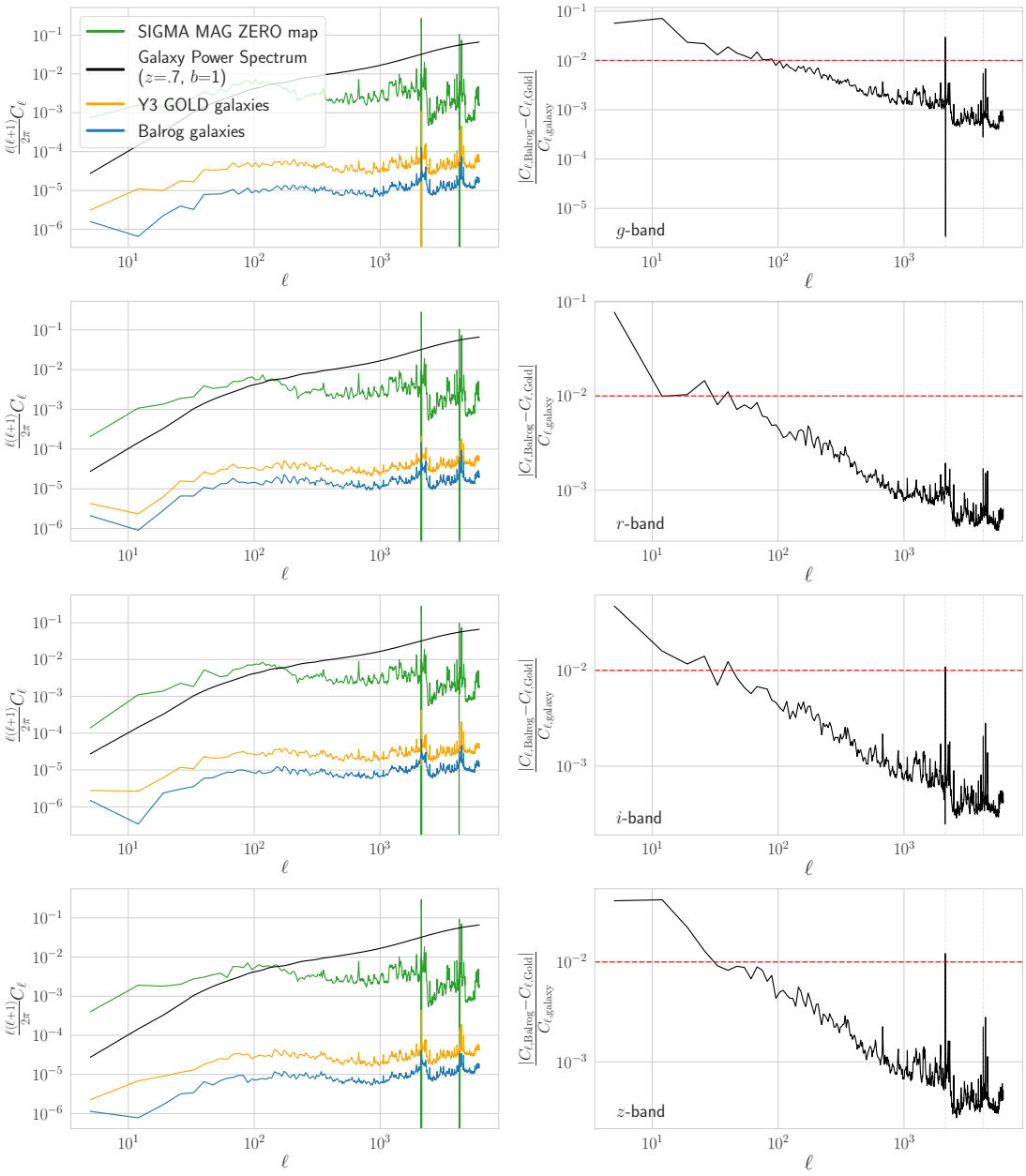

Figure B.4: Power spectra of the mean error on the grey zeropoint calibration and associated interpolated `Balrog` and Y3 GOLD galaxy count variations, as in Figure 5.4. The left panels show the angular power spectrum of the noted survey property (in green) and the corresponding power spectra of the number densities of the `Balrog` (in blue) and Y3 GOLD (in gold) MagLim-like galaxies across the Y3 footprint. The reference galaxy power spectrum in black represents a typical cosmological signal at $z = 0.7$ with linear galaxy bias parameter of 1. The right panels show the difference in power between Y3 GOLD and `Balrog` as a fraction of the fiducial cosmological power spectrum shown on the left.

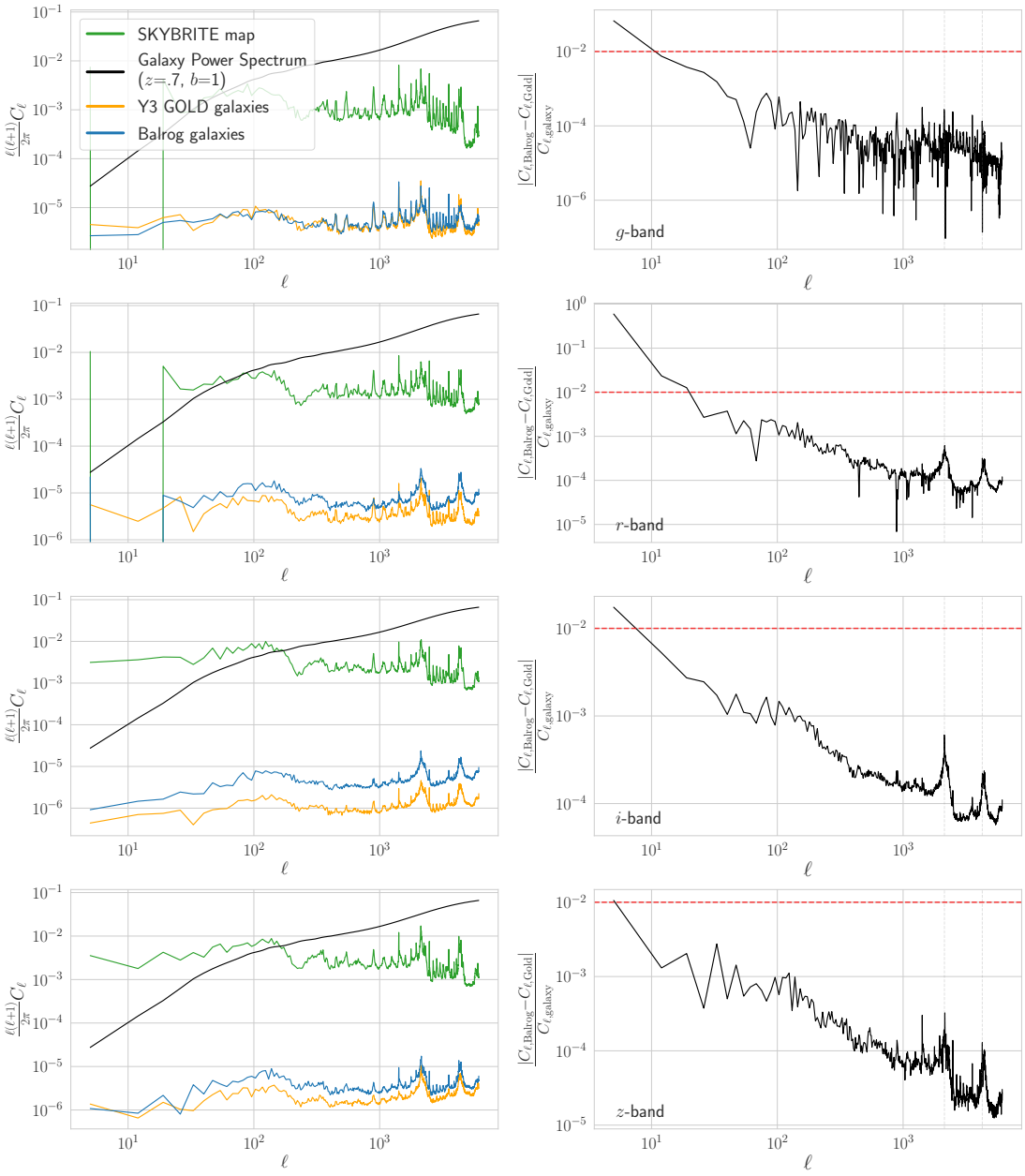

Figure B.5: Power spectra of the mean sky brightness, and associated interpolated `Balrog` and Y3 GOLD galaxy count variations, as in Figure 5.4. The left panels show the angular power spectrum of the noted survey property (in green) and the corresponding power spectra of the number densities of the `Balrog` (in blue) and Y3 GOLD (in gold) MagLim-like galaxies across the Y3 footprint. The reference galaxy power spectrum in black represents a typical cosmological signal at $z = 0.7$ with linear galaxy bias parameter of 1. The right panels show the difference in power between Y3 GOLD and `Balrog` as a fraction of the fiducial cosmological power spectrum shown on the left.

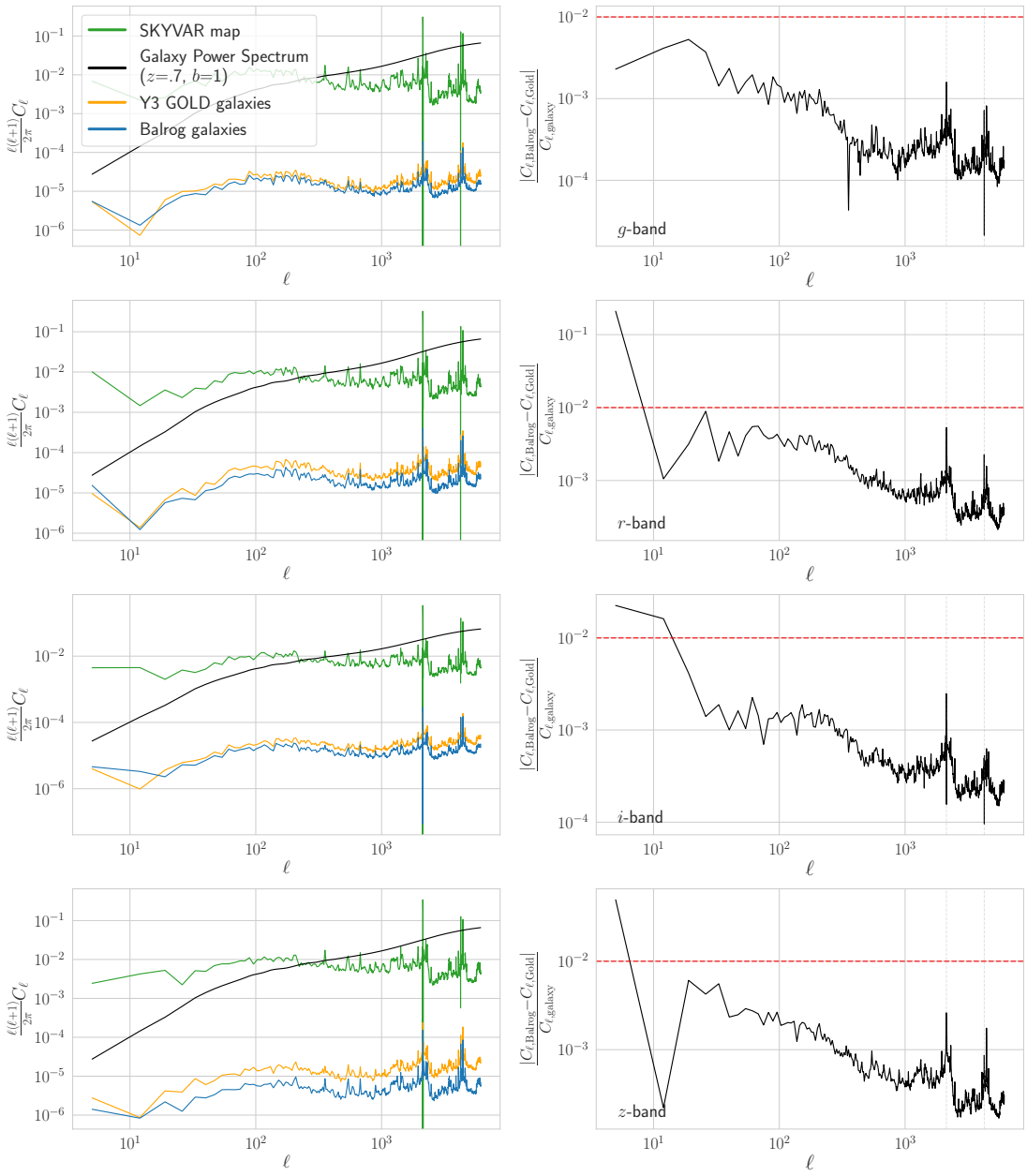

Figure B.6: Power spectra of the variance from sky background, and associated interpolated balrog and Y3 GOLD galaxy count variations, as in Figure 5.4. The left panels show the angular power spectrum of the noted survey property (in green) and the corresponding power spectra of the number densities of the `Balrog` (in blue) and Y3 GOLD (in gold) MagLim-like galaxies across the Y3 footprint. The reference galaxy power spectrum in black represents a typical cosmological signal at $z = 0.7$ with linear galaxy bias parameter of 1. The right panels show the difference in power between Y3 GOLD and `Balrog` as a fraction of the fiducial cosmological power spectrum shown on the left.

Appendix C

Tabular Results

Here we present the tabular results of many of the plots shown in Chapter 5. The mean ($<\Delta>$), median ($\widetilde{\Delta}$), and standard deviation (σ) of the `Balrog` *griz* magnitude responses binned in injection magnitude for the `y3-stars` and `y3-merged` samples are shown in Table C.1 and C.2 respectively. The equivalent quantities for the color responses are shown in Table C.3 and C.4. Measurements of the `Balrog` classification, or "confusion", matrix described in Section 5.4 are shown in Table C.5.

True Mag	$\langle\Delta g\rangle$ (mag)	$\widetilde{\Delta g}$ (mag)	σ_g (mag)	$\langle\Delta r\rangle$ (mag)	$\widetilde{\Delta r}$ (mag)	σ_r (mag)	$\langle\Delta i\rangle$ (mag)	$\widetilde{\Delta i}$ (mag)	σ_i (mag)	$\langle\Delta z\rangle$ (mag)	$\widetilde{\Delta z}$ (mag)	σ_z (mag)
17.00	0.001	0.000	0.004	0.002	0.003	0.005	0.003	0.004	0.010	0.005	0.006	0.006
17.25	0.001	0.003	0.013	0.002	0.003	0.009	0.004	0.005	0.008	0.006	0.006	0.006
17.50	0.001	0.002	0.005	0.002	0.004	0.026	0.005	0.006	0.009	0.006	0.007	0.012
17.75	0.001	0.002	0.006	0.003	0.004	0.007	0.005	0.006	0.006	0.006	0.007	0.011
18.00	0.002	0.003	0.015	0.004	0.005	0.006	0.006	0.006	0.011	0.007	0.007	0.008
18.25	0.003	0.003	0.006	0.005	0.005	0.008	0.006	0.007	0.013	0.006	0.007	0.011
18.50	0.004	0.004	0.006	0.005	0.006	0.008	0.006	0.007	0.009	0.007	0.008	0.014
18.75	0.004	0.004	0.014	0.005	0.006	0.010	0.006	0.007	0.008	0.007	0.008	0.017
19.00	0.004	0.004	0.008	0.005	0.006	0.014	0.005	0.007	0.022	0.007	0.008	0.017
19.25	0.004	0.005	0.008	0.004	0.006	0.017	0.006	0.007	0.013	0.007	0.009	0.021
19.50	0.004	0.005	0.008	0.004	0.006	0.021	0.005	0.007	0.026	0.007	0.009	0.026
19.75	0.004	0.005	0.015	0.004	0.006	0.023	0.006	0.008	0.022	0.007	0.010	0.023
20.00	0.003	0.005	0.015	0.004	0.006	0.029	0.006	0.008	0.028	0.008	0.010	0.034
20.25	0.003	0.005	0.029	0.004	0.007	0.024	0.006	0.009	0.019	0.009	0.011	0.025
20.50	0.003	0.005	0.031	0.004	0.007	0.030	0.007	0.010	0.028	0.009	0.012	0.037
20.75	0.003	0.005	0.033	0.005	0.008	0.028	0.007	0.010	0.038	0.010	0.013	0.041
21.00	0.003	0.005	0.032	0.005	0.008	0.030	0.008	0.011	0.033	0.012	0.014	0.043
21.25	0.003	0.006	0.029	0.005	0.009	0.027	0.009	0.012	0.033	0.013	0.015	0.052
21.50	0.003	0.006	0.030	0.006	0.010	0.031	0.011	0.014	0.042	0.016	0.017	0.059
21.75	0.002	0.006	0.033	0.006	0.010	0.037	0.012	0.015	0.048	0.018	0.019	0.072
22.00	0.002	0.006	0.047	0.007	0.011	0.042	0.014	0.016	0.053	0.022	0.021	0.085
22.25	0.002	0.006	0.044	0.009	0.013	0.049	0.017	0.018	0.065	0.026	0.024	0.107
22.50	0.002	0.006	0.055	0.011	0.014	0.064	0.020	0.020	0.076	0.031	0.026	0.126
22.75	0.003	0.006	0.065	0.014	0.016	0.070	0.023	0.022	0.108	0.038	0.028	0.159
23.00	0.004	0.008	0.083	0.017	0.019	0.083	0.028	0.025	0.107	0.047	0.033	0.218
23.25	0.006	0.009	0.093	0.022	0.022	0.098	0.031	0.025	0.131	0.062	0.035	0.304
23.50	0.010	0.012	0.124	0.027	0.024	0.116	0.033	0.024	0.162	0.084	0.031	0.521
23.75	0.015	0.014	0.147	0.034	0.029	0.154	0.031	0.018	0.200	0.140	0.037	0.876
24.00	0.021	0.016	0.174	0.045	0.034	0.208	0.017	-0.007	0.315	0.297	0.036	1.571
24.25	0.033	0.021	0.245	0.052	0.035	0.226	0.002	-0.041	0.463	0.456	-0.014	2.170

Table C.1: The mean ($\langle\Delta\rangle$), median ($\widetilde{\Delta}$), and standard deviation (σ) of the `Balrog` *griz* magnitude responses binned in injection magnitude for the `y3-stars` sample. The quoted magnitudes correspond to the left bin edge. Simple Gaussian statistics do not fully capture the complexity of the responses – see Figure 5.5.

True Mag	$\langle\Delta g\rangle$ (mag)	$\widetilde{\Delta g}$ (mag)	σ_g (mag)	$\langle\Delta r\rangle$ (mag)	$\widetilde{\Delta r}$ (mag)	σ_r (mag)	$\langle\Delta i\rangle$ (mag)	$\widetilde{\Delta i}$ (mag)	σ_i (mag)	$\langle\Delta z\rangle$ (mag)	$\widetilde{\Delta z}$ (mag)	σ_z (mag)
18.00	-0.066	-0.039	0.081	-0.055	-0.035	0.081	-0.048	-0.029	0.087	-0.043	-0.024	0.076
18.25	-0.063	-0.042	0.101	-0.052	-0.033	0.084	-0.042	-0.024	0.069	-0.039	-0.020	0.076
18.50	-0.059	-0.036	0.077	-0.046	-0.028	0.079	-0.039	-0.019	0.079	-0.040	-0.020	0.083
18.75	-0.055	-0.036	0.078	-0.039	-0.020	0.076	-0.039	-0.020	0.077	-0.034	-0.014	0.083
19.00	-0.055	-0.033	0.083	-0.041	-0.021	0.077	-0.035	-0.015	0.086	-0.031	-0.010	0.090
19.25	-0.044	-0.023	0.084	-0.036	-0.018	0.079	-0.031	-0.011	0.085	-0.026	-0.006	0.101
19.50	-0.040	-0.022	0.078	-0.033	-0.013	0.087	-0.027	-0.006	0.096	-0.022	-0.002	0.105
19.75	-0.040	-0.020	0.085	-0.030	-0.009	0.088	-0.025	-0.003	0.109	-0.019	0.002	0.115
20.00	-0.035	-0.015	0.078	-0.026	-0.006	0.105	-0.022	0.000	0.110	-0.016	0.005	0.125
20.25	-0.035	-0.015	0.098	-0.024	-0.003	0.105	-0.020	0.003	0.119	-0.012	0.009	0.134
20.50	-0.032	-0.012	0.090	-0.023	0.000	0.109	-0.016	0.006	0.126	-0.008	0.013	0.153
20.75	-0.030	-0.009	0.110	-0.020	0.002	0.122	-0.013	0.009	0.145	-0.003	0.017	0.161
21.00	-0.027	-0.006	0.107	-0.018	0.005	0.133	-0.010	0.013	0.155	0.001	0.021	0.174
21.25	-0.026	-0.005	0.116	-0.016	0.008	0.148	-0.007	0.017	0.163	0.003	0.025	0.194
21.50	-0.023	-0.002	0.127	-0.014	0.010	0.157	-0.005	0.020	0.176	0.006	0.028	0.211
21.75	-0.022	0.000	0.147	-0.012	0.014	0.171	-0.002	0.023	0.189	0.008	0.031	0.228
22.00	-0.020	0.002	0.154	-0.010	0.017	0.181	-0.001	0.026	0.203	0.011	0.034	0.254
22.25	-0.019	0.005	0.171	-0.009	0.020	0.192	0.001	0.030	0.222	0.015	0.036	0.291
22.50	-0.017	0.007	0.187	-0.007	0.024	0.212	0.003	0.033	0.248	0.020	0.039	0.339
22.75	-0.017	0.010	0.200	-0.005	0.028	0.231	0.005	0.036	0.279	0.022	0.037	0.403
23.00	-0.014	0.013	0.220	-0.004	0.031	0.259	0.004	0.036	0.314	0.024	0.030	0.496
23.25	-0.012	0.017	0.247	-0.004	0.034	0.293	-0.002	0.031	0.355	0.028	0.014	0.663
23.50	-0.011	0.020	0.279	-0.008	0.033	0.329	-0.023	0.013	0.391	0.037	-0.013	0.916
23.75	-0.009	0.022	0.323	-0.023	0.021	0.369	-0.064	-0.026	0.442	0.069	-0.053	1.312
24.00	-0.009	0.020	0.383	-0.055	-0.007	0.413	-0.132	-0.091	0.528	0.142	-0.115	1.874
24.25	-0.012	0.014	0.463	-0.108	-0.057	0.492	-0.233	-0.194	0.713	0.232	-0.217	2.463

Table C.2: The mean ($\langle\Delta\rangle$), median ($\widetilde{\Delta}$), and standard deviation (σ) of the `Balrog` *griz* magnitude responses binned in injection magnitude for the `y3-merged` sample. The quoted magnitudes correspond to the left bin edge. Simple Gaussian statistics do not fully capture the complexity of the responses – see Figure 5.8.

True Color	$\langle g-r \rangle$ (mag)	$\widetilde{g-r}$ (mag)	σ_{g-r} (mag)	$\langle r-i \rangle$ (mag)	$\widetilde{r-i}$ (mag)	σ_{r-i} (mag)	$\langle i-z \rangle$ (mag)	$\widetilde{i-z}$ (mag)	σ_{i-z} (mag)
-0.2	-0.006	-0.003	0.082	-0.006	-0.003	0.111	0.000	-0.003	0.156
-0.1	-0.004	-0.002	0.098	-0.007	-0.003	0.102	-0.002	-0.002	0.114
0.0	-0.003	-0.002	0.092	-0.004	-0.002	0.074	-0.002	-0.001	0.091
0.1	-0.004	-0.003	0.09	-0.004	-0.002	0.078	-0.002	-0.001	0.11
0.2	-0.002	-0.002	0.074	-0.003	-0.002	0.09	-0.002	-0.001	0.111
0.3	-0.001	-0.002	0.077	-0.002	-0.002	0.097	-0.002	-0.001	0.101
0.4	-0.001	-0.001	0.085	-0.001	-0.002	0.096	-0.002	-0.001	0.092
0.5	0.000	-0.001	0.09	0.000	-0.001	0.094	-0.001	-0.001	0.087
0.6	0.000	-0.001	0.103	0.001	-0.001	0.091	0.000	-0.001	0.083
0.7	-0.001	-0.001	0.109	0.001	-0.001	0.088	0.001	-0.001	0.078
0.8	-0.002	-0.001	0.113	0.002	-0.001	0.092	0.001	0.000	0.075
0.9	-0.003	-0.001	0.126	0.002	-0.001	0.097	0.001	0.000	0.081
1.0	-0.006	-0.001	0.131	0.002	-0.001	0.101	0.004	0.001	0.084
1.1	-0.010	-0.002	0.142	0.003	-0.001	0.106	0.003	0.001	0.078
1.2	-0.017	-0.003	0.154	0.002	-0.001	0.112	0.020	0.001	0.073
1.3	-0.021	-0.003	0.155	0.002	0.000	0.116	-0.024	0.000	0.177
1.4	-0.027	-0.004	0.17	0.000	0.001	0.123	0.006	-0.003	0.119
1.5	-0.044	-0.01	0.208	0.000	0.000	0.129	-0.008	-0.008	0.007
1.6	-0.061	-0.017	0.24	0.000	0.000	0.137	–	–	–
1.7	-0.076	-0.026	0.265	-0.004	-0.001	0.138	–	–	–

Table C.3: The mean ($\langle\Delta\rangle$), median ($\widetilde{\Delta}$), and standard deviation (σ) of the `Balrog` $g-r$, $r-i$, and $i-z$ color responses binned in injection color for the `y3-stars` sample. The quoted colors correspond to the left bin edge. Simple Gaussian statistics do not fully capture the complexity of the responses – see Figure 5.6.

True Color	$\langle g-r \rangle$ (mag)	$\widetilde{g-r}$ (mag)	σ_{g-r} (mag)	$\langle r-i \rangle$ (mag)	$\widetilde{r-i}$ (mag)	σ_{r-i} (mag)	$\langle i-z \rangle$ (mag)	$\widetilde{i-z}$ (mag)	σ_{i-z} (mag)
-0.2	0.081	0.053	0.211	0.079	0.043	0.216	0.092	0.047	0.239
-0.1	0.047	0.030	0.192	0.053	0.032	0.201	0.062	0.030	0.213
0.0	0.026	0.016	0.182	0.028	0.013	0.182	0.030	0.009	0.177
0.1	0.012	0.006	0.179	0.011	0.002	0.155	0.019	0.004	0.163
0.2	0.002	-0.002	0.178	0.004	0.000	0.140	0.011	0.001	0.145
0.3	-0.009	-0.006	0.169	0.001	-0.001	0.140	0.007	0.000	0.134
0.4	-0.015	-0.008	0.161	-0.003	-0.001	0.139	0.004	0.000	0.141
0.5	-0.019	-0.009	0.158	-0.007	-0.003	0.140	0.001	-0.001	0.160
0.6	-0.024	-0.010	0.157	-0.012	-0.005	0.146	-0.004	-0.003	0.161
0.7	-0.028	-0.011	0.158	-0.015	-0.007	0.147	-0.009	-0.005	0.159
0.8	-0.031	-0.011	0.159	-0.018	-0.007	0.146	-0.012	-0.007	0.161
0.9	-0.036	-0.011	0.162	-0.022	-0.008	0.152	-0.016	-0.009	0.171
1.0	-0.041	-0.011	0.167	-0.026	-0.010	0.161	-0.019	-0.011	0.176
1.1	-0.046	-0.011	0.173	-0.029	-0.012	0.170	-0.031	-0.016	0.193
1.2	-0.051	-0.010	0.184	-0.035	-0.013	0.178	-0.053	-0.024	0.210
1.3	-0.059	-0.011	0.194	-0.071	-0.030	0.221	-0.049	-0.024	0.215
1.4	-0.069	-0.013	0.210	-0.149	-0.091	0.276	-0.054	-0.018	0.223
1.5	-0.074	-0.015	0.222	-0.171	-0.105	0.288	-0.076	-0.028	0.236
1.6	-0.070	-0.016	0.224	-0.183	-0.112	0.300	-0.075	-0.015	0.220
1.7	-0.066	-0.016	0.224	-0.206	-0.126	0.314	-0.050	-0.007	0.240
1.8	-0.096	-0.028	0.265	-0.206	-0.127	0.334	-0.063	-0.017	0.255
1.9	-0.193	-0.092	0.358	-0.221	-0.112	0.363	-0.061	-0.003	0.220

Table C.4: The mean ($\langle\Delta\rangle$), median ($\widetilde{\Delta}$), and standard deviation (σ) of the `Balrog` $g-r$, $r-i$, and $i-z$ color responses binned in injection color for the `y3-merged` sample. The quoted colors correspond to the left bin edge. Simple Gaussian statistics do not fully capture the complexity of the responses – see Figure 5.10.

True Mag	Star->Star (TP; %)	Gal->Star (FP; %)	Star->Gal (FN; %)	Gal->Gal (TN; %)
18.50	99.6	1.6	0.4	98.4
18.75	99.6	2.9	0.4	97.1
19.00	99.4	2.9	0.6	97.1
19.25	99.3	2.6	0.7	97.4
19.50	99.2	2.8	0.8	97.2
19.75	99.1	2.3	0.9	97.7
20.00	98.7	1.9	1.3	98.1
20.25	98.6	1.8	1.4	98.2
20.50	98.2	1.8	1.8	98.2
20.75	97.8	1.9	2.2	98.1
21.00	97.3	1.8	2.7	98.2
21.25	96.7	1.7	3.3	98.3
21.50	95.9	2.2	4.1	97.8
21.75	95.1	2.0	4.9	98.0
22.00	93.4	2.3	6.6	97.7
22.25	90.8	3.2	9.2	96.8
22.50	86.4	4.1	13.6	95.9
22.75	79.5	5.2	20.5	94.8
23.00	70.3	6.7	29.7	93.3
23.25	58.2	8.3	41.8	91.7
23.50	46.4	10.1	53.6	89.9
23.75	37.5	12.4	62.5	87.6
24.00	30.9	14.5	69.1	85.5
24.25	25.9	15.0	74.1	85.0

Table C.5: Elements of the classification (or confusion) matrix for `Balrog` sources binned by injection magnitude when normalized by percent, where the measured classification is determined by `EXTENDED_CLASS_SOF`<= 1 for stars and `EXTENDED_CLASS_SOF`> 1 for galaxies. The second through fifth columns correspond to the true positive (TP), false positive (FP), false negative (FN), and true negative (TN) rates of `Balrog` stars respectively. The very pure `y3-stars` sample is used to compute the TP and FN rates, while the nosier classifications of the DF `y3-merged` injections are used for the rest. The quoted magnitudes correspond to the left bin edge. See Figure 5.15.

Bibliography

[1] Planck Collaboration, N. Aghanim, Y. Akrami, M. Ashdown, J. Aumont, C. Baccigalupi, M. Ballardini, A. J. Banday, R. B. Barreiro, N. Bartolo, S. Basak, R. Battye, K. Benabed, J. P. Bernard, M. Bersanelli, P. Bielewicz, J. J. Bock, J. R. Bond, J. Borrill, F. R. Bouchet, F. Boulanger, M. Bucher, C. Burigana, R. C. Butler, E. Calabrese, J. F. Cardoso, J. Carron, A. Challinor, H. C. Chiang, J. Chluba, L. P. L. Colombo, C. Combet, D. Contreras, B. P. Crill, F. Cuttaia, P. de Bernardis, G. de Zotti, J. Delabrouille, J. M. Delouis, E. Di Valentino, J. M. Diego, O. Doré, M. Douspis, A. Ducout, X. Dupac, S. Dusini, G. Efstathiou, F. Elsner, T. A. Enßlin, H. K. Eriksen, Y. Fantaye, M. Farhang, J. Fergusson, R. Fernandez-Cobos, F. Finelli, F. Forastieri, M. Frailis, A. A. Fraisse, E. Franceschi, A. Frolov, S. Galeotta, S. Galli, K. Ganga, R. T. Génova-Santos, M. Gerbino, T. Ghosh, J. González-Nuevo, K. M. Górski, S. Gratton, A. Gruppuso, J. E. Gudmundsson, J. Hamann, W. Handley, F. K. Hansen, D. Herranz, S. R. Hildebrandt, E. Hivon, Z. Huang, A. H. Jaffe, W. C. Jones, A. Karakci, E. Keihänen, R. Keskitalo, K. Kiiveri, J. Kim, T. S. Kisner, L. Knox, N. Krachmalnicoff, M. Kunz, H. Kurki-Suonio, G. Lagache, J. M. Lamarre, A. Lasenby, M. Lattanzi, C. R. Lawrence, M. Le Jeune, P. Lemos, J. Lesgourgues, F. Levrier, A. Lewis, M. Liguori, P. B. Lilje, M. Lilley, V. Lindholm, M. López-Caniego, P. M. Lubin, Y. Z. Ma, J. F. Macías-Pérez, G. Maggio, D. Maino, N. Mandolesi, A. Mangilli, A. Marcos-Caballero, M. Maris, P. G. Martin, M. Martinelli, E. Martínez-González, S. Matarrese, N. Mauri, J. D. McEwen, P. R. Meinhold, A. Melchiorri, A. Mennella, M. Migliaccio, M. Millea, S. Mitra, M. A. Miville-Deschênes, D. Molinari, L. Montier, G. Morgante, A. Moss, P. Natoli, H. U. Nørgaard-Nielsen, L. Pagano, D. Paoletti, B. Partridge, G. Patanchon, H. V. Peiris, F. Perrotta, V. Pettorino, F. Piacentini, L. Polastri, G. Polenta, J. L. Puget, J. P. Rachen, M. Reinecke, M. Remazeilles, A. Renzi, G. Rocha, C. Rosset, G. Roudier, J. A. Rubiño-Martín, B. Ruiz-Granados, L. Salvati, M. Sandri, M. Savelainen, D. Scott, E. P. S. Shellard, C. Sirignano, G. Sirri, L. D. Spencer, R. Sunyaev, A. S. Suur-Uski, J. A. Tauber, D. Tavagnacco, M. Tenti, L. Toffolatti, M. Tomasi, T. Trombetti, L. Valenziano, J. Valiviita, B. Van Tent, L. Vibert, P. Vielva, F. Villa, N. Vittorio, B. D. Wandelt, I. K. Wehus, M. White, S. D. M.

White, A. Zacchei, and A. Zonca. Planck 2018 results. VI. Cosmological parameters. A&A, 641:A6, September 2020.

[2] Teresa Marrodán Undagoitia and Ludwig Rauch. Dark matter direct-detection experiments. *Journal of Physics G Nuclear Physics*, 43(1):013001, January 2016.

[3] Ronald J. Adler, Brendan Casey, and Ovid C. Jacob. Vacuum catastrophe: An elementary exposition of the cosmological constant problem. *American Journal of Physics*, 63(7):620–626, July 1995.

[4] Jérôme Martin. Everything you always wanted to know about the cosmological constant problem (but were afraid to ask). *Comptes Rendus Physique*, 13(6-7):566–665, July 2012.

[5] Andreas Albrecht, Gary Bernstein, Robert Cahn, Wendy L. Freedman, Jacqueline Hewitt, Wayne Hu, John Huth, Marc Kamionkowski, Edward W. Kolb, Lloyd Knox, John C. Mather, Suzanne Staggs, and Nicholas B. Suntzeff. Report of the Dark Energy Task Force. *arXiv e-prints*, pages astro–ph/0609591, September 2006.

[6] Scott Dodelson, Katrin Heitmann, Chris Hirata, Klaus Honscheid, Aaron Roodman, Uroš Seljak, Anže Slosar, and Mark Trodden. Cosmic Visions Dark Energy: Science. *arXiv e-prints*, page arXiv:1604.07626, April 2016.

[7] Eleonora Di Valentino, Olga Mena, Supriya Pan, Luca Visinelli, Weiqiang Yang, Alessandro Melchiorri, David F. Mota, Adam G. Riess, and Joseph Silk. In the Realm of the Hubble tension − a Review of Solutions. *arXiv e-prints*, page arXiv:2103.01183, March 2021.

[8] Oliver Schlaudt and Lara Huber. *Standardization in Measurement. Philosophical, Historical and Sociological Issues*. 01 2015.

[9] Kyle S. Dawson, David J. Schlegel, Christopher P. Ahn, Scott F. Anderson, Éric Aubourg, Stephen Bailey, Robert H. Barkhouser, Julian E. Bautista, Alessandra Beifiori, Andreas A. Berlind, Vaishali Bhardwaj, Dmitry Bizyaev, Cullen H. Blake, Michael R. Blanton, Michael Blomqvist, Adam S. Bolton, Arnaud Borde, Jo Bovy, W. N. Brandt, Howard Brewington, Jon Brinkmann, Peter J. Brown, Joel R. Brownstein, Kevin Bundy, N. G. Busca, William Carithers, Aurelio R. Carnero, Michael A. Carr, Yanmei Chen, Johan Comparat, Natalia Connolly, Frances Cope, Rupert A. C. Croft, Antonio J. Cuesta, Luiz N. da Costa, James R. A. Davenport, Timothée Delubac, Roland de Putter, Saurav Dhital, Anne Ealet, Garrett L. Ebelke, Daniel J. Eisenstein, S. Escoffier, Xiaohui Fan, N. Filiz Ak, Hayley Finley, Andreu Font-Ribera, R. Génova-Santos, James E. Gunn, Hong

Guo, Daryl Haggard, Patrick B. Hall, Jean-Christophe Hamilton, Ben Harris, David W. Harris, Shirley Ho, David W. Hogg, Diana Holder, Klaus Honscheid, Joe Huehnerhoff, Beatrice Jordan, Wendell P. Jordan, Guinevere Kauffmann, Eyal A. Kazin, David Kirkby, Mark A. Klaene, Jean-Paul Kneib, Jean-Marc Le Goff, Khee-Gan Lee, Daniel C. Long, Craig P. Loomis, Britt Lundgren, Robert H. Lupton, Marcio A. G. Maia, Martin Makler, Elena Malanushenko, Viktor Malanushenko, Rachel Mandelbaum, Marc Manera, Claudia Maraston, Daniel Margala, Karen L. Masters, Cameron K. McBride, Patrick McDonald, Ian D. McGreer, Richard G. McMahon, Olga Mena, Jordi Miralda-Escudé, Antonio D. Montero-Dorta, Francesco Montesano, Demitri Muna, Adam D. Myers, Tracy Naugle, Robert C. Nichol, Pasquier Noterdaeme, Sebastián E. Nuza, Matthew D. Olmstead, Audrey Oravetz, Daniel J. Oravetz, Russell Owen, Nikhil Padmanabhan, Nathalie Palanque-Delabrouille, Kaike Pan, John K. Parejko, Isabelle Pâris, Will J. Percival, Ismael Pérez-Fournon, Ignasi Pérez-Ràfols, Patrick Petitjean, Robert Pfaffenberger, Janine Pforr, Matthew M. Pieri, Francisco Prada, Adrian M. Price-Whelan, M. Jordan Raddick, Rafael Rebolo, James Rich, Gordon T. Richards, Constance M. Rockosi, Natalie A. Roe, Ashley J. Ross, Nicholas P. Ross, Graziano Rossi, J. A. Rubiño-Martin, Lado Samushia, Ariel G. Sánchez, Conor Sayres, Sarah J. Schmidt, Donald P. Schneider, C. G. Scóccola, Hee-Jong Seo, Alaina Shelden, Erin Sheldon, Yue Shen, Yiping Shu, Anže Slosar, Stephen A. Smee, Stephanie A. Snedden, Fritz Stauffer, Oliver Steele, Michael A. Strauss, Alina Streblyanska, Nao Suzuki, Molly E. C. Swanson, Tomer Tal, Masayuki Tanaka, Daniel Thomas, Jeremy L. Tinker, Rita Tojeiro, Christy A. Tremonti, M. Vargas Magaña, Licia Verde, Matteo Viel, David A. Wake, Mike Watson, Benjamin A. Weaver, David H. Weinberg, Benjamin J. Weiner, Andrew A. West, Martin White, W. M. Wood-Vasey, Christophe Yeche, Idit Zehavi, Gong-Bo Zhao, and Zheng Zheng. The Baryon Oscillation Spectroscopic Survey of SDSS-III. AJ, 145(1):10, January 2013.

[10] Alexie Leauthaud, Shun Saito, Stefan Hilbert, Alexandre Barreira, Surhud More, Martin White, Shadab Alam, Peter Behroozi, Kevin Bundy, Jean Coupon, and et al. Lensing is low: cosmology, galaxy formation or new physics? *Monthly Notices of the Royal Astronomical Society*, 467(3):3024–3047, Feb 2017.

[11] The Dark Energy Survey Collaboration. The Dark Energy Survey. *arXiv e-prints*, pages astro–ph/0510346, October 2005.

[12] T. M. C. Abbott, M. Aguena, A. Alarcon, S. Allam, S. Allen, J. Annis, S. Avila, D. Bacon, K. Bechtol, A. Bermeo, G. M. Bernstein, E. Bertin, S. Bhargava, S. Bocquet, D. Brooks, D. Brout, E. Buckley-Geer, D. L.

Burke, A. Carnero Rosell, M. Carrasco Kind, J. Carretero, F. J. Castander, R. Cawthon, C. Chang, X. Chen, A. Choi, M. Costanzi, M. Crocce, L. N. da Costa, T. M. Davis, J. De Vicente, J. DeRose, S. Desai, H. T. Diehl, J. P. Dietrich, S. Dodelson, P. Doel, A. Drlica-Wagner, K. Eckert, T. F. Eifler, J. Elvin-Poole, J. Estrada, S. Everett, A. E. Evrard, A. Farahi, I. Ferrero, B. Flaugher, P. Fosalba, J. Frieman, J. García-Bellido, M. Gatti, E. Gaztanaga, D. W. Gerdes, T. Giannantonio, P. Giles, S. Grandis, D. Gruen, R. A. Gruendl, J. Gschwend, G. Gutierrez, W. G. Hartley, S. R. Hinton, D. L. Hollowood, K. Honscheid, B. Hoyle, D. Huterer, D. J. James, M. Jarvis, T. Jeltema, M. W. G. Johnson, M. D. Johnson, S. Kent, E. Krause, R. Kron, K. Kuehn, N. Kuropatkin, O. Lahav, T. S. Li, C. Lidman, M. Lima, H. Lin, N. MacCrann, M. A. G. Maia, A. Mantz, J. L. Marshall, P. Martini, J. Mayers, P. Melchior, J. Mena-Fernández, F. Menanteau, R. Miquel, J. J. Mohr, R. C. Nichol, B. Nord, R. L. C. Ogando, A. Palmese, F. Paz-Chinchón, A. A. Plazas, J. Prat, M. M. Rau, A. K. Romer, A. Roodman, P. Rooney, E. Rozo, E. S. Rykoff, M. Sako, S. Samuroff, C. Sánchez, E. Sanchez, A. Saro, V. Scarpine, M. Schubnell, D. Scolnic, S. Serrano, I. Sevilla-Noarbe, E. Sheldon, J. Allyn. Smith, M. Smith, E. Suchyta, M. E. C. Swanson, G. Tarle, D. Thomas, C. To, M. A. Troxel, D. L. Tucker, T. N. Varga, A. von der Linden, A. R. Walker, R. H. Wechsler, J. Weller, R. D. Wilkinson, H. Wu, B. Yanny, Y. Zhang, Z. Zhang, J. Zuntz, and DES Collaboration. Dark Energy Survey Year 1 Results: Cosmological constraints from cluster abundances and weak lensing. Phys. Rev. D, 102(2):023509, July 2020.

[13] J. Amiaux, R. Scaramella, Y. Mellier, B. Altieri, C. Burigana, Antonio Da Silva, P. Gomez, J. Hoar, R. Laureijs, E. Maiorano, D. Magalhães Oliveira, F. Renk, G. Saavedra Criado, I. Tereno, J. L. Auguères, J. Brinchmann, M. Cropper, L. Duvet, A. Ealet, P. Franzetti, B. Garilli, P. Gondoin, L. Guzzo, H. Hoekstra, R. Holmes, K. Jahnke, T. Kitching, M. Meneghetti, W. Percival, and S. Warren. Euclid mission: building of a reference survey. In Mark C. Clampin, Giovanni G. Fazio, Howard A. MacEwen, and Jr. Oschmann, Jacobus M., editors, *Space Telescopes and Instrumentation 2012: Optical, Infrared, and Millimeter Wave*, volume 8442 of *Society of Photo-Optical Instrumentation Engineers (SPIE) Conference Series*, page 84420Z, September 2012.

[14] D. Spergel, N. Gehrels, J. Breckinridge, M. Donahue, A. Dressler, B. S. Gaudi, T. Greene, O. Guyon, C. Hirata, J. Kalirai, N. J. Kasdin, W. Moos, S. Perlmutter, M. Postman, B. Rauscher, J. Rhodes, Y. Wang, D. Weinberg, J. Centrella, W. Traub, C. Baltay, J. Colbert, D. Bennett, A. Kiessling, B. Macintosh, J. Merten, M. Mortonson, M. Penny, E. Rozo, D. Savransky, K. Stapelfeldt, Y. Zu, C. Baker, E. Cheng, D. Content, J. Dooley, M. Foote,

R. Goullioud, K. Grady, C. Jackson, J. Kruk, M. Levine, M. Melton, C. Peddie, J. Ruffa, and S. Shaklan. Wide-Field InfraRed Survey Telescope-Astrophysics Focused Telescope Assets WFIRST-AFTA Final Report. *arXiv e-prints*, page arXiv:1305.5422, May 2013.

[15] Ž. Ivezić, S. M. Kahn, J. A. Tyson, B. Abel, E. Acosta, R. Allsman, D. Alonso, Y. AlSayyad, S. F. Anderson, J. Andrew, and et al. LSST: From Science Drivers to Reference Design and Anticipated Data Products. ApJ, 873:111, March 2019.

[16] J.R.R. Tolkien. *The Fellowship of the Ring*. Allen & Unwin, 1954.

[17] E. Suchyta, E. M. Huff, J. Aleksić, P. Melchior, S. Jouvel, N. MacCrann, A. J. Ross, M. Crocce, E. Gaztanaga, K. Honscheid, B. Leistedt, H. V. Peiris, E. S. Rykoff, E. Sheldon, T. Abbott, F. B. Abdalla, S. Allam, M. Banerji, A. Benoit-Lévy, E. Bertin, D. Brooks, D. L. Burke, A. Carnero Rosell, M. Carrasco Kind, J. Carretero, C. E. Cunha, C. B. D'Andrea, L. N. da Costa, D. L. DePoy, S. Desai, H. T. Diehl, J. P. Dietrich, P. Doel, T. F. Eifler, J. Estrada, A. E. Evrard, B. Flaugher, P. Fosalba, J. Frieman, D. W. Gerdes, D. Gruen, R. A. Gruendl, D. J. James, M. Jarvis, K. Kuehn, N. Kuropatkin, O. Lahav, M. Lima, M. A. G. Maia, M. March, J. L. Marshall, C. J. Miller, R. Miquel, E. Neilsen, R. C. Nichol, B. Nord, R. Ogando, W. J. Percival, K. Reil, A. Roodman, M. Sako, E. Sanchez, V. Scarpine, I. Sevilla-Noarbe, R. C. Smith, M. Soares-Santos, F. Sobreira, M. E. C. Swanson, G. Tarle, J. Thaler, D. Thomas, V. Vikram, A. R. Walker, R. H. Wechsler, Y. Zhang, and DES Collaboration. No galaxy left behind: accurate measurements with the faintest objects in the Dark Energy Survey. MNRAS, 457(1):786–808, March 2016.

[18] P. J. E. Peebles. *Principles of Physical Cosmology*. 1993.

[19] Scott Dodelson. *Modern cosmology*. 2003.

[20] Steven Weinberg. *Cosmology*. 2008.

[21] Albert Einstein. Die Feldgleichungen der Gravitation. *Sitzungsberichte der Königlich Preußischen Akademie der Wissenschaften (Berlin*, pages 844–847, January 1915.

[22] A. Einstein. Die Grundlage der allgemeinen Relativitätstheorie. *Annalen der Physik*, 354(7):769–822, January 1916.

[23] Charles W. Misner, Kip S. Thorne, and John A. Wheeler. *Gravitation*. 1973.

[24] A. Einstein. Erklarung der Perihelionbewegung der Merkur aus der allgemeinen Relativitatstheorie. *Sitzungsber. preuss.Akad. Wiss*, 47:831–839, January 1915.

[25] F. W. Dyson, A. S. Eddington, and C. Davidson. A Determination of the Deflection of Light by the Sun's Gravitational Field, from Observations Made at the Total Eclipse of May 29, 1919. *Philosophical Transactions of the Royal Society of London Series A*, 220:291–333, January 1920.

[26] B. P. Abbott, R. Abbott, T. D. Abbott, M. R. Abernathy, F. Acernese, K. Ackley, C. Adams, T. Adams, P. Addesso, R. X. Adhikari, V. B. Adya, C. Affeldt, M. Agathos, K. Agatsuma, N. Aggarwal, O. D. Aguiar, L. Aiello, A. Ain, P. Ajith, B. Allen, A. Allocca, P. A. Altin, S. B. Anderson, W. G. Anderson, K. Arai, M. A. Arain, M. C. Araya, C. C. Arceneaux, J. S. Areeda, N. Arnaud, K. G. Arun, S. Ascenzi, G. Ashton, M. Ast, S. M. Aston, P. Astone, P. Aufmuth, C. Aulbert, S. Babak, P. Bacon, M. K. M. Bader, P. T. Baker, F. Baldaccini, G. Ballardin, S. W. Ballmer, J. C. Barayoga, S. E. Barclay, B. C. Barish, D. Barker, F. Barone, B. Barr, L. Barsotti, M. Barsuglia, D. Barta, J. Bartlett, M. A. Barton, I. Bartos, R. Bassiri, A. Basti, J. C. Batch, C. Baune, V. Bavigadda, M. Bazzan, B. Behnke, M. Bejger, C. Belczynski, A. S. Bell, C. J. Bell, B. K. Berger, J. Bergman, G. Bergmann, C. P. L. Berry, D. Bersanetti, A. Bertolini, J. Betzwieser, S. Bhagwat, R. Bhandare, I. A. Bilenko, G. Billingsley, J. Birch, R. Birney, O. Birnholtz, S. Biscans, A. Bisht, M. Bitossi, C. Biwer, M. A. Bizouard, J. K. Blackburn, C. D. Blair, D. G. Blair, R. M. Blair, S. Bloemen, O. Bock, T. P. Bodiya, M. Boer, G. Bogaert, C. Bogan, A. Bohe, P. Bojtos, C. Bond, F. Bondu, R. Bonnand, B. A. Boom, R. Bork, V. Boschi, S. Bose, Y. Bouffanais, A. Bozzi, C. Bradaschia, P. R. Brady, V. B. Braginsky, M. Branchesi, J. E. Brau, T. Briant, A. Brillet, M. Brinkmann, V. Brisson, P. Brockill, A. F. Brooks, D. A. Brown, D. D. Brown, N. M. Brown, C. C. Buchanan, A. Buikema, T. Bulik, H. J. Bulten, A. Buonanno, D. Buskulic, C. Buy, R. L. Byer, M. Cabero, L. Cadonati, G. Cagnoli, C. Cahillane, J. Calderón Bustillo, T. Callister, E. Calloni, J. B. Camp, K. C. Cannon, J. Cao, C. D. Capano, E. Capocasa, F. Carbognani, S. Caride, J. Casanueva Diaz, C. Casentini, S. Caudill, M. Cavaglià, F. Cavalier, R. Cavalieri, G. Cella, C. B. Cepeda, L. Cerboni Baiardi, G. Cerretani, E. Cesarini, R. Chakraborty, T. Chalermsongsak, S. J. Chamberlin, M. Chan, S. Chao, P. Charlton, E. Chassande-Mottin, H. Y. Chen, Y. Chen, C. Cheng, A. Chincarini, A. Chiummo, H. S. Cho, M. Cho, J. H. Chow, N. Christensen, Q. Chu, S. Chua, S. Chung, G. Ciani, F. Clara, J. A. Clark, F. Cleva, E. Coccia, P. F. Cohadon, A. Colla, C. G. Collette, L. Cominsky, M. Constancio, A. Conte, L. Conti, D. Cook, T. R. Corbitt, N. Cornish, A. Corsi, S. Cortese, C. A. Costa, M. W. Coughlin, S. B. Coughlin, J. P. Coulon, S. T.

Countryman, P. Couvares, E. E. Cowan, D. M. Coward, M. J. Cowart, D. C. Coyne, R. Coyne, K. Craig, J. D. E. Creighton, T. D. Creighton, J. Cripe, S. G. Crowder, A. M. Cruise, A. Cumming, L. Cunningham, E. Cuoco, T. Dal Canton, S. L. Danilishin, S. D'Antonio, K. Danzmann, N. S. Darman, C. F. Da Silva Costa, V. Dattilo, I. Dave, H. P. Daveloza, M. Davier, G. S. Davies, E. J. Daw, R. Day, S. De, D. DeBra, G. Debreczeni, J. Degallaix, M. De Laurentis, S. Deléglise, W. Del Pozzo, T. Denker, T. Dent, H. Dereli, V. Dergachev, R. T. DeRosa, R. De Rosa, R. DeSalvo, S. Dhurandhar, M. C. Díaz, L. Di Fiore, M. Di Giovanni, A. Di Lieto, S. Di Pace, I. Di Palma, A. Di Virgilio, G. Dojcinoski, V. Dolique, F. Donovan, K. L. Dooley, S. Doravari, R. Douglas, T. P. Downes, M. Drago, R. W. P. Drever, J. C. Driggers, Z. Du, M. Ducrot, S. E. Dwyer, T. B. Edo, M. C. Edwards, A. Effler, H. B. Eggenstein, P. Ehrens, J. Eichholz, S. S. Eikenberry, W. Engels, R. C. Essick, T. Etzel, M. Evans, T. M. Evans, R. Everett, M. Factourovich, V. Fafone, H. Fair, S. Fairhurst, X. Fan, Q. Fang, S. Farinon, B. Farr, W. M. Farr, M. Favata, M. Fays, H. Fehrmann, M. M. Fejer, D. Feldbaum, I. Ferrante, E. C. Ferreira, F. Ferrini, F. Fidecaro, L. S. Finn, I. Fiori, D. Fiorucci, R. P. Fisher, R. Flaminio, M. Fletcher, H. Fong, J. D. Fournier, S. Franco, S. Frasca, F. Frasconi, M. Frede, Z. Frei, A. Freise, R. Frey, V. Frey, T. T. Fricke, P. Fritschel, V. V. Frolov, P. Fulda, M. Fyffe, H. A. G. Gabbard, J. R. Gair, L. Gammaitoni, S. G. Gaonkar, F. Garufi, A. Gatto, G. Gaur, N. Gehrels, G. Gemme, B. Gendre, E. Genin, A. Gennai, J. George, L. Gergely, V. Germain, Abhirup Ghosh, Archisman Ghosh, S. Ghosh, J. A. Giaime, K. D. Giardina, A. Giazotto, K. Gill, A. Glaefke, J. R. Gleason, E. Goetz, R. Goetz, L. Gondan, G. González, J. M. Gonzalez Castro, A. Gopakumar, N. A. Gordon, M. L. Gorodetsky, S. E. Gossan, M. Gosselin, R. Gouaty, C. Graef, P. B. Graff, M. Granata, A. Grant, S. Gras, C. Gray, G. Greco, A. C. Green, R. J. S. Greenhalgh, P. Groot, H. Grote, S. Grunewald, G. M. Guidi, X. Guo, A. Gupta, M. K. Gupta, K. E. Gushwa, E. K. Gustafson, R. Gustafson, J. J. Hacker, B. R. Hall, E. D. Hall, G. Hammond, M. Haney, M. M. Hanke, J. Hanks, C. Hanna, M. D. Hannam, J. Hanson, T. Hardwick, J. Harms, G. M. Harry, I. W. Harry, M. J. Hart, M. T. Hartman, C. J. Haster, K. Haughian, J. Healy, J. Heefner, A. Heidmann, M. C. Heintze, G. Heinzel, H. Heitmann, P. Hello, G. Hemming, M. Hendry, I. S. Heng, J. Hennig, A. W. Heptonstall, M. Heurs, S. Hild, D. Hoak, K. A. Hodge, D. Hofman, S. E. Hollitt, K. Holt, D. E. Holz, P. Hopkins, D. J. Hosken, J. Hough, E. A. Houston, E. J. Howell, Y. M. Hu, S. Huang, E. A. Huerta, D. Huet, B. Hughey, S. Husa, S. H. Huttner, T. Huynh-Dinh, A. Idrisy, N. Indik, D. R. Ingram, R. Inta, H. N. Isa, J. M. Isac, M. Isi, G. Islas, T. Isogai, B. R. Iyer, K. Izumi, M. B. Jacobson, T. Jacqmin, H. Jang, K. Jani, P. Jaranowski, S. Jawahar, F. Jiménez-Forteza, W. W. Johnson, N. K. Johnson-McDaniel, D. I. Jones,

R. Jones, R. J. G. Jonker, L. Ju, K. Haris, C. V. Kalaghatgi, V. Kalogera, S. Kandhasamy, G. Kang, J. B. Kanner, S. Karki, M. Kasprzack, E. Katsavounidis, W. Katzman, S. Kaufer, T. Kaur, K. Kawabe, F. Kawazoe, F. Kéfélian, M. S. Kehl, D. Keitel, D. B. Kelley, W. Kells, R. Kennedy, D. G. Keppel, J. S. Key, A. Khalaidovski, F. Y. Khalili, I. Khan, S. Khan, Z. Khan, E. A. Khazanov, N. Kijbunchoo, C. Kim, J. Kim, K. Kim, Nam-Gyu Kim, Namjun Kim, Y. M. Kim, E. J. King, P. J. King, D. L. Kinzel, J. S. Kissel, L. Kleybolte, S. Klimenko, S. M. Koehlenbeck, K. Kokeyama, S. Koley, V. Kondrashov, A. Kontos, S. Koranda, M. Korobko, W. Z. Korth, I. Kowalska, D. B. Kozak, V. Kringel, B. Krishnan, A. Królak, C. Krueger, G. Kuehn, P. Kumar, R. Kumar, L. Kuo, A. Kutynia, P. Kwee, B. D. Lackey, M. Landry, J. Lange, B. Lantz, P. D. Lasky, A. Lazzarini, C. Lazzaro, P. Leaci, S. Leavey, E. O. Lebigot, C. H. Lee, H. K. Lee, H. M. Lee, K. Lee, A. Lenon, M. Leonardi, J. R. Leong, N. Leroy, N. Letendre, Y. Levin, B. M. Levine, T. G. F. Li, A. Libson, T. B. Littenberg, N. A. Lockerbie, J. Logue, A. L. Lombardi, L. T. London, J. E. Lord, M. Lorenzini, V. Loriette, M. Lormand, G. Losurdo, J. D. Lough, C. O. Lousto, G. Lovelace, H. Lück, A. P. Lundgren, J. Luo, R. Lynch, Y. Ma, T. MacDonald, B. Machenschalk, M. MacInnis, D. M. Macleod, F. Magaña-Sandoval, R. M. Magee, M. Mageswaran, E. Majorana, I. Maksimovic, V. Malvezzi, N. Man, I. Mandel, V. Mandic, V. Mangano, G. L. Mansell, M. Manske, M. Mantovani, F. Marchesoni, F. Marion, S. Márka, Z. Márka, A. S. Markosyan, E. Maros, F. Martelli, L. Martellini, I. W. Martin, R. M. Martin, D. V. Martynov, J. N. Marx, K. Mason, A. Masserot, T. J. Massinger, M. Masso-Reid, F. Matichard, L. Matone, N. Mavalvala, N. Mazumder, G. Mazzolo, R. McCarthy, D. E. McClelland, S. McCormick, S. C. McGuire, G. McIntyre, J. McIver, D. J. McManus, S. T. McWilliams, D. Meacher, G. D. Meadors, J. Meidam, A. Melatos, G. Mendell, D. Mendoza-Gandara, R. A. Mercer, E. Merilh, M. Merzougui, S. Meshkov, C. Messenger, C. Messick, P. M. Meyers, F. Mezzani, H. Miao, C. Michel, H. Middleton, E. E. Mikhailov, L. Milano, J. Miller, M. Millhouse, Y. Minenkov, J. Ming, S. Mirshekari, C. Mishra, S. Mitra, V. P. Mitrofanov, G. Mitselmakher, R. Mittleman, A. Moggi, M. Mohan, S. R. P. Mohapatra, M. Montani, B. C. Moore, C. J. Moore, D. Moraru, G. Moreno, S. R. Morriss, K. Mossavi, B. Mours, C. M. Mow-Lowry, C. L. Mueller, G. Mueller, A. W. Muir, Arunava Mukherjee, D. Mukherjee, S. Mukherjee, N. Mukund, A. Mullavey, J. Munch, D. J. Murphy, P. G. Murray, A. Mytidis, I. Nardecchia, L. Naticchioni, R. K. Nayak, V. Necula, K. Nedkova, G. Nelemans, M. Neri, A. Neunzert, G. Newton, T. T. Nguyen, A. B. Nielsen, S. Nissanke, A. Nitz, F. Nocera, D. Nolting, M. E. N. Normandin, L. K. Nuttall, J. Oberling, E. Ochsner, J. O'Dell, E. Oelker, G. H. Ogin, J. J. Oh, S. H. Oh, F. Ohme, M. Oliver, P. Oppermann, Richard J. Oram, B. O'Reilly, R. O'Shaughnessy, C. D. Ott,

D. J. Ottaway, R. S. Ottens, H. Overmier, B. J. Owen, A. Pai, S. A. Pai, J. R. Palamos, O. Palashov, C. Palomba, A. Pal-Singh, H. Pan, Y. Pan, C. Pankow, F. Pannarale, B. C. Pant, F. Paoletti, A. Paoli, M. A. Papa, H. R. Paris, W. Parker, D. Pascucci, A. Pasqualetti, R. Passaquieti, D. Passuello, B. Patricelli, Z. Patrick, B. L. Pearlstone, M. Pedraza, R. Pedurand, L. Pekowsky, A. Pele, S. Penn, A. Perreca, H. P. Pfeiffer, M. Phelps, O. Piccinni, M. Pichot, M. Pickenpack, F. Piergiovanni, V. Pierro, G. Pillant, L. Pinard, I. M. Pinto, M. Pitkin, J. H. Poeld, R. Poggiani, P. Popolizio, A. Post, J. Powell, J. Prasad, V. Predoi, S. S. Premachandra, T. Prestegard, L. R. Price, M. Prijatelj, M. Principe, S. Privitera, R. Prix, G. A. Prodi, L. Prokhorov, O. Puncken, M. Punturo, P. Puppo, M. Pürrer, H. Qi, J. Qin, V. Quetschke, E. A. Quintero, R. Quitzow-James, F. J. Raab, D. S. Rabeling, H. Radkins, P. Raffai, S. Raja, M. Rakhmanov, C. R. Ramet, P. Rapagnani, V. Raymond, M. Razzano, V. Re, J. Read, C. M. Reed, T. Regimbau, L. Rei, S. Reid, D. H. Reitze, H. Rew, S. D. Reyes, F. Ricci, K. Riles, N. A. Robertson, R. Robie, F. Robinet, A. Rocchi, L. Rolland, J. G. Rollins, V. J. Roma, J. D. Romano, R. Romano, G. Romanov, J. H. Romie, D. Rosińska, S. Rowan, A. Rüdiger, P. Ruggi, K. Ryan, S. Sachdev, T. Sadecki, L. Sadeghian, L. Salconi, M. Saleem, F. Salemi, A. Samajdar, L. Sammut, L. M. Sampson, E. J. Sanchez, V. Sandberg, B. Sandeen, G. H. Sanders, J. R. Sanders, B. Sassolas, B. S. Sathyaprakash, P. R. Saulson, O. Sauter, R. L. Savage, A. Sawadsky, P. Schale, R. Schilling, J. Schmidt, P. Schmidt, R. Schnabel, R. M. S. Schofield, A. Schönbeck, E. Schreiber, D. Schuette, B. F. Schutz, J. Scott, S. M. Scott, D. Sellers, A. S. Sengupta, D. Sentenac, V. Sequino, A. Sergeev, G. Serna, Y. Setyawati, A. Sevigny, D. A. Shaddock, T. Shaffer, S. Shah, M. S. Shahriar, M. Shaltev, Z. Shao, B. Shapiro, P. Shawhan, A. Sheperd, D. H. Shoemaker, D. M. Shoemaker, K. Siellez, X. Siemens, D. Sigg, A. D. Silva, D. Simakov, A. Singer, L. P. Singer, A. Singh, R. Singh, A. Singhal, A. M. Sintes, B. J. J. Slagmolen, J. R. Smith, M. R. Smith, N. D. Smith, R. J. E. Smith, E. J. Son, B. Sorazu, F. Sorrentino, T. Souradeep, A. K. Srivastava, A. Staley, M. Steinke, J. Steinlechner, S. Steinlechner, D. Steinmeyer, B. C. Stephens, S. P. Stevenson, R. Stone, K. A. Strain, N. Straniero, G. Stratta, N. A. Strauss, S. Strigin, R. Sturani, A. L. Stuver, T. Z. Summerscales, L. Sun, P. J. Sutton, B. L. Swinkels, M. J. Szczepańczyk, M. Tacca, D. Talukder, D. B. Tanner, M. Tápai, S. P. Tarabrin, A. Taracchini, R. Taylor, T. Theeg, M. P. Thirugnanasambandam, E. G. Thomas, M. Thomas, P. Thomas, K. A. Thorne, K. S. Thorne, E. Thrane, S. Tiwari, V. Tiwari, K. V. Tokmakov, C. Tomlinson, M. Tonelli, C. V. Torres, C. I. Torrie, D. Töyrä, F. Travasso, G. Traylor, D. Trifirò, M. C. Tringali, L. Trozzo, M. Tse, M. Turconi, D. Tuyenbayev, D. Ugolini, C. S. Unnikrishnan, A. L. Urban, S. A. Usman, H. Vahlbruch, G. Vajente, G. Valdes, M. Vallisneri, N. van Bakel, M. van Beuzekom, J. F. J.

van den Brand, C. Van Den Broeck, D. C. Vander-Hyde, L. van der Schaaf, J. V. van Heijningen, A. A. van Veggel, M. Vardaro, S. Vass, M. Vasúth, R. Vaulin, A. Vecchio, G. Vedovato, J. Veitch, P. J. Veitch, K. Venkateswara, D. Verkindt, F. Vetrano, A. Viceré, S. Vinciguerra, D. J. Vine, J. Y. Vinet, S. Vitale, T. Vo, H. Vocca, C. Vorvick, D. Voss, W. D. Vousden, S. P. Vyatchanin, A. R. Wade, L. E. Wade, M. Wade, S. J. Waldman, M. Walker, L. Wallace, S. Walsh, G. Wang, H. Wang, M. Wang, X. Wang, Y. Wang, H. Ward, R. L. Ward, J. Warner, M. Was, B. Weaver, L. W. Wei, M. Weinert, A. J. Weinstein, R. Weiss, T. Welborn, L. Wen, P. Weßels, T. Westphal, K. Wette, J. T. Whelan, S. E. Whitcomb, D. J. White, B. F. Whiting, K. Wiesner, C. Wilkinson, P. A. Willems, L. Williams, R. D. Williams, A. R. Williamson, J. L. Willis, B. Willke, M. H. Wimmer, L. Winkelmann, W. Winkler, C. C. Wipf, A. G. Wiseman, H. Wittel, G. Woan, J. Worden, J. L. Wright, G. Wu, J. Yablon, I. Yakushin, W. Yam, H. Yamamoto, C. C. Yancey, M. J. Yap, H. Yu, M. Yvert, A. ZadroŻny, L. Zangrando, M. Zanolin, J. P. Zendri, M. Zevin, F. Zhang, L. Zhang, M. Zhang, Y. Zhang, C. Zhao, M. Zhou, Z. Zhou, X. J. Zhu, M. E. Zucker, S. E. Zuraw, J. Zweizig, LIGO Scientific Collaboration, and Virgo Collaboration. Observation of Gravitational Waves from a Binary Black Hole Merger. Phys. Rev. Lett., 116(6):061102, February 2016.

[27] Francesco Sylos Labini and Yuri V. Baryshev. Testing the Copernican and Cosmological Principles in the local universe with galaxy surveys. J. Cosmology Astropart. Phys., 2010(6):021, June 2010.

[28] Edward Arthur Milne. *Relativity, gravitation and world-structure*. 1935.

[29] H. P. Robertson. Kinematics and World-Structure. ApJ, 82:284, November 1935.

[30] A. G. Walker. On Milne's Theory of World-Structure. *Proceedings of the London Mathematical Society*, 42:90–127, January 1937.

[31] A. Friedmann. Über die Krümmung des Raumes. *Zeitschrift fur Physik*, 10:377–386, January 1922.

[32] Ethan Siegel. *Beyond the Galaxy: How Humanity Looked Beyond Our Milky Way and Discovered the Entire Universe*. World Scientific Publishing Co, 2015.

[33] Saul Perlmutter. Supernovae, Dark Energy, and the Accelerating Universe. *Physics Today*, 56(4):53–62, April 2003.

[34] N. W. Boggess, J. C. Mather, R. Weiss, C. L. Bennett, E. S. Cheng, E. Dwek, S. Gulkis, M. G. Hauser, M. A. Janssen, T. Kelsall, S. S. Meyer, S. H.

Moseley, T. L. Murdock, R. A. Shafer, R. F. Silverberg, G. F. Smoot, D. T. Wilkinson, and E. L. Wright. The COBE Mission: Its Design and Performance Two Years after Launch. ApJ, 397:420, October 1992.

[35] G. Hinshaw, D. Larson, E. Komatsu, D. N. Spergel, C. L. Bennett, J. Dunkley, M. R. Nolta, M. Halpern, R. S. Hill, N. Odegard, L. Page, K. M. Smith, J. L. Weiland, B. Gold, N. Jarosik, A. Kogut, M. Limon, S. S. Meyer, G. S. Tucker, E. Wollack, and E. L. Wright. Nine-year Wilkinson Microwave Anisotropy Probe (WMAP) Observations: Cosmological Parameter Results. ApJS, 208(2):19, October 2013.

[36] Planck Collaboration, P. A. R. Ade, N. Aghanim, M. I. R. Alves, C. Armitage-Caplan, M. Arnaud, M. Ashdown, F. Atrio-Barandela, J. Aumont, H. Aussel, C. Baccigalupi, A. J. Banday, R. B. Barreiro, R. Barrena, M. Bartelmann, J. G. Bartlett, N. Bartolo, S. Basak, E. Battaner, R. Battye, K. Benabed, A. Benoît, A. Benoit-Lévy, J. P. Bernard, M. Bersanelli, B. Bertincourt, M. Bethermin, P. Bielewicz, I. Bikmaev, A. Blanchard, J. Bobin, J. J. Bock, H. Böhringer, A. Bonaldi, L. Bonavera, J. R. Bond, J. Borrill, F. R. Bouchet, F. Boulanger, H. Bourdin, J. W. Bowyer, M. Bridges, M. L. Brown, M. Bucher, R. Burenin, C. Burigana, R. C. Butler, E. Calabrese, B. Cappellini, J. F. Cardoso, R. Carr, P. Carvalho, M. Casale, G. Castex, A. Catalano, A. Challinor, A. Chamballu, R. R. Chary, X. Chen, H. C. Chiang, L. Y. Chiang, G. Chon, P. R. Christensen, E. Churazov, S. Church, M. Clemens, D. L. Clements, S. Colombi, L. P. L. Colombo, C. Combet, B. Comis, F. Couchot, A. Coulais, B. P. Crill, M. Cruz, A. Curto, F. Cuttaia, A. Da Silva, H. Dahle, L. Danese, R. D. Davies, R. J. Davis, P. de Bernardis, A. de Rosa, G. de Zotti, T. Déchelette, J. Delabrouille, J. M. Delouis, J. Démoclès, F. X. Désert, J. Dick, C. Dickinson, J. M. Diego, K. Dolag, H. Dole, S. Donzelli, O. Doré, M. Douspis, A. Ducout, J. Dunkley, X. Dupac, G. Efstathiou, F. Elsner, T. A. Enßlin, H. K. Eriksen, O. Fabre, E. Falgarone, M. C. Falvella, Y. Fantaye, J. Fergusson, C. Filliard, F. Finelli, I. Flores-Cacho, S. Foley, O. Forni, P. Fosalba, M. Frailis, A. A. Fraisse, E. Franceschi, M. Freschi, S. Fromenteau, M. Frommert, T. C. Gaier, S. Galeotta, J. Gallegos, S. Galli, B. Gandolfo, K. Ganga, C. Gauthier, R. T. Génova-Santos, T. Ghosh, M. Giard, G. Giardino, M. Gilfanov, D. Girard, Y. Giraud-Héraud, E. Gjerløw, J. González-Nuevo, K. M. Górski, S. Gratton, A. Gregorio, A. Gruppuso, J. E. Gudmundsson, J. Haissinski, J. Hamann, F. K. Hansen, M. Hansen, D. Hanson, D. L. Harrison, A. Heavens, G. Helou, A. Hempel, S. Henrot-Versillé, C. Hernández-Monteagudo, D. Herranz, S. R. Hildebrandt, E. Hivon, S. Ho, M. Hobson, W. A. Holmes, A. Hornstrup, Z. Hou, W. Hovest, G. Huey, K. M. Huffenberger, G. Hurier, S. Ilić, A. H. Jaffe, T. R. Jaffe, J. Jasche, J. Jewell, W. C. Jones, M. Juvela, P. Kalberla, P. Kangaslahti, E. Keihänen, J. Kerp, R. Keskitalo, I. Khami-

tov, K. Kiiveri, J. Kim, T. S. Kisner, R. Kneissl, J. Knoche, L. Knox, M. Kunz, H. Kurki-Suonio, F. Lacasa, G. Lagache, A. Lähteenmäki, J. M. Lamarre, M. Langer, A. Lasenby, M. Lattanzi, R. J. Laureijs, A. Lavabre, C. R. Lawrence, M. Le Jeune, S. Leach, J. P. Leahy, R. Leonardi, J. León-Tavares, C. Leroy, J. Lesgourgues, A. Lewis, C. Li, A. Liddle, M. Liguori, P. B. Lilje, M. Linden-Vørnle, V. Lindholm, M. López-Caniego, S. Lowe, P. M. Lubin, J. F. Macías-Pérez, C. J. MacTavish, B. Maffei, G. Maggio, D. Maino, N. Mandolesi, A. Mangilli, A. Marcos-Caballero, D. Marinucci, M. Maris, F. Marleau, D. J. Marshall, P. G. Martin, E. Martínez-González, S. Masi, M. Massardi, S. Matarrese, T. Matsumura, F. Matthai, L. Maurin, P. Mazzotta, A. McDonald, J. D. McEwen, P. McGehee, S. Mei, P. R. Meinhold, A. Melchiorri, J. B. Melin, L. Mendes, E. Menegoni, A. Mennella, M. Migliaccio, K. Mikkelsen, M. Millea, R. Miniscalco, S. Mitra, M. A. Miville-Deschênes, D. Molinari, A. Moneti, L. Montier, G. Morgante, N. Morisset, D. Mortlock, A. Moss, D. Munshi, J. A. Murphy, P. Naselsky, F. Nati, P. Natoli, M. Negrello, N. P. H. Nesvadba, C. B. Netterfield, H. U. Nørgaard-Nielsen, C. North, F. Noviello, D. Novikov, I. Novikov, I. J. O'Dwyer, F. Orieux, S. Osborne, C. O'Sullivan, C. A. Oxborrow, F. Paci, L. Pagano, F. Pajot, R. Paladini, S. Pandolfi, D. Paoletti, B. Partridge, F. Pasian, G. Patanchon, P. Paykari, D. Pearson, T. J. Pearson, M. Peel, H. V. Peiris, O. Perdereau, L. Perotto, F. Perrotta, V. Pettorino, F. Piacentini, M. Piat, E. Pierpaoli, D. Pietrobon, S. Plaszczynski, P. Platania, D. Pogosyan, E. Pointecouteau, G. Polenta, N. Ponthieu, L. Popa, T. Poutanen, G. W. Pratt, G. Prézeau, S. Prunet, J. L. Puget, A. R. Pullen, J. P. Rachen, B. Racine, A. Rahlin, C. Räth, W. T. Reach, R. Rebolo, M. Reinecke, M. Remazeilles, C. Renault, A. Renzi, A. Riazuelo, S. Ricciardi, T. Riller, C. Ringeval, I. Ristorcelli, G. Robbers, G. Rocha, M. Roman, C. Rosset, M. Rossetti, G. Roudier, M. Rowan-Robinson, J. A. Rubiño-Martín, B. Ruiz-Granados, B. Rusholme, E. Salerno, M. Sandri, L. Sanselme, D. Santos, M. Savelainen, G. Savini, B. M. Schaefer, F. Schiavon, D. Scott, M. D. Seiffert, P. Serra, E. P. S. Shellard, K. Smith, G. F. Smoot, T. Souradeep, L. D. Spencer, J. L. Starck, V. Stolyarov, R. Stompor, R. Sudiwala, R. Sunyaev, F. Sureau, P. Sutter, D. Sutton, A. S. Suur-Uski, J. F. Sygnet, J. A. Tauber, D. Tavagnacco, D. Taylor, L. Terenzi, D. Texier, L. Toffolatti, M. Tomasi, J. P. Torre, M. Tristram, M. Tucci, J. Tuovinen, M. Türler, M. Tuttlebee, G. Umana, L. Valenziano, J. Valiviita, B. Van Tent, J. Varis, L. Vibert, M. Viel, P. Vielva, F. Villa, N. Vittorio, L. A. Wade, B. D. Wandelt, C. Watson, R. Watson, I. K. Wehus, N. Welikala, J. Weller, M. White, S. D. M. White, A. Wilkinson, B. Winkel, J. Q. Xia, D. Yvon, A. Zacchei, J. P. Zibin, and A. Zonca. Planck 2013 results. I. Overview of products and scientific results. A&A, 571:A1, November 2014.

[37] Edwin Hubble. A Relation between Distance and Radial Velocity among Extra-Galactic Nebulae. *Proceedings of the National Academy of Science*, 15(3):168–173, March 1929.

[38] Adam G. Riess, Stefano Casertano, Wenlong Yuan, J. Bradley Bowers, Lucas Macri, Joel C. Zinn, and Dan Scolnic. Cosmic Distances Calibrated to 1% Precision with Gaia EDR3 Parallaxes and Hubble Space Telescope Photometry of 75 Milky Way Cepheids Confirm Tension with ΛCDM. ApJ, 908(1):L6, February 2021.

[39] David W. Hogg. Distance measures in cosmology. *arXiv e-prints*, pages astro–ph/9905116, May 1999.

[40] Alan H. Guth. Inflationary universe: A possible solution to the horizon and flatness problems. *Phys. Rev. D*, 23:347–356, Jan 1981.

[41] J. Alberto Vázquez, Luis E. Padilla, and Tonatiuh Matos. Inflationary Cosmology: From Theory to Observations. *arXiv e-prints*, page arXiv:1810.09934, October 2018.

[42] Andrew R. Liddle and David H. Lyth. *Cosmological Inflation and Large-Scale Structure*. 2000.

[43] *Gravitation and the universe*, January 1970.

[44] W. Rindler. Visual horizons in world models. MNRAS, 116:662, January 1956.

[45] P. J. E. Peebles. *The large-scale structure of the universe*. 1980.

[46] H. J. Mo and S. D. M. White. An analytic model for the spatial clustering of dark matter haloes. MNRAS, 282(2):347–361, September 1996.

[47] Leszek Roszkowski, Enrico Maria Sessolo, and Sebastian Trojanowski. WIMP dark matter candidates and searches—current status and future prospects. *Reports on Progress in Physics*, 81(6):066201, June 2018.

[48] P. J. E. Peebles. Statistical Analysis of Catalogs of Extragalactic Objects. I. Theory. ApJ, 185:413–440, October 1973.

[49] M. Davis and P. J. E. Peebles. A survey of galaxy redshifts. V. The two-point position and velocity correlations. ApJ, 267:465–482, April 1983.

[50] Stephen D. Landy and Alexander S. Szalay. Bias and Variance of Angular Correlation Functions. ApJ, 412:64, July 1993.

[51] Harry Johnston, Angus H. Wright, Benjamin Joachimi, Maciej Bilicki, Nora Elisa Chisari, Andrej Dvornik, Thomas Erben, Benjamin Giblin, Catherine Heymans, Hendrik Hildebrandt, Henk Hoekstra, Shahab Joudaki, and Mohammadjavad Vakili. Organised Randoms: learning and correcting for systematic galaxy clustering patterns in KiDS using self-organising maps. *arXiv e-prints*, page arXiv:2012.08467, December 2020.

[52] B. Hoyle, D. Gruen, G. M. Bernstein, M. M. Rau, J. De Vicente, W. G. Hartley, E. Gaztanaga, J. DeRose, M. A. Troxel, C. Davis, A. Alarcon, N. MacCrann, J. Prat, C. Sánchez, E. Sheldon, R. H. Wechsler, J. Asorey, M. R. Becker, C. Bonnett, A. Carnero Rosell, D. Carollo, M. Carrasco Kind, F. J. Castander, R. Cawthon, C. Chang, M. Childress, T. M. Davis, A. Drlica-Wagner, M. Gatti, K. Glazebrook, J. Gschwend, S. R. Hinton, J. K. Hoormann, A. G. Kim, A. King, K. Kuehn, G. Lewis, C. Lidman, H. Lin, E. Macaulay, M. A. G. Maia, P. Martini, D. Mudd, A. Möller, R. C. Nichol, R. L. C. Ogando, R. P. Rollins, A. Roodman, A. J. Ross, E. Rozo, E. S. Rykoff, S. Samuroff, I. Sevilla-Noarbe, R. Sharp, N. E. Sommer, B. E. Tucker, S. A. Uddin, T. N. Varga, P. Vielzeuf, F. Yuan, B. Zhang, T. M. C. Abbott, F. B. Abdalla, S. Allam, J. Annis, K. Bechtol, A. Benoit-Lévy, E. Bertin, D. Brooks, E. Buckley-Geer, D. L. Burke, M. T. Busha, D. Capozzi, J. Carretero, M. Crocce, C. B. D'Andrea, L. N. da Costa, D. L. DePoy, S. Desai, H. T. Diehl, P. Doel, T. F. Eifler, J. Estrada, A. E. Evrard, E. Fernandez, B. Flaugher, P. Fosalba, J. Frieman, J. García-Bellido, D. W. Gerdes, T. Giannantonio, D. A. Goldstein, R. A. Gruendl, G. Gutierrez, K. Honscheid, D. J. James, M. Jarvis, T. Jeltema, M. W. G. Johnson, M. D. Johnson, D. Kirk, E. Krause, S. Kuhlmann, N. Kuropatkin, O. Lahav, T. S. Li, M. Lima, M. March, J. L. Marshall, P. Melchior, F. Menanteau, R. Miquel, B. Nord, C. R. O'Neill, A. A. Plazas, A. K. Romer, M. Sako, E. Sanchez, B. Santiago, V. Scarpine, R. Schindler, M. Schubnell, M. Smith, R. C. Smith, M. Soares-Santos, F. Sobreira, E. Suchyta, M. E. C. Swanson, G. Tarle, D. Thomas, D. L. Tucker, V. Vikram, A. R. Walker, J. Weller, W. Wester, R. C. Wolf, B. Yanny, J. Zuntz, and DES Collaboration. Dark Energy Survey Year 1 Results: redshift distributions of the weak-lensing source galaxies. MNRAS, 478(1):592–610, July 2018.

[53] Martín Crocce, Anna Cabré, and Enrique Gaztañaga. Modelling the angular correlation function and its full covariance in photometric galaxy surveys. MNRAS, 414(1):329–349, June 2011.

[54] Vincent Desjacques, Donghui Jeong, and Fabian Schmidt. Large-scale galaxy bias. Phys. Rep., 733:1–193, February 2018.

[55] Risa H. Wechsler and Jeremy L. Tinker. The Connection Between Galaxies and Their Dark Matter Halos. ARA&A, 56:435–487, September 2018.

[56] F. W. Dyson, A. S. Eddington, and C. Davidson. A Determination of the Deflection of Light by the Sun's Gravitational Field, from Observations Made at the Total Eclipse of May 29, 1919. *Philosophical Transactions of the Royal Society of London Series A*, 220:291–333, January 1920.

[57] Tommaso Treu. Strong lensing by galaxies. *Annual Review of Astronomy and Astrophysics*, 48(1):87–125, 2010.

[58] Peter Schneider and Dominique Sluse. Mass-sheet degeneracy, power-law models and external convergence: Impact on the determination of the Hubble constant from gravitational lensing. A&A, 559:A37, November 2013.

[59] Huan Lin, Scott Dodelson, Hee-Jong Seo, Marcelle Soares-Santos, James Annis, Jiangang Hao, David Johnston, Jeffrey M. Kubo, Ribamar R. R. Reis, and Melanie Simet. The SDSS Co-add: Cosmic Shear Measurement. ApJ, 761(1):15, December 2012.

[60] M. A. Troxel, N. MacCrann, J. Zuntz, T. F. Eifler, E. Krause, S. Dodelson, D. Gruen, J. Blazek, O. Friedrich, S. Samuroff, J. Prat, L. F. Secco, C. Davis, A. Ferté, J. DeRose, A. Alarcon, A. Amara, E. Baxter, M. R. Becker, G. M. Bernstein, S. L. Bridle, R. Cawthon, C. Chang, A. Choi, J. De Vicente, A. Drlica-Wagner, J. Elvin-Poole, J. Frieman, M. Gatti, W. G. Hartley, K. Honscheid, B. Hoyle, E. M. Huff, D. Huterer, B. Jain, M. Jarvis, T. Kacprzak, D. Kirk, N. Kokron, C. Krawiec, O. Lahav, A. R. Liddle, J. Peacock, M. M. Rau, A. Refregier, R. P. Rollins, E. Rozo, E. S. Rykoff, C. Sánchez, I. Sevilla-Noarbe, E. Sheldon, A. Stebbins, T. N. Varga, P. Vielzeuf, M. Wang, R. H. Wechsler, B. Yanny, T. M. C. Abbott, F. B. Abdalla, S. Allam, J. Annis, K. Bechtol, A. Benoit-Lévy, E. Bertin, D. Brooks, E. Buckley-Geer, D. L. Burke, A. Carnero Rosell, M. Carrasco Kind, J. Carretero, F. J. Castander, M. Crocce, C. E. Cunha, C. B. D'Andrea, L. N. da Costa, D. L. DePoy, S. Desai, H. T. Diehl, J. P. Dietrich, P. Doel, E. Fernandez, B. Flaugher, P. Fosalba, J. García-Bellido, E. Gaztanaga, D. W. Gerdes, T. Giannantonio, D. A. Goldstein, R. A. Gruendl, J. Gschwend, G. Gutierrez, D. J. James, T. Jeltema, M. W. G. Johnson, M. D. Johnson, S. Kent, K. Kuehn, S. Kuhlmann, N. Kuropatkin, T. S. Li, M. Lima, H. Lin, M. A. G. Maia, M. March, J. L. Marshall, P. Martini, P. Melchior, F. Menanteau, R. Miquel, J. J. Mohr, E. Neilsen, R. C. Nichol, B. Nord, D. Petravick, A. A. Plazas, A. K. Romer, A. Roodman, M. Sako, E. Sanchez, V. Scarpine, R. Schindler, M. Schubnell, M. Smith, R. C. Smith, M. Soares-Santos, F. Sobreira, E. Suchyta, M. E. C. Swanson, G. Tarle, D. Thomas, D. L. Tucker, V. Vikram, A. R. Walker, J. Weller, Y. Zhang, and DES Collaboration. Dark Energy Survey Year 1 results: Cosmological constraints from cosmic shear. Phys. Rev. D, 98(4):043528, August 2018.

[61] H. Hildebrandt, M. Viola, C. Heymans, S. Joudaki, K. Kuijken, C. Blake, T. Erben, B. Joachimi, D. Klaes, L. Miller, C. B. Morrison, R. Nakajima, G. Verdoes Kleijn, A. Amon, A. Choi, G. Covone, J. T. A. de Jong, A. Dvornik, I. Fenech Conti, A. Grado, J. Harnois-Déraps, R. Herbonnet, H. Hoekstra, F. Köhlinger, J. McFarland, A. Mead, J. Merten, N. Napolitano, J. A. Peacock, M. Radovich, P. Schneider, P. Simon, E. A. Valentijn, J. L. van den Busch, E. van Uitert, and L. Van Waerbeke. KiDS-450: cosmological parameter constraints from tomographic weak gravitational lensing. MNRAS, 465(2):1454–1498, February 2017.

[62] Takashi Hamana, Masato Shirasaki, Satoshi Miyazaki, Chiaki Hikage, Masamune Oguri, Surhud More, Robert Armstrong, Alexie Leauthaud, Rachel Mandelbaum, Hironao Miyatake, Atsushi J. Nishizawa, Melanie Simet, Masahiro Takada, Hiroaki Aihara, James Bosch, Yutaka Komiyama, Robert Lupton, Hitoshi Murayama, Michael A. Strauss, and Masayuki Tanaka. Cosmological constraints from cosmic shear two-point correlation functions with HSC survey first-year data. PASJ, 72(1):16, February 2020.

[63] G. M. Bernstein and M. Jarvis. Shapes and Shears, Stars and Smears: Optimal Measurements for Weak Lensing. AJ, 123(2):583–618, February 2002.

[64] Eric Huff and Rachel Mandelbaum. Metacalibration: Direct Self-Calibration of Biases in Shear Measurement. *arXiv e-prints*, page arXiv:1702.02600, February 2017.

[65] N. MacCrann, M. R. Becker, J. McCullough, A. Amon, D. Gruen, M. Jarvis, A. Choi, M. A. Troxel, E. Sheldon, B. Yanny, K. Herner, S. Dodelson, J. Zuntz, K. Eckert, R. P. Rollins, T. N. Varga, G. M. Bernstein, R. A. Gruendl, I. Harrison, W. G. Hartley, I. Sevilla-Noarbe, A. Pieres, S. L. Bridle, J. Myles, A. Alarcon, S. Everett, C. Sánchez, E. M. Huff, F. Tarsitano, M. Gatti, L. F. Secco, T. M. C. Abbott, M. Aguena, S. Allam, J. Annis, D. Bacon, E. Bertin, D. Brooks, D. L. Burke, A. Carnero Rosell, M. Carrasco Kind, J. Carretero, M. Costanzi, M. Crocce, M. E. S. Pereira, J. De Vicente, S. Desai, H. T. Diehl, J. P. Dietrich, P. Doel, T. F. Eifler, I. Ferrero, A. Ferté, B. Flaugher, P. Fosalba, J. Frieman, J. García-Bellido, E. Gaztanaga, D. W. Gerdes, T. Giannantonio, J. Gschwend, G. Gutierrez, S. R. Hinton, D. L. Hollowood, K. Honscheid, D. J. James, O. Lahav, M. Lima, M. A. G. Maia, M. March, J. L. Marshall, P. Martini, P. Melchior, F. Menanteau, R. Miquel, J. J. Mohr, R. Morgan, J. Muir, R. L. C. Ogando, A. Palmese, F. Paz-Chinchón, A. A. Plazas, M. Rodriguez-Monroy, A. Roodman, S. Samuroff, E. Sanchez, V. Scarpine, S. Serrano, M. Smith, M. Soares-Santos, E. Suchyta, M. E. C. Swanson, G. Tarle, D. Thomas,

C. To, and R. D. Wilkinson. DES Y3 results: Blending shear and redshift biases in image simulations. *arXiv e-prints*, page arXiv:2012.08567, December 2020.

[66] M. Bartelmann and P. Schneider. Weak gravitational lensing. Phys. Rep., 340(4-5):291–472, January 2001.

[67] Peter Schneider, Jürgen Ehlers, and Emilio E. Falco. *Gravitational Lenses*. 1992.

[68] Björn Malte Schäfer, Lavinia Heisenberg, Angelos F. Kalovidouris, and David J. Bacon. On the validity of the Born approximation for weak cosmic flexions. MNRAS, 420(1):455–467, February 2012.

[69] R. D. Blandford, A. B. Saust, T. G. Brainerd, and J. V. Villumsen. The distortion of distant galaxy images by large-scale structure. MNRAS, 251:600, August 1991.

[70] Peter Schneider. Weak Gravitational Lensing. *arXiv e-prints*, pages astro–ph/0509252, September 2005.

[71] M. A. Troxel and Mustapha Ishak. The intrinsic alignment of galaxies and its impact on weak gravitational lensing in an era of precision cosmology. Phys. Rep., 558:1–59, February 2015.

[72] A. A. Plazas, G. M. Bernstein, and E. S. Sheldon. On-Sky Measurements of the Transverse Electric Fields' Effects in the Dark Energy Camera CCDs. PASP, 126(942):750, August 2014.

[73] P. Antilogus, P. Astier, P. Doherty, A. Guyonnet, and N. Regnault. The brighter-fatter effect and pixel correlations in CCD sensors. *Journal of Instrumentation*, 9(3):C03048, March 2014.

[74] F. William High, Jason Rhodes, Richard Massey, and Richard Ellis. Pixelation Effects in Weak Lensing. PASP, 119(861):1295–1307, November 2007.

[75] M. Jarvis, G. M. Bernstein, A. Amon, C. Davis, P. F. Léget, K. Bechtol, I. Harrison, M. Gatti, A. Roodman, C. Chang, R. Chen, A. Choi, S. Desai, A. Drlica-Wagner, D. Gruen, R. A. Gruendl, A. Hernandez, N. MacCrann, J. Meyers, A. Navarro-Alsina, S. Pandey, A. A. Plazas, L. F. Secco, E. Sheldon, M. A. Troxel, S. Vorperian, K. Wei, J. Zuntz, T. M. C. Abbott, M. Aguena, S. Allam, S. Avila, S. Bhargava, S. L. Bridle, D. Brooks, A. Carnero Rosell, M. Carrasco Kind, J. Carretero, M. Costanzi, L. N. da Costa, J. De Vicente, H. T. Diehl, P. Doel, S. Everett, B. Flaugher, P. Fosalba, J. Frieman, J. García-Bellido, E. Gaztanaga, D. W. Gerdes, G. Gutierrez, S. R. Hinton, D. L. Hollowood, K. Honscheid, D. J. James, S. Kent,

K. Kuehn, N. Kuropatkin, O. Lahav, M. A. G. Maia, M. March, J. L. Marshall, P. Melchior, F. Menanteau, R. Miquel, R. L. C. Ogando, F. Paz-Chinchón, E. S. Rykoff, E. Sanchez, V. Scarpine, M. Schubnell, S. Serrano, I. Sevilla-Noarbe, M. Smith, E. Suchyta, M. E. C. Swanson, G. Tarle, T. N. Varga, A. R. Walker, W. Wester, R. D. Wilkinson, and (DES Collaboration). Dark Energy Survey year 3 results: point spread function modelling. MNRAS, 501(1):1282–1299, February 2021.

[76] Dragan Huterer, Masahiro Takada, Gary Bernstein, and Bhuvnesh Jain. Systematic errors in future weak-lensing surveys: requirements and prospects for self-calibration. MNRAS, 366(1):101–114, February 2006.

[77] I. Fenech Conti, R. Herbonnet, H. Hoekstra, J. Merten, L. Miller, and M. Viola. Calibration of weak-lensing shear in the Kilo-Degree Survey. MNRAS, 467(2):1627–1651, May 2017.

[78] Erin S. Sheldon and Eric M. Huff. Practical Weak-lensing Shear Measurement with Metacalibration. ApJ, 841(1):24, May 2017.

[79] Erin S. Sheldon, Matthew R. Becker, Niall MacCrann, and Michael Jarvis. Mitigating Shear-dependent Object Detection Biases with Metacalibration. ApJ, 902(2):138, October 2020.

[80] Gary M. Bernstein and Robert Armstrong. Bayesian lensing shear measurement. MNRAS, 438(2):1880–1893, February 2014.

[81] Gary M. Bernstein, Robert Armstrong, Christina Krawiec, and Marisa C. March. An accurate and practical method for inference of weak gravitational lensing from galaxy images. MNRAS, 459(4):4467–4484, July 2016.

[82] L. Miller, T. D. Kitching, C. Heymans, A. F. Heavens, and L. van Waerbeke. Bayesian galaxy shape measurement for weak lensing surveys - I. Methodology and a fast-fitting algorithm. MNRAS, 382(1):315–324, November 2007.

[83] Arushi Gupta, José Manuel Zorrilla Matilla, Daniel Hsu, and Zoltán Haiman. Non-Gaussian information from weak lensing data via deep learning. Phys. Rev. D, 97(10):103515, May 2018.

[84] Pedro H. Bernardinelli, Gary M. Bernstein, Masao Sako, Tongtian Liu, William R. Saunders, Tali Khain, Hsing Wen Lin, David W. Gerdes, Dillon Brout, Fred C. Adams, Matthew Belyakov, Aditya Inada Somasundaram, Lakshay Sharma, Jennifer Locke, Kyle Franson, Juliette C. Becker, Kevin Napier, Larissa Markwardt, James Annis, T. M. C. Abbott, S. Avila, D. Brooks, D. L. Burke, A. Carnero Rosell, M. Carrasco Kind, F. J. Castander, L. N. da Costa, J. De Vicente, S. Desai, H. T. Diehl, P. Doel, S. Everett, B. Flaugher, J. García-Bellido, D. Gruen, R. A. Gruendl, J. Gschwend,

G. Gutierrez, D. L. Hollowood, D. J. James, M. W. G. Johnson, M. D. Johnson, E. Krause, N. Kuropatkin, M. A. G. Maia, M. March, R. Miquel, F. Paz-Chinchón, A. A. Plazas, A. K. Romer, E. S. Rykoff, C. Sánchez, E. Sanchez, V. Scarpine, S. Serrano, I. Sevilla-Noarbe, M. Smith, F. Sobreira, E. Suchyta, M. E. C. Swanson, G. Tarle, A. R. Walker, W. Wester, Y. Zhang, and DES Collaboration. Trans-Neptunian Objects Found in the First Four Years of the Dark Energy Survey. ApJS, 247(1):32, March 2020.

[85] Pedro H. Bernardinelli, Gary M. Bernstein, Masao Sako, Stephanie Hamilton, David W. Gerdes, Fred C. Adams, William R. Saunders, M. Aguena, S. Allam, S. Avila, D. Brooks, H. T. Diehl, P. Doel, S. Everett, J. García-Bellido, E. Gaztanaga, R. A. Gruendl, K. Honscheid, R. L. C. Ogando, A. Palmese, D. L. Tucker, A. R. Walker, W. Wester, and (The DES Collaboration). Testing the Isotropy of the Dark Energy Survey's Extreme Trans-Neptunian Objects. *The Planetary Science Journal*, 1(2):28, September 2020.

[86] K. J. Napier, D. W. Gerdes, Hsing Wen Lin, S. J. Hamilton, G. M. Bernstein, P. H. Bernardinelli, T. M. C. Abbott, M. Aguena, J. Annis, S. Avila, D. Bacon, E. Bertin, D. Brooks, D. L. Burke, A. Carnero Rosell, M. Carrasco Kind, J. Carretero, M. Costanzi, L. N. da Costa, J. De Vicente, H. T. Diehl, P. Doel, S. Everett, I. Ferrero, P. Fosalba, J. García-Bellido, D. Gruen, R. A. Gruendl, G. Gutierrez, D. L. Hollowood, K. Honscheid, B. Hoyle, D. J. James, S. Kent, K. Kuehn, N. Kuropatkin, M. A. G. Maia, F. Menanteau, R. Miquel, R. Morgan, A. Palmese, F. Paz-Chinchón, A. A. Plazas, E. Sanchez, V. Scarpine, S. Serrano, I. Sevilla-Noarbe, M. Smith, E. Suchyta, M. E. C. Swanson, C. To, A. R. Walker, R. D. Wilkinson, and DES Collaboration. No Evidence for Orbital Clustering in the Extreme Trans-Neptunian Objects. *The Planetary Science Journal*, 2(2):59, April 2021.

[87] N. Shipp, A. Drlica-Wagner, E. Balbinot, P. Ferguson, D. Erkal, T. S. Li, K. Bechtol, V. Belokurov, B. Buncher, D. Carollo, M. Carrasco Kind, K. Kuehn, J. L. Marshall, A. B. Pace, E. S. Rykoff, I. Sevilla-Noarbe, E. Sheldon, L. Strigari, A. K. Vivas, B. Yanny, A. Zenteno, T. M. C. Abbott, F. B. Abdalla, S. Allam, S. Avila, E. Bertin, D. Brooks, D. L. Burke, J. Carretero, F. J. Castander, R. Cawthon, M. Crocce, C. E. Cunha, C. B. D'Andrea, L. N. da Costa, C. Davis, J. De Vicente, S. Desai, H. T. Diehl, P. Doel, A. E. Evrard, B. Flaugher, P. Fosalba, J. Frieman, J. García-Bellido, E. Gaztanaga, D. W. Gerdes, D. Gruen, R. A. Gruendl, J. Gschwend, G. Gutierrez, W. Hartley, K. Honscheid, B. Hoyle, D. J. James, M. D. Johnson, E. Krause, N. Kuropatkin, O. Lahav, H. Lin, M. A. G. Maia, M. March, P. Martini, F. Menanteau, C. J. Miller, R. Miquel, R. C. Nichol, A. A. Plazas, A. K. Romer, M. Sako, E. Sanchez, B. Santiago, V. Scarpine,

R. Schindler, M. Schubnell, M. Smith, R. C. Smith, F. Sobreira, E. Suchyta, M. E. C. Swanson, G. Tarle, D. Thomas, D. L. Tucker, A. R. Walker, R. H. Wechsler, and DES Collaboration. Stellar Streams Discovered in the Dark Energy Survey. ApJ, 862(2):114, August 2018.

[88] N. Shipp, A. Drlica-Wagner, E. Balbinot, P. Ferguson, D. Erkal, T. S. Li, K. Bechtol, V. Belokurov, B. Buncher, D. Carollo, M. Carrasco Kind, K. Kuehn, J. L. Marshall, A. B. Pace, E. S. Rykoff, I. Sevilla-Noarbe, E. Sheldon, L. Strigari, A. K. Vivas, B. Yanny, A. Zenteno, T. M. C. Abbott, F. B. Abdalla, S. Allam, S. Avila, E. Bertin, D. Brooks, D. L. Burke, J. Carretero, F. J. Castander, R. Cawthon, M. Crocce, C. E. Cunha, C. B. D'Andrea, L. N. da Costa, C. Davis, J. De Vicente, S. Desai, H. T. Diehl, P. Doel, A. E. Evrard, B. Flaugher, P. Fosalba, J. Frieman, J. García-Bellido, E. Gaztanaga, D. W. Gerdes, D. Gruen, R. A. Gruendl, J. Gschwend, G. Gutierrez, W. Hartley, K. Honscheid, B. Hoyle, D. J. James, M. D. Johnson, E. Krause, N. Kuropatkin, O. Lahav, H. Lin, M. A. G. Maia, M. March, P. Martini, F. Menanteau, C. J. Miller, R. Miquel, R. C. Nichol, A. A. Plazas, A. K. Romer, M. Sako, E. Sanchez, B. Santiago, V. Scarpine, R. Schindler, M. Schubnell, M. Smith, R. C. Smith, F. Sobreira, E. Suchyta, M. E. C. Swanson, G. Tarle, D. Thomas, D. L. Tucker, A. R. Walker, R. H. Wechsler, and DES Collaboration. Stellar Streams Discovered in the Dark Energy Survey. ApJ, 862(2):114, August 2018.

[89] D. Capozzi, J. Etherington, D. Thomas, C. Maraston, E. S. Rykoff, I. Sevilla-Noarbe, K. Bechtol, M. Carrasco Kind, A. Drlica-Wagner, J. Pforr, J. Gschwend, A. Carnero Rosell, P. Pellegrini, M. A. G. Maia, L. N. da Costa, A. Benoit-Lévy, M. E. C. Swanson, R. H. Wechsler, M. Banerji, C. Papovich, X. Morice-Atkinson, F. Abdalla, D. Brooks, J. Carretero, C. Cunha, C. D'Andrea, S. Desai, T. H. Diehl, A. Evrards, B. Flaugher, P. Fosalba, J. Frieman, J. García-Bellido, E. Gaztanaga, D. W. Gerdes, D. Gruen, R. A. Gruendl, G. Gutierrez, W. G. Hartley, D. James, T. Jeltema, K. Kuehn, S. Kuhlmann, N. Kuropatkin, O. Lahav, M. Lima, J. L. Marshall, P. Martini, F. Menanteau, R. Miquel, B. Nord, R. L. C. Ogando, A. A. Plazas Malagòn, A. K. Romer, E. Sanchez, V. Scarpine, R. Schindler, M. Schubnell, M. Smith, M. Soares-Santos, F. Sobreira, E. Suchyta, and G. Tarle. Evolution of Galaxy Luminosity and Stellar-Mass Functions since $z = 1$ with the Dark Energy Survey Science Verification Data. *arXiv e-prints*, page arXiv:1707.09066, July 2017.

[90] E. Bufanda, D. Hollowood, T. E. Jeltema, E. S. Rykoff, E. Rozo, P. Martini, T. M. C. Abbott, F. B. Abdalla, S. Allam, M. Banerji, A. Benoit-Lévy, E. Bertin, D. Brooks, A. Carnero Rosell, M. Carrasco Kind, J. Carretero, C. E. Cunha, L. N. da Costa, S. Desai, H. T. Diehl, J. P. Dietrich, A. E.

Evrard, A. Fausti Neto, B. Flaugher, J. Frieman, D. W. Gerdes, D. A. Goldstein, D. Gruen, R. A. Gruendl, G. Gutierrez, K. Honscheid, D. J. James, K. Kuehn, N. Kuropatkin, M. Lima, M. A. G. Maia, J. L. Marshall, P. Melchior, R. Miquel, J. J. Mohr, R. Ogando, A. A. Plazas, A. K. Romer, P. Rooney, E. Sanchez, B. Santiago, V. Scarpine, I. Sevilla-Noarbe, R. C. Smith, M. Soares-Santos, F. Sobreira, E. Suchyta, G. Tarle, D. Thomas, D. L. Tucker, A. R. Walker, and DES Collaboration. The evolution of active galactic nuclei in clusters of galaxies from the Dark Energy Survey. MNRAS, 465(3):2531–2539, March 2017.

[91] Pierandrea Guarnieri, Claudia Maraston, Daniel Thomas, Janine Pforr, Violeta Gonzalez-Perez, James Etherington, Joakim Carlsen, Xan Morice-Atkinson, Christopher J. Conselice, Julia Gschwend, Matias Carrasco Kind, Tim Abbott, Sahar Allam, David Brooks, David Burke, Aurelio Carnero Rosell, Jorge Carretero, Carlos Cunha, Chris D'Andrea, Luiz da Costa, Juan De Vincente, Darren DePoy, H. Thomas Diehl, Peter Doel, Josh Frieman, Juan Garcia-Bellido, Daniel Gruen, Gaston Gutierrez, Dominic Hanley, Devon Hollowood, Klaus Honscheid, David James, Tesla Jeltema, Kyler Kuehn, Marcos Lima, Marcio A. G. Maia, Jennifer Marshall, Paul Martini, Peter Melchior, Felipe Menanteau, Ramon Miquel, Andres Plazas Malagon, Samuel Richardson, Kathy Romer, Eusebio Sanchez, Vic Scarpine, Rafe Schindler, Ignacio Sevilla, Mathew Smith, Marcelle Soares-Santos, Flavia Sobreira, Eric Suchyta, Gregory Tarle, Alistair Walker, and William Wester. Candidate massive galaxies at z $\sim$ 4 in the Dark Energy Survey. MNRAS, 483(3):3060–3081, March 2019.

[92] M. Soares-Santos, D. E. Holz, J. Annis, R. Chornock, K. Herner, E. Berger, D. Brout, H. Y. Chen, R. Kessler, M. Sako, S. Allam, D. L. Tucker, R. E. Butler, A. Palmese, Z. Doctor, H. T. Diehl, J. Frieman, B. Yanny, H. Lin, D. Scolnic, P. Cowperthwaite, E. Neilsen, J. Marriner, N. Kuropatkin, W. G. Hartley, F. Paz-Chinchón, K. D. Alexander, E. Balbinot, P. Blanchard, D. A. Brown, J. L. Carlin, C. Conselice, E. R. Cook, A. Drlica-Wagner, M. R. Drout, F. Durret, T. Eftekhari, B. Farr, D. A. Finley, R. J. Foley, W. Fong, C. L. Fryer, J. García-Bellido, M. S. S. Gill, R. A. Gruendl, C. Hanna, D. Kasen, T. S. Li, P. A. A. Lopes, A. C. C. Lourenço, R. Margutti, J. L. Marshall, T. Matheson, G. E. Medina, B. D. Metzger, R. R. Muñoz, J. Muir, M. Nicholl, E. Quataert, A. Rest, M. Sauseda, D. J. Schlegel, L. F. Secco, F. Sobreira, A. Stebbins, V. A. Villar, K. Vivas, A. R. Walker, W. Wester, P. K. G. Williams, A. Zenteno, Y. Zhang, T. M. C. Abbott, F. B. Abdalla, M. Banerji, K. Bechtol, A. Benoit-Lévy, E. Bertin, D. Brooks, E. Buckley-Geer, D. L. Burke, A. Carnero Rosell, M. Carrasco Kind, J. Carretero, F. J. Castander, M. Crocce, C. E. Cunha, C. B. D'Andrea, L. N. da Costa, C. Davis, S. Desai, J. P. Dietrich, P. Doel, T. F. Eifler, E. Fernan-

dez, B. Flaugher, P. Fosalba, E. Gaztanaga, D. W. Gerdes, T. Giannantonio, D. A. Goldstein, D. Gruen, J. Gschwend, G. Gutierrez, K. Honscheid, B. Jain, D. J. James, T. Jeltema, M. W. G. Johnson, M. D. Johnson, S. Kent, E. Krause, R. Kron, K. Kuehn, S. Kuhlmann, O. Lahav, M. Lima, M. A. G. Maia, M. March, R. G. McMahon, F. Menanteau, R. Miquel, J. J. Mohr, R. C. Nichol, B. Nord, R. L. C. Ogando, D. Petravick, A. A. Plazas, A. K. Romer, A. Roodman, E. S. Rykoff, E. Sanchez, V. Scarpine, M. Schubnell, I. Sevilla-Noarbe, M. Smith, R. C. Smith, E. Suchyta, M. E. C. Swanson, G. Tarle, D. Thomas, R. C. Thomas, M. A. Troxel, V. Vikram, R. H. Wechsler, J. Weller, Dark Energy Survey, and Dark Energy Camera GW-EM Collaboration. The Electromagnetic Counterpart of the Binary Neutron Star Merger LIGO/Virgo GW170817. I. Discovery of the Optical Counterpart Using the Dark Energy Camera. ApJ, 848(2):L16, October 2017.

[93] B. P. Abbott, R. Abbott, T. D. Abbott, F. Acernese, K. Ackley, C. Adams, T. Adams, P. Addesso, R. X. Adhikari, V. B. Adya, C. Affeldt, M. Afrough, B. Agarwal, M. Agathos, K. Agatsuma, N. Aggarwal, O. D. Aguiar, L. Aiello, A. Ain, P. Ajith, B. Allen, G. Allen, A. Allocca, P. A. Altin, A. Amato, A. Ananyeva, S. B. Anderson, W. G. Anderson, S. V. Angelova, S. Antier, S. Appert, K. Arai, M. C. Araya, J. S. Areeda, N. Arnaud, K. G. Arun, S. Ascenzi, G. Ashton, M. Ast, S. M. Aston, P. Astone, D. V. Atallah, P. Aufmuth, C. Aulbert, K. Aultoneal, C. Austin, A. Avila-Alvarez, S. Babak, P. Bacon, M. K. M. Bader, S. Bae, P. T. Baker, F. Baldaccini, G. Ballardin, S. W. Ballmer, S. Banagiri, J. C. Barayoga, S. E. Barclay, B. C. Barish, D. Barker, K. Barkett, F. Barone, B. Barr, L. Barsotti, M. Barsuglia, D. Barta, J. Bartlett, I. Bartos, R. Bassiri, A. Basti, J. C. Batch, M. Bawaj, J. C. Bayley, M. Bazzan, B. Bécsy, C. Beer, M. Bejger, I. Belahcene, A. S. Bell, B. K. Berger, G. Bergmann, J. J. Bero, C. P. L. Berry, D. Bersanetti, A. Bertolini, J. Betzwieser, S. Bhagwat, R. Bhandare, I. A. Bilenko, G. Billingsley, C. R. Billman, J. Birch, R. Birney, O. Birnholtz, S. Biscans, S. Biscoveanu, A. Bisht, M. Bitossi, C. Biwer, M. A. Bizouard, J. K. Blackburn, J. Blackman, C. D. Blair, D. G. Blair, R. M. Blair, S. Bloemen, O. Bock, N. Bode, M. Boer, G. Bogaert, A. Bohe, F. Bondu, E. Bonilla, R. Bonnand, B. A. Boom, R. Bork, V. Boschi, S. Bose, K. Bossie, Y. Bouffanais, A. Bozzi, C. Bradaschia, P. R. Brady, M. Branchesi, J. E. Brau, T. Briant, A. Brillet, M. Brinkmann, V. Brisson, P. Brockill, J. E. Broida, A. F. Brooks, D. A. Brown, D. D. Brown, S. Brunett, C. C. Buchanan, A. Buikema, T. Bulik, H. J. Bulten, A. Buonanno, D. Buskulic, C. Buy, R. L. Byer, M. Cabero, L. Cadonati, G. Cagnoli, C. Cahillane, J. Calderón Bustillo, T. A. Callister, E. Calloni, J. B. Camp, M. Canepa, P. Canizares, K. C. Cannon, H. Cao, J. Cao, C. D. Capano, E. Capocasa, F. Carbognani, S. Caride, M. F. Carney, J. Casanueva Diaz, C. Casentini, S. Caudill,

M. Cavaglià, F. Cavalier, R. Cavalieri, G. Cella, C. B. Cepeda, P. Cerdá-Durán, G. Cerretani, E. Cesarini, S. J. Chamberlin, M. Chan, S. Chao, P. Charlton, E. Chase, E. Chassande-Mottin, D. Chatterjee, K. Chatziioannou, B. D. Cheeseboro, H. Y. Chen, X. Chen, Y. Chen, H. P. Cheng, H. Chia, A. Chincarini, A. Chiummo, T. Chmiel, H. S. Cho, M. Cho, J. H. Chow, N. Christensen, Q. Chu, A. J. K. Chua, S. Chua, A. K. W. Chung, S. Chung, G. Ciani, R. Ciolfi, C. E. Cirelli, A. Cirone, F. Clara, J. A. Clark, P. Clearwater, F. Cleva, C. Cocchieri, E. Coccia, P. F. Cohadon, D. Cohen, A. Colla, C. G. Collette, L. R. Cominsky, M. Constancio, L. Conti, S. J. Cooper, P. Corban, T. R. Corbitt, I. Cordero-Carrión, K. R. Corley, N. Cornish, A. Corsi, S. Cortese, C. A. Costa, M. W. Coughlin, S. B. Coughlin, J. P. Coulon, S. T. Countryman, P. Couvares, P. B. Covas, E. E. Cowan, D. M. Coward, M. J. Cowart, D. C. Coyne, R. Coyne, J. D. E. Creighton, T. D. Creighton, J. Cripe, S. G. Crowder, T. J. Cullen, A. Cumming, L. Cunningham, E. Cuoco, T. Dal Canton, G. Dálya, S. L. Danilishin, S. D'Antonio, K. Danzmann, A. Dasgupta, C. F. da Silva Costa, L. E. H. Datrier, V. Dattilo, I. Dave, M. Davier, D. Davis, E. J. Daw, B. Day, S. de, D. Debra, J. Degallaix, M. de Laurentis, S. Deléglise, W. Del Pozzo, N. Demos, T. Denker, T. Dent, R. de Pietri, V. Dergachev, R. De Rosa, R. T. Derosa, C. de Rossi, R. Desalvo, O. de Varona, J. Devenson, S. Dhurandhar, M. C. Díaz, L. di Fiore, M. di Giovanni, T. di Girolamo, A. di Lieto, S. di Pace, I. di Palma, F. di Renzo, Z. Doctor, V. Dolique, F. Donovan, K. L. Dooley, S. Doravari, I. Dorrington, R. Douglas, M. Dovale Álvarez, T. P. Downes, M. Drago, C. Dreissigacker, J. C. Driggers, Z. Du, M. Ducrot, P. Dupej, S. E. Dwyer, T. B. Edo, M. C. Edwards, A. Effler, H. B. Eggenstein, P. Ehrens, J. Eichholz, S. S. Eikenberry, R. A. Eisenstein, R. C. Essick, D. Estevez, Z. B. Etienne, T. Etzel, M. Evans, T. M. Evans, M. Factourovich, V. Fafone, H. Fair, S. Fairhurst, X. Fan, S. Farinon, B. Farr, W. M. Farr, E. J. Fauchon-Jones, M. Favata, M. Fays, C. Fee, H. Fehrmann, J. Feicht, M. M. Fejer, A. Fernandez-Galiana, I. Ferrante, E. C. Ferreira, F. Ferrini, F. Fidecaro, D. Finstad, I. Fiori, D. Fiorucci, M. Fishbach, R. P. Fisher, M. Fitz-Axen, R. Flaminio, M. Fletcher, H. Fong, J. A. Font, P. W. F. Forsyth, S. S. Forsyth, J. D. Fournier, S. Frasca, F. Frasconi, Z. Frei, A. Freise, R. Frey, V. Frey, E. M. Fries, P. Fritschel, V. V. Frolov, P. Fulda, M. Fyffe, H. Gabbard, B. U. Gadre, S. M. Gaebel, J. R. Gair, L. Gammaitoni, M. R. Ganija, S. G. Gaonkar, C. Garcia-Quiros, F. Garufi, B. Gateley, S. Gaudio, G. Gaur, V. Gayathri, N. Gehrels, G. Gemme, E. Genin, A. Gennai, D. George, J. George, L. Gergely, V. Germain, S. Ghonge, Abhirup Ghosh, Archisman Ghosh, S. Ghosh, J. A. Giaime, K. D. Giardina, A. Giazotto, K. Gill, L. Glover, E. Goetz, R. Goetz, S. Gomes, B. Goncharov, G. González, J. M. Gonzalez Castro, A. Gopakumar, M. L. Gorodetsky, S. E. Gossan, M. Gosselin, R. Gouaty, A. Grado, C. Graef, M. Granata,

A. Grant, S. Gras, C. Gray, G. Greco, A. C. Green, E. M. Gretarsson, P. Groot, H. Grote, S. Grunewald, P. Gruning, G. M. Guidi, X. Guo, A. Gupta, M. K. Gupta, K. E. Gushwa, E. K. Gustafson, R. Gustafson, O. Halim, B. R. Hall, E. D. Hall, E. Z. Hamilton, G. Hammond, M. Haney, M. M. Hanke, J. Hanks, C. Hanna, M. D. Hannam, O. A. Hannuksela, J. Hanson, T. Hardwick, J. Harms, G. M. Harry, I. W. Harry, M. J. Hart, C. J. Haster, K. Haughian, J. Healy, A. Heidmann, M. C. Heintze, H. Heitmann, P. Hello, G. Hemming, M. Hendry, I. S. Heng, J. Hennig, A. W. Heptonstall, M. Heurs, S. Hild, T. Hinderer, D. Hoak, D. Hofman, K. Holt, D. E. Holz, P. Hopkins, C. Horst, J. Hough, E. A. Houston, E. J. Howell, A. Hreibi, Y. M. Hu, E. A. Huerta, D. Huet, B. Hughey, S. Husa, S. H. Huttner, T. Huynh-Dinh, N. Indik, R. Inta, G. Intini, H. N. Isa, J. M. Isac, M. Isi, B. R. Iyer, K. Izumi, T. Jacqmin, K. Jani, P. Jaranowski, S. Jawahar, F. Jiménez-Forteza, W. W. Johnson, D. I. Jones, R. Jones, R. J. G. Jonker, L. Ju, J. Junker, C. V. Kalaghatgi, V. Kalogera, B. Kamai, S. Kandhasamy, G. Kang, J. B. Kanner, S. J. Kapadia, S. Karki, K. S. Karvinen, M. Kasprzack, M. Katolik, E. Katsavounidis, W. Katzman, S. Kaufer, K. Kawabe, F. Kéfélian, D. Keitel, A. J. Kemball, R. Kennedy, C. Kent, J. S. Key, F. Y. Khalili, I. Khan, S. Khan, Z. Khan, E. A. Khazanov, N. Kijbunchoo, Chunglee Kim, J. C. Kim, K. Kim, W. Kim, W. S. Kim, Y. M. Kim, S. J. Kimbrell, E. J. King, P. J. King, M. Kinley-Hanlon, R. Kirchhoff, J. S. Kissel, L. Kleybolte, S. Klimenko, T. D. Knowles, P. Koch, S. M. Koehlenbeck, S. Koley, V. Kondrashov, A. Kontos, M. Korobko, W. Z. Korth, I. Kowalska, D. B. Kozak, C. Krämer, V. Kringel, B. Krishnan, A. Królak, G. Kuehn, P. Kumar, R. Kumar, S. Kumar, L. Kuo, A. Kutynia, S. Kwang, B. D. Lackey, K. H. Lai, M. Landry, R. N. Lang, J. Lange, B. Lantz, R. K. Lanza, A. Lartaux-Vollard, P. D. Lasky, M. Laxen, A. Lazzarini, C. Lazzaro, P. Leaci, S. Leavey, C. H. Lee, H. K. Lee, H. M. Lee, H. W. Lee, K. Lee, J. Lehmann, A. Lenon, M. Leonardi, N. Leroy, N. Letendre, Y. Levin, T. G. F. Li, S. D. Linker, T. B. Littenberg, J. Liu, X. Liu, R. K. L. Lo, N. A. Lockerbie, L. T. London, J. E. Lord, M. Lorenzini, V. Loriette, M. Lormand, G. Losurdo, J. D. Lough, C. O. Lousto, G. Lovelace, H. Lück, D. Lumaca, A. P. Lundgren, R. Lynch, Y. Ma, R. Macas, S. Macfoy, B. Machenschalk, M. Macinnis, D. M. MacLeod, I. Magaña Hernandez, F. Magaña-Sandoval, L. Magaña Zertuche, R. M. Magee, E. Majorana, I. Maksimovic, N. Man, V. Mandic, V. Mangano, G. L. Mansell, M. Manske, M. Mantovani, F. Marchesoni, F. Marion, S. Márka, Z. Márka, C. Markakis, A. S. Markosyan, A. Markowitz, E. Maros, A. Marquina, F. Martelli, L. Martellini, I. W. Martin, R. M. Martin, D. V. Martynov, K. Mason, E. Massera, A. Masserot, T. J. Massinger, M. Masso-Reid, S. Mastrogiovanni, A. Matas, F. Matichard, L. Matone, N. Mavalvala, N. Mazumder, R. McCarthy, D. E. McClelland, S. McCormick, L. Mc-

Culler, S. C. McGuire, G. McIntyre, J. McIver, D. J. McManus, L. McNeill, T. McRae, S. T. McWilliams, D. Meacher, G. D. Meadors, M. Mehmet, J. Meidam, E. Mejuto-Villa, A. Melatos, G. Mendell, R. A. Mercer, E. L. Merilh, M. Merzougui, S. Meshkov, C. Messenger, C. Messick, R. Metzdorff, P. M. Meyers, H. Miao, C. Michel, H. Middleton, E. E. Mikhailov, L. Milano, A. L. Miller, B. B. Miller, J. Miller, M. Millhouse, M. C. Milovich-Goff, O. Minazzoli, Y. Minenkov, J. Ming, C. Mishra, S. Mitra, V. P. Mitrofanov, G. Mitselmakher, R. Mittleman, D. Moffa, A. Moggi, K. Mogushi, M. Mohan, S. R. P. Mohapatra, M. Montani, C. J. Moore, D. Moraru, G. Moreno, S. R. Morriss, B. Mours, C. M. Mow-Lowry, G. Mueller, A. W. Muir, Arunava Mukherjee, D. Mukherjee, S. Mukherjee, N. Mukund, A. Mullavey, J. Munch, E. A. Muñiz, M. Muratore, P. G. Murray, K. Napier, I. Nardecchia, L. Naticchioni, R. K. Nayak, J. Neilson, G. Nelemans, T. J. N. Nelson, M. Nery, A. Neunzert, L. Nevin, J. M. Newport, G. Newton, K. K. Y. Ng, T. T. Nguyen, D. Nichols, A. B. Nielsen, S. Nissanke, A. Nitz, A. Noack, F. Nocera, D. Nolting, C. North, L. K. Nuttall, J. Oberling, G. D. O'Dea, G. H. Ogin, J. J. Oh, S. H. Oh, F. Ohme, M. A. Okada, M. Oliver, P. Oppermann, Richard J. Oram, B. O'Reilly, R. Ormiston, L. F. Ortega, R. O'Shaughnessy, S. Ossokine, D. J. Ottaway, H. Overmier, B. J. Owen, A. E. Pace, J. Page, M. A. Page, A. Pai, S. A. Pai, J. R. Palamos, O. Palashov, C. Palomba, A. Pal-Singh, Howard Pan, Huang-Wei Pan, B. Pang, P. T. H. Pang, C. Pankow, F. Pannarale, B. C. Pant, F. Paoletti, A. Paoli, M. A. Papa, A. Parida, W. Parker, D. Pascucci, A. Pasqualetti, R. Passaquieti, D. Passuello, M. Patil, B. Patricelli, B. L. Pearlstone, M. Pedraza, R. Pedurand, L. Pekowsky, A. Pele, S. Penn, C. J. Perez, A. Perreca, L. M. Perri, H. P. Pfeiffer, M. Phelps, O. J. Piccinni, M. Pichot, F. Piergiovanni, V. Pierro, G. Pillant, L. Pinard, I. M. Pinto, M. Pirello, M. Pitkin, M. Poe, R. Poggiani, P. Popolizio, E. K. Porter, A. Post, J. Powell, J. Prasad, J. W. W. Pratt, G. Pratten, V. Predoi, T. Prestegard, M. Prijatelj, M. Principe, S. Privitera, G. A. Prodi, L. G. Prokhorov, O. Puncken, M. Punturo, P. Puppo, M. Pürrer, H. Qi, V. Quetschke, E. A. Quintero, R. Quitzow-James, F. J. Raab, D. S. Rabeling, H. Radkins, P. Raffai, S. Raja, C. Rajan, B. Rajbhandari, M. Rakhmanov, K. E. Ramirez, A. Ramos-Buades, P. Rapagnani, V. Raymond, M. Razzano, J. Read, T. Regimbau, L. Rei, S. Reid, D. H. Reitze, W. Ren, S. D. Reyes, F. Ricci, P. M. Ricker, S. Rieger, K. Riles, M. Rizzo, N. A. Robertson, R. Robie, F. Robinet, A. Rocchi, L. Rolland, J. G. Rollins, V. J. Roma, J. D. Romano, R. Romano, C. L. Romel, J. H. Romie, D. Rosińska, M. P. Ross, S. Rowan, A. Rüdiger, P. Ruggi, G. Rutins, K. Ryan, S. Sachdev, T. Sadecki, L. Sadeghian, M. Sakellariadou, L. Salconi, M. Saleem, F. Salemi, A. Samajdar, L. Sammut, L. M. Sampson, E. J. Sanchez, L. E. Sanchez, N. Sanchis-Gual, V. Sandberg, J. R. Sanders,

B. Sassolas, B. S. Sathyaprakash, P. R. Saulson, O. Sauter, R. L. Savage, A. Sawadsky, P. Schale, M. Scheel, J. Scheuer, J. Schmidt, P. Schmidt, R. Schnabel, R. M. S. Schofield, A. Schönbeck, E. Schreiber, D. Schuette, B. W. Schulte, B. F. Schutz, S. G. Schwalbe, J. Scott, S. M. Scott, E. Seidel, D. Sellers, A. S. Sengupta, D. Sentenac, V. Sequino, A. Sergeev, D. A. Shaddock, T. J. Shaffer, A. A. Shah, M. S. Shahriar, M. B. Shaner, L. Shao, B. Shapiro, P. Shawhan, A. Sheperd, D. H. Shoemaker, D. M. Shoemaker, K. Siellez, X. Siemens, M. Sieniawska, D. Sigg, A. D. Silva, L. P. Singer, A. Singh, A. Singhal, A. M. Sintes, B. J. J. Slagmolen, B. Smith, J. R. Smith, R. J. E. Smith, S. Somala, E. J. Son, J. A. Sonnenberg, B. Sorazu, F. Sorrentino, T. Souradeep, A. P. Spencer, A. K. Srivastava, K. Staats, A. Staley, D. Steer, M. Steinke, J. Steinlechner, S. Steinlechner, D. Steinmeyer, S. P. Stevenson, R. Stone, D. J. Stops, K. A. Strain, G. Stratta, S. E. Strigin, A. Strunk, R. Sturani, A. L. Stuver, T. Z. Summerscales, L. Sun, S. Sunil, J. Suresh, P. J. Sutton, B. L. Swinkels, M. J. Szczepańczyk, M. Tacca, S. C. Tait, C. Talbot, D. Talukder, D. B. Tanner, M. Tápai, A. Taracchini, J. D. Tasson, J. A. Taylor, R. Taylor, S. V. Tewari, T. Theeg, F. Thies, E. G. Thomas, M. Thomas, P. Thomas, K. A. Thorne, E. Thrane, S. Tiwari, V. Tiwari, K. V. Tokmakov, K. Toland, M. Tonelli, Z. Tornasi, A. Torres-Forné, C. I. Torrie, D. Töyrä, F. Travasso, G. Traylor, J. Trinastic, M. C. Tringali, L. Trozzo, K. W. Tsang, M. Tse, R. Tso, L. Tsukada, D. Tsuna, D. Tuyenbayev, K. Ueno, D. Ugolini, C. S. Unnikrishnan, A. L. Urban, S. A. Usman, H. Vahlbruch, G. Vajente, G. Valdes, N. van Bakel, M. van Beuzekom, J. F. J. van den Brand, C. van den Broeck, D. C. Vander-Hyde, L. van der Schaaf, J. V. van Heijningen, A. A. van Veggel, M. Vardaro, V. Varma, S. Vass, M. Vasúth, A. Vecchio, G. Vedovato, J. Veitch, P. J. Veitch, K. Venkateswara, G. Venugopalan, D. Verkindt, F. Vetrano, A. Viceré, A. D. Viets, S. Vinciguerra, D. J. Vine, J. Y. Vinet, S. Vitale, T. Vo, H. Vocca, C. Vorvick, S. P. Vyatchanin, A. R. Wade, L. E. Wade, M. Wade, R. Walet, M. Walker, L. Wallace, S. Walsh, G. Wang, H. Wang, J. Z. Wang, W. H. Wang, Y. F. Wang, R. L. Ward, J. Warner, M. Was, J. Watchi, B. Weaver, L. W. Wei, M. Weinert, A. J. Weinstein, R. Weiss, L. Wen, E. K. Wessel, P. Weßels, J. Westerweck, T. Westphal, K. Wette, J. T. Whelan, S. E. Whitcomb, B. F. Whiting, C. Whittle, D. Wilken, D. Williams, R. D. Williams, A. R. Williamson, J. L. Willis, B. Willke, M. H. Wimmer, W. Winkler, C. C. Wipf, H. Wittel, G. Woan, J. Woehler, J. Wofford, K. W. K. Wong, J. Worden, J. L. Wright, D. S. Wu, D. M. Wysocki, S. Xiao, H. Yamamoto, C. C. Yancey, L. Yang, M. J. Yap, M. Yazback, Hang Yu, Haocun Yu, M. Yvert, A. Zadrożny, M. Zanolin, T. Zelenova, J. P. Zendri, M. Zevin, L. Zhang, M. Zhang, T. Zhang, Y. H. Zhang, C. Zhao, M. Zhou, Z. Zhou, S. J. Zhu, X. J. Zhu, A. B. Zimmerman, M. E. Zucker, J. Zweizig, R. J. Foley, D. A. Coulter, M. R. Drout, D. Kasen,

C. D. Kilpatrick, B. F. Madore, A. Murguia-Berthier, Y. C. Pan, A. L. Piro, J. X. Prochaska, E. Ramirez-Ruiz, A. Rest, C. Rojas-Bravo, B. J. Shappee, M. R. Siebert, J. D. Simon, N. Ulloa, J. Annis, M. Soares-Santos, D. Brout, D. Scolnic, H. T. Diehl, J. Frieman, E. Berger, K. D. Alexander, S. Allam, E. Balbinot, P. Blanchard, R. E. Butler, R. Chornock, E. R. Cook, P. Cowperthwaite, A. Drlica-Wagner, M. R. Drout, F. Durret, T. Eftekhari, D. A. Finley, W. Fong, C. L. Fryer, J. García-Bellido, M. S. S. Gill, R. A. Gruendl, C. Hanna, W. Hartley, K. Herner, D. Huterer, D. Kasen, R. Kessler, T. S. Li, H. Lin, P. A. A. Lopes, A. C. C. Lourenço, R. Margutti, J. Marriner, J. L. Marshall, T. Matheson, G. E. Medina, B. D. Metzger, R. R. Muñoz, J. Muir, M. Nicholl, P. Nugent, A. Palmese, F. Paz-Chinchón, E. Quataert, M. Sako, M. Sauseda, D. J. Schlegel, L. F. Secco, N. Smith, F. Sobreira, A. Stebbins, V. A. Villar, A. K. Vivas, W. Wester, P. K. G. Williams, B. Yanny, A. Zenteno, T. M. C. Abbott, F. B. Abdalla, K. Bechtol, A. Benoit-Lévy, E. Bertin, S. L. Bridle, D. Brooks, E. Buckley-Geer, D. L. Burke, A. Carnero Rosell, M. Carrasco Kind, J. Carretero, F. J. Castander, C. E. Cunha, C. B. D'Andrea, L. N. da Costa, C. Davis, D. L. Depoy, S. Desai, J. P. Dietrich, J. Estrada, E. Fernandez, B. Flaugher, P. Fosalba, E. Gaztanaga, D. W. Gerdes, T. Giannantonio, D. A. Goldstein, D. Gruen, G. Gutierrez, W. G. Hartley, K. Honscheid, B. Jain, D. J. James, T. Jeltema, M. W. G. Johnson, S. Kent, E. Krause, R. Kron, K. Kuehn, S. Kuhlmann, N. Kuropatkin, O. Lahav, M. Lima, M. A. G. Maia, M. March, C. J. Miller, R. Miquel, E. Neilsen, B. Nord, R. L. C. Ogando, A. A. Plazas, A. K. Romer, A. Roodman, E. S. Rykoff, E. Sanchez, V. Scarpine, M. Schubnell, I. Sevilla-Noarbe, M. Smith, R. C. Smith, E. Suchyta, G. Tarle, D. Thomas, R. C. Thomas, M. A. Troxel, D. L. Tucker, V. Vikram, A. R. Walker, J. Weller, Y. Zhang, J. B. Haislip, V. V. Kouprianov, D. E. Reichart, L. Tartaglia, D. J. Sand, S. Valenti, S. Yang, Iair Arcavi, Griffin Hosseinzadeh, D. Andrew Howell, Curtis McCully, Dovi Poznanski, Sergiy Vasylyev, N. R. Tanvir, A. J. Levan, J. Hjorth, Z. Cano, C. Copperwheat, A. de Ugarte-Postigo, P. A. Evans, J. P. U. Fynbo, C. González-Fernández, J. Greiner, M. Irwin, J. Lyman, I. Mandel, R. McMahon, B. Milvang-Jensen, P. O'Brien, J. P. Osborne, D. A. Perley, E. Pian, E. Palazzi, E. Rol, S. Rosetti, S. Rosswog, A. Rowlinson, S. Schulze, D. T. H. Steeghs, C. C. Thöne, K. Ulaczyk, D. Watson, K. Wiersema, V. M. Lipunov, E. Gorbovskoy, V. G. Kornilov, N. Tyurina, P. Balanutsa, D. Vlasenko, I. Gorbunov, R. Podesta, H. Levato, C. Saffe, D. A. H. Buckley, N. M. Budnev, O. Gress, V. Yurkov, R. Rebolo, and M. Serra-Ricart. A gravitational-wave standard siren measurement of the Hubble constant. Nature, 551(7678):85–88, November 2017.

[94] DES Collaboration, A. Garcia, R. Morgan, K. Herner, A. Palmese, M. Soares-Santos, J. Annis, D. Brout, A. K. Vivas, A. Drlica-Wagner,

L. Santana-Silva, D. L. Tucker, S. Allam, M. Wiesner, J. García-Bellido, M. S. S. Gill, M. Sako, R. Kessler, T. M. Davis, D. Scolnic, F. Olivares E., F. Paz-Chinchón, N. Sherman, C. Conselice, H. Chen, R. J. Foley, Z. Doctor, J. Horvath, D. A. Howell, C. D. Kilpatrick, J. Casares, J. Cooke, A. Rest, T. M. C. Abbott, M. Aguena, S. Avila, E. Bertin, S. Bhargava, D. Brooks, D. L. Burke, A. Carnero Rosell, M. Carrasco Kind, J. Carretero, M. Costanzi, L. N. da Costa, S. Desai, H. T. Diehl, J. P. Dietrich, P. Doel, S. Everett, B. Flaugher, P. Fosalba, D. Friedel, J. Frieman, E. Gaztanaga, D. W. Gerdes, D. Gruen, R. A. Gruendl, J. Gschwend, G. Gutierrez, S. R. Hinton, D. L. Hollowood, K. Honscheid, D. J. James, K. Kuehn, N. Kuropatkin, O. Lahav, M. Lima, M. A. G. Maia, M. March, J. L. Marshall, F. Menanteau, R. Miquel, R. L. C. Ogando, A. A. Plazas, A. K. Romer, A. Roodman, E. Sanchez, V. Scarpine, M. Schubnell, S. Serrano, I. Sevilla-Noarbe, M. Smith, E. Suchyta, M. E. C. Swanson, G. Tarle, D. Thomas, T. N. Varga, A. R. Walker, and J. Weller. A DESGW Search for the Electromagnetic Counterpart to the LIGO/Virgo Gravitational Wave Binary Neutron Star Merger Candidate S190510g. *arXiv e-prints*, page arXiv:2007.00050, June 2020.

[95] Dark Energy Survey Collaboration, T. Abbott, F. B. Abdalla, J. Aleksić, S. Allam, A. Amara, D. Bacon, E. Balbinot, M. Banerji, K. Bechtol, A. Benoit-Lévy, G. M. Bernstein, E. Bertin, J. Blazek, C. Bonnett, S. Bridle, D. Brooks, R. J. Brunner, E. Buckley-Geer, D. L. Burke, G. B. Caminha, D. Capozzi, J. Carlsen, A. Carnero-Rosell, M. Carollo, M. Carrasco-Kind, J. Carretero, F. J. Castander, L. Clerkin, T. Collett, C. Conselice, M. Crocce, C. E. Cunha, C. B. D'Andrea, L. N. da Costa, T. M. Davis, S. Desai, H. T. Diehl, J. P. Dietrich, S. Dodelson, P. Doel, A. Drlica-Wagner, J. Estrada, J. Etherington, A. E. Evrard, J. Fabbri, D. A. Finley, B. Flaugher, R. J. Foley, P. Fosalba, J. Frieman, J. García-Bellido, E. Gaztanaga, D. W. Gerdes, T. Giannantonio, D. A. Goldstein, D. Gruen, R. A. Gruendl, P. Guarnieri, G. Gutierrez, W. Hartley, K. Honscheid, B. Jain, D. J. James, T. Jeltema, S. Jouvel, R. Kessler, A. King, D. Kirk, R. Kron, K. Kuehn, N. Kuropatkin, O. Lahav, T. S. Li, M. Lima, H. Lin, M. A. G. Maia, M. Makler, M. Manera, C. Maraston, J. L. Marshall, P. Martini, R. G. McMahon, P. Melchior, A. Merson, C. J. Miller, R. Miquel, J. J. Mohr, X. Morice-Atkinson, K. Naidoo, E. Neilsen, R. C. Nichol, B. Nord, R. Ogando, F. Ostrovski, A. Palmese, A. Papadopoulos, H. V. Peiris, J. Peoples, W. J. Percival, A. A. Plazas, S. L. Reed, A. Refregier, A. K. Romer, A. Roodman, A. Ross, E. Rozo, E. S. Rykoff, I. Sadeh, M. Sako, C. Sánchez, E. Sanchez, B. Santiago, V. Scarpine, M. Schubnell, I. Sevilla-Noarbe, E. Sheldon, M. Smith, R. C. Smith, M. Soares-Santos, F. Sobreira, M. Soumagnac, E. Suchyta, M. Sullivan, M. Swanson, G. Tarle, J. Thaler,

D. Thomas, R. C. Thomas, D. Tucker, J. D. Vieira, V. Vikram, A. R. Walker, R. H. Wechsler, J. Weller, W. Wester, L. Whiteway, H. Wilcox, B. Yanny, Y. Zhang, and J. Zuntz. The Dark Energy Survey: more than dark energy - an overview. MNRAS, 460(2):1270–1299, August 2016.

[96] Y. Park, E. Krause, S. Dodelson, B. Jain, A. Amara, M. R. Becker, S. L. Bridle, J. Clampitt, M. Crocce, P. Fosalba, E. Gaztanaga, K. Honscheid, E. Rozo, F. Sobreira, C. Sánchez, R. H. Wechsler, T. Abbott, F. B. Abdalla, S. Allam, A. Benoit-Lévy, E. Bertin, D. Brooks, E. Buckley-Geer, D. L. Burke, A. Carnero Rosell, M. Carrasco Kind, J. Carretero, F. J. Castander, L. N. da Costa, D. L. DePoy, S. Desai, J. P. Dietrich, P. Doel, T. F. Eifler, A. Fausti Neto, E. Fernandez, D. A. Finley, B. Flaugher, D. W. Gerdes, D. Gruen, R. A. Gruendl, G. Gutierrez, D. J. James, S. Kent, K. Kuehn, N. Kuropatkin, M. Lima, M. A. G. Maia, J. L. Marshall, P. Melchior, C. J. Miller, R. Miquel, R. C. Nichol, R. Ogando, A. A. Plazas, N. Roe, A. K. Romer, E. S. Rykoff, E. Sanchez, V. Scarpine, M. Schubnell, I. Sevilla-Noarbe, M. Soares-Santos, E. Suchyta, M. E. C. Swanson, G. Tarle, J. Thaler, V. Vikram, A. R. Walker, J. Weller, J. Zuntz, and DES Collaboration. Joint analysis of galaxy-galaxy lensing and galaxy clustering: Methodology and forecasts for Dark Energy Survey. Phys. Rev. D, 94(6):063533, September 2016.

[97] Jelte T. A. de Jong, Gijs A. Verdoes Kleijn, Konrad H. Kuijken, and Edwin A. Valentijn. The Kilo-Degree Survey. *Experimental Astronomy*, 35(1-2):25–44, January 2013.

[98] Hiroaki Aihara, Nobuo Arimoto, Robert Armstrong, Stéphane Arnouts, Neta A. Bahcall, Steven Bickerton, James Bosch, Kevin Bundy, Peter L. Capak, James H. H. Chan, Masashi Chiba, Jean Coupon, Eiichi Egami, Motohiro Enoki, Francois Finet, Hiroki Fujimori, Seiji Fujimoto, Hisanori Furusawa, Junko Furusawa, Tomotsugu Goto, Andy Goulding, Johnny P. Greco, Jenny E. Greene, James E. Gunn, Takashi Hamana, Yuichi Harikane, Yasuhiro Hashimoto, Takashi Hattori, Masao Hayashi, Yusuke Hayashi, Krzysztof G. Hełminiak, Ryo Higuchi, Chiaki Hikage, Paul T. P. Ho, Bau-Ching Hsieh, Kuiyun Huang, Song Huang, Hiroyuki Ikeda, Masatoshi Imanishi, Akio K. Inoue, Kazushi Iwasawa, Ikuru Iwata, Anton T. Jaelani, Hung-Yu Jian, Yukiko Kamata, Hiroshi Karoji, Nobunari Kashikawa, Nobuhiko Katayama, Satoshi Kawanomoto, Issha Kayo, Jin Koda, Michitaro Koike, Takashi Kojima, Yutaka Komiyama, Akira Konno, Shintaro Koshida, Yusei Koyama, Haruka Kusakabe, Alexie Leauthaud, Chien-Hsiu Lee, Lihwai Lin, Yen-Ting Lin, Robert H. Lupton, Rachel Mandelbaum, Yoshiki Matsuoka, Elinor Medezinski, Sogo Mineo, Shoken Miyama, Hironao Miyatake, Satoshi Miyazaki, Rieko Momose, Anupreeta More, Surhud More,

Yuki Moritani, Takashi J. Moriya, Tomoki Morokuma, Shiro Mukae, Ryoma Murata, Hitoshi Murayama, Tohru Nagao, Fumiaki Nakata, Mana Niida, Hiroko Niikura, Atsushi J. Nishizawa, Yoshiyuki Obuchi, Masamune Oguri, Yukie Oishi, Nobuhiro Okabe, Sakurako Okamoto, Yuki Okura, Yoshiaki Ono, Masato Onodera, Masafusa Onoue, Ken Osato, Masami Ouchi, Paul A. Price, Tae-Soo Pyo, Masao Sako, Marcin Sawicki, Takatoshi Shibuya, Kazuhiro Shimasaku, Atsushi Shimono, Masato Shirasaki, John D. Silverman, Melanie Simet, Joshua Speagle, David N. Spergel, Michael A. Strauss, Yuma Sugahara, Naoshi Sugiyama, Yasushi Suto, Sherry H. Suyu, Nao Suzuki, Philip J. Tait, Masahiro Takada, Tadafumi Takata, Naoyuki Tamura, Manobu M. Tanaka, Masaomi Tanaka, Masayuki Tanaka, Yoko Tanaka, Tsuyoshi Terai, Yuichi Terashima, Yoshiki Toba, Nozomu Tominaga, Jun Toshikawa, Edwin L. Turner, Tomohisa Uchida, Hisakazu Uchiyama, Keiichi Umetsu, Fumihiro Uraguchi, Yuji Urata, Tomonori Usuda, Yousuke Utsumi, Shiang-Yu Wang, Wei-Hao Wang, Kenneth C. Wong, Kiyoto Yabe, Yoshihiko Yamada, Hitomi Yamanoi, Naoki Yasuda, Sherry Yeh, Atsunori Yonehara, and Suraphong Yuma. The Hyper Suprime-Cam SSP Survey: Overview and survey design. PASJ, 70:S4, January 2018.

[99] Donald G. York, J. Adelman, Jr. Anderson, John E., Scott F. Anderson, James Annis, Neta A. Bahcall, J. A. Bakken, Robert Barkhouser, Steven Bastian, Eileen Berman, William N. Boroski, Steve Bracker, Charlie Briegel, John W. Briggs, J. Brinkmann, Robert Brunner, Scott Burles, Larry Carey, Michael A. Carr, Francisco J. Castander, Bing Chen, Patrick L. Colestock, A. J. Connolly, J. H. Crocker, István Csabai, Paul C. Czarapata, John Eric Davis, Mamoru Doi, Tom Dombeck, Daniel Eisenstein, Nancy Ellman, Brian R. Elms, Michael L. Evans, Xiaohui Fan, Glenn R. Federwitz, Larry Fiscelli, Scott Friedman, Joshua A. Frieman, Masataka Fukugita, Bruce Gillespie, James E. Gunn, Vijay K. Gurbani, Ernst de Haas, Merle Haldeman, Frederick H. Harris, J. Hayes, Timothy M. Heckman, G. S. Hennessy, Robert B. Hindsley, Scott Holm, Donald J. Holmgren, Chi-hao Huang, Charles Hull, Don Husby, Shin-Ichi Ichikawa, Takashi Ichikawa, Željko Ivezić, Stephen Kent, Rita S. J. Kim, E. Kinney, Mark Klaene, A. N. Kleinman, S. Kleinman, G. R. Knapp, John Korienek, Richard G. Kron, Peter Z. Kunszt, D. Q. Lamb, B. Lee, R. French Leger, Siriluk Limmongkol, Carl Lindenmeyer, Daniel C. Long, Craig Loomis, Jon Loveday, Rich Lucinio, Robert H. Lupton, Bryan MacKinnon, Edward J. Mannery, P. M. Mantsch, Bruce Margon, Peregrine McGehee, Timothy A. McKay, Avery Meiksin, Aronne Merelli, David G. Monet, Jeffrey A. Munn, Vijay K. Narayanan, Thomas Nash, Eric Neilsen, Rich Neswold, Heidi Jo Newberg, R. C. Nichol, Tom Nicinski, Mario Nonino, Norio Okada, Sadanori Okamura, Jeremiah P. Ostriker, Russell Owen, A. George Pauls, John Peoples, R. L. Peterson, Don-

ald Petravick, Jeffrey R. Pier, Adrian Pope, Ruth Pordes, Angela Prosapio, Ron Rechenmacher, Thomas R. Quinn, Gordon T. Richards, Michael W. Richmond, Claudio H. Rivetta, Constance M. Rockosi, Kurt Ruthmansdorfer, Dale Sandford, David J. Schlegel, Donald P. Schneider, Maki Sekiguchi, Gary Sergey, Kazuhiro Shimasaku, Walter A. Siegmund, Stephen Smee, J. Allyn Smith, S. Snedden, R. Stone, Chris Stoughton, Michael A. Strauss, Christopher Stubbs, Mark SubbaRao, Alexander S. Szalay, Istvan Szapudi, Gyula P. Szokoly, Anirudda R. Thakar, Christy Tremonti, Douglas L. Tucker, Alan Uomoto, Dan Vanden Berk, Michael S. Vogeley, Patrick Waddell, Shu-i. Wang, Masaru Watanabe, David H. Weinberg, Brian Yanny, Naoki Yasuda, and SDSS Collaboration. The Sloan Digital Sky Survey: Technical Summary. AJ, 120(3):1579–1587, September 2000.

[100] T. M. C. Abbott, M. Adamow, M. Aguena, S. Allam, A. Amon, S. Avila, D. Bacon, M. Banerji, K. Bechtol, M. R. Becker, G. M. Bernstein, E. Bertin, S. Bhargava, S. L. Bridle, D. Brooks, D. L. Burke, A. Carnero Rosell, M. Carrasco Kind, J. Carretero, F. J. Castander, R. Cawthon, C. Chang, A. Choi, C. Conselice, M. Costanzi, M. Crocce, L. N. da Costa, T. M. Davis, J. De Vicente, J. DeRose, S. Desai, H. T. Diehl, J. P. Dietrich, A. Drlica-Wagner, K. Eckert, J. Elvin-Poole, S. Everett, A. E. Evrard, I. Ferrero, A. Ferté, B. Flaugher, P. Fosalba, D. Friedel, J. Frieman, J. García-Bellido, L. Gelman, D. W. Gerdes, T. Giannantonio, M. Gill, D. Gruen, R. A. Gruendl, J. Gschwend, G. Gutierrez, W. G. Hartley, S. R. Hinton, D. L. Hollowood, D. Huterer, D. J. James, T. Jeltema, M. D. Johnson, S. Kent, R. Kron, K. Kuehn, N. Kuropatkin, O. Lahav, T. S. Li, C. Lidman, H. Lin, N. MacCrann, M. A. G. Maia, T. Manning, M. March, J. L. Marshall, P. Martini, P. Melchior, F. Menanteau, R. Miquel, R. Morgan, J. Myles, E. Neilsen, R. L. C. Ogando, A. Palmese, F. Paz-Chinchón, D. Petravick, A. Pieres, A. A. Plazas, C. Pond, M. Rodriguez-Monroy, A. K. Romer, A. Roodman, E. S. Rykoff, M. Sako, E. Sanchez, B. Santiago, S. Serrano, I. Sevilla-Noarbe, J. Allyn. Smith, M. Smith, M. Soares-Santos, E. Suchyta, M. E. C. Swanson, G. Tarle, D. Thomas, C. To, P. E. Tremblay, M. A. Troxel, D. L. Tucker, D. J Turner, T. N. Varga, A. R. Walker, R. H. Wechsler, J. Weller, W. Wester, R. D. Wilkinson, B. Yanny, Y. Zhang, R. Nikutta, M. Fitzpatrick, A. Jacques, A. Scott, K. Olsen, L. Huang, D. Herrera, S. Juneau, D. Nidever, B. A. Weaver, C. Adean, V. Correia, M. de Freitas, F. N. Freitas, C. Singulani, and G. Vila-Verde. The Dark Energy Survey Data Release 2. *arXiv e-prints*, page arXiv:2101.05765, January 2021.

[101] T. M. C. Abbott, A. Alarcon, S. Allam, P. Andersen, F. Andrade-Oliveira, J. Annis, J. Asorey, S. Avila, D. Bacon, N. Banik, B. A. Bassett, E. Baxter, K. Bechtol, M. R. Becker, G. M. Bernstein, E. Bertin, J. Blazek, S. L. Bridle, D. Brooks, D. Brout, D. L. Burke, J. Calcino, H. Camacho, A. Cam-

pos, A. Carnero Rosell, D. Carollo, M. Carrasco Kind, J. Carretero, F. J. Castander, R. Cawthon, P. Challis, K. C. Chan, C. Chang, M. Childress, M. Crocce, C. E. Cunha, C. B. D'Andrea, L. N. da Costa, C. Davis, T. M. Davis, J. De Vicente, D. L. DePoy, J. DeRose, S. Desai, H. T. Diehl, J. P. Dietrich, S. Dodelson, P. Doel, A. Drlica-Wagner, T. F. Eifler, J. Elvin-Poole, J. Estrada, A. E. Evrard, E. Fernandez, B. Flaugher, R. J. Foley, P. Fosalba, J. Frieman, L. Galbany, J. García-Bellido, M. Gatti, E. Gaztanaga, D. W. Gerdes, T. Giannantonio, K. Glazebrook, D. A. Goldstein, D. Gruen, R. A. Gruendl, J. Gschwend, G. Gutierrez, W. G. Hartley, S. R. Hinton, D. L. Hollowood, K. Honscheid, J. K. Hoormann, B. Hoyle, D. Huterer, B. Jain, D. J. James, M. Jarvis, T. Jeltema, E. Kasai, S. Kent, R. Kessler, A. G. Kim, N. Kokron, E. Krause, R. Kron, K. Kuehn, N. Kuropatkin, O. Lahav, J. Lasker, P. Lemos, G. F. Lewis, T. S. Li, C. Lidman, M. Lima, H. Lin, E. Macaulay, N. MacCrann, M. A. G. Maia, M. March, J. Marriner, J. L. Marshall, P. Martini, R. G. McMahon, P. Melchior, F. Menanteau, R. Miquel, J. J. Mohr, E. Morganson, J. Muir, A. Möller, E. Neilsen, R. C. Nichol, B. Nord, R. L. C. Ogando, A. Palmese, Y. C. Pan, H. V. Peiris, W. J. Percival, A. A. Plazas, A. Porredon, J. Prat, A. K. Romer, A. Roodman, R. Rosenfeld, A. J. Ross, E. S. Rykoff, S. Samuroff, C. Sánchez, E. Sanchez, V. Scarpine, R. Schindler, M. Schubnell, D. Scolnic, L. F. Secco, S. Serrano, I. Sevilla-Noarbe, R. Sharp, E. Sheldon, M. Smith, M. Soares-Santos, F. Sobreira, N. E. Sommer, E. Swann, M. E. C. Swanson, G. Tarle, D. Thomas, R. C. Thomas, M. A. Troxel, B. E. Tucker, S. A. Uddin, P. Vielzeuf, A. R. Walker, M. Wang, N. Weaverdyck, R. H. Wechsler, J. Weller, B. Yanny, B. Zhang, Y. Zhang, J. Zuntz, and DES Collaboration. Cosmological Constraints from Multiple Probes in the Dark Energy Survey. Phys. Rev. Lett., 122(17):171301, May 2019.

[102] E. Morganson, R. A. Gruendl, F. Menanteau, M. Carrasco Kind, Y. C. Chen, G. Daues, A. Drlica-Wagner, D. N. Friedel, M. Gower, M. W. G. Johnson, M. D. Johnson, R. Kessler, F. Paz-Chinchón, D. Petravick, C. Pond, B. Yanny, S. Allam, R. Armstrong, W. Barkhouse, K. Bechtol, A. Benoit-Lévy, G. M. Bernstein, E. Bertin, E. Buckley-Geer, R. Covarrubias, S. Desai, H. T. Diehl, D. A. Goldstein, D. Gruen, T. S. Li, H. Lin, J. Marriner, J. J. Mohr, E. Neilsen, C. C. Ngeow, K. Paech, E. S. Rykoff, M. Sako, I. Sevilla-Noarbe, E. Sheldon, F. Sobreira, D. L. Tucker, W. Wester, and DES Collaboration. The Dark Energy Survey Image Processing Pipeline. PASP, 130(989):074501, July 2018.

[103] B. Flaugher, H. T. Diehl, K. Honscheid, T. M. C. Abbott, O. Alvarez, R. Angstadt, J. T. Annis, M. Antonik, O. Ballester, L. Beaufore, G. M. Bernstein, R. A. Bernstein, B. Bigelow, M. Bonati, D. Boprie, D. Brooks, E. J. Buckley-Geer, J. Campa, L. Cardiel-Sas, F. J. Castander, J. Castilla,

H. Cease, J. M. Cela-Ruiz, S. Chappa, E. Chi, C. Cooper, L. N. da Costa, E. Dede, G. Derylo, D. L. DePoy, J. de Vicente, P. Doel, A. Drlica-Wagner, J. Eiting, A. E. Elliott, J. Emes, J. Estrada, A. Fausti Neto, D. A. Finley, R. Flores, J. Frieman, D. Gerdes, M. D. Gladders, B. Gregory, G. R. Gutierrez, J. Hao, S. E. Holland, S. Holm, D. Huffman, C. Jackson, D. J. James, M. Jonas, A. Karcher, I. Karliner, S. Kent, R. Kessler, M. Kozlovsky, R. G. Kron, D. Kubik, K. Kuehn, S. Kuhlmann, K. Kuk, O. Lahav, A. Lathrop, J. Lee, M. E. Levi, P. Lewis, T. S. Li, I. Mandrichenko, J. L. Marshall, G. Martinez, K. W. Merritt, R. Miquel, F. Muñoz, E. H. Neilsen, R. C. Nichol, B. Nord, R. Ogando, J. Olsen, N. Palaio, K. Patton, J. Peoples, A. A. Plazas, J. Rauch, K. Reil, J. P. Rheault, N. A. Roe, H. Rogers, A. Roodman, E. Sanchez, V. Scarpine, R. H. Schindler, R. Schmidt, R. Schmitt, M. Schubnell, K. Schultz, P. Schurter, L. Scott, S. Serrano, T. M. Shaw, R. C. Smith, M. Soares-Santos, A. Stefanik, W. Stuermer, E. Suchyta, A. Sypniewski, G. Tarle, J. Thaler, R. Tighe, C. Tran, D. Tucker, A. R. Walker, G. Wang, M. Watson, C. Weaverdyck, W. Wester, R. Woods, B. Yanny, and DES Collaboration. The Dark Energy Camera. AJ, 150(5):150, November 2015.

[104] H. T. Diehl, E. Neilsen, R. Gruendl, B. Yanny, T. M. C. Abbott, J. Aleksić, S. Allam, J. Annis, E. Balbinot, M. Baumer, L. Beaufore, K. Bechtol, G. Bernstein, S. Birrer, C. Bonnett, D. Brout, C. Bruderer, E. J. Buckley-Geer, D. Capozzi, A. Carnero Rosell, F. J. Castander, R. Cawthon, C. Chang, L. Clerkin, R. Covarrubias, C. Cuhna, C. D'Andrea, L. da Costa, R. Das, C. Davis, J. Dietrich, A. Drlica-Wagner, A. Elliott, T. F. Eifler, J. Etherington, B. L. Flaugher, J. Frieman, A. Fausti Neto, M. G. Fernández, C. Furlanetto, D. Gangkofner, D. W. Gerdes, D. A. Goldstein, K. Grabowski, R. R. Gupta, S. Hamilton, H. Head, J. Helsby, D. Hollowood, K. Honscheid, D. James, M. Johnson, M. W. G. Johnson, S. Jouvel, T. Kacprzac, S. Kent, R. Kessler, A. Kim, E. Krause, C. I. Krawiec, A. Kremin, R. Kron, S. Kuhlmann, N. Kuropatkin, O. Lahav, J. Lasker, T. S. Li, E. Luque, N. Maccrann, M. March, J. Marshall, N. P. Mondrik, E. P. Morganson, D. Mudd, A. Nadolski, P. Nugent, P. Melchior, F. Menanteau, D. Q. Nagasawa, B. Nord, R. Ogando, L. Old, A. Palmese, D. Petravick, A. A. Plazas, A. Pujol, A. B. A. Queiroz, K. Reil, A. K. Romer, R. Rosenfeld, A. Roodman, P. Rooney, M. Sako, A. I. Salvador, C. Sánchez, E. Sánchez Álvaro, B. X. Santiago, A. Schooneveld, M. Schubnell, E. Sheldon, A. Smith, R. C. Smith, M. Soares-Santos, F. Sobreira, M. Soumagnac, H. Spinka, S. S. Tie, D. Tucker, V. Vikram, K. Vivas, A. R. Walker, W. Wester, M. Wiesner, H. Wilcox, P. Williams, A. Zenteno, Y. Zhang, and Z. Zhang. The dark energy survey and operations: years 1 to 3. In Alison B. Peck, Robert L. Seaman, and Chris R. Benn, editors, *Observatory Operations: Strategies, Processes, and Systems VI*, volume 9910

of *Society of Photo-Optical Instrumentation Engineers (SPIE) Conference Series*, page 99101D, July 2016.

[105] H. T. Diehl, E. Neilsen, R. A. Gruendl, T. M. C. Abbott, S. Allam, O. Alvarez, J. Annis, E. Balbinot, S. Bhargava, K. Bechtol, G. M. Bernstein, R. Bhatawdekar, S. Bocquet, D. Brout, R. Capasso, R. Cawthon, C. Chang, E. Cook, C. J. Conselice, J. Cruz, C. D'Andrea, L. da Costa, R. Das, D. L. DePoy, A. Drlica-Wagner, A. Elliott, S. W. Everett, J. Frieman, A. Fausti Neto, A. Ferté, I. Friswell, K. E. Furnell, L. Gelman, D. W. Gerdes, M. S. S. Gill, D. A. Goldstein, D. Gruen, D. J. Gulledge, S. Hamilton, D. Hollowood, K. Honscheid, D. J. James, M. D. Johnson, M. W. G. Johnson, S. Kent, R. S. Kessler, G. Khullar, E. Kovacs, A. Kremin, R. Kron, N. Kuropatkin, J. Lasker, A. Lathrop, T. S. Li, M. Manera, M. March, J. L. Marshall, M. Medford, F. Menanteau, I. Mohammed, M. Monroy, B. Moraes, E. Morganson, J. Muir, M. Murphy, B. Nord, A. B. Pace, A. Palmese, Y. Park, F. Paz-Chinchón, M. E. S. Pereira, D. Petravick, A. A. Plazas, J. Poh, T. Prochaska, A. K. Romer, K. Reil, A. Roodman, M. Sako, M. Sauseda, D. Scolnic, L. F. Secco, I. Sevilla-Noarbe, N. Shipp, J. A. Smith, M. Soares-Santos, B. Soergel, A. Stebbins, K. T. Story, K. Stringer, F. Tarsitano, B. Thomas, D. L. Tucker, K. Vivas, A. R. Walker, M. Y. Wang, C. Weaverdyck, N. Weaverdyck, W. Wester, C. F. Wethers, R. Wilkenson, H. Y. Wu, B. Yanny, A. Zenteno, and Y. Zhang. Dark energy survey operations: years 4 and 5. In *Observatory Operations: Strategies, Processes, and Systems VII*, volume 10704 of *Society of Photo-Optical Instrumentation Engineers (SPIE) Conference Series*, page 107040D, July 2018.

[106] H. T. Diehl et al. The Dark Energy Survey and Operations: Year 6 – The Finale. October 2019.

[107] Dark Energy Camera (DECam). http://www.ctio.noao.edu/noao/content/dark-energy-camera-decam/. Accessed: 2020-04-07.

[108] Eric Jr. Neilsen, James T. Annis, H. Thomas Diehl, Molly E.C. Swanson, Chris D'Andrea, Stephen Kent, and Alex Drlica-Wagner. Dark Energy Survey's Observation Strategy, Tactics, and Exposure Scheduler. November 2019.

[109] Jr. H. Neilsen, Gary Bernstein, Robert Gruendl, and Stephen Kent. Limiting Magnitude, τ, t_{eff}, and Image Quality in DES Year 1. *Tech. Rep. FERMILAB-TM-2610-AE-CD*, March 2016.

[110] I. Sevilla, R. Armstrong, E. Bertin, A. Carlson, G. Daues, S. Desai, M. Gower, R. Gruendl, W. Hanlon, M. Jarvis, R. Kessler, N. Kuropatkin,

H. Lin, J. Marriner, J. Mohr, D. Petravick, E. Sheldon, M. E. C. Swanson, T. Tomashek, D. Tucker, Y. Yang, and B. Yanny. The Dark Energy Survey Data Management System. *arXiv e-prints*, page arXiv:1109.6741, September 2011.

[111] D. L. Tucker, J. T. Annis, H. Lin, S. Kent, C. Stoughton, J. Peoples, S. S. Allam, J. J. Mohr, W. A. Barkhouse, C. Ngeow, T. Alam, C. Beldica, D. Cai, G. Daues, R. Plante, C. Miller, C. Smith, and N. B. Suntzeff. The Photometric Calibration of the Dark Energy Survey. In C. Sterken, editor, *The Future of Photometric, Spectrophotometric and Polarimetric Standardization*, volume 364 of *Astronomical Society of the Pacific Conference Series*, page 187, April 2007.

[112] Marcelle Soares-Santos, J. Hao, J. Estrada, E. Buckley-Geer, H. Cease, G. Derylo, H. T. Diehl, B. Flaugher, R. Flores, K. Honscheid, I. Karliner, D. Kubik, K. Kuk, N. Kuropatkin, H. Lin, A. Lathrop, J. Montes, V. Scarpine, K. Schultz, L. Scott, T. Shaw, W. Stuermer, W. Wester, and Dark Energy Survey. Calibration Of The Dark Energy Survey Camera: Measurements Of Focal Plane Flatness And Crosstalk Among CCDs. In *American Astronomical Society Meeting Abstracts #217*, volume 217 of *American Astronomical Society Meeting Abstracts*, page 239.04, January 2011.

[113] D. Gruen, G. M. Bernstein, M. Jarvis, B. Rowe, V. Vikram, A. A. Plazas, and S. Seitz. Characterization and correction of charge-induced pixel shifts in DECam. *Journal of Instrumentation*, 10(5):C05032, May 2015.

[114] G. M. Bernstein, T. M. C. Abbott, S. Desai, D. Gruen, R. A. Gruendl, M. D. Johnson, H. Lin, F. Menanteau, E. Morganson, E. Neilsen, K. Paech, A. R. Walker, W. Wester, B. Yanny, and DES Collaboration. Instrumental response model and detrending for the Dark Energy Camera. PASP, 129(981):114502, November 2017.

[115] E. Bertin. Automatic Astrometric and Photometric Calibration with SCAMP. In C. Gabriel, C. Arviset, D. Ponz, and S. Enrique, editors, *Astronomical Data Analysis Software and Systems XV*, volume 351 of *Astronomical Society of the Pacific Conference Series*, page 112, July 2006.

[116] E. Bertin. Automated Morphometry with SExtractor and PSFEx. In I. N. Evans, A. Accomazzi, D. J. Mink, and A. H. Rots, editors, *Astronomical Data Analysis Software and Systems XX*, volume 442 of *Astronomical Society of the Pacific Conference Series*, page 435, July 2011.

[117] D. L. Burke, E. S. Rykoff, S. Allam, J. Annis, K. Bechtol, G. M. Bernstein, A. Drlica-Wagner, D. A. Finley, R. A. Gruendl, D. J. James, S. Kent, R. Kessler, S. Kuhlmann, J. Lasker, T. S. Li, D. Scolnic, J. Smith,

D. L. Tucker, W. Wester, B. Yanny, T. M. C. Abbott, F. B. Abdalla, A. Benoit-Lévy, E. Bertin, A. Carnero Rosell, M. Carrasco Kind, J. Carretero, C. E. Cunha, C. B. D'Andrea, L. N. da Costa, S. Desai, H. T. Diehl, P. Doel, J. Estrada, J. García-Bellido, D. Gruen, G. Gutierrez, K. Honscheid, K. Kuehn, N. Kuropatkin, M. A. G. Maia, M. March, J. L. Marshall, P. Melchior, F. Menanteau, R. Miquel, A. A. Plazas, M. Sako, E. Sanchez, V. Scarpine, R. Schindler, I. Sevilla-Noarbe, M. Smith, R. C. Smith, M. Soares-Santos, F. Sobreira, E. Suchyta, G. Tarle, A. R. Walker, and DES Collaboration. Forward Global Photometric Calibration of the Dark Energy Survey. AJ, 155(1):41, January 2018.

[118] Emmanuel Bertin, Yannick Mellier, Mario Radovich, Gilles Missonnier, Pierre Didelon, and Bertrand Morin. The TERAPIX Pipeline. In David A. Bohlender, Daniel Durand, and Thomas H. Handley, editors, *Astronomical Data Analysis Software and Systems XI*, volume 281 of *Astronomical Society of the Pacific Conference Series*, page 228, January 2002.

[119] Emmanuel Bertin. SWarp: Resampling and Co-adding FITS Images Together, October 2010.

[120] William A. Dawson, Michael D. Schneider, J. Anthony Tyson, and M. James Jee. The Ellipticity Distribution of Ambiguously Blended Objects. ApJ, 816(1):11, January 2016.

[121] N. MacCrann, M. R. Becker, J. McCullough, A. Amon, D. Gruen, M. Jarvis, A. Choi, M. A. Troxel, E. Sheldon, B. Yanny, K. Herner, S. Dodelson, J. Zuntz, K. Eckert, R. P. Rollins, T. N. Varga, G. M. Bernstein, R. A. Gruendl, I. Harrison, W. G. Hartley, I. Sevilla-Noarbe, A. Pieres, S. L. Bridle, J. Myles, A. Alarcon, S. Everett, C. Sánchez, E. M. Huff, F. Tarsitano, M. Gatti, L. F. Secco, T. M. C. Abbott, M. Aguena, S. Allam, J. Annis, D. Bacon, E. Bertin, D. Brooks, D. L. Burke, A. Carnero Rosell, M. Carrasco Kind, J. Carretero, M. Costanzi, M. Crocce, M. E. S. Pereira, J. De Vicente, S. Desai, H. T. Diehl, J. P. Dietrich, P. Doel, T. F. Eifler, I. Ferrero, A. Ferté, B. Flaugher, P. Fosalba, J. Frieman, J. García-Bellido, E. Gaztanaga, D. W. Gerdes, T. Giannantonio, J. Gschwend, G. Gutierrez, S. R. Hinton, D. L. Hollowood, K. Honscheid, D. J. James, O. Lahav, M. Lima, M. A. G. Maia, M. March, J. L. Marshall, P. Martini, P. Melchior, F. Menanteau, R. Miquel, J. J. Mohr, R. Morgan, J. Muir, R. L. C. Ogando, A. Palmese, F. Paz-Chinchón, A. A. Plazas, M. Rodriguez-Monroy, A. Roodman, S. Samuroff, E. Sanchez, V. Scarpine, S. Serrano, M. Smith, M. Soares-Santos, E. Suchyta, M. E. C. Swanson, G. Tarle, D. Thomas, C. To, and R. D. Wilkinson. DES Y3 results: Blending shear and redshift biases in image simulations. *arXiv e-prints*, page arXiv:2012.08567, December 2020.

[122] M. Jarvis, E. Sheldon, J. Zuntz, T. Kacprzak, S. L. Bridle, A. Amara, R. Armstrong, M. R. Becker, G. M. Bernstein, C. Bonnett, C. Chang, R. Das, J. P. Dietrich, A. Drlica-Wagner, T. F. Eifler, C. Gangkofner, D. Gruen, M. Hirsch, E. M. Huff, B. Jain, S. Kent, D. Kirk, N. MacCrann, P. Melchior, A. A. Plazas, A. Refregier, B. Rowe, E. S. Rykoff, S. Samuroff, C. Sánchez, E. Suchyta, M. A. Troxel, V. Vikram, T. Abbott, F. B. Abdalla, S. Allam, J. Annis, A. Benoit-Lévy, E. Bertin, D. Brooks, E. Buckley-Geer, D. L. Burke, D. Capozzi, A. Carnero Rosell, M. Carrasco Kind, J. Carretero, F. J. Castander, J. Clampitt, M. Crocce, C. E. Cunha, C. B. D'Andrea, L. N. da Costa, D. L. DePoy, S. Desai, H. T. Diehl, P. Doel, A. Fausti Neto, B. Flaugher, P. Fosalba, J. Frieman, E. Gaztanaga, D. W. Gerdes, R. A. Gruendl, G. Gutierrez, K. Honscheid, D. J. James, K. Kuehn, N. Kuropatkin, O. Lahav, T. S. Li, M. Lima, M. March, P. Martini, R. Miquel, J. J. Mohr, E. Neilsen, B. Nord, R. Ogando, K. Reil, A. K. Romer, A. Roodman, M. Sako, E. Sanchez, V. Scarpine, M. Schubnell, I. Sevilla-Noarbe, R. C. Smith, M. Soares-Santos, F. Sobreira, M. E. C. Swanson, G. Tarle, J. Thaler, D. Thomas, A. R. Walker, and R. H. Wechsler. The DES Science Verification weak lensing shear catalogues. MNRAS, 460(2):2245–2281, August 2016.

[123] E. S. Sheldon. An implementation of Bayesian lensing shear measurement. MNRAS, 444:L25–L29, October 2014.

[124] David W. Hogg and Dustin Lang. Replacing Standard Galaxy Profiles with Mixtures of Gaussians. PASP, 125(928):719, June 2013.

[125] J. L. Sérsic. Influence of the atmospheric and instrumental dispersion on the brightness distribution in a galaxy. *Boletin de la Asociacion Argentina de Astronomia La Plata Argentina*, 6:41–43, February 1963.

[126] Gerard de Vaucouleurs. Recherches sur les Nebuleuses Extragalactiques. *Annales d'Astrophysique*, 11:247, January 1948.

[127] A. Drlica-Wagner, I. Sevilla-Noarbe, E. S. Rykoff, R. A. Gruendl, B. Yanny, D. L. Tucker, B. Hoyle, A. Carnero Rosell, G. M. Bernstein, K. Bechtol, M. R. Becker, A. Benoit-Lévy, E. Bertin, M. Carrasco Kind, C. Davis, J. de Vicente, H. T. Diehl, D. Gruen, W. G. Hartley, B. Leistedt, T. S. Li, J. L. Marshall, E. Neilsen, M. M. Rau, E. Sheldon, J. Smith, M. A. Troxel, S. Wyatt, Y. Zhang, T. M. C. Abbott, F. B. Abdalla, S. Allam, M. Banerji, D. Brooks, E. Buckley-Geer, D. L. Burke, D. Capozzi, J. Carretero, C. E. Cunha, C. B. D'Andrea, L. N. da Costa, D. L. DePoy, S. Desai, J. P. Dietrich, P. Doel, A. E. Evrard, A. Fausti Neto, B. Flaugher, P. Fosalba, J. Frieman, J. García-Bellido, D. W. Gerdes, T. Giannantonio, J. Gschwend, G. Gutierrez, K. Honscheid, D. J. James, T. Jeltema,

K. Kuehn, S. Kuhlmann, N. Kuropatkin, O. Lahav, M. Lima, H. Lin, M. A. G. Maia, P. Martini, R. G. McMahon, P. Melchior, F. Menanteau, R. Miquel, R. C. Nichol, R. L. C. Ogando, A. A. Plazas, A. K. Romer, A. Roodman, E. Sanchez, V. Scarpine, R. Schindler, M. Schubnell, M. Smith, R. C. Smith, M. Soares-Santos, F. Sobreira, E. Suchyta, G. Tarle, V. Vikram, A. R. Walker, R. H. Wechsler, J. Zuntz, and DES Collaboration. Dark Energy Survey Year 1 Results: The Photometric Data Set for Cosmology. ApJS, 235(2):33, April 2018.

[128] I. Sevilla-Noarbe, K. Bechtol, M. Carrasco Kind, A. Carnero Rosell, M. R. Becker, A. Drlica-Wagner, R. A. Gruendl, E. S. Rykoff, E. Sheldon, B. Yanny, A. Alarcon, S. Allam, A. Amon, A. Benoit-Lévy, G. M. Bernstein, E. Bertin, D. L. Burke, J. Carretero, A. Choi, H. T. Diehl, S. Everett, B. Flaugher, E. Gaztanaga, J. Gschwend, I. Harrison, W. G. Hartley, B. Hoyle, M. Jarvis, M. D. Johnson, R. Kessler, R. Kron, N. Kuropatkin, B. Leistedt, T. S. Li, F. Menanteau, E. Morganson, R. L. C. Ogando, A. Palmese, F. Paz-Chinchón, A. Pieres, C. Pond, M. Rodriguez-Monroy, J. Allyn-Smith, K. M. Stringer, M. A. Troxel, D. L. Tucker, J. de Vicente, W. Wester, Y. Zhang, T. M. C. Abbott, M. Aguena, J. Annis, S. Avila, S. Bhargava, S. L. Bridle, D. Brooks, D. Brout, F. J. Castander, R. Cawthon, C. Chang, C. Conselice, M. Costanzi, M. Crocce, L. N. da Costa, M. E. E. Pereira, T. M. Davis, S. Desai, J. P. Dietrich, P. Doel, K. Eckert, A. E. Evrard, I. Ferrero, P. Fosalba, J. García-Bellido, D. W. Gerdes, T. Giannantonio, D. Gruen, G. Gutierrez, S. R. Hinton, D. L. Hollowood, K. Honscheid, E. M. Huff, D. Huterer, D. J. James, T. Jeltema, K. Kuehn, O. Lahav, C. Lidman, M. Lima, H. Lin, M. A. G. Maia, J. L. Marshall, P. Martini, P. Melchior, R. Miquel, J. J. Mohr, R. Morgan, E. Neilsen, A. A. Plazas, A. K. Romer, A. Roodman, E. Sanchez, V. Scarpine, M. Schubnell, S. Serrano, M. Smith, E. Suchyta, G. Tarle, D. Thomas, C. To, T. N. Varga, R. H. Wechsler, J. Weller, and R. D. Wilkinson. Dark Energy Survey Year 3 Results: Photometric Data Set for Cosmology. *arXiv e-prints*, page arXiv:2011.03407, November 2020.

[129] E. S. Rykoff, E. Rozo, D. Hollowood, A. Bermeo-Hernandez, T. Jeltema, J. Mayers, A. K. Romer, P. Rooney, A. Saro, C. Vergara Cervantes, R. H. Wechsler, H. Wilcox, T. M. C. Abbott, F. B. Abdalla, S. Allam, J. Annis, A. Benoit-Lévy, G. M. Bernstein, E. Bertin, D. Brooks, D. L. Burke, D. Capozzi, A. Carnero Rosell, M. Carrasco Kind, F. J. Castander, M. Childress, C. A. Collins, C. E. Cunha, C. B. D'Andrea, L. N. da Costa, T. M. Davis, S. Desai, H. T. Diehl, J. P. Dietrich, P. Doel, A. E. Evrard, D. A. Finley, B. Flaugher, P. Fosalba, J. Frieman, K. Glazebrook, D. A. Goldstein, D. Gruen, R. A. Gruendl, G. Gutierrez, M. Hilton, K. Honscheid, B. Hoyle, D. J. James, S. T. Kay, K. Kuehn, N. Kuropatkin, O. Lahav,

G. F. Lewis, C. Lidman, M. Lima, M. A. G. Maia, R. G. Mann, J. L. Marshall, P. Martini, P. Melchior, C. J. Miller, R. Miquel, J. J. Mohr, R. C. Nichol, B. Nord, R. Ogando, A. A. Plazas, K. Reil, M. Sahlén, E. Sanchez, B. Santiago, V. Scarpine, M. Schubnell, I. Sevilla-Noarbe, R. C. Smith, M. Soares-Santos, F. Sobreira, J. P. Stott, E. Suchyta, M. E. C. Swanson, G. Tarle, D. Thomas, D. Tucker, S. Uddin, P. T. P. Viana, V. Vikram, A. R. Walker, Y. Zhang, and DES Collaboration. The RedMaPPer Galaxy Cluster Catalog From DES Science Verification Data. ApJS, 224(1):1, May 2016.

[130] J. Zuntz, E. Sheldon, S. Samuroff, M. A. Troxel, M. Jarvis, N. MacCrann, D. Gruen, J. Prat, C. Sánchez, A. Choi, S. L. Bridle, G. M. Bernstein, S. Dodelson, A. Drlica-Wagner, Y. Fang, R. A. Gruendl, B. Hoyle, E. M. Huff, B. Jain, D. Kirk, T. Kacprzak, C. Krawiec, A. A. Plazas, R. P. Rollins, E. S. Rykoff, I. Sevilla-Noarbe, B. Soergel, T. N. Varga, T. M. C. Abbott, F. B. Abdalla, S. Allam, J. Annis, K. Bechtol, A. Benoit-Lévy, E. Bertin, E. Buckley-Geer, D. L. Burke, A. Carnero Rosell, M. Carrasco Kind, J. Carretero, F. J. Castander, M. Crocce, C. E. Cunha, C. B. D'Andrea, L. N. da Costa, C. Davis, S. Desai, H. T. Diehl, J. P. Dietrich, P. Doel, T. F. Eifler, J. Estrada, A. E. Evrard, A. Fausti Neto, E. Fernandez, B. Flaugher, P. Fosalba, J. Frieman, J. García-Bellido, E. Gaztanaga, D. W. Gerdes, T. Giannantonio, J. Gschwend, G. Gutierrez, W. G. Hartley, K. Honscheid, D. J. James, T. Jeltema, M. W. G. Johnson, M. D. Johnson, K. Kuehn, S. Kuhlmann, N. Kuropatkin, O. Lahav, T. S. Li, M. Lima, M. A. G. Maia, M. March, P. Martini, P. Melchior, F. Menanteau, C. J. Miller, R. Miquel, J. J. Mohr, E. Neilsen, R. C. Nichol, R. L. C. Ogando, N. Roe, A. K. Romer, A. Roodman, E. Sanchez, V. Scarpine, R. Schindler, M. Schubnell, M. Smith, R. C. Smith, M. Soares-Santos, F. Sobreira, E. Suchyta, M. E. C. Swanson, G. Tarle, D. Thomas, D. L. Tucker, V. Vikram, A. R. Walker, R. H. Wechsler, Y. Zhang, and DES Collaboration. Dark Energy Survey Year 1 results: weak lensing shape catalogues. MNRAS, 481(1):1149–1182, November 2018.

[131] M. Gatti, E. Sheldon, A. Amon, M. Becker, M. Troxel, A. Choi, C. Doux, N. MacCrann, A. Navarro Alsina, I. Harrison, D. Gruen, G. Bernstein, M. Jarvis, L. F. Secco, A. Ferté, T. Shin, J. McCullough, R. P. Rollins, R. Chen, C. Chang, S. Pandey, I. Tutusaus, J. Prat, J. Elvin-Poole, C. Sanchez, A. A. Plazas, A. Roodman, J. Zuntz, T. M. C. Abbott, M. Aguena, S. Allam, J. Annis, S. Avila, D. Bacon, E. Bertin, S. Bhargava, D. Brooks, D. L. Burke, A. Carnero Rosell, M. Carrasco Kind, J. Carretero, F. J. Castander, C. Conselice, M. Costanzi, L. N. da Costa, T. M. Davis, J. De Vicente, S. Desai, H. T. Diehl, J. P. Dietrich, P. Doel, A. Drlica-Wagner, K. Eckert, S. Everett, I. Ferrero, J. Frieman, J. García-

Bellido, D. W. Gerdes, T. Giannantonio, R. A. Gruendl, J. Gschwend, G. Gutierrez, W. G. Hartley, S. R. Hinton, D. L. Hollowood, K. Honscheid, B. Hoyle, E. M. Huff, D. Huterer, B. Jain, D. J. James, T. Jeltema, E. Krause, R. Kron, N. Kuropatkin, M. Lima, M. A. G. Maia, J. L. Marshall, R. Miquel, R. Morgan, J. Myles, A. Palmese, F. Paz-Chinchón, E. S. Rykoff, S. Samuroff, E. Sanchez, V. Scarpine, M. Schubnell, S. Serrano, I. Sevilla-Noarbe, M. Smith, E. Suchyta, M. E. C. Swanson, G. Tarle, D. Thomas, C. To, D. L. Tucker, T. N. Varga, R. H. Wechsler, J. Weller, W. Wester, and R. D. Wilkinson. Dark Energy Survey Year 3 Results: Weak Lensing Shape Catalogue. *arXiv e-prints*, page arXiv:2011.03408, November 2020.

[132] Narciso Benítez. Bayesian Photometric Redshift Estimation. ApJ, 536(2):571–583, June 2000.

[133] J. De Vicente, E. Sánchez, and I. Sevilla-Noarbe. DNF - Galaxy photometric redshift by Directional Neighbourhood Fitting. MNRAS, 459(3):3078–3088, July 2016.

[134] I. Sadeh, F. B. Abdalla, and O. Lahav. ANNz2: Photometric Redshift and Probability Distribution Function Estimation using Machine Learning. PASP, 128(968):104502, October 2016.

[135] J. Myles, A. Alarcon, A. Amon, C. Sánchez, S. Everett, J. DeRose, J. McCullough, D. Gruen, G. M. Bernstein, M. A. Troxel, S. Dodelson, A. Campos, N. MacCrann, B. Yin, M. Raveri, A. Amara, M. R. Becker, A. Choi, J. Cordero, K. Eckert, M. Gatti, G. Giannini, J. Gschwend, R. A. Gruendl, I. Harrison, W. G. Hartley, E. M. Huff, N. Kuropatkin, H. Lin, D. Masters, R. Miquel, J. Prat, A. Roodman, E. S. Rykoff, I. Sevilla-Noarbe, E. Sheldon, R. H. Wechsler, B. Yanny, T. M. C. Abbott, M. Aguena, S. Allam, J. Annis, D. Bacon, E. Bertin, S. Bhargava, S. L. Bridle, D. Brooks, D. L. Burke, A. Carnero Rosell, M. Carrasco Kind, J. Carretero, F. J. Castander, C. Conselice, M. Costanzi, M. Crocce, L. N. da Costa, M. E. S. Pereira, S. Desai, H. T. Diehl, T. F. Eifler, J. Elvin-Poole, A. E. Evrard, I. Ferrero, A. Ferté, B. Flaugher, P. Fosalba, J. Frieman, J. García-Bellido, E. Gaztanaga, T. Giannantonio, S. R. Hinton, D. L. Hollowood, K. Honscheid, B. Hoyle, D. Huterer, D. J. James, E. Krause, K. Kuehn, O. Lahav, M. Lima, M. A. G. Maia, J. L. Marshall, P. Martini, P. Melchior, F. Menanteau, J. J. Mohr, R. Morgan, J. Muir, R. L. C. Ogando, A. Palmese, F. Paz-Chinchón, A. A. Plazas, M. Rodriguez-Monroy, S. Samuroff, E. Sanchez, V. Scarpine, L. F. Secco, S. Serrano, M. Smith, M. Soares-Santos, E. Suchyta, M. E. C. Swanson, G. Tarle, D. Thomas, C. To, T. N. Varga, J. Weller, and W. Wester. Dark Energy Survey Year 3 Results: Redshift Calibration of the Weak Lensing Source Galaxies. *arXiv e-prints*, page arXiv:2012.08566, December 2020.

[136] J. Elvin-Poole, M. Crocce, A. J. Ross, T. Giannantonio, E. Rozo, E. S. Rykoff, S. Avila, N. Banik, J. Blazek, S. L. Bridle, R. Cawthon, A. Drlica-Wagner, O. Friedrich, N. Kokron, E. Krause, N. MacCrann, J. Prat, C. Sánchez, L. F. Secco, I. Sevilla-Noarbe, M. A. Troxel, T. M. C. Abbott, F. B. Abdalla, S. Allam, J. Annis, J. Asorey, K. Bechtol, M. R. Becker, A. Benoit-Lévy, G. M. Bernstein, E. Bertin, D. Brooks, E. Buckley-Geer, D. L. Burke, A. Carnero Rosell, D. Carollo, M. Carrasco Kind, J. Carretero, F. J. Castander, C. E. Cunha, C. B. D'Andrea, L. N. da Costa, T. M. Davis, C. Davis, S. Desai, H. T. Diehl, J. P. Dietrich, S. Dodelson, P. Doel, T. F. Eifler, A. E. Evrard, E. Fernandez, B. Flaugher, P. Fosalba, J. Frieman, J. García-Bellido, E. Gaztanaga, D. W. Gerdes, K. Glazebrook, D. Gruen, R. A. Gruendl, J. Gschwend, G. Gutierrez, W. G. Hartley, S. R. Hinton, K. Honscheid, J. K. Hoormann, B. Jain, D. J. James, M. Jarvis, T. Jeltema, M. W. G. Johnson, M. D. Johnson, A. King, K. Kuehn, S. Kuhlmann, N. Kuropatkin, O. Lahav, G. Lewis, T. S. Li, C. Lidman, M. Lima, H. Lin, E. Macaulay, M. March, J. L. Marshall, P. Martini, P. Melchior, F. Menanteau, R. Miquel, J. J. Mohr, A. Möller, R. C. Nichol, B. Nord, C. R. O'Neill, W. J. Percival, D. Petravick, A. A. Plazas, A. K. Romer, M. Sako, E. Sanchez, V. Scarpine, R. Schindler, M. Schubnell, E. Sheldon, M. Smith, R. C. Smith, M. Soares-Santos, F. Sobreira, N. E. Sommer, E. Suchyta, M. E. C. Swanson, G. Tarle, D. Thomas, B. E. Tucker, D. L. Tucker, S. A. Uddin, V. Vikram, A. R. Walker, R. H. Wechsler, J. Weller, W. Wester, R. C. Wolf, F. Yuan, B. Zhang, J. Zuntz, and DES Collaboration. Dark Energy Survey year 1 results: Galaxy clustering for combined probes. Phys. Rev. D, 98(4):042006, August 2018.

[137] T. M. C. Abbott, F. B. Abdalla, S. Allam, A. Amara, J. Annis, J. Asorey, S. Avila, O. Ballester, M. Banerji, W. Barkhouse, L. Baruah, M. Baumer, K. Bechtol, M. R. Becker, A. Benoit-Lévy, G. M. Bernstein, E. Bertin, J. Blazek, S. Bocquet, D. Brooks, D. Brout, E. Buckley-Geer, D. L. Burke, V. Busti, R. Campisano, L. Cardiel-Sas, A. Carnero Rosell, M. Carrasco Kind, J. Carretero, F. J. Castander, R. Cawthon, C. Chang, X. Chen, C. Conselice, G. Costa, M. Crocce, C. E. Cunha, C. B. D'Andrea, L. N. da Costa, R. Das, G. Daues, T. M. Davis, C. Davis, J. De Vicente, D. L. DePoy, J. DeRose, S. Desai, H. T. Diehl, J. P. Dietrich, S. Dodelson, P. Doel, A. Drlica-Wagner, T. F. Eifler, A. E. Elliott, A. E. Evrard, A. Farahi, A. Fausti Neto, E. Fernandez, D. A. Finley, B. Flaugher, R. J. Foley, P. Fosalba, D. N. Friedel, J. Frieman, J. García-Bellido, E. Gaztanaga, D. W. Gerdes, T. Giannantonio, M. S. S. Gill, K. Glazebrook, D. A. Goldstein, M. Gower, D. Gruen, R. A. Gruendl, J. Gschwend, R. R. Gupta, G. Gutierrez, S. Hamilton, W. G. Hartley, S. R. Hinton, J. M. Hislop, D. Hollowood, K. Honscheid, B. Hoyle, D. Huterer, B. Jain, D. J. James, T. Jeltema,

M. W. G. Johnson, M. D. Johnson, T. Kacprzak, S. Kent, G. Khullar, M. Klein, A. Kovacs, A. M. G. Koziol, E. Krause, A. Kremin, R. Kron, K. Kuehn, S. Kuhlmann, N. Kuropatkin, O. Lahav, J. Lasker, T. S. Li, R. T. Li, A. R. Liddle, M. Lima, H. Lin, P. López-Reyes, N. MacCrann, M. A. G. Maia, J. D. Maloney, M. Manera, M. March, J. Marriner, J. L. Marshall, P. Martini, T. McClintock, T. McKay, R. G. McMahon, P. Melchior, F. Menanteau, C. J. Miller, R. Miquel, J. J. Mohr, E. Morganson, J. Mould, E. Neilsen, R. C. Nichol, F. Nogueira, B. Nord, P. Nugent, L. Nunes, R. L. C. Ogando, L. Old, A. B. Pace, A. Palmese, F. Paz-Chinchón, H. V. Peiris, W. J. Percival, D. Petravick, A. A. Plazas, J. Poh, C. Pond, A. Porredon, A. Pujol, A. Refregier, K. Reil, P. M. Ricker, R. P. Rollins, A. K. Romer, A. Roodman, P. Rooney, A. J. Ross, E. S. Rykoff, M. Sako, M. L. Sanchez, E. Sanchez, B. Santiago, A. Saro, V. Scarpine, D. Scolnic, S. Serrano, I. Sevilla-Noarbe, E. Sheldon, N. Shipp, M. L. Silveira, M. Smith, R. C. Smith, J. A. Smith, M. Soares-Santos, F. Sobreira, J. Song, A. Stebbins, E. Suchyta, M. Sullivan, M. E. C. Swanson, G. Tarle, J. Thaler, D. Thomas, R. C. Thomas, M. A. Troxel, D. L. Tucker, V. Vikram, A. K. Vivas, A. R. Walker, R. H. Wechsler, J. Weller, W. Wester, R. C. Wolf, H. Wu, B. Yanny, A. Zenteno, Y. Zhang, J. Zuntz, DES Collaboration, S. Juneau, M. Fitzpatrick, R. Nikutta, D. Nidever, K. Olsen, A. Scott, and NOAO Data Lab. The Dark Energy Survey: Data Release 1. ApJS, 239(2):18, December 2018.

[138] DES Data Management. Des sva1 gold release, 2016.

[139] T. M. C. Abbott, F. B. Abdalla, A. Alarcon, J. Aleksić, S. Allam, S. Allen, A. Amara, J. Annis, J. Asorey, S. Avila, D. Bacon, E. Balbinot, M. Banerji, N. Banik, W. Barkhouse, M. Baumer, E. Baxter, K. Bechtol, M. R. Becker, A. Benoit-Lévy, B. A. Benson, G. M. Bernstein, E. Bertin, J. Blazek, S. L. Bridle, D. Brooks, D. Brout, E. Buckley-Geer, D. L. Burke, M. T. Busha, A. Campos, D. Capozzi, A. Carnero Rosell, M. Carrasco Kind, J. Carretero, F. J. Castander, R. Cawthon, C. Chang, N. Chen, M. Childress, A. Choi, C. Conselice, R. Crittenden, M. Crocce, C. E. Cunha, C. B. D'Andrea, L. N. da Costa, R. Das, T. M. Davis, C. Davis, J. De Vicente, D. L. DePoy, J. DeRose, S. Desai, H. T. Diehl, J. P. Dietrich, S. Dodelson, P. Doel, A. Drlica-Wagner, T. F. Eifler, A. E. Elliott, F. Elsner, J. Elvin-Poole, J. Estrada, A. E. Evrard, Y. Fang, E. Fernandez, A. Ferté, D. A. Finley, B. Flaugher, P. Fosalba, O. Friedrich, J. Frieman, J. García-Bellido, M. Garcia-Fernandez, M. Gatti, E. Gaztanaga, D. W. Gerdes, T. Giannantonio, M. S. S. Gill, K. Glazebrook, D. A. Goldstein, D. Gruen, R. A. Gruendl, J. Gschwend, G. Gutierrez, S. Hamilton, W. G. Hartley, S. R. Hinton, K. Honscheid, B. Hoyle, D. Huterer, B. Jain, D. J. James, M. Jarvis, T. Jeltema, M. D. Johnson, M. W. G. Johnson, T. Kacprzak, S. Kent, A. G. Kim, A. King, D. Kirk, N. Kokron, A. Kovacs, E. Krause, C. Krawiec, A. Kremin,

K. Kuehn, S. Kuhlmann, N. Kuropatkin, F. Lacasa, O. Lahav, T. S. Li, A. R. Liddle, C. Lidman, M. Lima, H. Lin, N. MacCrann, M. A. G. Maia, M. Makler, M. Manera, M. March, J. L. Marshall, P. Martini, R. G. McMahon, P. Melchior, F. Menanteau, R. Miquel, V. Miranda, D. Mudd, J. Muir, A. Möller, E. Neilsen, R. C. Nichol, B. Nord, P. Nugent, R. L. C. Ogando, A. Palmese, J. Peacock, H. V. Peiris, J. Peoples, W. J. Percival, D. Petravick, A. A. Plazas, A. Porredon, J. Prat, A. Pujol, M. M. Rau, A. Refregier, P. M. Ricker, N. Roe, R. P. Rollins, A. K. Romer, A. Roodman, R. Rosenfeld, A. J. Ross, E. Rozo, E. S. Rykoff, M. Sako, A. I. Salvador, S. Samuroff, C. Sánchez, E. Sanchez, B. Santiago, V. Scarpine, R. Schindler, D. Scolnic, L. F. Secco, S. Serrano, I. Sevilla-Noarbe, E. Sheldon, R. C. Smith, M. Smith, J. Smith, M. Soares-Santos, F. Sobreira, E. Suchyta, G. Tarle, D. Thomas, M. A. Troxel, D. L. Tucker, B. E. Tucker, S. A. Uddin, T. N. Varga, P. Vielzeuf, V. Vikram, A. K. Vivas, A. R. Walker, M. Wang, R. H. Wechsler, J. Weller, W. Wester, R. C. Wolf, B. Yanny, F. Yuan, A. Zenteno, B. Zhang, Y. Zhang, J. Zuntz, and Dark Energy Survey Collaboration. Dark Energy Survey year 1 results: Cosmological constraints from galaxy clustering and weak lensing. Phys. Rev. D, 98(4):043526, August 2018.

[140] J. Prat, C. Sánchez, Y. Fang, D. Gruen, J. Elvin-Poole, N. Kokron, L. F. Secco, B. Jain, R. Miquel, N. MacCrann, M. A. Troxel, A. Alarcon, D. Bacon, G. M. Bernstein, J. Blazek, R. Cawthon, C. Chang, M. Crocce, C. Davis, J. De Vicente, J. P. Dietrich, A. Drlica-Wagner, O. Friedrich, M. Gatti, W. G. Hartley, B. Hoyle, E. M. Huff, M. Jarvis, M. M. Rau, R. P. Rollins, A. J. Ross, E. Rozo, E. S. Rykoff, S. Samuroff, E. Sheldon, T. N. Varga, P. Vielzeuf, J. Zuntz, T. M. C. Abbott, F. B. Abdalla, S. Allam, J. Annis, K. Bechtol, A. Benoit-Lévy, E. Bertin, D. Brooks, E. Buckley-Geer, D. L. Burke, A. Carnero Rosell, M. Carrasco Kind, J. Carretero, F. J. Castander, C. E. Cunha, C. B. D'Andrea, L. N. da Costa, S. Desai, H. T. Diehl, S. Dodelson, T. F. Eifler, E. Fernandez, B. Flaugher, P. Fosalba, J. Frieman, J. García-Bellido, E. Gaztanaga, D. W. Gerdes, T. Giannantonio, D. A. Goldstein, R. A. Gruendl, J. Gschwend, G. Gutierrez, K. Honscheid, D. J. James, T. Jeltema, M. W. G. Johnson, M. D. Johnson, D. Kirk, E. Krause, K. Kuehn, S. Kuhlmann, O. Lahav, T. S. Li, M. Lima, M. A. G. Maia, M. March, J. L. Marshall, P. Martini, P. Melchior, F. Menanteau, J. J. Mohr, R. C. Nichol, B. Nord, A. A. Plazas, A. K. Romer, A. Roodman, M. Sako, E. Sanchez, V. Scarpine, R. Schindler, M. Schubnell, I. Sevilla-Noarbe, M. Smith, R. C. Smith, M. Soares-Santos, F. Sobreira, E. Suchyta, M. E. C. Swanson, G. Tarle, D. Thomas, D. L. Tucker, V. Vikram, A. R. Walker, R. H. Wechsler, B. Yanny, Y. Zhang, and DES Collaboration. Dark Energy Survey year 1 results: Galaxy-galaxy lensing. Phys. Rev. D, 98(4):042005, August 2018.

[141] E. Krause, T. F. Eifler, J. Zuntz, O. Friedrich, M. A. Troxel, S. Dodelson, J. Blazek, L. F. Secco, N. MacCrann, E. Baxter, C. Chang, N. Chen, M. Crocce, J. DeRose, A. Ferte, N. Kokron, F. Lacasa, V. Miranda, Y. Omori, A. Porredon, R. Rosenfeld, S. Samuroff, M. Wang, R. H. Wechsler, T. M. C. Abbott, F. B. Abdalla, S. Allam, J. Annis, K. Bechtol, A. Benoit-Levy, G. M. Bernstein, D. Brooks, D. L. Burke, D. Capozzi, M. Carrasco Kind, J. Carretero, C. B. D'Andrea, L. N. da Costa, C. Davis, D. L. DePoy, S. Desai, H. T. Diehl, J. P. Dietrich, A. E. Evrard, B. Flaugher, P. Fosalba, J. Frieman, J. Garcia-Bellido, E. Gaztanaga, T. Giannantonio, D. Gruen, R. A. Gruendl, J. Gschwend, G. Gutierrez, K. Honscheid, D. J. James, T. Jeltema, K. Kuehn, S. Kuhlmann, O. Lahav, M. Lima, M. A. G. Maia, M. March, J. L. Marshall, P. Martini, F. Menanteau, R. Miquel, R. C. Nichol, A. A. Plazas, A. K. Romer, E. S. Rykoff, E. Sanchez, V. Scarpine, R. Schindler, M. Schubnell, I. Sevilla-Noarbe, M. Smith, M. Soares-Santos, F. Sobreira, E. Suchyta, M. E. C. Swanson, G. Tarle, D. L. Tucker, V. Vikram, A. R. Walker, and J. Weller. Dark Energy Survey Year 1 Results: Multi-Probe Methodology and Simulated Likelihood Analyses. *arXiv e-prints*, page arXiv:1706.09359, June 2017.

[142] T. M. C. Abbott, S. Allam, P. Andersen, C. Angus, J. Asorey, A. Avelino, S. Avila, B. A. Bassett, K. Bechtol, G. M. Bernstein, E. Bertin, D. Brooks, D. Brout, P. Brown, D. L. Burke, J. Calcino, A. Carnero Rosell, D. Carollo, M. Carrasco Kind, J. Carretero, R. Casas, F. J. Castander, R. Cawthon, P. Challis, M. Childress, A. Clocchiatti, C. E. Cunha, C. B. D'Andrea, L. N. da Costa, C. Davis, T. M. Davis, J. De Vicente, D. L. DePoy, S. Desai, H. T. Diehl, P. Doel, A. Drlica-Wagner, T. F. Eifler, A. E. Evrard, E. Fernandez, A. V. Filippenko, D. A. Finley, B. Flaugher, R. J. Foley, P. Fosalba, J. Frieman, L. Galbany, J. García-Bellido, E. Gaztanaga, T. Giannantonio, K. Glazebrook, D. A. Goldstein, S. González-Gaitán, D. Gruen, R. A. Gruendl, J. Gschwend, R. R. Gupta, G. Gutierrez, W. G. Hartley, S. R. Hinton, D. L. Hollowood, K. Honscheid, J. K. Hoormann, B. Hoyle, D. J. James, T. Jeltema, M. W. G. Johnson, M. D. Johnson, E. Kasai, S. Kent, R. Kessler, A. G. Kim, R. P. Kirshner, E. Kovacs, E. Krause, R. Kron, K. Kuehn, S. Kuhlmann, N. Kuropatkin, O. Lahav, J. Lasker, G. F. Lewis, T. S. Li, C. Lidman, M. Lima, H. Lin, E. Macaulay, M. A. G. Maia, K. S. Mandel, M. March, J. Marriner, J. L. Marshall, P. Martini, F. Menanteau, C. J. Miller, R. Miquel, V. Miranda, J. J. Mohr, E. Morganson, D. Muthukrishna, A. Möller, E. Neilsen, R. C. Nichol, B. Nord, P. Nugent, R. L. C. Ogando, A. Palmese, Y. C. Pan, A. A. Plazas, M. Pursiainen, A. K. Romer, A. Roodman, E. Rozo, E. S. Rykoff, M. Sako, E. Sanchez, V. Scarpine, R. Schindler, M. Schubnell, D. Scolnic, S. Serrano, I. Sevilla-Noarbe, R. Sharp, M. Smith, M. Soares-Santos, F. Sobreira, N. E. Sommer,

H. Spinka, E. Suchyta, M. Sullivan, E. Swann, G. Tarle, D. Thomas, R. C. Thomas, M. A. Troxel, B. E. Tucker, S. A. Uddin, A. R. Walker, W. Wester, P. Wiseman, R. C. Wolf, B. Yanny, B. Zhang, Y. Zhang, and DES Collaboration. First Cosmology Results using Type Ia Supernovae from the Dark Energy Survey: Constraints on Cosmological Parameters. ApJ, 872(2):L30, February 2019.

[143] T. M. C. Abbott, F. B. Abdalla, A. Alarcon, S. Allam, F. Andrade-Oliveira, J. Annis, S. Avila, M. Banerji, N. Banik, K. Bechtol, R. A. Bernstein, G. M. Bernstein, E. Bertin, D. Brooks, E. Buckley-Geer, D. L. Burke, H. Camacho, A. Carnero Rosell, M. Carrasco Kind, J. Carretero, F. J. Castander, R. Cawthon, K. C. Chan, M. Crocce, C. E. Cunha, C. B. D'Andrea, L. N. da Costa, C. Davis, J. De Vicente, D. L. DePoy, S. Desai, H. T. Diehl, P. Doel, A. Drlica-Wagner, T. F. Eifler, J. Elvin-Poole, J. Estrada, A. E. Evrard, B. Flaugher, P. Fosalba, J. Frieman, J. García-Bellido, E. Gaztanaga, D. W. Gerdes, T. Giannantonio, D. Gruen, R. A. Gruendl, J. Gschwend, G. Gutierrez, W. G. Hartley, D. Hollowood, K. Honscheid, B. Hoyle, B. Jain, D. J. James, T. Jeltema, M. D. Johnson, S. Kent, N. Kokron, E. Krause, K. Kuehn, S. Kuhlmann, N. Kuropatkin, F. Lacasa, O. Lahav, M. Lima, H. Lin, M. A. G. Maia, M. Manera, J. Marriner, J. L. Marshall, P. Martini, P. Melchior, F. Menanteau, C. J. Miller, R. Miquel, J. J. Mohr, E. Neilsen, W. J. Percival, A. A. Plazas, A. Porredon, A. K. Romer, A. Roodman, R. Rosenfeld, A. J. Ross, E. Rozo, E. S. Rykoff, M. Sako, E. Sanchez, B. Santiago, V. Scarpine, R. Schindler, M. Schubnell, S. Serrano, I. Sevilla-Noarbe, E. Sheldon, R. C. Smith, M. Smith, F. Sobreira, E. Suchyta, M. E. C. Swanson, G. Tarle, D. Thomas, M. A. Troxel, D. L. Tucker, V. Vikram, A. R. Walker, R. H. Wechsler, J. Weller, B. Yanny, and Y. Zhang. Dark Energy Survey Year 1 Results: Measurement of the Baryon Acoustic Oscillation scale in the distribution of galaxies to redshift 1. MNRAS, 483(4):4866–4883, March 2019.

[144] H. Jeffreys. *Theory of Probability*. Oxford, Oxford, England, third edition, 1961.

[145] Chris Blake, Sarah Brough, Matthew Colless, Warrick Couch, Scott Croom, Tamara Davis, Michael J. Drinkwater, Karl Forster, Karl Glazebrook, Ben Jelliffe, Russell J. Jurek, I. Hui Li, Barry Madore, Chris Martin, Kevin Pimbblet, Gregory B. Poole, Michael Pracy, Rob Sharp, Emily Wisnioski, David Woods, and Ted Wyder. The WiggleZ Dark Energy Survey: the selection function and z = 0.6 galaxy power spectrum. MNRAS, 406(2):803–821, August 2010.

[146] Ashley J. Ross, Will J. Percival, Ariel G. Sánchez, Lado Samushia, Shirley Ho, Eyal Kazin, Marc Manera, Beth Reid, Martin White, Rita Tojeiro,

Cameron K. McBride, Xiaoying Xu, David A. Wake, Michael A. Strauss, Francesco Montesano, Molly E. C. Swanson, Stephen Bailey, Adam S. Bolton, Antonio Montero Dorta, Daniel J. Eisenstein, Hong Guo, Jean-Christophe Hamilton, Robert C. Nichol, Nikhil Padmanabhan, Francisco Prada, David J. Schlegel, Mariana Vargas Magaña, Idit Zehavi, Michael Blanton, Dmitry Bizyaev, Howard Brewington, Antonio J. Cuesta, Elena Malanushenko, Viktor Malanushenko, Daniel Oravetz, John Parejko, Kaike Pan, Donald P. Schneider, Alaina Shelden, Audrey Simmons, Stephanie Snedden, and Gong-bo Zhao. The clustering of galaxies in the SDSS-III Baryon Oscillation Spectroscopic Survey: analysis of potential systematics. MNRAS, 424(1):564–590, July 2012.

[147] B. Leistedt, H. V. Peiris, F. Elsner, A. Benoit-Lévy, A. Amara, A. H. Bauer, M. R. Becker, C. Bonnett, C. Bruderer, M. T. Busha, M. Carrasco Kind, C. Chang, M. Crocce, L. N. da Costa, E. Gaztanaga, E. M. Huff, O. Lahav, A. Palmese, W. J. Percival, A. Refregier, A. J. Ross, E. Rozo, E. S. Rykoff, C. Sánchez, I. Sadeh, I. Sevilla-Noarbe, F. Sobreira, E. Suchyta, M. E. C. Swanson, R. H. Wechsler, F. B. Abdalla, S. Allam, M. Banerji, G. M. Bernstein, R. A. Bernstein, E. Bertin, S. L. Bridle, D. Brooks, E. Buckley-Geer, D. L. Burke, D. Capozzi, A. Carnero Rosell, J. Carretero, C. E. Cunha, C. B. D'Andrea, D. L. DePoy, S. Desai, H. T. Diehl, P. Doel, T. F. Eifler, A. E. Evrard, A. Fausti Neto, B. Flaugher, P. Fosalba, J. Frieman, D. W. Gerdes, D. Gruen, R. A. Gruendl, G. Gutierrez, K. Honscheid, D. J. James, M. Jarvis, S. Kent, K. Kuehn, N. Kuropatkin, T. S. Li, M. Lima, M. A. G. Maia, M. March, J. L. Marshall, P. Martini, P. Melchior, C. J. Miller, R. Miquel, R. C. Nichol, B. Nord, R. Ogando, A. A. Plazas, K. Reil, A. K. Romer, A. Roodman, E. Sanchez, B. Santiago, V. Scarpine, M. Schubnell, R. C. Smith, M. Soares-Santos, G. Tarle, J. Thaler, D. Thomas, V. Vikram, A. R. Walker, W. Wester, Y. Zhang, and J. Zuntz. Mapping and Simulating Systematics due to Spatially Varying Observing Conditions in DES Science Verification Data. ApJS, 226(2):24, October 2016.

[148] Noah Weaverdyck and Dragan Huterer. Mitigating contamination in LSS surveys: a comparison of methods. *arXiv e-prints*, page arXiv:2007.14499, July 2020.

[149] Richard Massey, Henk Hoekstra, Thomas Kitching, Jason Rhodes, Mark Cropper, Jérôme Amiaux, David Harvey, Yannick Mellier, Massimo Meneghetti, Lance Miller, Stéphane Paulin-Henriksson, Sandrine Pires, Roberto Scaramella, and Tim Schrabback. Origins of weak lensing systematics, and requirements on future instrumentation (or knowledge of instrumentation). MNRAS, 429(1):661–678, February 2013.

[150] S. Everett, B. Yanny, N. Kuropatkin, E. M. Huff, Y. Zhang, J. Myles,

A. Masegian, J. Elvin-Poole, S. Allam, G. M. Bernstein, I. Sevilla-Noarbe, M. Splettstoesser, E. Sheldon, M. Jarvis, A. Amon, I. Harrison, A. Choi, W. G. Hartley, A. Alarcon, C. Sánchez, D. Gruen, K. Eckert, J. Prat, M. Tabbutt, V. Busti, M. R. Becker, N. MacCrann, H. T. Diehl, D. L. Tucker, E. Bertin, T. Jeltema, A. Drlica-Wagner, R. A. Gruendl, K. Bechtol, A. Carnero Rosell, T. M. C. Abbott, M. Aguena, J. Annis, D. Bacon, S. Bhargava, D. Brooks, D. L. Burke, M. Carrasco Kind, J. Carretero, F. J. Castander, C. Conselice, M. Costanzi, L. N. da Costa, M. E. S. Pereira, J. De Vicente, J. DeRose, S. Desai, T. F. Eifler, A. E. Evrard, I. Ferrero, P. Fosalba, J. Frieman, J. García-Bellido, E. Gaztanaga, D. W. Gerdes, G. Gutierrez, S. R. Hinton, D. L. Hollowood, K. Honscheid, D. Huterer, D. J. James, S. Kent, E. Krause, K. Kuehn, O. Lahav, M. Lima, H. Lin, M. A. G. Maia, J. L. Marshall, P. Melchior, F. Menanteau, R. Miquel, J. J. Mohr, R. Morgan, J. Muir, R. L. C. Ogando, A. Palmese, F. Paz-Chinchón, A. A. Plazas, M. Rodriguez-Monroy, A. K. Romer, A. Roodman, E. Sanchez, V. Scarpine, S. Serrano, M. Smith, M. Soares-Santos, E. Suchyta, M. E. C. Swanson, G. Tarle, C. To, M. A. Troxel, T. N. Varga, J. Weller, and R. D. Wilkinson. Dark Energy Survey Year 3 Results: Measuring the Survey Transfer Function with Balrog. *arXiv e-prints*, page arXiv:2012.12825, December 2020.

[151] G. R. Blumenthal, S. M. Faber, J. R. Primack, and M. J. Rees. Formation of galaxies and large-scale structure with cold dark matter. Nature, 311:517–525, October 1984.

[152] Max Tegmark, Daniel J. Eisenstein, Michael A. Strauss, David H. Weinberg, Michael R. Blanton, Joshua A. Frieman, Masataka Fukugita, James E. Gunn, Andrew J. S. Hamilton, Gillian R. Knapp, Robert C. Nichol, Jeremiah P. Ostriker, Nikhil Padmanabhan, Will J. Percival, David J. Schlegel, Donald P. Schneider, Roman Scoccimarro, Uroš Seljak, Hee-Jong Seo, Molly Swanson, Alexander S. Szalay, Michael S. Vogeley, Jaiyul Yoo, Idit Zehavi, Kevork Abazajian, Scott F. Anderson, James Annis, Neta A. Bahcall, Bruce Bassett, Andreas Berlind, Jon Brinkmann, Tamás Budavari, Francisco Castander, Andrew Connolly, Istvan Csabai, Mamoru Doi, Douglas P. Finkbeiner, Bruce Gillespie, Karl Glazebrook, Gregory S. Hennessy, David W. Hogg, Željko Ivezić, Bhuvnesh Jain, David Johnston, Stephen Kent, Donald Q. Lamb, Brian C. Lee, Huan Lin, Jon Loveday, Robert H. Lupton, Jeffrey A. Munn, Kaike Pan, Changbom Park, John Peoples, Jeffrey R. Pier, Adrian Pope, Michael Richmond, Constance Rockosi, Ryan Scranton, Ravi K. Sheth, Albert Stebbins, Christopher Stoughton, István Szapudi, Douglas L. Tucker, Daniel E. vanden Berk, Brian Yanny, and Donald G. York. Cosmological constraints from the SDSS luminous red galaxies. Phys. Rev. D, 74(12):123507, December 2006.

[153] Tereasa G. Brainerd, Roger D. Blandford, and Ian Smail. Weak Gravitational Lensing by Galaxies. ApJ, 466:623, August 1996.

[154] Rachel Mandelbaum. Weak Lensing for Precision Cosmology. ARA&A, 56:393–433, September 2018.

[155] C. Chang, M. T. Busha, R. H. Wechsler, A. Refregier, A. Amara, E. Rykoff, M. R. Becker, C. Bruderer, L. Gamper, B. Leistedt, H. Peiris, T. Abbott, F. B. Abdalla, E. Balbinot, M. Banerji, R. A. Bernstein, E. Bertin, D. Brooks, A. Carnero, S. Desai, L. N. da Costa, C. E. Cunha, T. Eifler, A. E. Evrard, A. Fausti Neto, D. Gerdes, D. Gruen, D. James, K. Kuehn, M. A. G. Maia, M. Makler, R. Ogando, A. Plazas, E. Sanchez, B. Santiago, M. Schubnell, I. Sevilla-Noarbe, C. Smith, M. Soares-Santos, E. Suchyta, M. E. C. Swanson, G. Tarle, and J. Zuntz. Modeling the Transfer Function for the Dark Energy Survey. ApJ, 801(2):73, March 2015.

[156] A. J. Connolly, John Peterson, J. Garrett Jernigan, Robert Abel, Justin Bankert, Chihway Chang, Charles F. Claver, Robert Gibson, David K. Gilmore, Emily Grace, R. Lynne Jones, Zeljko Ivezic, James Jee, Mario Juric, Steven M. Kahn, Victor L. Krabbendam, Simon Krughoff, Suzanne Lorenz, James Pizagno, Andrew Rasmussen, Nathan Todd, J. Anthony Tyson, and Mallory Young. Simulating the LSST system. In George Z. Angeli and Philippe Dierickx, editors, *Modeling, Systems Engineering, and Project Management for Astronomy IV*, volume 7738, pages 612 – 621. International Society for Optics and Photonics, SPIE, 2010.

[157] Hiroaki Aihara, Carlos Allende Prieto, Deokkeun An, Scott F. Anderson, Éric Aubourg, Eduardo Balbinot, Timothy C. Beers, Andreas A. Berlind, Steven J. Bickerton, Dmitry Bizyaev, Michael R. Blanton, John J. Bochanski, Adam S. Bolton, Jo Bovy, W. N. Brandt, J. Brinkmann, Peter J. Brown, Joel R. Brownstein, Nicolas G. Busca, Heather Campbell, Michael A. Carr, Yanmei Chen, Cristina Chiappini, Johan Comparat, Natalia Connolly, Marina Cortes, Rupert A. C. Croft, Antonio J. Cuesta, Luiz N. da Costa, James R. A. Davenport, Kyle Dawson, Saurav Dhital, Anne Ealet, Garrett L. Ebelke, Edward M. Edmondson, Daniel J. Eisenstein, Stephanie Escoffier, Massimiliano Esposito, Michael L. Evans, Xiaohui Fan, Bruno Femenía Castellá, Andreu Font-Ribera, Peter M. Frinchaboy, Jian Ge, Bruce A. Gillespie, G. Gilmore, Jonay I. González Hernández, J. Richard Gott, Andrew Gould, Eva K. Grebel, James E. Gunn, Jean-Christophe Hamilton, Paul Harding, David W. Harris, Suzanne L. Hawley, Frederick R. Hearty, Shirley Ho, David W. Hogg, Jon A. Holtzman, Klaus Honscheid, Naohisa Inada, Inese I. Ivans, Linhua Jiang, Jennifer A. Johnson, Cathy Jordan, Wendell P. Jordan, Eyal A. Kazin, David Kirkby, Mark A. Klaene, G. R. Knapp, Jean-Paul Kneib, C. S. Kochanek, Lars Koesterke,

Juna A. Kollmeier, Richard G. Kron, Hubert Lampeitl, Dustin Lang, Jean-Marc Le Goff, Young Sun Lee, Yen-Ting Lin, Daniel C. Long, Craig P. Loomis, Sara Lucatello, Britt Lundgren, Robert H. Lupton, Zhibo Ma, Nicholas MacDonald, Suvrath Mahadevan, Marcio A. G. Maia, Martin Makler, Elena Malanushenko, Viktor Malanushenko, Rachel Mandelbaum, Claudia Maraston, Daniel Margala, Karen L. Masters, Cameron K. McBride, Peregrine M. McGehee, Ian D. McGreer, Brice Ménard, Jordi Miralda-Escudé, Heather L. Morrison, F. Mullally, Demitri Muna, Jeffrey A. Munn, Hitoshi Murayama, Adam D. Myers, Tracy Naugle, Angelo Fausti Neto, Duy Cuong Nguyen, Robert C. Nichol, Robert W. O'Connell, Ricardo L. C. Ogando, Matthew D. Olmstead, Daniel J. Oravetz, Nikhil Padmanabhan, Nathalie Palanque-Delabrouille, Kaike Pan, Parul Pandey, Isabelle Pâris, Will J. Percival, Patrick Petitjean, Robert Pfaffenberger, Janine Pforr, Stefanie Phleps, Christophe Pichon, Matthew M. Pieri, Francisco Prada, Adrian M. Price-Whelan, M. Jordan Raddick, Beatriz H. F. Ramos, Céline Reylé, James Rich, Gordon T. Richards, Hans-Walter Rix, Annie C. Robin, Helio J. Rocha-Pinto, Constance M. Rockosi, Natalie A. Roe, Emmanuel Rollinde, Ashley J. Ross, Nicholas P. Ross, Bruno M. Rossetto, Ariel G. Sánchez, Conor Sayres, David J. Schlegel, Katharine J. Schlesinger, Sarah J. Schmidt, Donald P. Schneider, Erin Sheldon, Yiping Shu, Jennifer Simmerer, Audrey E. Simmons, Thirupathi Sivarani, Stephanie A. Snedden, Jennifer S. Sobeck, Matthias Steinmetz, Michael A. Strauss, Alexander S. Szalay, Masayuki Tanaka, Aniruddha R. Thakar, Daniel Thomas, Jeremy L. Tinker, Benjamin M. Tofflemire, Rita Tojeiro, Christy A. Tremonti, Jan Vandenberg, M. Vargas Magaña, Licia Verde, Nicole P. Vogt, David A. Wake, Ji Wang, Benjamin A. Weaver, David H. Weinberg, Martin White, Simon D. M. White, Brian Yanny, Naoki Yasuda, Christophe Yeche, and Idit Zehavi. The Eighth Data Release of the Sloan Digital Sky Survey: First Data from SDSS-III. ApJS, 193(2):29, April 2011.

[158] H. Hildebrandt. Observational biases in flux magnification measurements. MNRAS, 455(4):3943–3951, February 2016.

[159] I. Fenech Conti, R. Herbonnet, H. Hoekstra, J. Merten, L. Miller, and M. Viola. Calibration of weak-lensing shear in the Kilo-Degree Survey. MNRAS, 467(2):1627–1651, May 2017.

[160] Jinchi Lv and Jun S. Liu. Model Selection Principles in Misspecified Models. *arXiv e-prints*, page arXiv:1005.5483, May 2010.

[161] Arnau Pujol, Florent Sureau, Jerome Bobin, Frederic Courbin, Marc Gentile, and Martin Kilbinger. Shear measurement bias. I. Dependencies on methods, simulation parameters, and measured parameters. A&A, 641:A164, September 2020.

[162] R. D. McClure, J. E. Hesser, P. B. Stetson, and L. L. Stryker. CCD photometry of the sparse halo cluster E 3. PASP, 97:665–675, August 1985.

[163] G. H. Smith, R. D. McClure, P. B. Stetson, J. E. Hesser, and R. A. Bell. CCD photometry of the globular cluster Palomar 5. AJ, 91:842–854, April 1986.

[164] Peter B. Stetson. DAOPHOT: A Computer Program for Crowded-Field Stellar Photometry. PASP, 99:191, March 1987.

[165] G. Bunce. A monte carlo/data hybrid: A general technique to measure detection efficiency. *Nuclear Instruments and Methods*, 172(3):553–557, 1980.

[166] B. P. Abbott, R. Abbott, R. Adhikari, P. Ajith, B. Allen, G. Allen, R. S. Amin, S. B. Anderson, W. G. Anderson, M. A. Arain, M. Araya, H. Armandula, P. Armor, Y. Aso, S. Aston, P. Aufmuth, C. Aulbert, S. Babak, P. Baker, S. Ballmer, C. Barker, D. Barker, B. Barr, P. Barriga, L. Barsotti, M. A. Barton, I. Bartos, R. Bassiri, M. Bastarrika, B. Behnke, M. Benacquista, J. Betzwieser, P. T. Beyersdorf, I. A. Bilenko, G. Billingsley, R. Biswas, E. Black, J. K. Blackburn, L. Blackburn, D. Blair, B. Bland, T. P. Bodiya, L. Bogue, R. Bork, V. Boschi, S. Bose, P. R. Brady, V. B. Braginsky, J. E. Brau, D. O. Bridges, M. Brinkmann, A. F. Brooks, D. A. Brown, A. Brummit, G. Brunet, A. Bullington, A. Buonanno, O. Burmeister, R. L. Byer, L. Cadonati, J. B. Camp, J. Cannizzo, K. C. Cannon, J. Cao, L. Cardenas, S. Caride, G. Castaldi, S. Caudill, M. Cavaglià, C. Cepeda, T. Chalermsongsak, E. Chalkley, P. Charlton, S. Chatterji, S. Chelkowski, Y. Chen, N. Christensen, C. T. Y. Chung, D. Clark, J. Clark, J. H. Clayton, T. Cokelaer, C. N. Colacino, R. Conte, D. Cook, T. R. C. Corbitt, N. Cornish, D. Coward, D. C. Coyne, J. D. E. Creighton, T. D. Creighton, A. M. Cruise, R. M. Culter, A. Cumming, L. Cunningham, S. L. Danilishin, K. Danzmann, B. Daudert, G. Davies, E. J. Daw, D. DeBra, J. Degallaix, V. Dergachev, S. Desai, R. DeSalvo, S. Dhurandhar, M. Díaz, A. Dietz, F. Donovan, K. L. Dooley, E. E. Doomes, R. W. P. Drever, J. Dueck, I. Duke, J. C. Dumas, J. G. Dwyer, C. Echols, M. Edgar, A. Effler, P. Ehrens, E. Espinoza, T. Etzel, M. Evans, T. Evans, S. Fairhurst, Y. Faltas, Y. Fan, D. Fazi, H. Fehrmenn, L. S. Finn, K. Flasch, S. Foley, C. Forrest, N. Fotopoulos, A. Franzen, M. Frede, M. Frei, Z. Frei, A. Freise, R. Frey, T. Fricke, P. Fritschel, V. V. Frolov, M. Fyffe, V. Galdi, J. A. Garofoli, I. Gholami, J. A. Giaime, S. Giampanis, K. D. Giardina, K. Goda, E. Goetz, L. M. Goggin, G. González, M. L. Gorodetsky, S. Goßler, R. Gouaty, A. Grant, S. Gras, C. Gray, M. Gray, R. J. S. Greenhalgh, A. M. Gretarsson, F. Grimaldi, R. Grosso, H. Grote, S. Grunewald, M. Guenther, E. K. Gustafson, R. Gustafson, B. Hage, J. M. Hallam, D. Hammer, G. D. Hammond, C. Hanna, J. Hanson, J. Harms, G. M. Harry, I. W. Harry,

E. D. Harstad, K. Haughian, K. Hayama, J. Heefner, I. S. Heng, A. Heptonstall, M. Hewitson, S. Hild, E. Hirose, D. Hoak, K. A. Hodge, K. Holt, D. J. Hosken, J. Hough, D. Hoyland, B. Hughey, S. H. Huttner, D. R. Ingram, T. Isogai, M. Ito, A. Ivanov, B. Johnson, W. W. Johnson, D. I. Jones, G. Jones, R. Jones, L. Ju, P. Kalmus, V. Kalogera, S. Kandhasamy, J. Kanner, D. Kasprzyk, E. Katsavounidis, K. Kawabe, S. Kawamura, F. Kawazoe, W. Kells, D. G. Keppel, A. Khalaidovski, F. Y. Khalili, R. Khan, E. Khazanov, P. King, J. S. Kissel, S. Klimenko, K. Kokeyama, V. Kondrashov, R. Kopparapu, S. Koranda, D. Kozak, B. Krishnan, R. Kumar, P. Kwee, P. K. Lam, M. Landry, B. Lantz, A. Lazzarini, H. Lei, M. Lei, N. Leindecker, I. Leonor, C. Li, H. Lin, P. E. Lindquist, T. B. Littenberg, N. A. Lockerbie, D. Lodhia, M. Longo, M. Lormand, P. Lu, M. Lubiński, A. Lucianetti, H. Lück, B. Machenschalk, M. MacInnis, M. Mageswaran, K. Mailand, I. Mandel, V. Mandic, S. Márka, Z. Márka, A. Markosyan, J. Markowitz, E. Maros, I. W. Martin, R. M. Martin, J. N. Marx, K. Mason, F. Matichard, L. Matone, R. A. Matzner, N. Mavalvala, R. McCarthy, D. E. McClelland, S. C. McGuire, M. McHugh, G. McIntyre, D. J. A. McKechan, K. McKenzie, M. Mehmet, A. Melatos, A. C. Melissinos, D. F. Menéndez, G. Mendell, R. A. Mercer, S. Meshkov, C. Messenger, M. S. Meyer, J. Miller, J. Minelli, Y. Mino, V. P. Mitrofanov, G. Mitselmakher, R. Mittleman, O. Miyakawa, B. Moe, S. D. Mohanty, S. R. P. Mohapatra, G. Moreno, T. Morioka, K. Mors, K. Mossavi, C. Mow Lowry, G. Mueller, H. Müller-Ebhardt, D. Muhammad, S. Mukherjee, H. Mukhopadhyay, A. Mullavey, J. Munch, P. G. Murray, E. Myers, J. Myers, T. Nash, J. Nelson, G. Newton, A. Nishizawa, K. Numata, J. O'Dell, B. O'Reilly, R. O'Shaughnessy, E. Ochsner, G. H. Ogin, D. J. Ottaway, R. S. Ottens, H. Overmier, B. J. Owen, Y. Pan, C. Pankow, M. A. Papa, V. Parameshwaraiah, P. Patel, M. Pedraza, S. Penn, A. Perraca, V. Pierro, I. M. Pinto, M. Pitkin, H. J. Pletsch, M. V. Plissi, F. Postiglione, M. Principe, R. Prix, L. Prokhorov, O. Punken, V. Quetschke, F. J. Raab, D. S. Rabeling, H. Radkins, P. Raffai, Z. Raics, N. Rainer, M. Rakhmanov, V. Raymond, C. M. Reed, T. Reed, H. Rehbein, S. Reid, D. H. Reitze, R. Riesen, K. Riles, B. Rivera, P. Roberts, N. A. Robertson, C. Robinson, E. L. Robinson, S. Roddy, C. Röver, J. Rollins, J. D. Romano, J. H. Romie, S. Rowan, A. Rüdiger, P. Russell, K. Ryan, S. Sakata, L. Sancho de la Jordana, V. Sandberg, V. Sannibale, L. Santamaría, S. Saraf, P. Sarin, B. S. Sathyaprakash, S. Sato, M. Satterthwaite, P. R. Saulson, R. Savage, P. Savov, M. Scanlan, R. Schilling, R. Schnabel, R. Schofield, B. Schulz, B. F. Schutz, P. Schwinberg, J. Scott, S. M. Scott, A. C. Searle, B. Sears, F. Seifert, D. Sellers, A. S. Sengupta, A. Sergeev, B. Shapiro, P. Shawhan, D. H. Shoemaker, A. Sibley, X. Siemens, D. Sigg, S. Sinha, A. M. Sintes, B. J. J. Slagmolen, J. Slutsky, J. R. Smith, M. R. Smith, N. D. Smith, K. Somiya, B. Sorazu, A. Stein,

L. C. Stein, S. Steplewski, A. Stochino, R. Stone, K. A. Strain, S. Strigin, A. Stroeer, A. L. Stuver, T. Z. Summerscales, K. X. Sun, M. Sung, P. J. Sutton, G. P. Szokoly, D. Talukder, L. Tang, D. B. Tanner, S. P. Tarabrin, J. R. Taylor, R. Taylor, J. Thacker, K. A. Thorne, A. Thüring, K. V. Tokmakov, C. Torres, C. Torrie, G. Traylor, M. Trias, D. Ugolini, J. Ulmen, K. Urbanek, H. Vahlbruch, M. Vallisneri, C. van den Broeck, M. V. van der Sluys, A. A. van Veggel, S. Vass, R. Vaulin, A. Vecchio, J. Veitch, P. Veitch, C. Veltkamp, A. Villar, C. Vorvick, S. P. Vyachanin, S. J. Waldman, L. Wallace, R. L. Ward, A. Weidner, M. Weinert, A. J. Weinstein, R. Weiss, L. Wen, S. Wen, K. Wette, J. T. Whelan, S. E. Whitcomb, B. F. Whiting, C. Wilkinson, P. A. Willems, H. R. Williams, L. Williams, B. Willke, I. Wilmut, L. Winkelmann, W. Winkler, C. C. Wipf, A. G. Wiseman, G. Woan, R. Wooley, J. Worden, W. Wu, I. Yakushin, H. Yamamoto, Z. Yan, S. Yoshida, M. Zanolin, J. Zhang, L. Zhang, C. Zhao, N. Zotov, M. E. Zucker, H. zur Mühlen, and J. Zweizig. LIGO: the Laser Interferometer Gravitational-Wave Observatory. *Reports on Progress in Physics*, 72(7):076901, July 2009.

[167] D. S. Akerib, X. Bai, S. Bedikian, E. Bernard, A. Bernstein, A. Bolozdynya, A. Bradley, D. Byram, S. B. Cahn, C. Camp, M. C. Carmona-Benitez, D. Carr, J. J. Chapman, A. Chiller, C. Chiller, K. Clark, T. Classen, T. Coffey, A. Curioni, E. Dahl, S. Dazeley, L. de Viveiros, A. Dobi, E. Dragowsky, E. Druszkiewicz, B. Edwards, C. H. Faham, S. Fiorucci, R. J. Gaitskell, K. R. Gibson, M. Gilchriese, C. Hall, M. Hanhardt, B. Holbrook, M. Ihm, R. G. Jacobsen, L. Kastens, K. Kazkaz, R. Knoche, S. Kyre, J. Kwong, R. Lander, N. A. Larsen, C. Lee, D. S. Leonard, K. T. Lesko, A. Lindote, M. I. Lopes, A. Lyashenko, D. C. Malling, R. Mannino, Z. Marquez, D. N. McKinsey, D. M. Mei, J. Mock, M. Moongweluwan, M. Morii, H. Nelson, F. Neves, J. A. Nikkel, M. Pangilinan, P. D. Parker, E. K. Pease, K. Pech, P. Phelps, A. Rodionov, P. Roberts, A. Shei, T. Shutt, C. Silva, W. Skulski, V. N. Solovov, C. J. Sofka, P. Sorensen, J. Spaans, T. Stiegler, D. Stolp, R. Svoboda, M. Sweany, M. Szydagis, D. Taylor, J. Thomson, M. Tripathi, S. Uvarov, J. R. Verbus, N. Walsh, R. Webb, D. White, J. T. White, T. J. Whitis, M. Wlasenko, F. L. H. Wolfs, M. Woods, and C. Zhang. The Large Underground Xenon (LUX) experiment. *Nuclear Instruments and Methods in Physics Research A*, 704:111–126, March 2013.

[168] C. Biwer, D. Barker, J. C. Batch, J. Betzwieser, R. P. Fisher, E. Goetz, S. Kandhasamy, S. Karki, J. S. Kissel, A. P. Lundgren, D. M. Macleod, A. Mullavey, K. Riles, J. G. Rollins, K. A. Thorne, E. Thrane, T. D. Abbott, B. Allen, D. A. Brown, P. Charlton, S. G. Crowder, P. Fritschel, J. B. Kanner, M. Landry, C. Lazzaro, M. Millhouse, M. Pitkin, R. L. Savage, P. Shawhan, D. H. Shoemaker, J. R. Smith, L. Sun, J. Veitch, S. Vi-

tale, A. J. Weinstein, N. Cornish, R. C. Essick, M. Fays, E. Katsavounidis, J. Lange, T. B. Littenberg, R. Lynch, P. M. Meyers, F. Pannarale, R. Prix, R. O'Shaughnessy, and D. Sigg. Validating gravitational-wave detections: The Advanced LIGO hardware injection system. Phys. Rev. D, 95(6):062002, March 2017.

[169] D. S. Akerib, S. Alsum, H. M. Araújo, X. Bai, A. J. Bailey, J. Balajthy, P. Beltrame, E. P. Bernard, A. Bernstein, T. P. Biesiadzinski, E. M. Boulton, R. Bramante, P. Brás, D. Byram, S. B. Cahn, M. C. Carmona-Benitez, C. Chan, A. A. Chiller, C. Chiller, A. Currie, J. E. Cutter, T. J. R. Davison, A. Dobi, J. E. Y. Dobson, E. Druszkiewicz, B. N. Edwards, C. H. Faham, S. Fiorucci, R. J. Gaitskell, V. M. Gehman, C. Ghag, K. R. Gibson, M. G. D. Gilchriese, C. R. Hall, M. Hanhardt, S. J. Haselschwardt, S. A. Hertel, D. P. Hogan, M. Horn, D. Q. Huang, C. M. Ignarra, M. Ihm, R. G. Jacobsen, W. Ji, K. Kamdin, K. Kazkaz, D. Khaitan, R. Knoche, N. A. Larsen, C. Lee, B. G. Lenardo, K. T. Lesko, A. Lindote, M. I. Lopes, A. Manalaysay, R. L. Mannino, M. F. Marzioni, D. N. McKinsey, D. M. Mei, J. Mock, M. Moongweluwan, J. A. Morad, A. St. J. Murphy, C. Nehrkorn, H. N. Nelson, F. Neves, K. O'Sullivan, K. C. Oliver-Mallory, K. J. Palladino, E. K. Pease, P. Phelps, L. Reichhart, C. Rhyne, S. Shaw, T. A. Shutt, C. Silva, M. Solmaz, V. N. Solovov, P. Sorensen, S. Stephenson, T. J. Sumner, M. Szydagis, D. J. Taylor, W. C. Taylor, B. P. Tennyson, P. A. Terman, D. R. Tiedt, W. H. To, M. Tripathi, L. Tvrznikova, S. Uvarov, J. R. Verbus, R. C. Webb, J. T. White, T. J. Whitis, M. S. Witherell, F. L. H. Wolfs, J. Xu, K. Yazdani, S. K. Young, C. Zhang, and LUX Collaboration. Results from a Search for Dark Matter in the Complete LUX Exposure. Phys. Rev. Lett., 118(2):021303, January 2017.

[170] Song Huang, Alexie Leauthaud, Ryoma Murata, James Bosch, Paul Price, Robert Lupton, Rachel Mandelbaum, Claire Lackner, Steven Bickerton, Satoshi Miyazaki, Jean Coupon, and Masayuki Tanaka. Characterization and photometric performance of the Hyper Suprime-Cam Software Pipeline. PASJ, 70:S6, January 2018.

[171] Paul Martini, Stephen Bailey, Robert W. Besuner, David Brooks, Peter Doel, Jerry Edelstein, Daniel Eisenstein, Brenna Flaugher, Gaston Gutierrez, Stewart E. Harris, Klaus Honscheid, Patrick Jelinsky, Richard Joyce, Stephen Kent, Michael Levi, Francisco Prada, Claire Poppett, David Rabinowitz, Constance Rockosi, Laia Cardiel Sas, David J. Schlegel, Michael Schubnell, Ray Sharples, Joseph H. Silber, David Sprayberry, and Risa Wechsler. Overview of the Dark Energy Spectroscopic Instrument. In Christopher J. Evans, Luc Simard, and Hideki Takami, editors, *Ground-based and Airborne Instrumentation for Astronomy VII*, volume 10702 of

Society of Photo-Optical Instrumentation Engineers (SPIE) Conference Series, page 107021F, July 2018.

[172] Hui Kong, Kaylan J. Burleigh, Ashley Ross, John Moustakas, Chia-Hsun Chuang, Johan Comparat, Arnaud de Mattia, Hélion du Mas des Bourboux, Klaus Honscheid, Sichen Lin, Anand Raichoor, Graziano Rossi, and Cheng Zhao. Removing imaging systematics from galaxy clustering measurements with Obiwan: application to the SDSS-IV extended Baryon Oscillation Spectroscopic Survey emission-line galaxy sample. MNRAS, 499(3):3943–3960, September 2020.

[173] W. G. Hartley, A. Choi, A. Amon, R. A. Gruendl, E. Sheldon, I. Harrison, G. M. Bernstein, I. Sevilla-Noarbe, B. Yanny, K. Eckert, H. T. Diehl, A. Alarcon, M. Banerji, K. Bechtol, R. Buchs, S. Cantu, C. Conselice, J. Cordero, C. Davis, T. M. Davis, S. Dodelson, A. Drlica-Wagner, S. Everett, A. Ferté, D. Gruen, K. Honscheid, M. Jarvis, M. D. Johnson, N. Kokron, N. MacCrann, J. Myles, A. B. Pace, A. Palmese, F. Paz-Chinchón, M. E. S. Pereira, A. A. Plazas, J. Prat, M. Rodriguez-Monroy, E. S. Rykoff, S. Samuroff, C. Sánchez, L. F. Secco, F. Tarsitano, A. Tong, M. A. Troxel, Z. Vasquez, K. Wang, C. Zhou, T. M. C. Abbott, M. Aguena, S. Allam, J. Annis, D. Bacon, E. Bertin, S. Bhargava, D. Brooks, D. L. Burke, A. Carnero Rosell, M. Carrasco Kind, J. Carretero, F. J. Castander, M. Costanzi, M. Crocce, L. N. da Costa, J. De Vicente, J. DeRose, S. Desai, J. P. Dietrich, T. F. Eifler, J. Elvin-Poole, I. Ferrero, B. Flaugher, P. Fosalba, J. García-Bellido, E. Gaztanaga, D. W. Gerdes, J. Gschwend, G. Gutierrez, S. R. Hinton, D. L. Hollowood, D. Huterer, D. J. James, S. Kent, E. Krause, K. Kuehn, N. Kuropatkin, O. Lahav, H. Lin, M. A. G. Maia, M. March, J. L. Marshall, P. Martini, P. Melchior, F. Menanteau, R. Miquel, J. J. Mohr, R. Morgan, E. Neilsen, R. L. C. Ogando, S. Pandey, A. K. Romer, A. Roodman, M. Sako, E. Sanchez, V. Scarpine, S. Serrano, M. Smith, M. Soares-Santos, E. Suchyta, M. E. C. Swanson, G. Tarle, D. Thomas, C. To, T. N. Varga, A. R. Walker, W. Wester, R. D. Wilkinson, and J. Zuntz. Dark Energy Survey Year 3 Results: Deep Field Optical + Near-Infrared Images and Catalogue. *arXiv e-prints*, page arXiv:2012.12824, December 2020.

[174] N. Scoville, H. Aussel, M. Brusa, P. Capak, C. M. Carollo, M. Elvis, M. Giavalisco, L. Guzzo, G. Hasinger, C. Impey, J. P. Kneib, O. LeFevre, S. J. Lilly, B. Mobasher, A. Renzini, R. M. Rich, D. B. Sanders, E. Schinnerer, D. Schminovich, P. Shopbell, Y. Taniguchi, and N. D. Tyson. The Cosmic Evolution Survey (COSMOS): Overview. ApJS, 172(1):1–8, September 2007.

[175] M. Jarvis, G. M. Bernstein, A. Amon, C. Davis, P. F. Léget, K. Bechtol, I. Harrison, M. Gatti, A. Roodman, C. Chang, R. Chen, A. Choi, S. De-

sai, A. Drlica-Wagner, D. Gruen, R. A. Gruendl, A. Hernandez, N. MacCrann, J. Meyers, A. Navarro-Alsina, S. Pandey, A. A. Plazas, L. F. Secco, E. Sheldon, M. A. Troxel, S. Vorperian, K. Wei, J. Zuntz, T. M. C. Abbott, M. Aguena, S. Allam, S. Avila, S. Bhargava, S. L. Bridle, D. Brooks, A. Carnero Rosell, M. Carrasco Kind, J. Carretero, M. Costanzi, L. N. da Costa, J. De Vicente, H. T. Diehl, P. Doel, S. Everett, B. Flaugher, P. Fosalba, J. Frieman, J. García-Bellido, E. Gaztanaga, D. W. Gerdes, G. Gutierrez, S. R. Hinton, D. L. Hollowood, K. Honscheid, D. J. James, S. Kent, K. Kuehn, N. Kuropatkin, O. Lahav, M. A. G. Maia, M. March, J. L. Marshall, P. Melchior, F. Menanteau, R. Miquel, R. L. C. Ogando, F. Paz-Chinchón, E. S. Rykoff, E. Sanchez, V. Scarpine, M. Schubnell, S. Serrano, I. Sevilla-Noarbe, M. Smith, E. Suchyta, M. E. C. Swanson, G. Tarle, T. N. Varga, A. R. Walker, W. Wester, R. D. Wilkinson, and (DES Collaboration). Dark Energy Survey year 3 results: point spread function modelling. MNRAS, 501(1):1282–1299, February 2021.

[176] B. T. P. Rowe, M. Jarvis, R. Mandelbaum, G. M. Bernstein, J. Bosch, M. Simet, J. E. Meyers, T. Kacprzak, R. Nakajima, J. Zuntz, H. Miyatake, J. P. Dietrich, R. Armstrong, P. Melchior, and M. S. S. Gill. GALSIM: The modular galaxy image simulation toolkit. *Astronomy and Computing*, 10:121–150, April 2015.

[177] David J. Schlegel, Douglas P. Finkbeiner, and Marc Davis. Maps of Dust Infrared Emission for Use in Estimation of Reddening and Cosmic Microwave Background Radiation Foregrounds. *The Astrophysical Journal*, 500(2):525–553, jun 1998.

[178] O. Bienaymé, J. Leca, and A. C. Robin. A new dynamically self-consistent version of the Besançon Galaxy model. A&A, 620:A103, December 2018.

[179] H. J. McCracken, B. Milvang-Jensen, J. Dunlop, M. Franx, J. P. U. Fynbo, O. Le Fèvre, J. Holt, K. I. Caputi, Y. Goranova, F. Buitrago, J. P. Emerson, W. Freudling, P. Hudelot, C. López-Sanjuan, F. Magnard, Y. Mellier, P. Møller, K. K. Nilsson, W. Sutherland, L. Tasca, and J. Zabl. UltraVISTA: a new ultra-deep near-infrared survey in COSMOS. A&A, 544:A156, August 2012.

[180] D. Tanoglidis, A. Drlica-Wagner, K. Wei, T. S. Li, F. J. Sánchez, Y. Zhang, A. H. G. Peter, A. Feldmeier-Krause, J. Prat, K. Casey, A. Palmese, C. Sánchez, J. DeRose, C. Conselice, T. M. C. Abbott, M. Aguena, S. Allam, S. Avila, K. Bechtol, E. Bertin, S. Bhargava, D. Brooks, D. L. Burke, A. Carnero Rosell, M. Carrasco Kind, J. Carretero, C. Chang, M. Costanzi, L. N. da Costa, J. De Vicente, S. Desai, H. T. Diehl, P. Doel, T. F. Eifler, S. Everett, A. E. Evrard, B. Flaugher, J. Frieman, J. García-Bellido, D. W.

Gerdes, R. A. Gruendl, J. Gschwend, G. Gutierrez, W. G. Hartley, D. L. Hollowood, D. Huterer, D. J. James, E. Krause, K. Kuehn, N. Kuropatkin, M. A. G. Maia, M. March, J. L. Marshall, F. Menanteau, R. Miquel, R. L. C. Ogando, F. Paz-Chinchón, A. K. Romer, A. Roodman, E. Sanchez, V. Scarpine, S. Serrano, I. Sevilla-Noarbe, M. Smith, E. Suchyta, G. Tarle, D. Thomas, D. L. Tucker, and A. R. Walker. Shadows in the Dark: Low-Surface-Brightness Galaxies Discovered in the Dark Energy Survey. *arXiv e-prints*, page arXiv:2006.04294, June 2020.

[181] J. Elvin-Poole et al. Dark Energy Survey Year 3 Results: Measurement, modelling and cosmological impact of magnification in galaxy clustering and galaxy-galaxy lensing. *To be submitted to MNRAS*, 2021.

[182] Kuijken, K. Gaap: Psf- and aperture-matched photometry using shapelets. *A&A*, 482(3):1053–1067, 2008.

[183] Vernesa Smolčić, Željko Ivezić, Gillian R. Knapp, Robert H. Lupton, Krešimir Pavlovski, Saša Ilijić, David Schlegel, J. Allyn Smith, Peregrine M. McGehee, Nicole M. Silvestri, Suzanne L. Hawley, Constance Rockosi, James E. Gunn, Michael A. Strauss, Xiaohui Fan, Daniel Eisenstein, and Hugh Harris. A Second Stellar Color Locus: a Bridge from White Dwarfs to M stars. ApJ, 615(2):L141–L144, November 2004.

[184] M. Rodríguez-Monroy et al. Dark Energy Survey Year 3 Results: Galaxy clustering and systematics treatment for lens galaxy samples. *To be submitted to MNRAS*, 2020.

[185] K. M. Górski, E. Hivon, A. J. Banday, B. D. Wandelt, F. K. Hansen, M. Reinecke, and M. Bartelmann. HEALPix: A Framework for High-Resolution Discretization and Fast Analysis of Data Distributed on the Sphere. ApJ, 622(2):759–771, April 2005.

[186] A. Choi, C. Heymans, C. Blake, H. Hildebrandt, C. A. J. Duncan, T. Erben, R. Nakajima, L. Van Waerbeke, and M. Viola. CFHTLenS and RCSLenS: testing photometric redshift distributions using angular cross-correlations with spectroscopic galaxy surveys. MNRAS, 463(4):3737–3754, December 2016.

[187] M. Garcia-Fernandez, E. Sanchez, I. Sevilla-Noarbe, E. Suchyta, E. M. Huff, E. Gaztanaga, Aleksić, J. , R. Ponce, F. J. Castander, B. Hoyle, T. M. C. Abbott, F. B. Abdalla, S. Allam, J. Annis, A. Benoit-Lévy, G. M. Bernstein, E. Bertin, D. Brooks, E. Buckley-Geer, D. L. Burke, A. Carnero Rosell, M. Carrasco Kind, J. Carretero, M. Crocce, C. E. Cunha, C. B. D'Andrea, L. N. da Costa, D. L. DePoy, S. Desai, H. T. Diehl, T. F. Eifler, A. E. Evrard, E. Fernandez, B. Flaugher, P. Fosalba, J. Frieman, J. García-Bellido, D. W.

Gerdes, T. Giannantonio, D. Gruen, R. A. Gruendl, J. Gschwend, G. Gutierrez, D. J. James, M. Jarvis, D. Kirk, E. Krause, K. Kuehn, N. Kuropatkin, O. Lahav, M. Lima, N. MacCrann, M. A. G. Maia, M. March, J. L. Marshall, P. Melchior, R. Miquel, J. J. Mohr, A. A. Plazas, A. K. Romer, A. Roodman, E. S. Rykoff, V. Scarpine, M. Schubnell, R. C. Smith, M. Soares-Santos, F. Sobreira, G. Tarle, D. Thomas, A. R. Walker, W. Wester, and DES Collaboration. Weak lensing magnification in the Dark Energy Survey Science Verification data. MNRAS, 476(1):1071–1085, May 2018.

[188] A. Porredon, M. Crocce, P. Fosalba, J. Elvin-Poole, A. Carnero Rosell, R. Cawthon, T. F. Eifler, X. Fang, I. Ferrero, E. Krause, N. MacCrann, N. Weaverdyck, T. M. C. Abbott, M. Aguena, S. Allam, A. Amon, S. Avila, D. Bacon, E. Bertin, S. Bhargava, S. L. Bridle, D. Brooks, M. Carrasco Kind, J. Carretero, F. J. Castander, A. Choi, M. Costanzi, L. N. da Costa, M. E. S. Pereira, J. De Vicente, S. Desai, H. T. Diehl, P. Doel, A. Drlica-Wagner, K. Eckert, A. Ferté, B. Flaugher, J. Frieman, J. García-Bellido, E. Gaztanaga, D. W. Gerdes, T. Giannantonio, D. Gruen, R. A. Gruendl, J. Gschwend, G. Gutierrez, W. G. Hartley, S. R. Hinton, D. L. Hollowood, K. Honscheid, B. Hoyle, D. J. James, M. Jarvis, K. Kuehn, N. Kuropatkin, M. A. G. Maia, J. L. Marshall, F. Menanteau, R. Miquel, R. Morgan, A. Palmese, S. Pandey, F. Paz-Chinchón, A. A. Plazas, M. Rodriguez-Monroy, A. Roodman, S. Samuroff, E. Sanchez, V. Scarpine, S. Serrano, I. Sevilla-Noarbe, M. Smith, M. Soares-Santos, E. Suchyta, M. E. C. Swanson, G. Tarle, C. To, T. N. Varga, J. Weller, R. D. Wilkinson, and DES Collaboration. Dark Energy Survey Year 3 results: Optimizing the lens sample in a combined galaxy clustering and galaxy-galaxy lensing analysis. Phys. Rev. D, 103(4):043503, February 2021.

[189] David Alonso, Javier Sanchez, Anže Slosar, and LSST Dark Energy Science Collaboration. A unified pseudo-C_ℓ framework. MNRAS, 484(3):4127–4151, April 2019.

[190] Antony Lewis, Anthony Challinor, and Anthony Lasenby. Efficient Computation of Cosmic Microwave Background Anisotropies in Closed Friedmann-Robertson-Walker Models. ApJ, 538(2):473–476, August 2000.

[191] A. J. Mead, J. A. Peacock, C. Heymans, S. Joudaki, and A. F. Heavens. An accurate halo model for fitting non-linear cosmological power spectra and baryonic feedback models. MNRAS, 454(2):1958–1975, December 2015.

[192] Gaia Collaboration, A. G. A. Brown, A. Vallenari, T. Prusti, J. H. J. de Bruijne, C. Babusiaux, C. A. L. Bailer-Jones, M. Biermann, D. W. Evans, L. Eyer, F. Jansen, C. Jordi, S. A. Klioner, U. Lammers, L. Lindegren, X. Luri, F. Mignard, C. Panem, D. Pourbaix, S. Randich, P. Sartoretti,

H. I. Siddiqui, C. Soubiran, F. van Leeuwen, N. A. Walton, F. Arenou, U. Bastian, M. Cropper, R. Drimmel, D. Katz, M. G. Lattanzi, J. Bakker, C. Cacciari, J. Castañeda, L. Chaoul, N. Cheek, F. De Angeli, C. Fabricius, R. Guerra, B. Holl, E. Masana, R. Messineo, N. Mowlavi, K. Nienartowicz, P. Panuzzo, J. Portell, M. Riello, G. M. Seabroke, P. Tanga, F. Thévenin, G. Gracia-Abril, G. Comoretto, M. Garcia-Reinaldos, D. Teyssier, M. Altmann, R. Andrae, M. Audard, I. Bellas-Velidis, K. Benson, J. Berthier, R. Blomme, P. Burgess, G. Busso, B. Carry, A. Cellino, G. Clementini, M. Clotet, O. Creevey, M. Davidson, J. De Ridder, L. Delchambre, A. Dell'Oro, C. Ducourant, J. Fernández-Hernández, M. Fouesneau, Y. Frémat, L. Galluccio, M. García-Torres, J. González-Núñez, J. J. González-Vidal, E. Gosset, L. P. Guy, J. L. Halbwachs, N. C. Hambly, D. L. Harrison, J. Hernández, D. Hestroffer, S. T. Hodgkin, A. Hutton, G. Jasniewicz, A. Jean-Antoine-Piccolo, S. Jordan, A. J. Korn, A. Krone-Martins, A. C. Lanzafame, T. Lebzelter, W. Löffler, M. Manteiga, P. M. Marrese, J. M. Martín-Fleitas, A. Moitinho, A. Mora, K. Muinonen, J. Osinde, E. Pancino, T. Pauwels, J. M. Petit, A. Recio-Blanco, P. J. Richards, L. Rimoldini, A. C. Robin, L. M. Sarro, C. Siopis, M. Smith, A. Sozzetti, M. Süveges, J. Torra, W. van Reeven, U. Abbas, A. Abreu Aramburu, S. Accart, C. Aerts, G. Altavilla, M. A. Álvarez, R. Alvarez, J. Alves, R. I. Anderson, A. H. Andrei, E. Anglada Varela, E. Antiche, T. Antoja, B. Arcay, T. L. Astraatmadja, N. Bach, S. G. Baker, L. Balaguer-Núñez, P. Balm, C. Barache, C. Barata, D. Barbato, F. Barblan, P. S. Barklem, D. Barrado, M. Barros, M. A. Barstow, S. Bartholomé Muñoz, J. L. Bassilana, U. Becciani, M. Bellazzini, A. Berihuete, S. Bertone, L. Bianchi, O. Bienaymé, S. Blanco-Cuaresma, T. Boch, C. Boeche, A. Bombrun, R. Borrachero, D. Bossini, S. Bouquillon, G. Bourda, A. Bragaglia, L. Bramante, M. A. Breddels, A. Bressan, N. Brouillet, T. Brüsemeister, E. Brugaletta, B. Bucciarelli, A. Burlacu, D. Busonero, A. G. Butkevich, R. Buzzi, E. Caffau, R. Cancelliere, G. Cannizzaro, T. Cantat-Gaudin, R. Carballo, T. Carlucci, J. M. Carrasco, L. Casamiquela, M. Castellani, A. Castro-Ginard, P. Charlot, L. Chemin, A. Chiavassa, G. Cocozza, G. Costigan, S. Cowell, F. Crifo, M. Crosta, C. Crowley, J. Cuypers, C. Dafonte, Y. Damerdji, A. Dapergolas, P. David, M. David, P. de Laverny, F. De Luise, R. De March, D. de Martino, R. de Souza, A. de Torres, J. Debosscher, E. del Pozo, M. Delbo, A. Delgado, H. E. Delgado, P. Di Matteo, S. Diakite, C. Diener, E. Distefano, C. Dolding, P. Drazinos, J. Durán, B. Edvardsson, H. Enke, K. Eriksson, P. Esquej, G. Eynard Bontemps, C. Fabre, M. Fabrizio, S. Faigler, A. J. Falcão, M. Farràs Casas, L. Federici, G. Fedorets, P. Fernique, F. Figueras, F. Filippi, K. Findeisen, A. Fonti, E. Fraile, M. Fraser, B. Frézouls, M. Gai, S. Galleti, D. Garabato, F. García-Sedano, A. Garofalo, N. Garralda, A. Gavel, P. Gavras, J. Gerssen, R. Geyer, P. Giacobbe, G. Gilmore, S. Girona,

G. Giuffrida, F. Glass, M. Gomes, M. Granvik, A. Gueguen, A. Guerrier, J. Guiraud, R. Gutiérrez-Sánchez, R. Haigron, D. Hatzidimitriou, M. Hauser, M. Haywood, U. Heiter, A. Helmi, J. Heu, T. Hilger, D. Hobbs, W. Hofmann, G. Holland, H. E. Huckle, A. Hypki, V. Icardi, K. Janßen, G. Jevardat de Fombelle, P. G. Jonker, Á. L. Juhász, F. Julbe, A. Karampelas, A. Kewley, J. Klar, A. Kochoska, R. Kohley, K. Kolenberg, M. Kontizas, E. Kontizas, S. E. Koposov, G. Kordopatis, Z. Kostrzewa-Rutkowska, P. Koubsky, S. Lambert, A. F. Lanza, Y. Lasne, J. B. Lavigne, Y. Le Fustec, C. Le Poncin-Lafitte, Y. Lebreton, S. Leccia, N. Leclerc, I. Lecoeur-Taibi, H. Lenhardt, F. Leroux, S. Liao, E. Licata, H. E. P. Lindstrøm, T. A. Lister, E. Livanou, A. Lobel, M. López, S. Managau, R. G. Mann, G. Mantelet, O. Marchal, J. M. Marchant, M. Marconi, S. Marinoni, G. Marschalkó, D. J. Marshall, M. Martino, G. Marton, N. Mary, D. Massari, G. Matijevič, T. Mazeh, P. J. McMillan, S. Messina, D. Michalik, N. R. Millar, D. Molina, R. Molinaro, L. Molnár, P. Montegriffo, R. Mor, R. Morbidelli, T. Morel, D. Morris, A. F. Mulone, T. Muraveva, I. Musella, G. Nelemans, L. Nicastro, L. Noval, W. O'Mullane, C. Ordénovic, D. Ordóñez-Blanco, P. Osborne, C. Pagani, I. Pagano, F. Pailler, H. Palacin, L. Palaversa, A. Panahi, M. Pawlak, A. M. Piersimoni, F. X. Pineau, E. Plachy, G. Plum, E. Poggio, E. Poujoulet, A. Prša, L. Pulone, E. Racero, S. Ragaini, N. Rambaux, M. Ramos-Lerate, S. Regibo, C. Reylé, F. Riclet, V. Ripepi, A. Riva, A. Rivard, G. Rixon, T. Roegiers, M. Roelens, M. Romero-Gómez, N. Rowell, F. Royer, L. Ruiz-Dern, G. Sadowski, T. Sagristà Sellés, J. Sahlmann, J. Salgado, E. Salguero, N. Sanna, T. Santana-Ros, M. Sarasso, H. Savietto, M. Schultheis, E. Sciacca, M. Segol, J. C. Segovia, D. Ségransan, I. C. Shih, L. Siltala, A. F. Silva, R. L. Smart, K. W. Smith, E. Solano, F. Solitro, R. Sordo, S. Soria Nieto, J. Souchay, A. Spagna, F. Spoto, U. Stampa, I. A. Steele, H. Steidelmüller, C. A. Stephenson, H. Stoev, F. F. Suess, J. Surdej, L. Szabados, E. Szegedi-Elek, D. Tapiador, F. Taris, G. Tauran, M. B. Taylor, R. Teixeira, D. Terrett, P. Teyssandier, W. Thuillot, A. Titarenko, F. Torra Clotet, C. Turon, A. Ulla, E. Utrilla, S. Uzzi, M. Vaillant, G. Valentini, V. Valette, A. van Elteren, E. Van Hemelryck, M. van Leeuwen, M. Vaschetto, A. Vecchiato, J. Veljanoski, Y. Viala, D. Vicente, S. Vogt, C. von Essen, H. Voss, V. Votruba, S. Voutsinas, G. Walmsley, M. Weiler, O. Wertz, T. Wevers, Ł. Wyrzykowski, A. Yoldas, M. Žerjal, H. Ziaeepour, J. Zorec, S. Zschocke, S. Zucker, C. Zurbach, and T. Zwitter. Gaia Data Release 2. Summary of the contents and survey properties. A&A, 616:A1, August 2018.

[193] K. Eckert, G. M. Bernstein, A. Amara, A. Amon, A. Choi, S. Everett, D. Gruen, R. A. Gruendl, E. M. Huff, N. Kuropatkin, A. Roodman, E. Sheldon, B. Yanny, Y. Zhang, T. M. C. Abbott, M. Aguena, S. Avila, K. Bechtol,

D. Brooks, D. L. Burke, A. Carnero Rosell, M. Carrasco Kind, J. Carretero, M. Costanzi, L. N. da Costa, J. De Vicente, S. Desai, H. T. Diehl, J. P. Dietrich, T. F. Eifler, A. E. Evrard, B. Flaugher, J. Frieman, J. García-Bellido, E. Gaztanaga, J. Gschwend, G. Gutierrez, W. G. Hartley, D. L. Hollowood, K. Honscheid, D. J. James, R. Kron, K. Kuehn, M. A. G. Maia, J. L. Marshall, P. Melchior, F. Menanteau, R. Miquel, R. L. C. Ogando, A. Palmese, F. Paz-Chinchón, A. A. Plazas, A. K. Romer, E. Sanchez, V. Scarpine, S. Serrano, I. Sevilla-Noarbe, M. Smith, M. Soares-Santos, E. Suchyta, M. E. C. Swanson, G. Tarle, D. Thomas, T. N. Varga, A. R. Walker, W. Wester, R. D. Wilkinson, J. Zuntz, and DES Collaboration. Noise from undetected sources in Dark Energy Survey images. MNRAS, 497(3):2529–2539, September 2020.

[194] R. Buchs, C. Davis, D. Gruen, J. DeRose, A. Alarcon, G. M. Bernstein, C. Sánchez, J. Myles, A. Roodman, S. Allen, A. Amon, A. Choi, D. C. Masters, R. Miquel, M. A. Troxel, R. H. Wechsler, T. M. C. Abbott, J. Annis, S. Avila, K. Bechtol, S. L. Bridle, D. Brooks, E. Buckley-Geer, D. L. Burke, A. Carnero Rosell, M. Carrasco Kind, J. Carretero, F. J. Castander, R. Cawthon, C. B. D'Andrea, L. N. da Costa, J. De Vicente, S. Desai, H. T. Diehl, P. Doel, A. Drlica-Wagner, T. F. Eifler, A. E. Evrard, B. Flaugher, P. Fosalba, J. Frieman, J. García-Bellido, E. Gaztanaga, R. A. Gruendl, J. Gschwend, G. Gutierrez, W. G. Hartley, D. L. Hollowood, K. Honscheid, D. J. James, K. Kuehn, N. Kuropatkin, M. Lima, H. Lin, M. A. G. Maia, M. March, J. L. Marshall, P. Melchior, F. Menanteau, R. L. C. Ogando, A. A. Plazas, E. S. Rykoff, E. Sanchez, V. Scarpine, S. Serrano, I. Sevilla-Noarbe, M. Smith, M. Soares-Santos, F. Sobreira, E. Suchyta, M. E. C. Swanson, G. Tarle, D. Thomas, V. Vikram, and DES Collaboration. Phenotypic redshifts with self-organizing maps: A novel method to characterize redshift distributions of source galaxies for weak lensing. MNRAS, 489(1):820–841, October 2019.

[195] Jeffrey A. Newman. Calibrating Redshift Distributions beyond Spectroscopic Limits with Cross-Correlations. ApJ, 684(1):88–101, September 2008.

[196] R. Cawthon, J. Elvin-Poole, A. Porredon, M. Crocce, G. Giannini, M. Gatti, A. J. Ross, E. S. Rykoff, A. Carnero Rosell, J. DeRose, S. Lee, M. Rodriguez-Monroy, A. Amon, K. Bechtol, J. De Vicente, D. Gruen, R. Morgan, E. Sanchez, J. Sanchez, I. Sevilla-Noarbe, T. M. C. Abbott, M. Aguena, S. Allam, J. Annis, S. Avila, D. Bacon, E. Bertin, D. Brooks, D. L. Burke, M. Carrasco Kind, J. Carretero, F. J. Castander, A. Choi, M. Costanzi, L. N. da Costa, M. E. S. Pereira, K. Dawson, S. Desai, H. T. Diehl, K. Eckert, S. Everett, I. Ferrero, P. Fosalba, J. Frieman, J. García-Bellido, E. Gaztanaga, R. A. Gruendl, J. Gschwend, G. Gutierrez, S. R. Hinton, D. L.

Hollowood, K. Honscheid, D. Huterer, D. J. James, A. G. Kim, J. P. Kneib, K. Kuehn, N. Kuropatkin, O. Lahav, M. Lima, H. Lin, M. A. G. Maia, P. Melchior, F. Menanteau, R. Miquel, J. J. Mohr, J. Muir, J. Myles, A. Palmese, S. Pandey, F. Paz-Chinchón, W. J. Percival, A. A. Plazas, A. Roodman, G. Rossi, V. Scarpine, S. Serrano, M. Smith, M. Soares-Santos, E. Suchyta, M. E. C. Swanson, G. Tarle, C. To, M. A. Troxel, R. D. Wilkinson, and the DES Collaboration. Dark Energy Survey Year 3 Results: Calibration of Lens Sample Redshift Distributions using Clustering Redshifts with BOSS/eBOSS. *arXiv e-prints*, page arXiv:2012.12826, December 2020.

[197] M. Gatti, G. Giannini, G. M. Bernstein, A. Alarcon, J. Myles, A. Amon, R. Cawthon, M. Troxel, J. DeRose, S. Everett, A. J. Ross, E. S. Rykoff, J. Elvin-Poole, J. Cordero, I. Harrison, C. Sanchez, J. Prat, D. Gruen, H. Lin, M. Crocce, E. Rozo, T. M. C. Abbott, M. Aguena, S. Allam, J. Annis, S. Avila, D. Bacon, E. Bertin, D. Brooks, D. L. Burke, A. Carnero Rosell, M. Carrasco Kind, J. Carretero, F. J. Castander, A. Choi, C. Conselice, M. Costanzi, M. Crocce, L. N. da Costa, M. E. S. Pereira, K. Dawson, S. Desai, H. T. Diehl, K. Eckert, T. F. Eifler, A. E. Evrard, I. Ferrero, B. Flaugher, P. Fosalba, J. Frieman, J. Garcia-Bellido, E. Gaztanaga, T. Giannantonio, R. A. Gruendl, J. Gschwend, S. R. Hinton, D. L. Hollowood, K. Honscheid, B. Hoyle, D. Huterer, D. J. James, K. Kuehn, N. Kuropatkin, O. Lahav, M. Lima, N. MacCrann, M. A. G. Maia, M. March, J. L. Marshall, P. Melchior, F. Menanteau, R. Miquel, J. J. Mohr, R. Morgan, R. L. C. Ogando, A. Palmese, F. Paz-Chinchon, W. J. Percival, A. A. Plazas, M. Rodriguez-Monroy, A. Roodman, G. Rossi, S. Samuroff, E. Sanchez, V. Scarpine, L. F. Secco, S. Serrano, I. Sevilla-Noarbe, M. Smith, M. Soares-Santos, E. Suchyta, M. E. C. Swanson, G. Tarle, D. Thomas, C. To, T. N. Varga, J. Weller, and R. D. Wilkinson. Dark Energy Survey Year 3 Results: Clustering Redshifts – Calibration of the Weak Lensing Source Redshift Distributions with redMaGiC and BOSS/eBOSS. *arXiv e-prints*, page arXiv:2012.08569, December 2020.

[198] Bhuvnesh Jain and Andy Taylor. Cross-correlation tomography: Measuring dark energy evolution with weak lensing. *Phys. Rev. Lett.*, 91:141302, Oct 2003.

[199] C. Sánchez, J. Prat, et al. Dark Energy Survey Year 3 Results: Exploiting Small-Scale Information with Lensing Ratios. *To be submitted to MNRAS*, 2021.

[200] J. P. Cordero, I. Harrison, et al. Dark Energy Survey Year 3 Results: Marginalisation Over Redshift Distribution Uncertainties Using Ranking of Discrete Realisations. *To be submitted to MNRAS*, 2020.

[201] Teuvo Kohonen. Self-organized formation of topologically correct feature maps. *Biological Cybernetics*, 43(1):59–69, January 1982.

[202] D. Gruen and F. Brimioulle. Selection biases in empirical p(z) methods for weak lensing. MNRAS, 468(1):769–782, June 2017.

[203] C. Laigle, H. J. McCracken, O. Ilbert, B. C. Hsieh, I. Davidzon, P. Capak, G. Hasinger, J. D. Silverman, C. Pichon, J. Coupon, H. Aussel, D. Le Borgne, K. Caputi, P. Cassata, Y. Y. Chang, F. Civano, J. Dunlop, J. Fynbo, J. S. Kartaltepe, A. Koekemoer, O. Le Fèvre, E. Le Floc'h, A. Leauthaud, S. Lilly, L. Lin, S. Marchesi, B. Milvang-Jensen, M. Salvato, D. B. Sanders, N. Scoville, V. Smolcic, M. Stockmann, Y. Taniguchi, L. Tasca, S. Toft, Mattia Vaccari, and J. Zabl. The COSMOS2015 Catalog: Exploring the 1 $<$ z $<$ 6 Universe with Half a Million Galaxies. ApJS, 224(2):24, June 2016.

[204] B. Ménard, T. Hamana, M. Bartelmann, and N. Yoshida. Improving the accuracy of cosmic magnification statistics. A&A, 403:817–828, June 2003.

[205] R. Narayan and S. Wallington. Magnification bias and gravitational lensing statistics. In J. Surdej, D. Fraipont-Caro, E. Gosset, S. Refsdal, and M. Remy, editors, *Liege International Astrophysical Colloquia*, volume 31 of *Liege International Astrophysical Colloquia*, page 217, January 1993.

[206] E. Rozo, E. S. Rykoff, A. Abate, C. Bonnett, M. Crocce, C. Davis, B. Hoyle, B. Leistedt, H. V. Peiris, R. H. Wechsler, T. Abbott, F. B. Abdalla, M. Banerji, A. H. Bauer, A. Benoit-Lévy, G. M. Bernstein, E. Bertin, D. Brooks, E. Buckley-Geer, D. L. Burke, D. Capozzi, A. Carnero Rosell, D. Carollo, M. Carrasco Kind, J. Carretero, F. J. Castander, M. J. Childress, C. E. Cunha, C. B. D'Andrea, T. Davis, D. L. DePoy, S. Desai, H. T. Diehl, J. P. Dietrich, P. Doel, T. F. Eifler, A. E. Evrard, A. Fausti Neto, B. Flaugher, P. Fosalba, J. Frieman, E. Gaztanaga, D. W. Gerdes, K. Glazebrook, D. Gruen, R. A. Gruendl, K. Honscheid, D. J. James, M. Jarvis, A. G. Kim, K. Kuehn, N. Kuropatkin, O. Lahav, C. Lidman, M. Lima, M. A. G. Maia, M. March, P. Martini, P. Melchior, C. J. Miller, R. Miquel, J. J. Mohr, R. C. Nichol, B. Nord, C. R. O'Neill, R. Ogando, A. A. Plazas, A. K. Romer, A. Roodman, M. Sako, E. Sanchez, B. Santiago, M. Schubnell, I. Sevilla-Noarbe, R. C. Smith, M. Soares-Santos, F. Sobreira, E. Suchyta, M. E. C. Swanson, J. Thaler, D. Thomas, S. Uddin, V. Vikram, A. R. Walker, W. Wester, Y. Zhang, and L. N. da Costa. redMaGiC: selecting luminous red galaxies from the DES Science Verification data. MNRAS, 461(2):1431–1450, September 2016.

[207] Michael D. Gladders and H. K. C. Yee. A New Method For Galaxy Cluster Detection. I. The Algorithm. AJ, 120(4):2148–2162, October 2000.

[208] E. S. Rykoff, E. Rozo, M. T. Busha, C. E. Cunha, A. Finoguenov, A. Evrard, J. Hao, B. P. Koester, A. Leauthaud, B. Nord, M. Pierre, R. Reddick, T. Sadibekova, E. S. Sheldon, and R. H. Wechsler. redMaPPer. I. Algorithm and SDSS DR8 Catalog. ApJ, 785(2):104, April 2014.

[209] P. Fosalba, M. Crocce, E. Gaztañaga, and F. J. Castander. The MICE grand challenge lightcone simulation - I. Dark matter clustering. MNRAS, 448(4):2987–3000, April 2015.

[210] M. Crocce, F. J. Castander, E. Gaztañaga, P. Fosalba, and J. Carretero. The MICE Grand Challenge lightcone simulation - II. Halo and galaxy catalogues. MNRAS, 453(2):1513–1530, October 2015.

[211] P. Fosalba, E. Gaztañaga, F. J. Castander, and M. Crocce. The MICE Grand Challenge light-cone simulation - III. Galaxy lensing mocks from all-sky lensing maps. MNRAS, 447(2):1319–1332, February 2015.

[212] Joseph DeRose, Risa H. Wechsler, Matthew R. Becker, Michael T. Busha, Eli S. Rykoff, Niall MacCrann, Brandon Erickson, August E. Evrard, Andrey Kravtsov, Daniel Gruen, Sahar Allam, Santiago Avila, Sarah Bridle, David Brooks, Elizabeth Buckley-Geer, Aurelio Carnero Rosell, Matias Carrasco Kind, Jorge Carretero, Francisco J. Castander, Ross Cawthon, Martin Crocce, Luiz N. da Costa, Christopher Davis, Juan De Vicente, Jörg P. Dietrich, Peter Doel, Alex Drlica-Wagner, Pablo Fosalba, Josh Frieman, Juan Garcia-Bellido, Gaston Gutierrez, Will G. Hartley, Devon L. Hollowood, Ben Hoyle, David J. James, Elisabeth Krause, Kyler Kuehn, Nikolay Kuropatkin, Marcos Lima, Marcio A. G. Maia, Felipe Menanteau, Christopher J. Miller, Ramon Miquel, Ricardo L. C. Ogando, Andrés Plazas Malagón, A. Kathy Romer, Eusebio Sanchez, Rafe Schindler, Santiago Serrano, Ignacio Sevilla-Noarbe, Mathew Smith, Eric Suchyta, Molly E. C. Swanson, Gregory Tarle, and Vinu Vikram. The Buzzard Flock: Dark Energy Survey Synthetic Sky Catalogs. *arXiv e-prints*, page arXiv:1901.02401, January 2019.

[213] J. DeRose et al. Dark Energy Survey Year 3 Results: Validating 3×2-point Modeling and Analysis Choices using Cosmological Simulations. *To be submitted to*, 2021.

[214] DES Collaboration et al. Dark Energy Survey Year 3 Results: Cosmological Constraints from Galaxy Clustering and Weak Lensing. *To be submitted to*, 2021.

[215] S. Samuroff, S. L. Bridle, J. Zuntz, M. A. Troxel, D. Gruen, R. P. Rollins, G. M. Bernstein, T. F. Eifler, E. M. Huff, T. Kacprzak, E. Krause, N. MacCrann, F. B. Abdalla, S. Allam, J. Annis, K. Bechtol, A. Benoit-Lévy,

E. Bertin, D. Brooks, E. Buckley-Geer, A. Carnero Rosell, M. Carrasco Kind, J. Carretero, M. Crocce, C. B. D'Andrea, L. N. da Costa, C. Davis, S. Desai, P. Doel, A. Fausti Neto, B. Flaugher, P. Fosalba, J. Frieman, J. García-Bellido, D. W. Gerdes, R. A. Gruendl, J. Gschwend, G. Gutierrez, K. Honscheid, D. J. James, M. Jarvis, T. Jeltema, D. Kirk, K. Kuehn, S. Kuhlmann, T. S. Li, M. Lima, M. A. G. Maia, M. March, J. L. Marshall, P. Martini, P. Melchior, F. Menanteau, R. Miquel, B. Nord, R. L. C. Ogando, A. A. Plazas, A. Roodman, E. Sanchez, V. Scarpine, R. Schindler, M. Schubnell, I. Sevilla-Noarbe, E. Sheldon, M. Smith, M. Soares-Santos, F. Sobreira, E. Suchyta, G. Tarle, D. Thomas, D. L. Tucker, and DES Collaboration. Dark Energy Survey Year 1 results: the impact of galaxy neighbours on weak lensing cosmology with IM3SHAPE. MNRAS, 475(4):4524–4543, April 2018.

[216] Joe Zuntz, Tomasz Kacprzak, Lisa Voigt, Michael Hirsch, Barnaby Rowe, and Sarah Bridle. IM3SHAPE: a maximum likelihood galaxy shear measurement code for cosmic gravitational lensing. MNRAS, 434(2):1604–1618, September 2013.

[217] Euclid Collaboration, N. Martinet, T. Schrabback, H. Hoekstra, M. Tewes, R. Herbonnet, P. Schneider, B. Hernandez-Martin, A. N. Taylor, J. Brinchmann, C. S. Carvalho, M. Castellano, G. Congedo, B. R. Gillis, E. Jullo, M. Kümmel, S. Ligori, P. B. Lilje, C. Padilla, D. Paris, J. A. Peacock, S. Pilo, A. Pujol, D. Scott, and R. Toledo-Moreo. Euclid preparation. IV. Impact of undetected galaxies on weak-lensing shear measurements. A&A, 627:A59, July 2019.

[218] Y. Zhang, B. Yanny, A. Palmese, D. Gruen, C. To, E. S. Rykoff, Y. Leung, C. Collins, M. Hilton, T. M. C. Abbott, J. Annis, S. Avila, E. Bertin, D. Brooks, D. L. Burke, A. Carnero Rosell, M. Carrasco Kind, J. Carretero, C. E. Cunha, C. B. D'Andrea, L. N. da Costa, J. De Vicente, S. Desai, H. T. Diehl, J. P. Dietrich, P. Doel, A. Drlica-Wagner, T. F. Eifler, A. E. Evrard, B. Flaugher, P. Fosalba, J. Frieman, J. García-Bellido, E. Gaztanaga, D. W. Gerdes, R. A. Gruendl, J. Gschwend, G. Gutierrez, W. G. Hartley, D. L. Hollowood, K. Honscheid, B. Hoyle, D. J. James, T. Jeltema, K. Kuehn, N. Kuropatkin, T. S. Li, M. Lima, M. A. G. Maia, M. March, J. L. Marshall, P. Melchior, F. Menanteau, C. J. Miller, R. Miquel, J. J. Mohr, R. L. C. Ogando, A. A. Plazas, A. K. Romer, E. Sanchez, V. Scarpine, M. Schubnell, S. Serrano, I. Sevilla-Noarbe, M. Smith, M. Soares-Santos, F. Sobreira, E. Suchyta, M. E. C. Swanson, G. Tarle, D. Thomas, W. Wester, and DES Collaboration. Dark Energy Survey Year 1 Results: Detection of Intracluster Light at Redshift ~ 0.25. ApJ, 874(2):165, April 2019.

[219] P. Melchior, F. Moolekamp, M. Jerdee, R. Armstrong, A. L. Sun, J. Bosch,

and R. Lupton. SCARLET: Source separation in multi-band images by Constrained Matrix Factorization. *Astronomy and Computing*, 24:129, July 2018.

[220] David M. Reiman and Brett E. Göhre. Deblending galaxy superpositions with branched generative adversarial networks. MNRAS, 485(2):2617–2627, May 2019.

[221] Harry Johnston, Angus H. Wright, Benjamin Joachimi, Maciej Bilicki, Nora Elisa Chisari, Andrej Dvornik, Thomas Erben, Benjamin Giblin, Catherine Heymans, Hendrik Hildebrandt, Henk Hoekstra, Shahab Joudaki, and Mohammadjavad Vakili. Organised Randoms: learning and correcting for systematic galaxy clustering patterns in KiDS using self-organising maps. *arXiv e-prints*, page arXiv:2012.08467, December 2020.